

Zinc oxide ultraviolet light-emitting devices : design and fabrication

Yuen, Clement

2007

Yuen, C. (2007). Zinc oxide ultraviolet light-emitting devices : design and fabrication.
Doctoral thesis, Nanyang Technological University, Singapore.

<https://hdl.handle.net/10356/42271>

<https://doi.org/10.32657/10356/42271>



**NANYANG
TECHNOLOGICAL
UNIVERSITY**

**ZINC OXIDE ULTRAVIOLET LIGHT-EMITTING
DEVICES: DESIGN AND FABRICATION**

CLEMENT YUEN

SCHOOL OF ELECTRICAL & ELECTRONICS ENGINEERING

2007

Zinc Oxide Ultraviolet Light-emitting Devices: Design and Fabrication

Clement Yuen

School of Electrical and Electronic Engineering

A thesis submitted to the Nanyang Technological University
in fulfillment of the requirement for the degree of
Doctor of Philosophy

2007

ACKNOWLEDGMENTS

Greatest thanks given to my Ph. D. project supervisor, Assoc. Prof. Yu Siu Fung. He is always advising, encouraging and supporting me throughout the project, especially in times of difficulties. In addition, he has been imparting his knowledge and expertise to me in the area of research. Without his guidance and motivations, it would not be possible for me to overcome the setbacks and obstacles encountered.

I have been fortunate to have Assoc. Prof. Lau Shu Ping as my mentor. He allowed me to have the privilege to be one of his research group members and to use his state of art experimental equipment. Furthermore, his creativity and intelligence are my sources of stimulations and initiations in my research work.

It is my honor and pleasure that the head of department of Electrical and Electronic Engineering (EEE) division 6, Assoc. Prof. Tan Ooi Kiang, the vice-dean of administration, Assoc. Prof. Tay Beng Kang, and the head of Ion Beam Processing (IBP) laboratory, Prof. Zhu Wei Guang, of Nanyang Technological University (NTU) approved me to be a research student in the IBP laboratory under the EEE division 6 in NTU.

I am also grateful to all the present and past members of our group, Dr. Li Hong Dong, Dr. Wang Yu Guang, Mr. Agus Putu Abiyasa, Mr. Chen Nan Shu, Mr. Herng Tun Seng, Mrs. Ji Xiao Hong, Mr. Lee Hiong Weng, Ms. Leong Sok Ping, Mr. Xie Hua and Ms. Yang Hui Ying, for offering their help to me in my project.

Acknowledgements

I would also like to give special thanks to Prof. Gyu Chul Yi and Dr. Won Il Park of Pohang University of Science and Technology, Korea, and Prof. Tanemura Masaki of Nagoya Institute of Technology, Japan, for providing me with their excellent experimental samples.

I am indebted to Assoc. Prof. Chen Tu Pei, Asst. Prof. Chen Chung Kit, Asst. Prof. Dong Zhi Li, Assoc. Prof. Fan Wei Jun, Asst. Prof. Hng Huey Hoon, Assoc. Prof. Rusli, Asst. Prof. Sean Li, Assoc. Prof. Sun Xiao Wei, Dr. Chen Bai Jun and Dr. Xu Chun Xiang for their advice and help during my research.

Gratitude is also given to the present and past staffs and students in the Photonics I and II laboratory, and the IBP laboratory, in particular Dr. Huang Lei, Dr. Sheeja Divakaran, Dr. Sun Zhuo, Dr. Yu Guo Qing, Mdm. Sze Jia Yin, and Mr. Koh Wee Shing, who had offered their aid to me in one way or another.

Appreciations would be given to all the laboratory technicians, Mr. Hasman Bin Hassan, Mdm. Teh Hsieh Foong and Mdm. Wee-Neo Bee Geok of IBP laboratory, Mr. Muhd Fauzi Bin Abudullah of clean room, Mdm. Seet Lye Ping, Mdm. Yee Yang Boey and Mr. Yong Kim Lam of Photonics I laboratory, Mr. Chow Kam Wah, Mdm. Leng-Low Poh Chee, Mr. Lim Teng Keng, Mr. Tan Ah Koon and Mdm. Yang-Chia Hwee Keng of Photonics II laboratory, and Mdm. Chia Ai Lay, Mdm. Kwek Lee Boon and Mdm. Yong-Koh Piak Yok of Microfabrication facilities laboratory. They have patiently taught me the experimental skills and the technical knowledge of the laboratory equipment.

Acknowledgements

My heartfelt gratitude to the Nippon Sheet Glass Foundation of Japan and the Agency for Science, Technology, and Research of Singapore (A*STAR) for financially supporting me in this project. I specially thank A*STAR for awarding me an A*STAR-NTU graduate fellowship and supporting me financially in pursuing this Ph. D. degree.

I also appreciate my friends, in particular Mr Neu Wee Teck, for helping me to check my thesis.

Deepest thanks to my parents for their unconditional care and love in supporting me throughout my life, especially their concerns and understanding showered upon me during this project. They are the strength that sustains me throughout the entire project.

Acknowledgements

Dedicated to my parents

SUMMARY

ZnO is one of the semiconductor materials that shows great potential in the fabrication of ultraviolet (UV) light-emitting devices for diverse applications. However, most of the high-quality ZnO thin films are fabricated on expensive lattice-matched sapphire substrates at high temperature ($>350\text{ }^{\circ}\text{C}$). They are not suitable to be manufactured in large quantities and integrated with other silicon-based devices. Besides that, the properties of the ZnO films grown at high temperature are difficult to be modified by post-growth process. Therefore, we proposed the use of filtered cathodic vacuum arc (FCVA) technique to fabricate ZnO thin films and UV light-emitting devices. This is because the FCVA technique has major advantages: 1) The lattice-matching requirement between the substrate and the deposited film is not needed, 2) it is a low-temperature deposition process ($<350\text{ }^{\circ}\text{C}$) due to the high kinetic energies of the deposited species, 3) it allows the fabrication of thin films on large substrates (as large as 6" in diameter), 4) it provides freedom of choices in the target materials for the fabrication of doped and undoped films, since the stoichiometry of the deposited films are independent of that of the targets, 5) it produces microparticle-free thin films, and 6) it is a cost-effective technique to fabricate thin films that is well established and accepted by the industry for mass production.

In this thesis, we report the fabrication of ZnO thin-film planar and ridge waveguides on Si at low deposition temperature by the FCVA technique. In addition, we have investigated the net optical gains and confinement characteristics

Summary

of the ZnO waveguides on Si. This study is important to the realization of ZnO UV light-emitting devices on Si in the ZnO research arena and in this work.

In this work, one category of the ZnO UV light-emitting devices that we have targeted to fabricate is the ZnO UV random laser. Its lasing mechanism is based on light scattering from the disordered grains that act as scatterers. Although it has been demonstrated, the sizes and distributions of the scatterers are difficult to control in the ZnO epilayers. In order to overcome this problem, we fabricated ZnO epilayers and they were used to embed with ZnO nanorod arrays. With the designed sizes and distributions of the ZnO nanorods acting as scatterers of light, the ZnO epilayers provide optical gains to them and result in random lasing action that is not observed in either alone.

Furthermore, this work has realized random lasing action in a ZnO thin-film ridge structure on Si fabricated by the FCVA technique at low deposition temperature. A post-growth annealing method has been proposed in the generation of disordered grains to act as scatterers in the random lasing action. The random lasing cavities inside the annealed ZnO films are effectively manipulated by the annealing temperature and time. Moreover, coherent and incoherent random lasing cavities were demonstrated in ZnO epilayers on Si by modification in the process and material engineering, based on this post-growth annealing method.

Although ZnO UV random lasers have been fabricated, the cavities of the lasers exhibit high losses and their output emission beams are not directional. Hence, in this thesis, a capping layer has been used to eliminate the undesired lasing

Summary

characteristics. A low-loss and directional output ZnO thin-film ridge waveguide random laser has been fabricated.

As aforesaid, the FCVA technique allows the fabrication of high-quality ZnO thin films at low deposition temperature. However, there is no report in employing the FCVA technique for the fabrication of high-quality UV ZnO light-emitting diodes (LEDs). In this thesis, the fabrication of a heterojunction ZnO/SiC UV LED at low deposition temperature by the FCVA method is described.

TABLE OF CONTENTS

ACKNOWLEDGMENTS.....	I
SUMMARY	V
TABLE OF CONTENTS	VIII
LIST OF FIGURES	XI
LIST OF TABLES	XIV
NOMENCLATURES	XV
CHAPTER 1 Introduction	1
1.1 Motivation.....	1
1.2 Objectives	4
1.3 Major Contributions of the Thesis	6
1.4 Organization of the Thesis.....	8
CHAPTER 2 Deposition Techniques of Zinc Oxide Films	10
2.1 Introduction.....	10
2.2 ZnO Deposition Techniques	10
2.3 Vacuum Arc Deposition Techniques	17
2.3.1 Macroparticle Control	19
2.3.2 Filtered Cathodic Vacuum Arc Deposition Technique	21
2.4 Conclusion	23
CHAPTER 3 ZnO Waveguides	28
3.1 Introduction.....	28
3.2 The ZnO Planar Waveguides on Silicon.....	28
3.2.1 Design of the ZnO Planar Waveguides on Silicon.....	28
3.2.2 Fabrication of the ZnO Planar Waveguides on Silicon	30
3.2.3 Characterization of the ZnO Planar Waveguides on Silicon.....	32
3.3 The ZnO Ridge Waveguides on Silicon	36
3.3.1 Design of the ZnO Ridge Waveguides on Silicon	36
3.3.2 Fabrication of the ZnO Ridge Waveguides on Silicon.....	37
3.3.3 Characterization of the ZnO Ridge Waveguides on Silicon and Discussion	39
3.4 Conclusion	43
CHAPTER 4 ZnO Random Lasers	44
4.1 Introduction.....	44
4.2 ZnO Nanorod Arrays Embedded in ZnO Epilayers.....	47
4.2.1 Design of the ZnO Nanorod Arrays Embedded in ZnO Epilayers.....	47
4.2.2 Fabrication of the ZnO Nanorods Arrays Embedded in ZnO Epilayers	49
4.2.3 Characterization of the ZnO Nanorod Arrays fabricated by Metalorganic Vapor-phase Epitaxy System	50
4.2.4 Characterization of the ZnO Nanorod Arrays Embedded in ZnO Epilayers.....	53
4.3 Conclusion	58

Table of Contents

CHAPTER 5 ZnO Thin-film Random Lasers	60
5.1 Introduction	60
5.2 ZnO Thin-film Random Lasers	60
5.2.1 Design of the ZnO Thin-film Random Lasers	60
5.2.2 Fabrication of the ZnO Thin-film Random Lasers	61
5.2.3 Characterization of ZnO Thin-film Random Lasers	63
5.3 Coherent and Incoherent ZnO Thin-film Random lasers	68
5.3.1 Design of the Coherent and Incoherent ZnO Thin-film Random Lasers	69
5.3.2 Fabrication of the Coherent and Incoherent ZnO Thin-film Random Lasers	70
5.3.3 Characterization of the Coherent and Incoherent ZnO Thin-film Random Lasers and Discussion	71
5.4 Conclusion	76
CHAPTER 6 Low-loss and Directional Output ZnO Thin-film Ridge Waveguide Random Lasers	78
6.1 Introduction	78
6.2 Low-loss and Directional Output ZnO Thin-film Ridge Waveguide Random Lasers	79
6.2.1 Design of the Low-loss and Directional Output ZnO Thin-film Ridge Waveguide Random Lasers	79
6.2.2 Fabrication of the Low-loss and Directional Output ZnO Thin-film Ridge Waveguide Random Lasers	80
6.2.3 Characterization of the Low-loss and Directional Output ZnO Thin-film Ridge Waveguide Random Lasers and Discussion	82
6.3 Conclusion	92
CHAPTER 7 ZnO Heterojunctions Light-emitting Diodes	93
7.1 Introduction	93
7.2 ZnO Heterojunction Light-emitting Diodes	93
7.2.1 Design of the ZnO Heterojunction Light-emitting Diodes	93
7.2.2 Fabrication of the ZnO Heterojunction Light-emitting Diodes	95
7.2.3 Characterization of the ZnO Heterojunction Light-emitting Diodes and Discussion	98
7.3 Conclusion	105
CHAPTER 8 Conclusion and Recommendations for Future Research	107
8.1 Conclusion	107
8.2 Recommendations for Future Research	110
AUTHOR'S PUBLICATIONS (Related to this thesis)	112
Journal Papers	112
Conference Papers	113
Patent	114
AUTHOR'S PUBLICATIONS (Not related to this thesis)	115
Journal Papers	115
Conference Papers	116
APPENDIX A ZnO Properties and ZnO Nanorods	117

Table of Contents

A.1	Crystal Structure	117
A.2	Band Structure and Other ZnO Properties	119
A.3	ZnO Nanorods.....	122
APPENDIX B	Photoluminescence	123
B.1	Optical Setup.....	123
B.2	Equipment Communication	125
B.3	Entire Layout	127
B.4	Pulse Controlling Circuit	128
B.5	Software Program	131
APPENDIX C	Variable Stripe Length Method Measurement	135
C.1	Optical Setup.....	135
C.2	Measurement for VSL Method	136
APPENDIX D	Far- and Near-Field Profile	137
D.1	Far-Field Profile	137
D.2	Near-Field Profile	137
APPENDIX E	Formation of UV and Visible Random Lasing Cavities at Different Annealing Temperature and Duration.....	139
APPENDIX F	Loss in Gain Threshold Equation.....	142
APPENDIX G	Derivation of Equation for One-mirror Random laser ..	144
APPENDIX H	Electroluminescence Measurement.....	148
H.1	Optical Setup.....	148
H.2	Equipment Communication	149
H.3	Entire layout.....	150
H.4	Pulse Modulating Circuit	151
H.5	Software Program	154
APPENDIX I	Current-voltage and Light-voltage Measurement	159
I.1	Experimental Setup	159
I.2	Software Program	160
APPENDIX J	Ideality Factor in the Diode Equation.....	162
REFERENCES	164

LIST OF FIGURES

Figure 2.1 Schematic diagram of the MOCVD deposition system [59].	11
Figure 2.2 Schematic diagram of the MBE deposition system [22].	12
Figure 2.3 Schematic diagram of the rf magnetron sputtering system [117].	14
Figure 2.4 Schematic diagram of the PLD system [157].	16
Figure 2.5 Schematic diagram of the typical vacuum arc deposition system.	18
Figure 2.6 Schematic diagram of the off-plane double-bend filter.	20
Figure 2.7 Schematic diagram of filter cathodic vacuum arc system [23].	21
Figure 2.8 RT photoluminescence (PL) spectra of ZnO films grown on quartz substrate at various oxygen pressures: (A) 3.5×10^{-4} , (B) 5×10^{-4} , (C) 6.5×10^{-4} , and (D) 8×10^{-4} Torr [23].	24
Figure 3.1 Proposed schematic diagram of the thin-film ZnO planar waveguide. ASE: amplified spontaneous emission. TM: transverse magnetic. TE: transverse electric.	29
Figure 3.2 (a) Light-light curves for the two polarizations of the thin-film planar waveguide and (b) the corresponding emission spectra of the two polarizations at different pump intensities.	32
Figure 3.3 Net optical gain versus pump intensities for TE and TM polarizations of the ZnO thin-film planar waveguide.	33
Figure 3.4 Scanning electron microscope image of the cross-sectional ZnO/SiO ₂ /Si interfaces.	34
Figure 3.5 (a) Far-field profiles of both polarizations under pump intensity of ~ 1.3 MW/cm ² . (b) Far-field profile of TE mode. (c) Far-field profile of TM mode. The dotted lines indicate the location of the sample.	35
Figure 3.6 Proposed schematic diagram of the thin-film ridge waveguide.	36
Figure 3.7 Fabrication procedures of the proposed ZnO ridge waveguide. (a) The SiO ₂ buffer layer is formed on the silicon substrate by thermal oxidation. (b) Deposition of ZnO thin film on a SiO ₂ buffer layer by FCVA. (c) Deposition of line masks on the ZnO thin film for the preparation of plasma etching. (d) Formation of ridge waveguide after plasma etching and removal of photoresist.	37
Figure 3.8 (a) Light-light curves for both polarizations and (b) corresponding spectra for the ZnO ridge waveguide.	40
Figure 3.9 Net optical gain of the ZnO ridge waveguide versus pump power for the TE and TM polarizations.	41
Figure 3.10 (a) Near-field of the TE mode at < 0.5 MW/cm ² excitation. (b) Far-field of the TE mode at ~ 1 MW/cm ² excitation. The dotted-dashed lines indicated the location of the sample.	42
Figure 4.1 Proposed design of the ZnO nanorod arrays embedded in the ZnO epilayers. TM: transverse magnetic. TE: transverse electric.	47
Figure 4.2 (a) Unpolarized light-light curve and (b) corresponding emission spectra for the ZnO nanorod arrays detected along the symmetric axis of the nanorod. The inset shows that the ZnO nanorod arrays were excited by a pump beam illuminated at an angle of 10° to surface normal of the sapphire substrate.	50
Figure 4.3 Emission spectra of the ZnO nanorod arrays detected parallel to the surface of the substrate.	52
Figure 4.4 Light-light curves and the corresponding emission spectra of the (a) TE and (b) TM polarizations from the ZnO nanorod arrays embedded in the	

List of Figures

	ZnO epilayers. The insets of the top-left-hand side corner are the emission spectra at various pump intensities and that on the bottom-right-hand side corner is a schematic diagram showing the formation of closed-loop path for light through recurrent scattering (dashed arrow) and single-broad ASE spectra (solid arrow) in the sample.....	53
Figure 4.5	Spectra of the TE polarization radiate from 30° to 60° from the sample surface. The pump intensity is 2 MW/cm^2 and the excitation area is kept at $3 \times 10^{-3} \text{ cm}^2$	55
Figure 4.6	Spectra of the TE polarization of the sample when the excitation area is (from top to bottom) 3×10^{-3} , 1.5×10^{-3} , 1×10^{-3} and $5 \times 10^{-4} \text{ cm}^2$. The excitation intensity is 2.6 MW/cm^2	56
Figure 4.7	Dependence of the threshold pump area (A_{th}) on the threshold pump power (P_{th}) of the ZnO nanorod arrays embedded in the ZnO epilayers for the TE polarization.	57
Figure 5.1	Schematic diagram of the ZnO thin-film random laser.....	61
Figure 5.2	Fabrication procedures of the proposed ZnO ridge waveguide random laser. (a) The SiO_2 buffer layer is formed on the silicon substrate by thermal oxidation, followed by the deposition of ZnO thin film on a SiO_2 buffer layer by the FCVA technique. (b) The sample is post-growth annealed. (c) Deposition of line masks on the ZnO thin film for the preparation of plasma etching. (d) ZnO ridge waveguide random laser is formed from plasma etching the photoresist unmask region and the subsequent removal of photoresist line mask that protects the ridge.	62
Figure 5.3	Light-light curve and the emission spectra of the sample after post-growth annealing for $T_a = 1 \text{ min}$	63
Figure 5.4	Light-light curve and the emission spectra of the sample after post-growth annealing for $T_a = 2 \text{ h}$	65
Figure 5.5	Scanning electron microscope (SEM) images of ZnO thin films: (a) as-grown, (b) $T_a = 1 \text{ min}$, and (c) $T_a = 2 \text{ h}$. (d) Emission spectra of the ZnO thin films: (i) as-grown, (ii) $T_a = 1 \text{ min}$, and (iii) $T_a = 2 \text{ h}$	66
Figure 5.6	Plot of $A_{th}^{2/3}$ against P_{th}^{-1} for the post-growth samples with $T_a = 1 \text{ min}$, and $T_a = 2 \text{ h}$	67
Figure 5.7	Proposed schematic of the two different configurations that give rise to MgO film that is dominated in the (a) (220)-orientation and (b) (200)-orientation.	69
Figure 5.8	X-ray diffraction spectra (XRD) of the as-deposited and the annealed (a) ZnO-MgO-Si and (b) ZnO-MgO-ZnO-Si samples.	71
Figure 5.9	SEM images of the ZnO surface of the (a) annealed ZnO-MgO-Si sample and (b) annealed ZnO-MgO-ZnO-Si sample.....	73
Figure 5.10	(a) Light-light curves for the two polarizations of the annealed ZnO-MgO-Si sample and (b) the corresponding emission spectra of the two polarizations, with the MgO layer pre-annealed prior to the deposition of the ZnO layer, followed by annealing of the entire sample. SE: spontaneous emission.	74
Figure 5.11	(a) Light-light curves for the two polarizations of the annealed ZnO-MgO-ZnO-Si sample and (b) the corresponding emission spectra of the two polarizations, with the entire sample annealed at 900°C for 3 h	75
Figure 6.1	Proposed schematic diagram of the ZnO thin-film ridge waveguide random laser with a MgO capped layer.	79

List of Figures

Figure 6.2 Scanning electron microscope image of the annealed ZnO thin film after etching a ridge structure by ion-beam sputtering.....	82
Figure 6.3 Transverse-electric (TE) emission far-fields of the samples (a) with and (b) without MgO capped layer at pump intensity of 1.2 MW/cm ² . The dashed lines indicate the location of the sample.....	83
Figure 6.4 Unpolarized (a) light-light curves and (b) emission spectra of the samples with (○) and without (●) MgO capped layer measured at room temperature.....	84
Figure 6.5 Schematic cross section of the annealed ZnO ridge waveguide with MgO capped layer. The dashed arrows indicate light rays that are being total internally reflected by the MgO capped and Zn _x Si _{1-x} O layers.....	85
Figure 6.6 Unpolarized (a) light-light curves and (b) emission spectra of the samples coated with Al on one of the facets with (●) and without (■) MgO capped layer measured at room temperature.....	86
Figure 6.7 Plots of $P_{th}b_N$ versus L^{-1} for the samples with (dashed line) and without (solid line) MgO capped layer where P_{th} was measured from the samples by varying L from 1 to 3 mm. $b_N = 0.77 \times 10^{-3} \text{ cmW}^{-1}$ is used in the plot.....	88
Figure 6.8 Plots of $P_{th,M}b_N$ (solid line) and $P_{th,M}/P_{th}$ (dashed line) versus L^{-1} . The solid line is obtained from linear regression fitting within 5% tolerance (i.e., $b_N P_{th} \pm 5 \text{ cm}^{-1}$). $b_N = 0.77 \times 10^{-3} \text{ cmW}^{-1}$ is used in the plot.....	89
Figure 6.9 Schematic illustrations of the pumping scheme of random cavity with a mirror proposed by (a) Feng and coworkers [268] and (b) our group..	91
Figure 7.1 Proposed schematic diagram of the $n\text{-ZnO:Al}/p\text{-SiC}$ (4H) heterojunction LED structure and the suggested setup for light detection.....	94
Figure 7.2 Fabrication procedures of the proposed ZnO heterojunction LED. (a) Deposition of a ZnO:Al (3%) layer on the polished surface of the $p\text{-SiC}$ substrate by the FCVA technique. (b) Deposition of an Al layer, then a Ti layer, by electron-beam evaporation. (c) Undergoing rapid thermal annealing with another identical sample stacked on top at 800 °C for 5 min in a N ₂ environment. (d) Deposition of ZnO:Al (7%) layer on top of the ZnO:Al (3%) layer by the FCVA technique.....	96
Figure 7.3 Solid lines: current-voltage characteristics of the Al/Ti metallization on $p\text{-SiC}$ before and after rapid thermal annealing at 800 °C for 5 min. Dash line: current-voltage characteristics of the Ni metallization on $n\text{-ZnO:Al(7%)}$	99
Figure 7.4 Room-temperature electroluminescence (EL) spectra of the $n\text{-ZnO:Al(3%)/}p\text{-SiC(4H)}$ heterojunction LED at various forward biased voltage.....	100
Figure 7.5 Room-temperature PL spectra of an annealed ZnO:Al(3%)/ $p\text{-SiC}$ and a bare $p\text{-SiC(4H)}$ substrate under the optical excitation by a frequency tripled Nd:YAG laser (355 nm) at pulsed operation (6 ns, 10 Hz).....	101
Figure 7.6 XRD pattern of the AlZnO thin film deposited on the SiC substrate at 150°C.....	102
Figure 7.7 Room-temperature current-voltage and light-voltage characteristics of the $n\text{-ZnO:Al(3%)/}p\text{-SiC(4H)}$ heterojunction LED. The insert shows the enlarged current –voltage curve at reverse biased.....	103
Figure 7.8 Proposed electrical circuit model for the heterojunction LED for the calculation of the ideal factor.....	104

LIST OF TABLES

Table 2.1 Characteristics of the different ZnO thin-film deposition techniques. ...26

NOMENCLATURES

ASCII	American Standard Code for Information Interchange
ASE	Amplified Spontaneous Emission
BNC	Bayonet Neill-Concelman
CPU	Central Processing Unit
DEZn	Diethylzinc
DI	Deionized
EHP	Electron Hole Plasma
EL	Electroluminescence
FCVA	Filtered Cathodic Vacuum Arc
FWHM	Full Width at Half Maximum
GPIB	General Purpose Interface Bus
GUI	Graphical User Interface
IRQ	Interrupt Request
LED	Light-emitting diode
MBE	Molecular Beam Epitaxy
MOCVD	Metalorganic Chemical Vapor Deposition
MOVPE	Metalorganic vapor-phase epitaxy
OPDB	Off-plane Double-bend
PL	Photoluminescence
PLD	Pulse Laser Deposition
PMT	Photomultiplier Tube
rf	Radio Frequency

Nomenclatures

RT	Room Temperature
RTA	Rapid Thermal Annealing
SE	Spontaneous Emission
SEL	Surface-Emitting Lasers
SEM	Scanning Electron Microscope
SSP	Surelite Separation Package
TE	Transverse Electric
TM	Transverse Magnetic
UV	Ultraviolet
VSL	Variable Stripe Length
XRD	X-ray Diffraction

CHAPTER 1 Introduction

1.1 Motivation

Ultraviolet (UV) light-emitting device is an indispensable and critical component for diverse applications ranging from commercial [1] to military uses [2] and from scientific [3,4,5] to biomedical technologies [6,7,8,9,10]. Hence, its importance has stimulated research to focus on the wide bandgap materials, especially for materials like diamond [11], SiC [12], BN [13], GaN [14], ZnO [15], ZnS [16] and ZnSe [17], with a bandgap of approximately or above 3 eV. Among them ZnO (its crystal structure, band diagram and other properties are given in APPENDIX A) is a good candidate as a room-temperature UV lasing material [15], since it is different from diamond [18], BN [13] and SiC [12] and has a direct bandgap, that allows direct carrier recombination. Besides, it has a large exciton binding energy of 60 meV [15], significantly larger than that of GaN [14], ZnS [16] and ZnSe [15]. Although fabrication of high-quality ZnO films has been demonstrated [19,20,21,22], they are required to deposit on lattice-matched substrates (as for example, expensive sapphire with 2" in diameter) at high deposition temperature ($>350^{\circ}\text{C}$). This is because 1) sapphire has a similar hexagonal crystal structure to that of the ZnO, and 2) high deposition temperature is required to ensure the high diffusion rate of the constituent species that form a ZnO film with good crystalline quality. The lattice-matching requirement makes the films difficult to integrate with other silicon-based optoelectronic devices. Besides that, high deposition temperature makes the properties and morphologies of the films difficult to be modified by other post-growth processes. Hence, a filtered cathodic vacuum arc

(FCVA) technique has been developed to deposit high-quality ZnO films on large Si wafers at low deposition temperature [23,24,25,26]. It can also be employed as one of the potential fabrication methods to mass-produce ZnO light-emitting devices at a lower cost when compared to other techniques that have been employed in the literature.

In the literature, the optically pumped lasers and the electrically powered light-emitting diodes (LEDs) are two main categories among the other types of ZnO light-emitting devices. In the category of optically pumped lasers, they are realized and evolved from investigations and optimizations in the net optical gain of epitaxial thin films and waveguides [27,28,29,30]. However, these investigations are based on the findings in the ZnO thin films fabricated on expensive sapphire substrates at high temperature. Notably, there is no detailed documentation in the study of optical gain and confinement in ZnO thin films and waveguides on Si substrate.

These ZnO waveguides [29,30] on silicon cannot achieve lasing action because they do not have structures that provide enough optical feedback to sustain lasing. Hence, periodically-organized hexagonal ZnO crystals [19], known as hexagonal microcrystallites have been fabricated to form Fabry-Perot lasing cavity from the facets of all hexagons that are parallel to those of the others. In contrast to these periodic structures, highly disordered grains in ZnO films on fused silica substrate has also been proposed [31] to achieve random lasing action with optical feedback based on the scattering of light, but the ZnO films probably cannot be introduced with scatterers of light that have designed sizes and distributions.

Another limitation in fabrication of the ZnO films is that the deposition process requires high temperature (500 °C). As a result, the properties of the ZnO films are difficult to be modified by post-growth process due to the high deposition temperature. Although the ZnO film [31] has realized one out of the two different types of random lasers, known as coherent random laser, the other type (incoherent random laser) is difficult to be realized by different post-growth processing procedures. These two different types of lasing cavities have different characteristics and are important to the understanding of the random lasing phenomena. Yet there is no detailed report on these two different types of random lasing actions [32] and their formation conditions in the ZnO thin films.

Although the random lasers mentioned have the merit that they do not need to form the Fabry-Perot lasing cavity or the hexagonal microcrystallites, they also have their disadvantages. The major ones are that the lasing output emission beams are not directional [33] and their cavities experience high losses [34]. These characteristics are undesirable but there is no effective design to eliminate these unwanted characteristics and to improve the conversion efficiency in the ZnO random lasers.

Apart from the optically pumped ZnO UV lasers, it is equally important to make ZnO UV LEDs that is the other major category of ZnO UV light-emitting devices to be used in the wide range of applications [5,9,10]. Although the FCVA technique has demonstrated using Al as substitutional elements for Zn to fabricate Al-doped ZnO films that show n-type conductivity and exhibit UV

photoluminescence (PL) at room temperature, there is no report in using this simple technique to fabricate ZnO UV LEDs.

In addition to all the motives mentioned, it is necessary to improvise and design experiments to characterise ZnO waveguides, random lasers and LEDs.

1.2 Objectives

The key objective of the thesis is to use the FCVA deposition method to fabricate ZnO UV optical devices on lattice-mismatched substrates, especially Si, at low deposition temperature. These ZnO UV optical devices are divided into three different categories, as stated in the motivation and they are 1) optical waveguides, 2) optically pumped lasers and 3) LEDs.

1. Optical waveguides:

- In this category, the aim is to design and fabricate a ZnO waveguide on lattice-mismatched Si substrate at a low deposition temperature. It is also important to investigate the optical gain and the enhancement of the optical confinement characteristics of the optical waveguide fabricated. Hence, the optical waveguide can be used as a stepping-stone from which the optically pumped Si-based lasers can be built on.

2. Optically pumped random lasers:

- In this second category, ZnO nanorod arrays with designed sizes and distributions are introduced into ZnO epilayers that comprised of a ZnO and a

MgO layer. 1) The nanorods are used to scatter light, and 2) the epilayers provide gain to the light that scattered between nanorods and confine light to be scattered inside the ZnO layer, to achieve random lasing action.

- Besides that, the exploration of a novel post-growth process that gives new degrees of freedom and control to the formation of thin-film ZnO random laser cavities on the Si substrates is the objective. Moreover, an original engineering technique is developed to form random cavities in the ZnO thin films in order to support coherent and incoherent random lasing action, based on the post-growth process.
- We propose a ZnO thin-film ridge waveguide structure deposited with a MgO film on top as a cap layer, to reduce scattering losses and eliminate non-directional beam emission in ZnO random lasers. Additionally, Al is to be coated on one of facets as an external optical feedback to improve the conversion efficiency in random lasers.

3. Electrically powered LEDs:

- It is intended to design and fabricate an electrically powered ZnO heterojunction LED using the FCVA technique. Al-doped ZnO is used as the electron injection layer and *p*-SiC substrate is used as the hole injection layer to realize the ZnO heterojunction LEDs.

Finally, we need to build experimental setups to determine PL characteristics and field profiles of waveguides and lasers. Moreover, another experimental system is required to study optical gains of waveguides. Finally, another set of apparatus has

to be established to examine electroluminescence (EL), current-voltage and light-voltage characteristics of electrically powered LEDs.

1.3 Major Contributions of the Thesis

Using the FCVA technique as a cost-effective method to fabricate the ZnO optical devices on lattice-mismatched substrates, especially Si, at low deposition temperature is the most significant achievement in this work. Other major contributions are the realizations of the three categories of ZnO optical devices in the objectives and are listed as follows:

1. Optical waveguides:

- ZnO planar and ridge waveguides on lattice-mismatched Si substrates were designed and fabricated by the cost-effective FCVA technique at a low temperature of ~ 230 °C temperature. At this deposition temperature, the ZnO films exhibit strong UV emission intensity that is ~ 60 times that of the visible emission in the emission spectra [225], similar to the observation made in ZnO films fabricated by other techniques at high temperature [212,213]. Moreover, the net optical gains for both waveguides were also studied. It was demonstrated that the ZnO ridge waveguide structure enhanced the optical confinement characteristics when compared to the planar waveguide.

2. Optically pumped random lasers:

- Random lasing action was realized in the ZnO nanorod arrays embedded in the ZnO planar waveguide structure that provided optical gain to the low-density ZnO nanorod arrays.
- A post-growth annealing method, effective in films deposited by the FCVA technique at low deposition temperature, was developed to control the random lasing cavities in the ZnO thin-film ridge waveguide laser. Moreover, coherent and incoherent random lasing actions were realized in the ZnO epilayers on Si substrates by varying the ZnO epilayers structures with different annealing procedures.
- Low-loss and directional output was achieved from the ZnO thin-film ridge waveguide random laser with a capping layer. It also provides a solution to the problem of high-loss and non-directional emission characteristics inherent in other random lasers. In addition, investigations of the improved efficiency of the lasing characteristics with optical feedback from the ZnO thin-film ridge waveguide laser with the capped layer were carried out.

3. Electrically powered LEDs:

- A n -ZnO:Al/ p -SiC(4H) heterojunction LED was fabricated by the FCVA technique at a low deposition temperature that exhibits UV emission in the EL measurement at room temperature.

In order to characterize and examine the optical characteristics of the ZnO optical devices, an experimental setup for photoluminescence measurement was established. It is used to study transverse-electric and transverse-magnetic

polarized emissions of the thin films. After modifying this system, it can also be employed to investigate the optical gain of the thin films. Furthermore, another setup was established to study near- and far-field emission profiles of the thin films. Finally, a different experimental apparatus was assembled and setup into a system to characterize EL properties of LEDs. It was also capable to measure current-voltage and light-voltage characteristics of LEDs by modifying the experimental setup.

1.4 Organization of the Thesis

The deposition techniques to fabricate ZnO thin films are reviewed in CHAPTER 2. CHAPTER 3 describes the FCVA low-temperature fabrication procedures of ZnO films and the optical characteristics of ZnO planar and ridge waveguides on Si substrates. In CHAPTER 4, amplified spontaneous emission characteristics of ZnO nanorod arrays are studied. Besides, we proposed the realization of ZnO epilayers embedded with ZnO nanorod arrays to achieving lasing. It is followed by the optical characterization results that verify the random lasing action observed from the ZnO nanorod arrays embedded in the ZnO epilayers. A post-growth annealing method was proposed and realized, in CHAPTER 5, to control the random lasing cavities formed in a ZnO thin-film ridge waveguide laser on Si substrate fabricated by the FCVA technique. Moreover, the optical characteristics that conform to the random laser theory are illustrated. In addition, variations in the compositions of the epilayers on silicon with modified fabrication procedures were hypothesized to realize coherent and incoherent random lasing actions in ZnO thin films. Their deposition steps were revealed and the two different samples

were verified by the optical characteristics given. CHAPTER 6 suggests the use of a capping layer on the ZnO ridge waveguide random lasers to reduce the high scattering losses and non-directional lasing emission. Its fabrication procedures and the improved low-loss and directional emission characteristics of the ridge waveguide random laser with the capping layer are presented. The enhanced conversion efficiency is also investigated in this chapter on the capped sample with improved external optical feedback in one of the facets. In CHAPTER 7, the design and fabrication of n -ZnO:Al/ p -SiC(4H) heterojunction LEDs are proposed. Its fabrication procedures by the FCVA technique are disclosed and the EL, PL, current-voltage and light-voltage characteristics of the LED are shown. Finally, CHAPTER 8 gives the conclusions and the recommendations for future research.

CHAPTER 2 Deposition Techniques of Zinc Oxide Films

2.1 Introduction

ZnO thin films can be fabricated by different deposition techniques. As for example, they are spray pyrolysis [35], screen printing [36], sol-gel [37], thermal oxidation [38], reactive sputtering [39], radio frequency (rf) magnetron sputtering [40], ion beam deposition [41], ion plating [42], cluster beam deposition [43], plasma enhanced chemical vapor deposition [44], metalorganic chemical vapor deposition (MOCVD) [45], atmospheric-pressure chemical vapor deposition [46], low-pressure chemical vapor deposition [47], molecular beam epitaxy (MBE) [20], liquid phase epitaxy [48], electrophoretic deposition [49] and pulse laser deposition (PLD) [31]. Each of the fabrication technologies has its own unique advantages and disadvantages in the fabrication of ZnO films. Hence, it is necessary to study their strengths and weaknesses in order to develop an effective technique to fabricate ZnO thin films to suit our applications. In our case, the selected technique should fabricate components that allow the integration with other silicon-based devices [50,51]. Moreover, the method should be simple and cost-effective to suit for large-scale production.

2.2 ZnO Deposition Techniques

Most of the ZnO thin films have been fabricated by either MOCVD, MBE, PLD or rf magnetron sputtering techniques. In the MOCVD technique, as shown in Figure

2.1, its principle is similar to that of the chemical vapor deposition technique. During the deposition process, atoms or molecules are deposited onto a substrate by the decomposition of a chemical-vapor precursor species that contains the material to be deposited. The choices of the precursors are mainly diethyl zinc [52], dimethyl zinc [59], zinc acetate [53] or zinc acetylacetonate [21]. These precursors are transported to close vicinity of a substrate surface at elevated temperature ($>350\text{ }^{\circ}\text{C}$), where they either reacted or oxidized to form ZnO molecules layer by layer. The oxidants mostly used are water [54], nitrous oxide [55], nitrogen peroxide [55], oxygen [45], carbon dioxide [52] or alcohols [56]. Among them, H_2O , N_2O , NO_2 and CO_2 , have an increased reaction rate with the precursors when excited by a plasma [52] or an ultraviolet (UV) light [55,57,58].

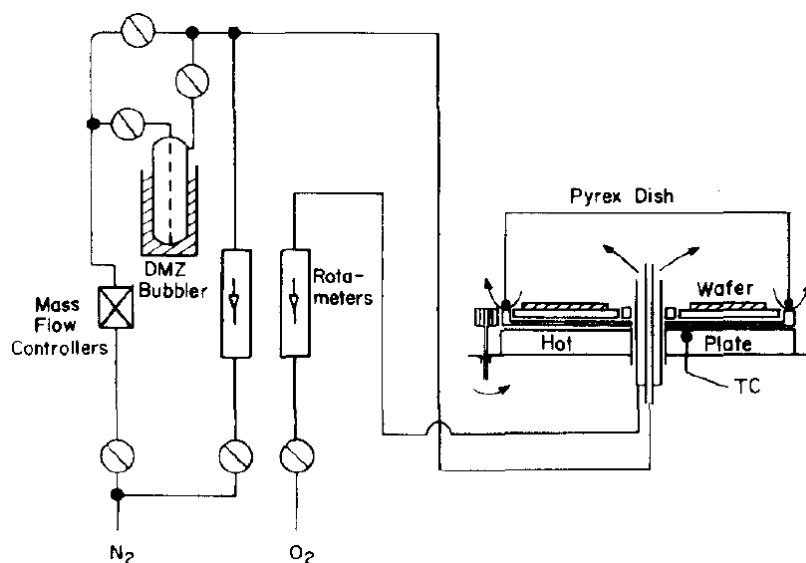


Figure 2.1 Schematic diagram of the MOCVD deposition system [59].

The ZnO films fabricated by MOCVD show good crystal quality [60], optical [61] and electrical properties [62]. Moreover, the ZnO thin films that demonstrated *p*-type behavior have been achieved by using NO [63,64,65], NH_3 [66] or P_2O_5 [67]

as dopant sources. For *n*-type ZnO films, $\text{AlCl}_3(6\text{H}_2\text{O})$ [68], triisopropylgallium [69], triethylgallium [70,71] or B_2H_6 [72] are widely used as dopant sources. In this method, the fabrication of high-quality ZnO films requires high deposition temperature ($>350^\circ\text{C}$) [21,45,59,60,61,76,73] and expensive lattice-matching sapphire as substrate to meet the lattice-matching criterion [21,52,60,61,62,74,75,76,77,78]. Their qualities are difficult to be matched by growing ZnO films on Si substrates at low deposition temperature ($<350^\circ\text{C}$) [55,59,79,80,81].

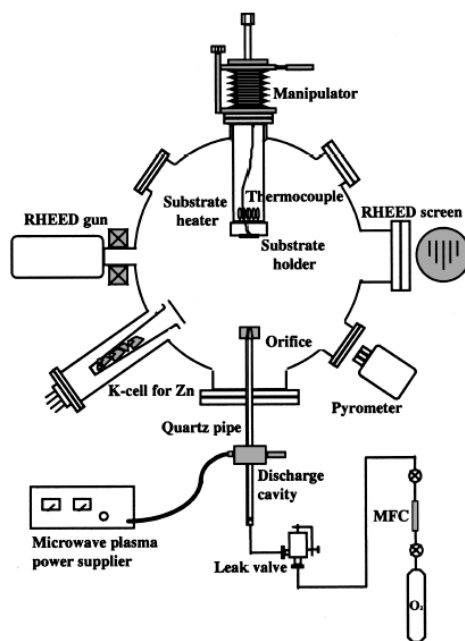


Figure 2.2 Schematic diagram of the MBE deposition system [22].

Figure 2.2 shows the schematic diagram of the MBE deposition system. In contrast to the MOCVD method, the MBE method requires no chemical reactions in the deposition process. Moreover, the vaporized species travel at a relatively higher velocity [82] to the substrate rather than in a slow laminar flow. In fact, the velocity of the vaporized atoms or molecules is determined by the amount of

thermal energy possessed rather than diffusion effect. In the fabrication of ZnO films, a Zn metal is kept in a Knudsen effusion source cell. It is slowly evaporated and directed onto a substrate that is held at a high temperature for reaction with the species that contain the oxygen source. Most of the oxygen sources used are generated from a rf plasma [83], an electron cyclotron resonance plasma [84,85], nitrogen dioxide [86], hydrogen dioxide [87] or rf radical sources [22,88,89]. Moreover, a reflection high-energy electron diffraction system is usually used for monitoring the surface during the deposition process. There are also shutters between the sources and the substrates to control uniformity, composition, thickness and interfaces of the different layers in the atomic scale. *P*-type ZnO films have been demonstrated by using As [90], Ga + N [91,92], Li [93] or N [94,95] as dopant sources. On the other hand, *n*-type ZnO films have been demonstrated by this method using Ga [96,97] or Al [98,99] as dopant. Films fabricated by this method exhibit high crystalline quality [19,20,93,100,101,102] at high deposition temperature [19,22,83,86,87,88,89,93,100,101,102] (>350 °C). Although there are films fabricated at lower temperature [84,85], these films have to be grown on lattice-matched substrates. Hence, most of the high-quality ZnO films are grown on expensive sapphire substrates [19,20,22,83,84,85,86,88,89,101,102], ScAlMgO₄ substrates [100], ZnO crystal substrates [93], and MgO- [103,104] or GaN-buffered [87,105] sapphire substrates. Their crystalline quality is difficult to be achieved by growing the ZnO films on lattice-mismatched Si substrates [106,107].

On the other hand, the high deposition temperature and the lattice matching condition of the substrate required in the MBE and the MOCVD methods are not

needed in the sputtering method. There are various kinds of sputtering technique to fabricate ZnO films and they are electron-cyclotron-resonance sputtering [108,109], ion-beam sputtering [110], dual-ion-beam sputtering [111], helicon-wave excited plasma [112], unbalance magnetron sputtering [113] and rf magnetron sputtering [40,114,115,116,117,118,119,120,121,122].

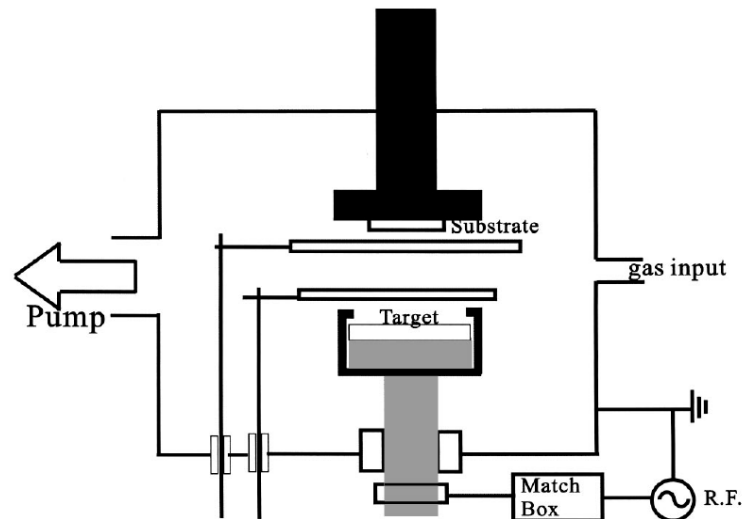


Figure 2.3 Schematic diagram of the rf magnetron sputtering system [117].

Figure 2.3 shows the schematic of a rf magnetron sputtering system. ZnO [40,114,118,119,120,121] is used as target material and is positioned in front of a permanent magnet. Besides, GaN target [123], P_2O_5 -doped ZnO target [124], Nitrogen [123,126], GaAs wafer [125], or Be sheet [126] are used for the fabrication of *p*-type ZnO films, whereas different kinds of doped ZnO targets are used for the *n*-type fabrication. They are the Al_2O_3 - [127,128,131], Al- [129], Ga_2O_3 - [128,130,131,132], B_2O_3 - [131], In_2O_3 - [128,131] or GeO_2 -doped target [128]. During the sputtering process, an ac-voltage is applied to the target. Plasma is formed between two electrodes and well confined to the surface of the target [133] due to the magnetic field. In the plasma, clouds of electrons are moving in a

sea of relatively stationary ions. The electron cloud approach the electrodes for a short period of time in each half biasing cycle. Hence, charged ions transfer their momentum to the target. Atoms or molecules are ejected from the target and they form a layer onto the substrate [134]. Since momentum transfer is the main mechanism in depositing the species onto substrates, the lattice-matching condition is not as critical as MBE and MOCVD. As a result, ZnO films can be fabricated on diamond [40], Si [114,122], sapphire [115], GaAs [116] or fused silica [117] substrates at low deposition temperature [40,117]. However, impurities are probably presented in the deposited ZnO films due to the working gas pressure for igniting the plasma and the sputtering process that takes place at both electrodes and other surfaces inside the sputtering chamber exposed to the plasma [135]. Furthermore, in this method, the deposited films generally have the same stoichiometry as the target [136]. As a result, most of the ZnO films are deposited from a more expensive high-purity ZnO target instead of a Zn target. Although ZnO films have been fabricated using a Zn target [116, 122], their crystalline qualities are difficult to achieve better than that of the ZnO films fabricated from a ZnO target [118].

Another well-known technique in fabricating ZnO thin films is PLD method. In this method, Zn target [137] or ZnO target [31,138,139,140,141,142,143,144,157,159,160,161,162] are mostly used as the target materials. For the fabrication of the *p*-type ZnO films, P₂O₅-doped target [145,146,147], or, Ga-doped target and N [148,149,150] are used. Besides, Al₂O₃- [151,152,153,154,155], Ga- [152] or Ga₂O₃-doped ZnO target [154,155,156] is used in the fabrication of the *n*-type ZnO films.

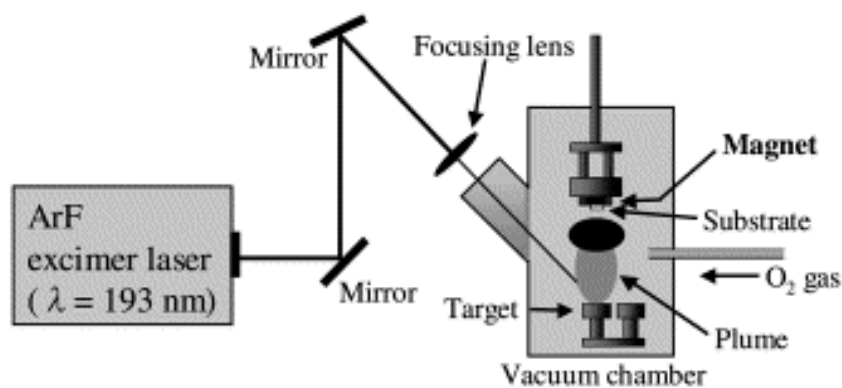


Figure 2.4 Schematic diagram of the PLD system [157].

Figure 2.4 shows the schematic diagram of the PLD system. The target material is vaporized by the radiation of a KrF (248 nm) laser [31,137,138,139,140,142,143,158,161,162,164], an ArF (193 nm) excimer laser [157,158,159] or a Nd:YAG (355 nm) [141] pulse laser focused onto the target. Moreover, lasers with femtosecond pulses [144,160,161] are employed to vaporize the target. Lasers with these wavelengths and ultrashort pulses are used to prevent melting the target that causes liquid droplets ejection and microscopic particles to form onto the deposited films [140,162]. When the laser pump power is above a certain threshold, a substantial amount of the target vaporizes and forms a plume. It propagates in a direction perpendicular to the surface of the substrate that is heated up and accumulates on the substrate surface and forms a thin film. In contrast to MBE and MOCVD, due to the high kinetic energy of the species emitted from the target [135], ZnO thin films can be deposited on substrates [31, 140,141,142,143,144,157,160,162] other than sapphire at lower deposition temperature [141,142,143,144,157]. These species with improved surface mobility enhances the growth of the crystalline ZnO films. Besides, the films that are fabricated using a two-step [163] or multiple-step [164] procedures show good

electrical and optical properties. Although the PLD technique can fabricate ZnO thin films on lattice-mismatched substrate at low temperature, ablated species eject from the target with high kinetic energy and bombard onto the substrate that probably lead to crystallographic defects in the film [135]. Furthermore, despite microscopic particulate is not detected in ZnO films fabricated by the PLD technique, it is observed in films made of other materials [165]. When compared to the MBE, MOCVD or rf magnetron sputtering techniques, the scalability of the PLD deposition method to the wafer size is limited [136].

2.3 Vacuum Arc Deposition Techniques

Arc deposition technique is proposed to grow the ZnO thin films because: 1) The requirement of substrate temperature during deposition is lower, 2) the fabrication of ZnO thin films on lattice-mismatched and large substrates is possible, 3) the fabricated films are free of the microscopic particulate, and 4) the ZnO thin films is mass-produced at a lower cost. ZnO thin films have been fabricated using this technique with modified deposition apparatus [166,167]. It is also shown that ZnO thin films fabricated by this method have promising potential applications in field emission displays [168], and solar cells [169]. However, the use of this method to make ZnO UV optical devices (e.g. optical waveguides, lasers and light-emitting diodes) has not been reported.

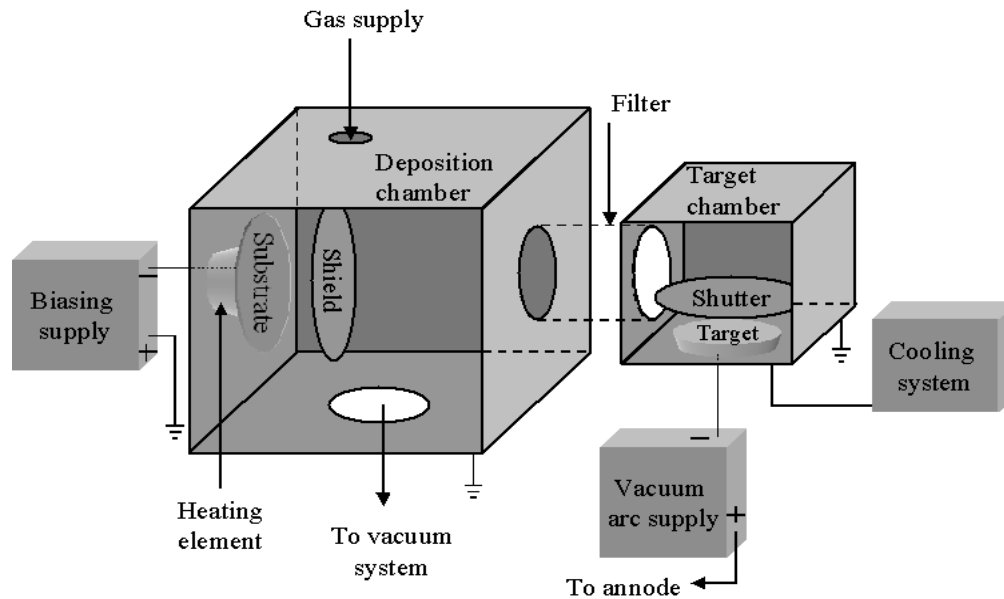


Figure 2.5 Schematic diagram of the typical vacuum arc deposition system.

In fact, the arc plasma deposition technique was suggested a long time ago [170] for coating thin films and had been developed [171,172,173] and investigated by different research groups. Figure 2.5 shows the schematic diagram of the typical vacuum arc deposition system. They comprise a deposition chamber, a target chamber and a filter. The film deposition process is carried out in a vacuum environment and, in this case, the deposition chamber is connected to a piping linked to a pump. Inside the deposition chamber, where a substrate is positioned on a substrate holder, there is a gas inlet to supply gas during the deposition process. For some of the designs, a heating element is located in close vicinity to the substrate area to control substrate temperature [174]. To reduce or eliminate macroparticle contamination in the deposited films, the substrate can be connected to a cathode of a biasing supply [175] and a shield [167,176] is located at some distance away from the substrate to avoid the substrate to be in line-of-sight with the target. Other than using substrate bias and a shield to filter out macroparticle,

macroparticle filter [177,178,179] can also perform the task. This macroparticle filter is usually located in between the deposition and target chamber. Inside the target chamber, a shutter [180,181] is possibly present to decide the exposure time of the substrate to the plasma and a target is connected to a negative terminal of a vacuum arc supply [182]. This is known as the cathodic arc deposition technique. Alternatively, the target can be connected to the anode [183,184] in the anodic arc deposition technique. The vacuum arc power supply can either be in a continuous [185] or pulse [179] operation. Besides that, the target is prevented from overheating by a cooling system to reduce the presence of macroparticles in the substrate. Furthermore, there are different designs to eliminate or lower the number of macroparticles in the substrate.

2.3.1 Macroparticle Control

In a lot of vacuum arc deposition system setups, the target is connected to the cathode. After triggering the vacuum arc [186,187], the current is concentrated at a small number of discrete sites called cathode spots. These cathode spots are non-stationary and macroparticles are generated [188] unless different arc modes operation is employed [183,184,189]. However, the latter is not preferred in applications where the generation of ions with high kinetic energies is crucial [190]. Hence, significant interests have been focused to reduce the contamination of macroparticles in the vacuum arc deposition technique. Field coils induced rapid cathode spot motion [191] and reduction of arc current [192] have shown to reduce macroparticle generation by lowering the target temperature [193], although the

latter seems to be counterproductive. Besides, negative biasing to the substrate [175] and manipulating the background pressure [192, 194] have been demonstrated to lessen the macroparticle contamination. Steered and shielded arc deposition methods [167, 176] are also used in solving this problem. In the steered arc deposition technique, a magnetic field guides the motion of the arc spot. In the shielded arc deposition method, there is a shield in between the substrate and the target, along the path of the plasma. Lastly, the conventional filter method, as for example dome filter [195], classical 90-duct filter [196], 45°-duct filter [197], S-duct filter [198], rectilinear filter [199], freestanding magnetic coil filter [200], stroboscopic filter [201], Venetian blind filter [202] and rotating blade filter [203], are used to filter out macroparticle. Among them, the more successful ones are the magnetic filters [204].

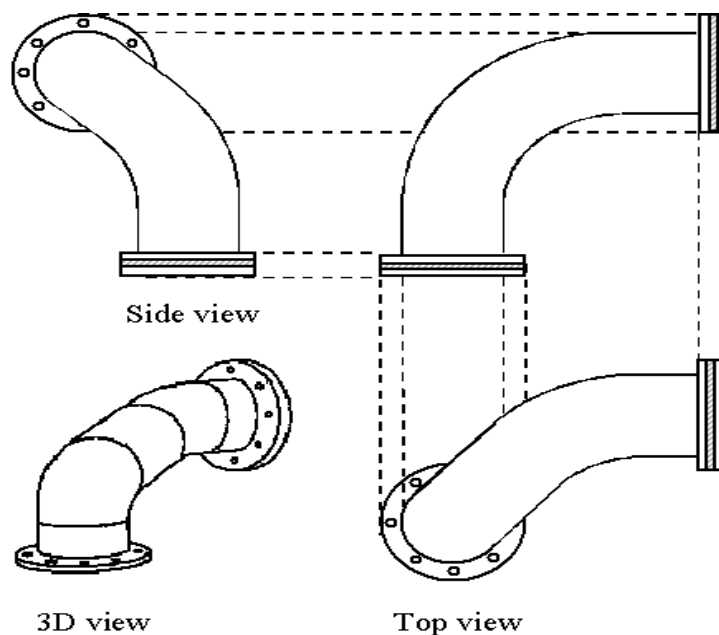


Figure 2.6 Schematic diagram of the off-plane double-bend filter.

Therefore, a magnetic filter is used in our deposition technique where the plasma ions are guided by a filtering-duct, as shown in Figure 2.6 known as an off-plane

double-bend (OPDB) filter [205]. It has two-torus bends at 90° and 45° with respect to axis of the cathodic vacuum arc source [206,207]. The exterior wall of the filtering duct is surrounded by a set of magnetic coils for the generation of magnetic field to guide the plasma ions, while its interior is equipped with baffles that are designed to catch or to reflect macroparticles. The OPDB filter is effective in eliminating macroparticle contamination in the deposited films with increasing number of macroparticles hitting the walls of the plasma duct [205]. Concurrently, the shape of the filter allows optimum output efficiency while keeping the losses of plasma in the filter to a low level [205].

2.3.2 Filtered Cathodic Vacuum Arc Deposition Technique

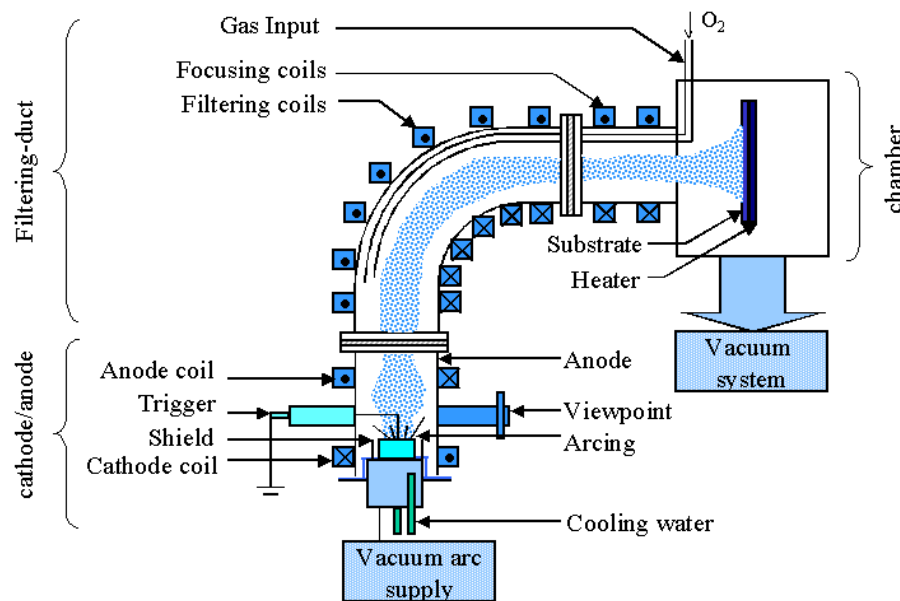


Figure 2.7 Schematic diagram of filter cathodic vacuum arc system [23].

Figure 2.7 shows the filter cathodic vacuum arc (FCVA) system that is used for the deposition of the ZnO thin films. A Zn target with purity of 99.9% is used as the

target material and it is connected to the cathode of a vacuum arc continuous biasing supply. A Zn target is used instead of a ZnO target because: 1) it is more economical, 2) it has a lower melting point such that a lower biasing voltage is needed to trigger an arc, and 3) it is a conductor so that an arc can be sustained more easily. On the other hand, the anode of the biasing supply is connected to the trigger that is grounded. The cathodic arc deposition method is selected over the anodic arc deposition because: 1) A higher percentage of the material evaporated from the target is ionized [208], 2) the ions exist as multiple charge states in the plasma [209], and 3) the kinetic energies of the ions generated are higher [190]. Furthermore, continuous biasing operation is preferred over pulsed operation since it is more suitable in fabricating large-areas thick films with high quantity [204]. Moreover, cooling water is circulating in close proximity to the target to lower the target temperature during deposition. This is to prevent the entire cathode/anode apparatus from over heating and melting, and also reduce generation of macroparticles [193].

When the trigger is rotated to strike and bring into contact with the target surface, an arc is formed. It is self-sustained and confined by the cathode coil. The arc spot is restricted to run on the target surface by the small gap between the target and the isolated shield, otherwise it leads to the destruction of the isolated shield and the contamination of the samples. The energetic plasma ions are then guided by the magnetic filtering-duct before arriving at the substrate.

2.4 Conclusion

Table 2.1 on pages 26 and 27 summarizes the characteristics of the different deposition techniques discussed. The table shows that the FCVA technique has many advantages over the other ZnO thin-film fabrication techniques. One of them is that the energetic ions in the plasma have high kinetic energy and part of their momentum is being transferred to the gas molecules. This momentum transfer causes excitation, disassociation, and ionization of the background gas molecules [210]. Hence, this technique allows the deposition of ZnO thin films on the lattice-mismatched substrate at low deposition temperature ($<350\text{ }^{\circ}\text{C}$) [23,24,25,26,211] due to the energetic ions. The x-ray diffraction (XRD) patterns of the ZnO films on Si fabricated by the FCVA technique at room temperature (RT) [23] shows a full width at half maximum (FWHM) of 0.23° in the (002) peaks. The result is compatible to that obtained by using other ZnO thin-film fabrication techniques on Si substrates at elevated temperatures [79,106,122,140].

Besides, a Zn target [23,24,25,26,211] instead of a more expensive ZnO target can be used since the ions inside the plasma can be steered and accelerated toward the substrate that lead to the enhancement of adhesion, film density and composition stoichiometry [204]. The flexibility in the choice of the target materials also provides more degree of freedom in the doped ZnO films in the *n*-type fabrication [211].

When compared to the PLD technique, the FCVA method also allows the fabrication of thin films on a relatively large substrate with uniformity of better

than $\pm 5\%$ over a 6" deposition area [205]. Moreover, having the OPDB filter and other advantages mentioned, the FCVA technique can fabricate ZnO thin films on Si substrates with electrical [211] and optical properties [26] comparable to those fabricated by the other methods [212,213,214]. In conclusion, the FCVA technique is a more suitable method that fits our objectives in the fabrication of the ZnO UV optical devices.

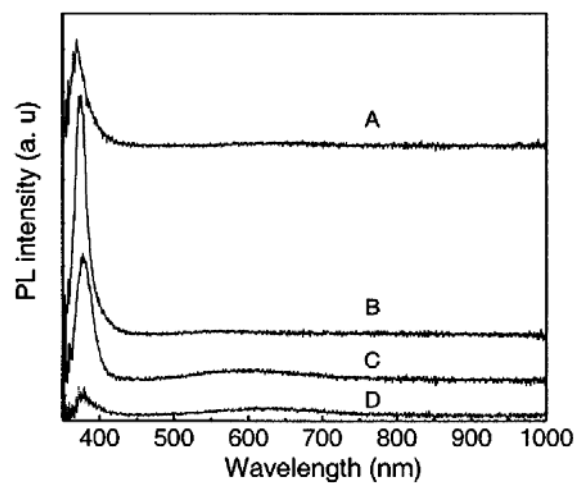


Figure 2.8 RT photoluminescence (PL) spectra of ZnO films grown on quartz substrate at various oxygen pressures: (A) 3.5×10^{-4} , (B) 5×10^{-4} , (C) 6.5×10^{-4} , and (D) 8×10^{-4} Torr [23].

Figure 2.8 gives the RT PL spectra of ZnO films deposited on quartz substrate at different oxygen pressure in RT by the FCVA technique. It is shown that the PL peak position of the samples prepared at oxygen pressures of 3.5×10^{-4} , 5×10^{-4} , 6.5×10^{-4} , and 8×10^{-4} Torr are 3.32, 3.31, 3.28 and 3.27 eV, respectively. Besides, a broad deep level emission peak is observed around 2.03 eV. In addition, the PL

peak FWHM is the lowest at 150 meV when the sample is deposited at oxygen pressure of 5×10^{-4} .

It is observed that the intensity ratio of the UV emission peak to that of the visible emission peak is compatible to the intensity ratio obtained from ZnO films fabricated at elevated temperature on lattice-matched sapphire substrate by other deposition methods [77,21, 215,22,118]. This indicated that although other deposition techniques can fabricate ZnO films on lattice-mismatch substrate and exhibit PL [143,81,107,122] similar to our FCVA technique, their deposition of ZnO requires be carried out at elevated temperature [143,81,107,122]. In addition, a ZnO buffer layer is needed to improved their ZnO films' quality [107] and some of their ZnO films exhibit high visible emission [143,81]. Hence, the FCVA technique is one of the most potential methods in depositing high-quality thin films at low temperature on lattice-mismatched substrate.

Table 2.1 Characteristics of the different ZnO thin-film deposition techniques.

Method	MOCVD	MBE	rf Sputtering	PLD	Vacuum Arc	FCVA
Mechanism in production of deposited films	Chemical reaction	Thermal energy	Momentum transfer	Thermal energy	Momentum transfer	Momentum transfer
Substrate	Sapphire [i] Si [ii] Glass [iii] GaAs [53,59] InP [53] GaN [61] Bulk ZnO [61]	Sapphire [vii] ScAlMgO ₄ [100] ZnO crystal [93] MgO/Sapphire [103,104] GaN/Sapphire [87,105] Si [106,107]	Diamond [40] Sapphire [x] Si [114,117,122] GaAs [116] Fused silica [117] Glass [119] InP [121]	Sapphire [xiii] Glass [xiv] Si [xv] Quartz [142,160] SiO ₂ /Si [160]	Si [167,168] Glass [166,167,169,176]	Si [23,24,25,26,211] Glass [23,211,26]
T < 200	[iv]		[xi]	[xvi]	[xix]	[xx]
200 < T < 450	[v]	[viii]	[xii]	[xvii]	[168]	[xxi]
450 < T	[vi]	[ix]	[118]	[xviii]		
Energy	Mostly low; can be high with plasma-aid [136]	~0.1-0.5 eV [136]	~10-100 eV [135]	~1-100 eV [135]	~20-200 eV depends on the material [190]	

T: Temperature of substrate during deposition

[i] 21,52,60,61,62,74,75,76,77,78

[ii] 53,55,59,73,79,80,81

[iii] 45,53,54,56,57,80

[iv] 52,54,55,57,79

[v] 45,52,53,55,56,59,60,61,62,75,76,77,80,81

[vi] 21,45,59,60,73,77,81

[vii] 19,20,22,83,84,85,86,88,89,101,102

[viii] 83,84,85,86,87,100,101,103,106

[ix] 19,22,83,87,88,89,93,100,101,102,103,105,107

[x] 115,118,120

[xi] 117,121

[xii] 40,114,115,116,117,119,120,122

[xiii] 137,138,139,158,161,163,164

[xiv] 157,141,143

[xv] 142,143,160,162

[xvi] 141,142,143,144,157,160,162

[xvii] 138,140,142,143,144,159,160,161,162

[xviii] 31,137,138,139,140,142,143,158,160,161,163,164

[xix] 166,167,168,169,176

[xx] 23,24,25,26,211

[xxi] 24,25,26,211

(Continued on next page)

Table 2.1 (Continued)

Source material	Diethylzinc [xxii] Dimethylzinc [xxiii] Zinc acetate [53] Zinc acetylacetonate [21]	ZnO [xxv] Zn [xxvi]	ZnO target [xxvii] Zn target [116, 122] ZnO powder [117]	ZnO target [xxix] Zn target [137]	Zn target [xxx]	Zn target [xxxi]
Source materials for P-type fabrication	NO [xxiv] NH ₃ [66] P ₂ O ₅ [67]	As [90] Ga + N [91,92] N [94,95] Li [93]	GaN target+ N [123] P ₂ O ₅ -doped target [124] GaAs [125] Be sheet + N [123,125]	P ₂ O ₅ -doped target [145,146,147] Ga-doped target + N [148,149,150]		
Source materials for N-type fabrication	AlCl ₃ (6H ₂ O) [68] triisopropylgallium [69] triethylgallium [70,71] B ₂ H ₆ [72]	Ga [96,97] Al [98,99]	Al ₂ O ₃ -doped target [127,128,131] Al-doped target [129] Ga ₂ O ₃ -doped target [xxviii] B ₂ O ₃ -doped target [131] In ₂ O ₃ -doped target [128,131] GeO ₂ -doped target [128]	Al ₂ O ₃ -doped target [151,152,153, 154,155] Ga-doped target [152] Ga ₂ O ₃ -doped target [154,155,156]	Al-doped Zn target [166]	Al-doped Zn target [211]
XRD results						
Film on sapphire	FWHM < 0.02° [21] (Dep. Temp. 450 °C)	FWHM = 0.06° [100] (Dep. Temp. 500 °C)	FWHM = 0.13° [118] (Dep. Temp. 600 °C)	FWHM = 0.17° [138] (Dep. Temp. 750 °C)		
Film on Si	FWHM = 0.44° [79] (Dep. Temp. 200 °C)	FWHM > 1° [106] (Dep. Temp. 200 °C)	FWHM = 0.3° [122] (Dep. Temp. 200 °C)	FWHM < 0.13° [140] (Dep. Temp. 350 °C)		FWHM = 0.23° (RT Dep.) [23]

[xxii] 45,52,54,56,57,60,61
 [xxiii] 55,59,62
 [xxiv] 63,64,65
 [xxv] 19,100
 [xxvi] 84,85,86,87,88,89,93,101,102,105,106,107
 [xxvii] 40,114,118,119,120,121
 [xxviii] 128,130,131,132
 [xxix] 31,138,139,140,141,142,143,144, 157,159,160,162,163,164
 [xxx] 166,167, 168,169,176
 [xxxi] 23,24,25,26,211

CHAPTER 3 ZnO Waveguides

3.1 Introduction

Optical gain of ZnO thin films deposited on sapphire by the various techniques has been investigated intensively [27,28,29,30]. However, these ZnO films under investigation are fabricated on expensive sapphire substrates at a high deposition temperature ($>350^{\circ}\text{C}$). Although ZnO thin films have been fabricated on Si substrates at lower deposition temperature ($<350^{\circ}\text{C}$) [216,217], there is no detailed report on the investigations of optical gain and confinement characteristic on them. Therefore, it is important to carry out the investigations, particularly for the ZnO films on Si at low temperature fabricated by the filtered cathodic vacuum arc (FCVA) technique. The results can be used as a reference for the realization of ZnO waveguide lasers fabricated on Si by the FCVA technique.

3.2 The ZnO Planar Waveguides on Silicon

3.2.1 Design of the ZnO Planar Waveguides on Silicon

A thin-film waveguide is selected as the geometry under investigation in this thesis for its simple fabrication steps. Moreover, when the thin-film waveguide is used in the development of the waveguide lasers, it allows: 1) simple focusing optics [218] or without the need of optics at all [219], 2) good thermal handling with effective cooling [220] from the large surface of the slab, 3) the fabrication to be carried out by the well-established thin-film deposition technology, 4) high component density

[221], and 5) integration with other planar devices in different applications [222,223].

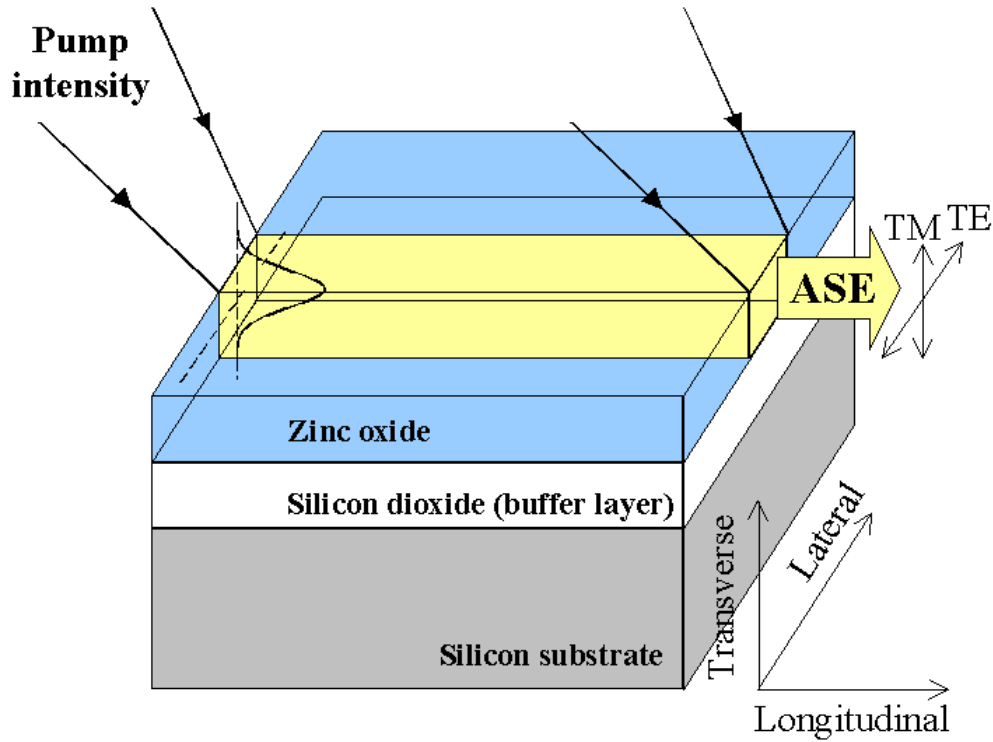


Figure 3.1 Proposed schematic diagram of the thin-film ZnO planar waveguide. ASE: amplified spontaneous emission. TM: transverse magnetic. TE: transverse electric.

Figure 3.1 shows the proposed schematic diagram of a ZnO planar waveguide. A layer of SiO_2 buffer layer is inserted between the ZnO thin-film layer and the Si substrate. SiO_2 is selected as the buffer layer because it has a smaller refractive index (1.45) than that of the ZnO film and a low absorption loss due to its wide energy gap [27]. Moreover, it can be grown on Si substrate easily by thermal oxidation [224]. The thickness of the SiO_2 buffer layer is selected so that more

pumping energy is being refracted back into the ZnO layer, while optimizing the oxidation time in making this layer. As for the ZnO film thickness, it is chosen to minimize the number of modes and to optimize the pump and signal intensities confined inside the waveguide.

3.2.2 Fabrication of the ZnO Planar Waveguides on Silicon

A piece of *n*-type (100) Si substrate was cleaned in the sequence by acetone, alcohol and deionized (DI) water in an ultrasonic bath. Following that, the Si wafer was pushed into the center portion of a quartz tube that was opened at both ends and inside a standard Lindberg-type furnace. This was to ensure the uniformity of the thermal gradient on the Si substrate so that the thickness of SiO₂ layer to be formed was uniform. The Si wafer was heated from room temperature to 1100 °C with ramp rate of ~20 °C/min so as to prevent the wafer from cracking. After ~10 hrs [224], a layer of 420 nm-thick SiO₂ was grown on the Si substrate by dry thermal oxidation (thermal oxidation that is carried out in the moisture-free oxygen). Before the wafer was taken out, the furnace was off and cooled to room temperature. Next, the sample was cleaned using the same procedures mentioned before. Then the sample was clipped onto a sample holder inside a FCVA chamber. It was noted that the entire wafer was in good physical contact with the sample holder. This was to guarantee uniform substrate heating by the heater that was located at the back of the sample holder. Before the deposition process, the chamber was pumped down to the typical base pressure of $\sim 2 \times 10^{-6}$ Torr and the heater was switched on. The substrate temperature was set to 230 °C because ZnO thin films grown at this temperature had a larger intensity ratio of the ultraviolet

(UV) emission peak to that of the visible emission peak [225] when compare to films fabricated at other temperature. Higher deposition temperature ($>230\text{ }^{\circ}\text{C}$) is not desirable since it probably causes more oxygen to be incorporated into the film and lead to more oxygen interstitial sites. On the other hand, lowering the deposition temperature is not preferred as the crystalline quality of the film is affected [225]. When the desired substrate temperature was reached, a zinc target (with purity of 99.9%) was manually struck to ignite an arc and to generate the plasma. The arc current was $\sim 60\text{ A}$ and the toroidal magnetic field was $\sim 40\text{ mT}$ to guide the plasma. The magnetic field is produced by three sections of copper coils wrapped around the off-plane double-bend filter. They are the focusing coil, the filtering coil and the anode coil. Each of them is powered by three individual sets of power supply, biasing at 3.6, 29.2 and 2.5 V, respectively. The corresponding current that flows through the coils is 12, 20 and 10 A. At the deposition rate of $\sim 0.53\text{ nm/s}$, a layer of ZnO thin film of thickness $\sim 160\text{ nm}$ was deposited on top of the SiO_2 layer in $\sim 5\text{ min}$. During the deposition process, the oxygen partial pressure was $\sim 2 \times 10^{-4}\text{ Torr}$. The pressure was slightly higher than that of our previous publication [225] because a higher pressure reduced the stress and the deposition rate of the ZnO films [23,226]. This lowered the surface roughness [227] that is a critical issue to improve the light confinement in the waveguide. At the specified conditions, the ZnO thin films have optical properties compatible with other techniques. After the deposition, the sample was cooled to room temperature before the chamber was purged and opened. The sample was then cleaved into a dimension of $5\text{ mm} \times 5\text{ mm}$.

3.2.3 Characterization of the ZnO Planar Waveguides on Silicon

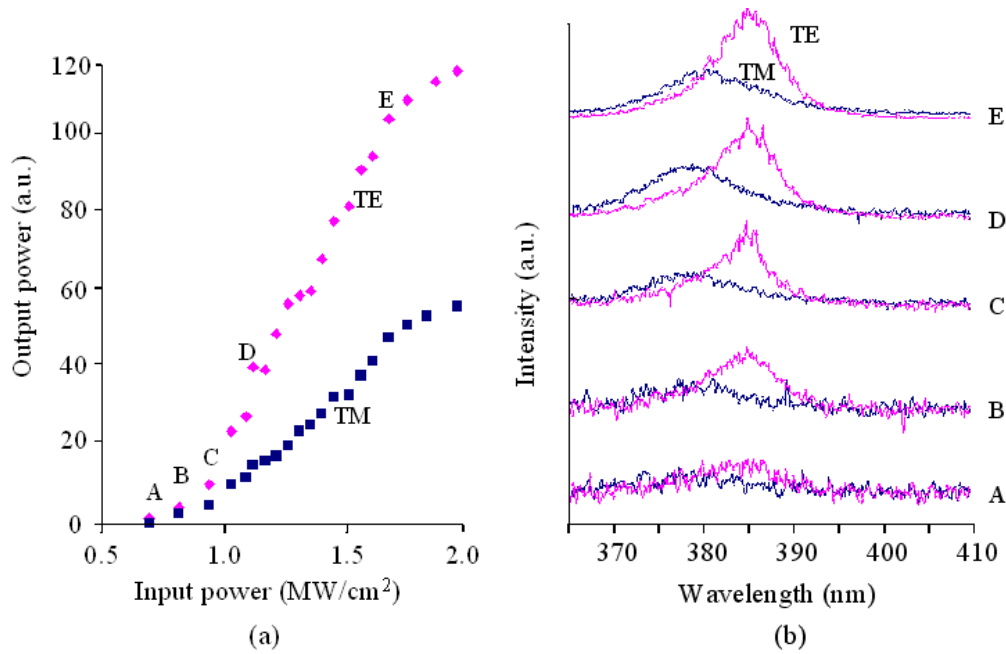


Figure 3.2 (a) Light-light curves for the two polarizations of the thin-film planar waveguide and (b) the corresponding emission spectra of the two polarizations at different pump intensities.

Figure 3.2 shows the light-light curves and the corresponding spectra for the two polarizations of the thin-film ZnO planar waveguide at different pump intensities. The details of the experimental setup are given in the APPENDIX B. The TE and TM directions are defined as the directions that are parallel and perpendicular to the lateral direction, respectively, as indicated in Figure 3.1. From the light-light curves, the optical intensities for both polarizations increase with the increase of the input pump power. Moreover, it is noted that the TE polarized output intensities double that of the TM mode, meaning that the TM modes are strongly suppressed. The emission spectra of the TE (TM) mode stretch from ~375 to ~395

nm (~ 370 to ~ 390 nm). The emission mechanism is made up of two recombination processes and they are namely exciton-exciton scattering and electron hole plasma (EHP) recombination [27] (Details about the two emission mechanisms are given in APPENDIX A). However, the latter is the main recombination process due to the fact that the excitation intensities are greater than the gain threshold in Figure 3.3, accompanied with the shifting of emission peak in the emission spectra (Figure 3.2). There is no threshold in the light-light curves for both polarizations and no distinct lasing modes in the spectra, indicating that lasing is not observed from the sample.

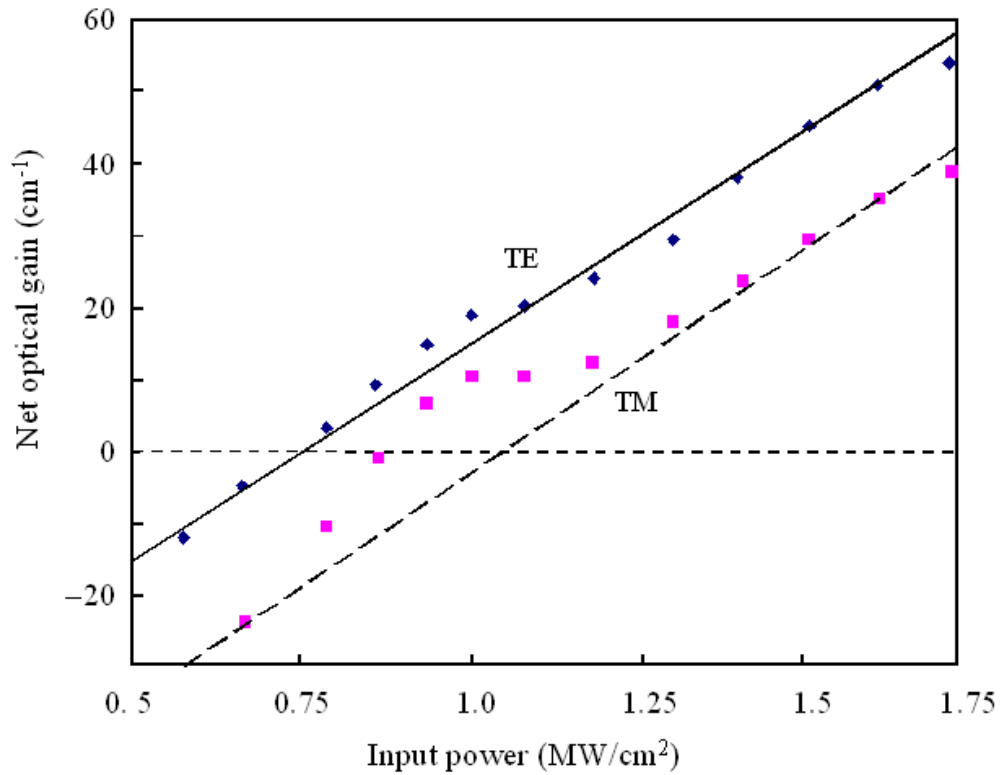


Figure 3.3 Net optical gain versus pump intensities for TE and TM polarizations of the ZnO thin-film planar waveguide.

Figure 3.3 (on the previous page 33) shows the variation of the net optical gain at different input pump power obtained by the variable stripe length (VSL) method [228], as summarized in APPENDIX C. As the input pump power is intensified, the net optical gain is enhanced for both polarizations. For both polarizations, the net optical gain is improved by $\sim 60 \text{ cm}^{-1}$ for every unit MW/cm^2 input power rise. The TE and TM mode have a zero net optical gain at input power of ~ 0.75 and $\sim 1.03 \text{ MW}/\text{cm}^2$, respectively. Moreover, it is noted that the TE mode is of $\sim 20 \text{ cm}^{-1}$ more than the TM mode at the same excitation power. The higher TE net optical gain explains that the TM mode is being suppressed by the waveguide.

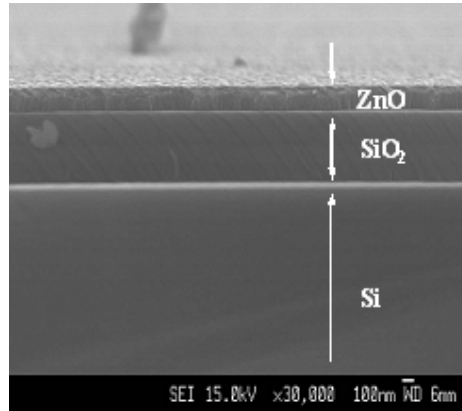


Figure 3.4 Scanning electron microscope image of the cross-sectional ZnO/SiO₂/Si interfaces.

The scanning electron microscope image of the cross-sectional view of the thin-film planar waveguide is shown in Figure 3.4. It shows clearly the three different layers. They are the $\sim 160 \text{ nm}$ -thick ZnO layer, the $\sim 420 \text{ nm}$ -thick SiO₂ layer and the Si substrate. The ZnO and SiO₂ interface is smooth, implying that the FCVA

technique is capable of fabricating ZnO films on lattice-mismatched Si with a smooth interface.

Figure 3.5 (a) gives the far-field profiles of both polarizations observed from the waveguide illuminated by an excitation stripe at a pumping intensity of ~ 1.3 MW/cm², using the setup given in the APPENDIX D. There are two round bright spots of different intensities noted. They are originated from the fundamental modes of the two polarizations, emitted at different angles due to the roughness of the facet. While the brighter spot is originated from the TE polarized emission, the dimmer spot comes from the TM polarized emission of the planar waveguide, as given in Figure 3.5 (b) and (c).

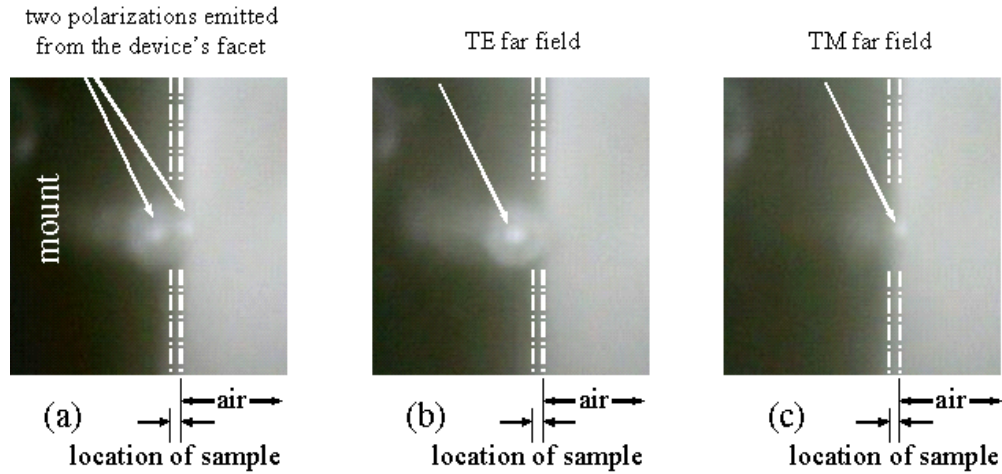


Figure 3.5 (a) Far-field profiles of both polarizations under pump intensity of ~ 1.3 MW/cm². (b) Far-field profile of TE mode. (c) Far-field profile of TM mode. The dotted lines indicate the location of the sample.

3.3 The ZnO Ridge Waveguides on Silicon

3.3.1 Design of the ZnO Ridge Waveguides on Silicon

In order to improve the optical characteristics of the planar ZnO waveguide in section 3.2, it is modified into a ridge waveguide. The ridge design is used because: 1) It is simple to be implemented by lithographic techniques, 2) it improves the confinement of light in the lateral direction, 3) it can be easily integrated with other optical and electrical components, and 4) its geometry is similar to that of the excitation pump strip.

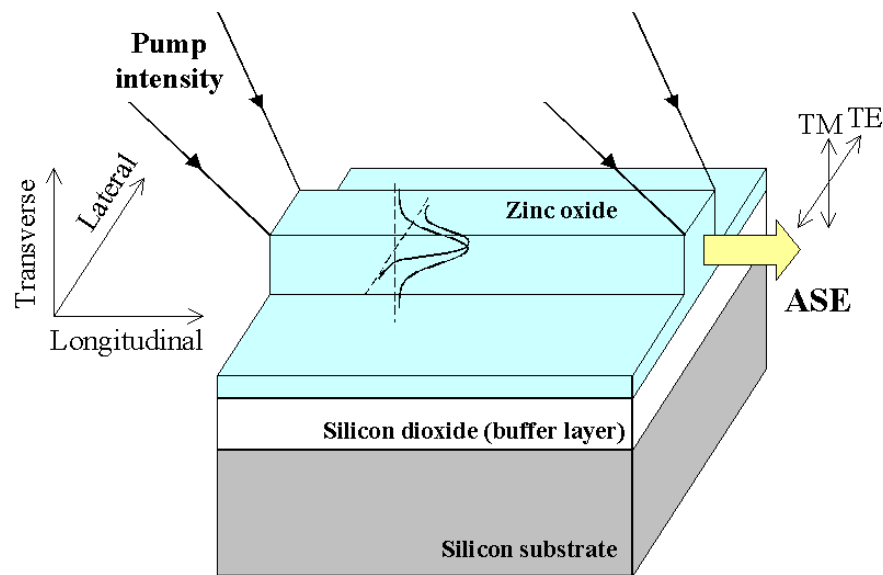


Figure 3.6 Proposed schematic diagram of the thin-film ridge waveguide.

Figure 3.6 shows the proposed schematic diagram of the thin-film ridge waveguide. Other than the criterions stated in section 3.2.1 have to be considered,

the etching depth and the width of the ridge waveguide have to be considered so that the number of modes within the ridge is minimized and the confinements of the signal and pump intensities are optimized. At the same time, the overlapping of the signal and pump intensities is maximized.

3.3.2 Fabrication of the ZnO Ridge Waveguides on Silicon

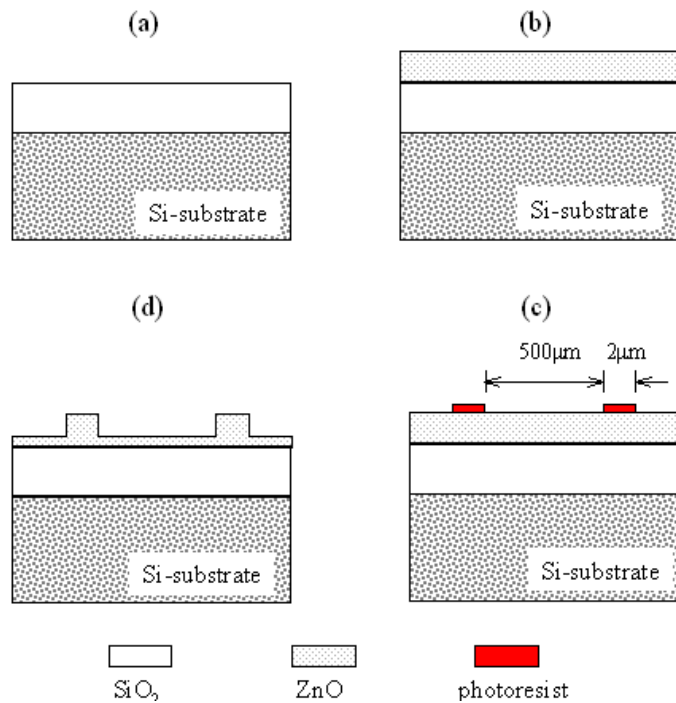


Figure 3.7 Fabrication procedures of the proposed ZnO ridge waveguide. (a) The SiO_2 buffer layer is formed on the silicon substrate by thermal oxidation. (b) Deposition of ZnO thin film on a SiO_2 buffer layer by FCVA. (c) Deposition of line masks on the ZnO thin film for the preparation of plasma etching. (d) Formation of ridge waveguide after plasma etching and removal of photoresist.

The fabrication procedures of the proposed ZnO ridge waveguide are shown in Figure 3.7. In Figure 3.7 (a), first, a piece of Si substrate underwent thermal

oxidation at 1100 °C for ~10 hrs [224] to form a SiO₂ layer of thickness 420 nm on a Si substrate. Subsequently, as shown in Figure 3.7 (b), a ~160 nm-thick ZnO thin film was deposited on top of the SiO₂ layer by the FCVA technique. The experiment procedures and parameters remained unchanged as they were stated in section 3.2.2. A drop of photoresist (AZ5214) was spread on top of the ZnO thin film that was placed on the vacuum chuck of a spin coater (Specialty Coating System, inc. model no. P6204). It was then evenly spin coated onto the ZnO thin film at 4000 rpm for 30 s. The estimated thickness of the photoresist was ~1.41 μm . After spin coating, the thin-film sample was pre-baked on a hotplate (Heidolph MR 3003 control G) at 90 °C for 2 min. Using a mask aligner (Quintel Corporation Q4000-4), a mask was aligned with the thin-film sample. The pattern on the mask was strips with width of 2 μm and separations of 500 μm . It was necessary to note that the strips were aligned perpendicularly to the facet of the thin-film sample. While the thin-film sample was in contact position with the mask, the photoresist was exposed with ultraviolet light for ~30 s. The lamp current was ~4 A and the lamp voltage was ~40 V. The lamp power and intensity were ~160 W and ~16 MW/cm², respectively. Subsequently, the thin-film sample was developed in a developer (AZ 300 MIF) for ~15 s and a photoresist strip pattern was obtained on the thin-film sample. Before the thin-film sample was hard-baked for ~3 min at 120 °C on the same hotplate, the sample was rinsed in DI water for ~30 s. It was ensured that the entire photolithographic process was carried out in room temperature and humidity of ~20 °C and ~40 %, respectively. Next, the photoresist pattern was checked using a microscope (Olympus BX 60). This was to guarantee that the unwanted pattern was totally removed and photoresist stripes were developed on the ZnO thin-film layer as shown Figure 3.7

(c). With the stripes pattern transferred, the unmasked region of the ZnO thin film was etched using plasma. This method is used because the band-edge photoluminescence of ZnO film can be enhanced by hydrogen-containing plasma etching [229]. The sample was placed onto a water-cooled copper electrode inside a stainless steel chamber. With impedance matched to an impedance network, the electrode was capacitatively coupled to a 13.56 MHz radio frequency generator. The measured radio frequency power was ~ 120 W and the thin-film sample was self-biased to -300 V. The thin-film sample was exposed to $\text{H}_2/\text{CH}_4/\text{Ar}$ (10/30/5) plasma, where the numbers represent the gas flow in standard cubic centimeters per minute [230]. A magnetic field intensity of ~ 150 Gs was applied perpendicularly to the thin film to increase the surface plasma density. During the etching process, the working pressure was at $\sim 45 \times 10^{-4}$ Torr and the etching rate was ~ 6 nm/min. After ~ 990 s, ridges with height, width and separation of 100 nm, $2 \mu\text{m}$ and $500 \mu\text{m}$, respectively, were formed on the ZnO thin film, as illustrated in Figure 3.7 (d).

3.3.3 Characterization of the ZnO Ridge Waveguides on Silicon and Discussion

Figure 3.8 on the next page gives the light-light curves and the corresponding spectra for the thin-film ridge waveguide. In the light-light curves, the output power of both polarizations increases linearly with the increase in excitation pump power. The polarized TE optical intensities are higher than that of the TM mode. When Figure 3.8 (a) is compared to Figure 3.2 (a) of the planar waveguide, the polarized TE output intensity of the ridge waveguide is doubled that of the planar

waveguide. Furthermore, it is observed that in the TM mode, the optical intensity of the ridge waveguide is ~ 3.5 times more than that of the planar waveguide. These results imply that the confinement in the lateral direction is being improved by the ridge structure. In Figure 3.8 (b), except for the difference in optical intensities, spectra for both polarizations are similar to that in Figure 3.2 (b). The EHP recombination process predominates the exciton-exciton scattering process in the recombination mechanisms [27], since the emission peak stretches from ~ 370 to ~ 395 nm in the emission spectra.

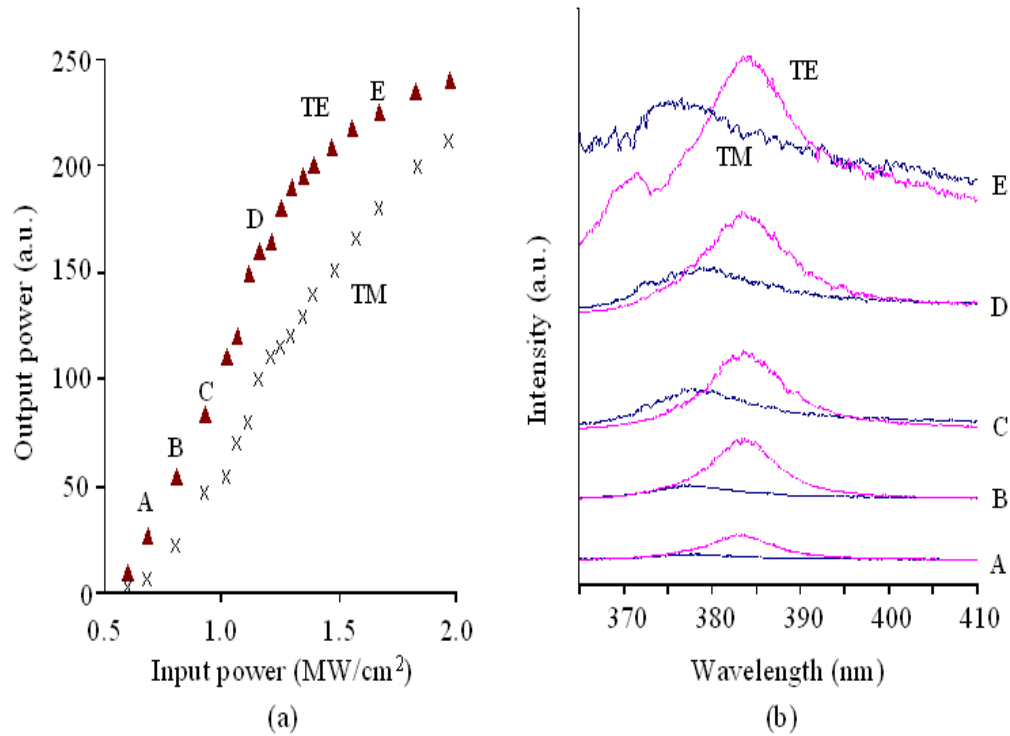


Figure 3.8 (a) Light-light curves for both polarizations and (b) corresponding spectra for the ZnO ridge waveguide.

The variation of the net optical gain for both polarizations of the ZnO ridge waveguide at different pump power is shown Figure 3.9. The net optical gain of both polarizations approximates a linear relationship with the increase in input power and gives a positive slope of ~ 60 cm/MW. The gradients of the two curves are similar to that obtained in Figure 3.3. Moreover, the net optical gain of the waveguide with the ridge structure for both polarizations approximately doubles that of the planar waveguide at the same excitation power. It is also noted that the zero net optical gains of the TE and TM modes are ~ 0.43 and ~ 0.59 MW/cm², respectively. They are reduced by ~ 0.6 times when compared to that of the planar waveguide.

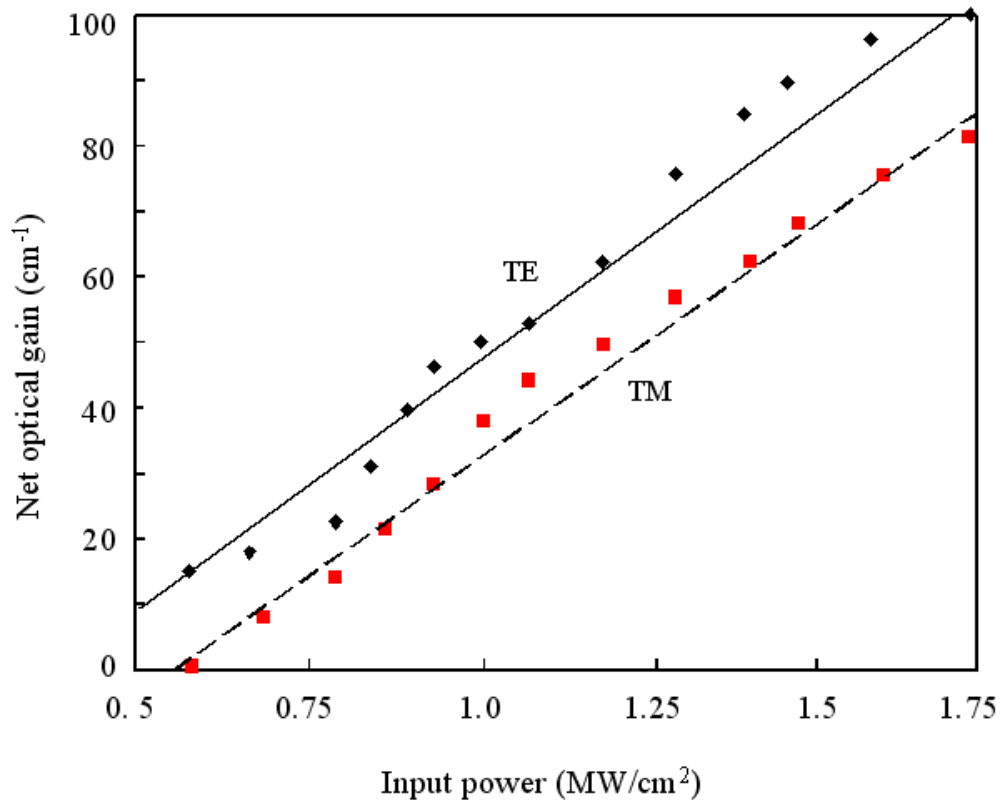


Figure 3.9 Net optical gain of the ZnO ridge waveguide versus pump power for the TE and TM polarizations.

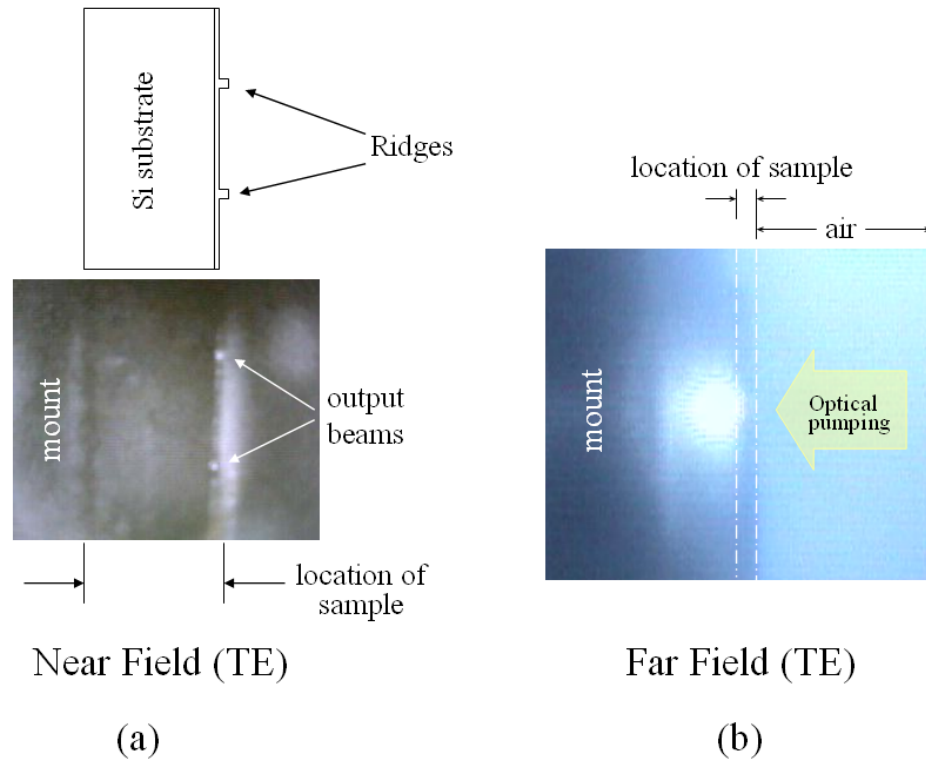


Figure 3.10 (a) Near-field of the TE mode at $<0.5 \text{ MW/cm}^2$ excitation. (b) Far-field of the TE mode at $\sim 1 \text{ MW/cm}^2$ excitation. The dotted-dashed lines indicated the location of the sample.

Figure 3.10 (a) shows the near-field of the TE mode of the ridge waveguide. It is observed when an excitation beam, of diameter and pump intensity of $9 \text{ }\mu\text{m}$ and $<0.5 \text{ MW/cm}^2$, respectively, illuminates onto several ridges. The image indicates that the emission is mainly confined inside the ridges, showing that the waveguide is effective in confining and guiding light. This is also reflected from the singular bright spot observed in the far-field of the TE mode under the excitation of a pump strip at pump intensity of $\sim 1 \text{ MW/cm}^2$, as given in Figure 3.10 (b).

3.4 Conclusion

In conclusion, our results show that the prepared thin-film waveguides exhibit amplified spontaneous emission with TE and TM peak intensity wavelength at ~ 385 and ~ 380 nm, respectively. It is also evident that the waveguides show single mode for both polarizations, with the TM mode suppressed. Furthermore, it is observed that the use of ridge waveguide is capable to enhance the optical characteristics of the ZnO films. Its net optical gain is $\sim 100 \text{ cm}^{-1}$ ($\sim 50 \text{ cm}^{-1}$) in the TE (TM) polarization at pump intensity of $\sim 1.75 \text{ MW/cm}^2$ and they are ~ 1.6 times (~ 2 times) larger than that of the planar waveguide. Apart from having larger net optical gain, the excitation power required to achieve a zero net optical gain in the ridge waveguide is reduced by ~ 0.6 times for both polarizations. These improvements show that the coupling between the signal and the pump wave is further improved in the ridge waveguide.

To summarize this chapter, it is demonstrated that the FCVA technique can fabricate device-quality silicon-based ZnO thin-film waveguides on the lattice-mismatched SiO_2 buffer layer. In addition, the waveguide is fabricated at low substrate temperature ($\sim 230^\circ\text{C}$) on large substrates ($\sim 6''$ in diameter in the system). More importantly, this cost-effective fabrication technique can be used as an advantageous approach for mass-production. Hence, the FCVA technique is the stepping-stone to develop and advance the making and integration of other optical and electrical silicon-based devices.

CHAPTER 4 ZnO Random Lasers

4.1 Introduction

Amplified spontaneous emission (ASE) is observed in the waveguides mentioned in CHAPTER 3 and yet no lasing is observed. This is because in order to fabricate conventional Fabry Perot cavity, two parallel smooth facets have to be realized [231]. These facets, however, are difficult to realize by cleaving the ZnO thin films without further polishing. The reason is due to the fact that ZnO films (i.e., wurtzite structure) growth on Si substrate has no (100) plane perpendicular to the substrate surface [232,233]. Therefore, it is difficult to cleave a smooth facet as if GaAs or InP films parallel to the growth direction. Hence, to introduce a feedback mechanism for lasing in ZnO materials, hexagonal ZnO microcrystallites [19] with parallel facets have been fabricated on sapphire to form the Fabry-Perot lasing cavities. In contrast to the feedback presented from these orderly structures, lasing action has also been demonstrated in ZnO polycrystalline thin films [31] and ZnO powder films [32]. When light waves travel in these active random media, the directions of propagation of each light wave are changed as it interacts with a scatterer [234]. A scattered light wave lost its initial direction completely after traveling an average distance of l_t , known as the transport mean free path. This distance is related to the average distance that light travels between two consecutive scattering events, known as the scattering mean free path (l_s) by the equation (4.1),

$$l_t = \frac{l_s}{1 - \langle \cos \theta \rangle}, \quad (4.1)$$

where $\langle \cos \theta \rangle$ is the average cosine of the scattering angle. The value of $\langle \cos \theta \rangle$ is 0, since the wavelength of the scattered light is of dimension much greater than that of the scatterer. Hence, the relation

$$l_t = l_s, \quad (4.2)$$

is resulted [235].

In addition to the characteristic that the directions of propagation of light waves are randomized in these active random media, the intensity of light waves is amplified. Besides, it is possible for a photon to trigger the formation of another photon via stimulated emission. The path length over which a photon travels before generating another photon is defined as the generation length (l_{gen}) and it is approximated to the gain length (l_g = path length over which the light intensity is amplified by a factor of e) [236]. Once this gain length equals to the average path length (l_{pat} = average distance that a photon travels before leaving the medium), the number of photons increase rapidly [236]. Mathematically, it is shown that the solution to the diffusion equation, including optical gain, increases exponentially [237]. At this threshold condition, a critical volume (V_{th}) is hypothesized by the relation [236],

$$V_{th} \sim l_t l_g^{3/2} \text{ or } V_{th} \sim l_s l_g^{3/2}, \quad (4.3)$$

based on the fact that $l_t = l_s$ in equation (4.2). After this threshold, a photon will multiply itself in a geometric progression (1, 2, 4, 8, 16.....) and this give rise to lasing with incoherent feedback [238]. For this type of laser, there exists a threshold when the light emission intensities are plotted against the corresponding

pumping powers (light-light curve). This sudden change in the gradient of the light-light curve is due to the drastic increase of photon density. It is also observed that above the threshold, suddenly spectral narrowing takes place. This is because the gain lengths are different for different wavelengths and the criterion $l_g = l_{pat}$ is first achieved for the range of wavelengths that have shorter gain lengths, leading to a rapid increase of photons at these wavelengths [238].

On the other hand, when the scattered light waves return to the point through different paths where they are originated from, closed-loop paths are formed. These paths interfere [239] with each other and the phase shift requirement along these closed-loop paths is $2m\pi$, where m is an integer. Hence, coherent random lasing is resulted as the amplification of light intensities in these paths equals to that of the loss. This coherent lasing phenomenon is different from that of the incoherent lasing in which the phase shift requirement is not met [238]. Moreover, a threshold is observed in the light-light curve, accompanied with distinct sharp peaks appearing in the emission spectrum. The number of sharp peaks increases as the pump power increases because more closed-loop cavities are having the gain greater than the loss [236]. Another characteristic for this type of laser is that these lasing peaks in the emission spectra can also be detected and changed with different observation angles. This is because the scattering paths that form different laser cavities with different lasing modes can be positioned in different orientations [32].

Although lasing is demonstrated from the disordered structures, the distributions and sizes of the scatterers are difficult to be controlled in epilayer films. Hence,

one of the methods is to introduce scatterers into the planar waveguide described in CHAPTER 3 to achieve random lasing. In addition, it is important that the distributions and sizes of the scatterers can be designed and controlled in advance.

4.2 ZnO Nanorod Arrays Embedded in ZnO Epilayers

4.2.1 Design of the ZnO Nanorod Arrays Embedded in ZnO Epilayers

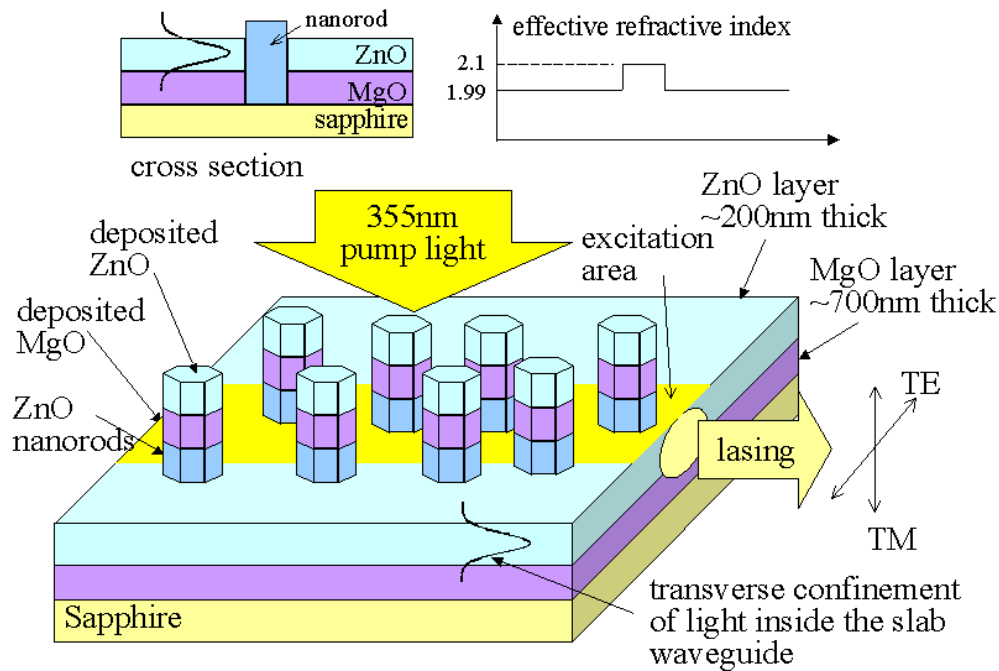


Figure 4.1 Proposed design of the ZnO nanorod arrays embedded in the ZnO epilayers. TM: transverse magnetic. TE: transverse electric.

The proposed random laser design of the ZnO planar waveguide introduced with scatterers is shown in Figure 4.1. It comprises of ZnO nanorod arrays embedded in the ZnO epilayers. The ZnO nanorod arrays are employed as scatterers for random lasing action because distributions and sizes of the nanorods can be easily

manipulated by the different growth methods and it have shown potential in nanodevice applications (APPENDIX A). On the other hand, the MgO and ZnO thin-film layers form the planar waveguide and act as the gain medium. The waveguide provides gain to the light that is scattering in between the ZnO nanorods, inside the epilayers. This causes a decrease in the gain length of the scattered light. It also leads to a reduction in the scattering mean free length, meaning that the average distance between two scattering events is shortened. Furthermore, it changes the contrast in the refractive index between the ZnO nanorods and the ZnO epilayers. From the inset of Figure 4.1, the effective refractive index of the ZnO epilayers without the ZnO nanorod is ~ 1.99 [240], since the refractive indices of MgO and ZnO are ~ 1.76 and 2.1 , respectively. Next, MgO are used as the material for the epilayer because: 1) It has a refractive index lower than that of ZnO, leading to total internal reflection of light into the ZnO thin film and confinement of light to propagate in the direction parallel to the substrate surface, 2) it has a low absorption loss, 3) it can be fabricated by the filtered cathodic vacuum arc (FCVA) technique at a low deposition temperature ($\sim 230^\circ\text{C}$) that is independent of the thermal oxidation step ($\sim 1100^\circ\text{C}$) for the SiO_2 growth, and 4) the investigation of this material provides important informations and links to the findings that are going to be discussed in section 5.3.

4.2.2 Fabrication of the ZnO Nanorods Arrays Embedded in ZnO Epilayers

The vertically aligned hexagonal ZnO nanorod arrays were fabricated by the metalorganic vapor-phase epitaxy (MOVPE) system from our collaborator. In the fabrication process, no metal catalyst was used and a thin ZnO layer was grown at low temperature on an Al₂O₃ (001) substrate as a buffer layer prior to the fabrication of the ZnO nanorods. The reactants were diethylzinc (DEZn) and oxygen and their flow rates were in the range of 20-100 and 0.5-5 standard cubic centimeters per minute, respectively. Argon was used as a carrier gas. The DEZn bubbler temperature and the growth temperature were -15-0 °C and 400-500 °C, respectively [241]. The hexagonal ZnO nanorods grown by this method have diameter, length, and density of 70 nm, 2 μm, and 1.7×10^{11} nanorods/cm², respectively [242].

A layer of MgO of thickness 700 nm was deposited onto the ZnO nanorods arrays by the FCVA technique, prepared by a high-purity Mg target (99.9 % in purity). After that, using a high-purity Zn target (99.9 % in purity), a 200 nm-thick ZnO thin film was deposited. During the deposition of the MgO and the ZnO thin films, the arc current, the substrate temperature and the oxygen partial pressure were set to 60 A, 230 °C and 3×10^{-4} torr, respectively. The substrate temperature was chosen to optimize the optical performance in the ultraviolet region [225]. The oxygen partial pressure was different to that used to prepare the SiO₂-buffered waveguide, described in CHAPTER 3; to reduce the stress induced between the ZnO and the MgO thin films [23,226]. This was because the difference in the

thermal expansion coefficient for ZnO ($\sim 5 \times 10^{-6}/^\circ\text{C}$) [243] and MgO ($\sim 11 \times 10^{-6}/^\circ\text{C}$) [244] was larger than that between ZnO and SiO₂ ($\sim 0.5 \times 10^{-6}/^\circ\text{C}$) [245]. Other procedures and parameters were identical as they were discussed in section 3.2.2.

4.2.3 Characterization of the ZnO Nanorod Arrays fabricated by Metalorganic Vapor-phase Epitaxy System

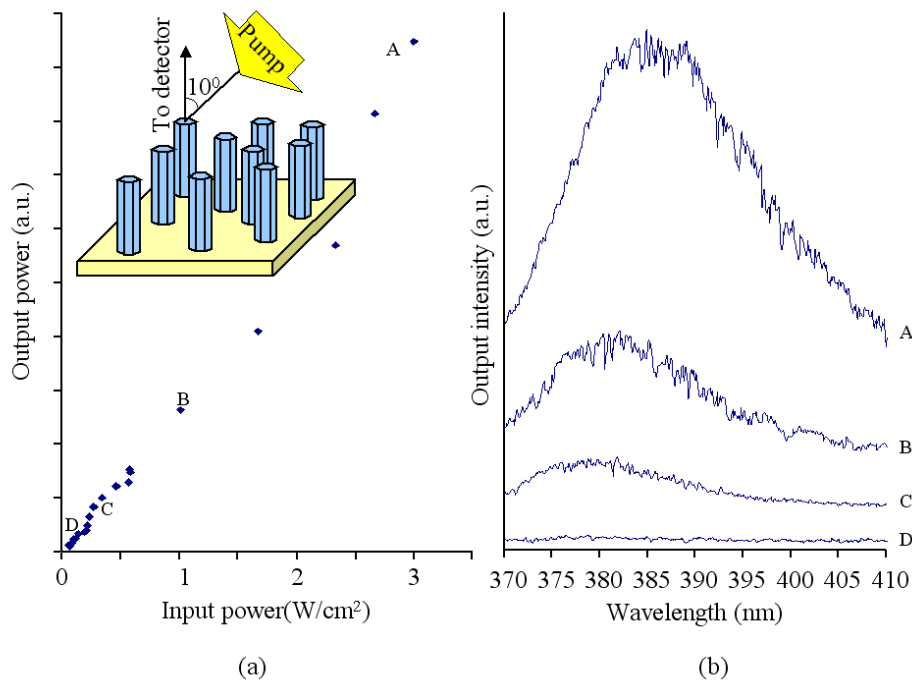


Figure 4.2 (a) Unpolarized light-light curve and (b) corresponding emission spectra for the ZnO nanorod arrays detected along the symmetric axis of the nanorod. The inset shows that the ZnO nanorod arrays were excited by a pump beam illuminated at an angle of 10° to surface normal of the sapphire substrate.

Before the deposition of the ZnO epilayers to embed the ZnO nanorods, the light-light curve and the corresponding spectra for the ZnO nanorod arrays were obtained, as shown in Figure 4.2 on the previous page. This was necessary to check that the sample without the ZnO epilayers did not exhibit lasing. The excitation beam was illuminated onto the sample at an angle of 10° to the surface normal of the sapphire substrate, to couple light effectively into the nanorods, as illustrated in the inset of Figure 4.2 (a). The emission from the facets of the nanorods was collimated into the monochromator through an objective lens. From Figure 4.2 (a), it is noted that the emission output intensity increases linearly with the increase of the input pump power. At pumping intensities of 3 MW/cm^2 , 955 kW/cm^2 , 454 kW/cm^2 and 52 kW/cm^2 , the corresponding emission output spectra A, B, C and D are observed as shown in Figure 4.2. The emission spectra stretch from ~ 370 to $\sim 410 \text{ nm}$ and they indicate that the electron hole plasma process is the main process behind the recombination mechanism. Besides, there is no lasing mode observed in the spectra since the threshold gain is lower than the theoretical value that is required to sustain Fabry-Perot lasing. Moreover, similar results are obtained for pump beam incident at other angles ($10^\circ - 80^\circ$ to the surface normal).

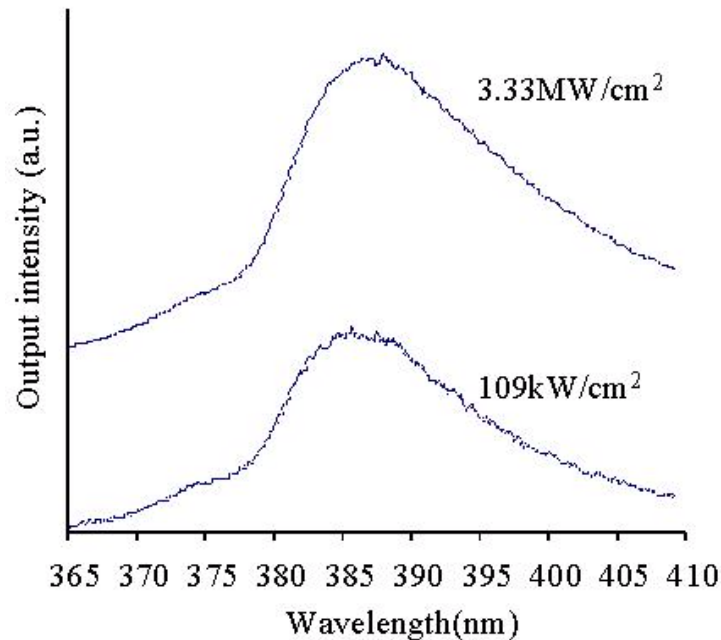


Figure 4.3 Emission spectra of the ZnO nanorod arrays detected parallel to the surface of the substrate.

The emission spectra of the ZnO nanorod arrays are shown in Figure 4.3. This is to check that the ZnO nanorod arrays alone cannot give rise to random lasing. It is observed that the output intensity is increased at a higher excitation pump power. Furthermore, the sample shows only ASE without any lasing mode, even at a higher pump excitation power of 3.33 MW/cm^2 . Random lasing is not supported in the ZnO nanorod arrays due to the low density of nanorods. The air spaces in between the sparsely distributed nanorods have weak scattering strength. It takes a long distance before light is scattered from one nanorod to another. Due to the long distance, the intensity of the scattered light is drastically reduced when it is scattered onto another nanorod. Therefore, without the ZnO epilayers, either Fabry-Perot or random lasing does not take place in the ZnO nanorods.

4.2.4 Characterization of the ZnO Nanorod Arrays Embedded in ZnO Epilayers

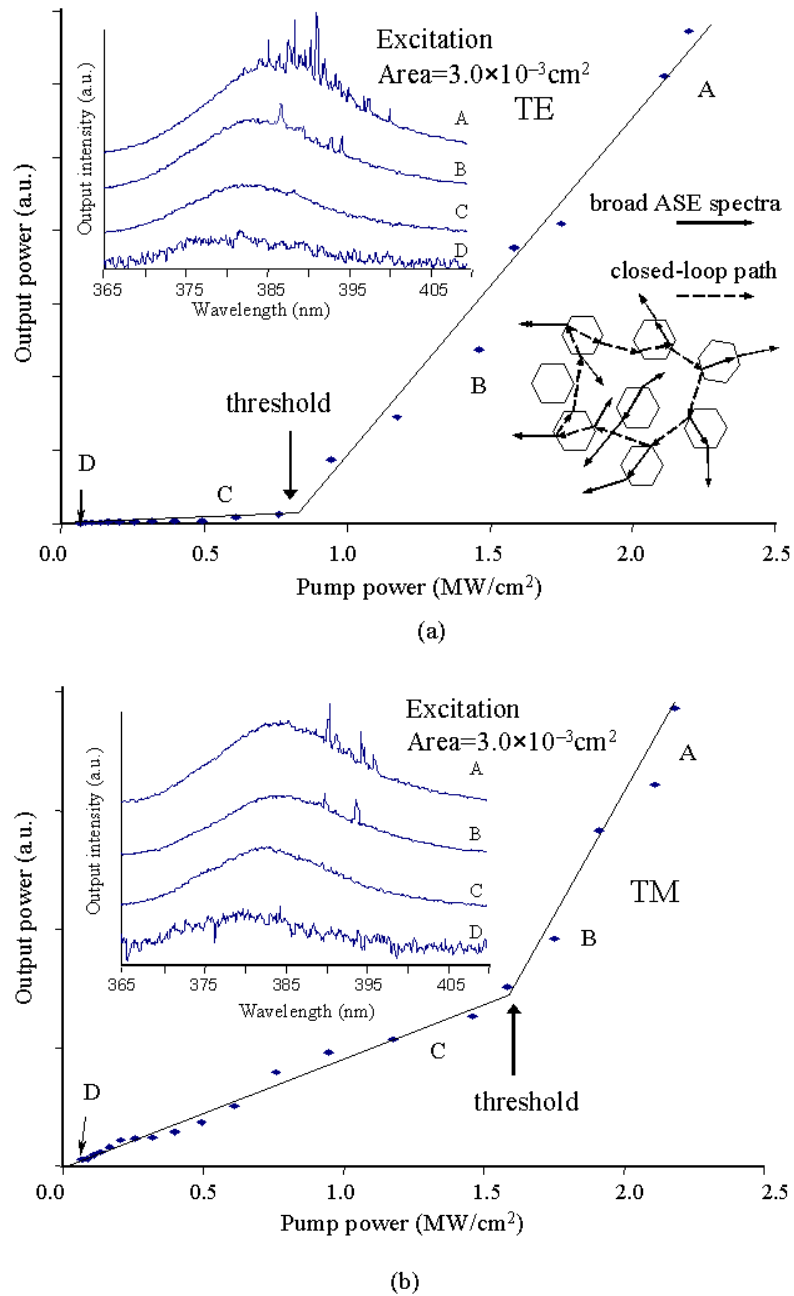


Figure 4.4 Light-light curves and the corresponding emission spectra of the (a) TE and (b) TM polarizations from the ZnO nanorod arrays embedded in the ZnO epilayers. The insets of the top-left-hand side corner are the emission spectra at

various pump intensities and that on the bottom-right-hand side corner is a schematic diagram showing the formation of closed-loop path for light through recurrent scattering (dashed arrow) and single-broad ASE spectra (solid arrow) in the sample.

In this section, we study the optical characteristics of ZnO nanorods after the ZnO epilayers were deposited and embedded into the ZnO nanorods. The light-light curves and the corresponding emission spectra of both polarizations from the ZnO nanorods embedded in the ZnO epilayers are shown in Figure 4.4 (a) and (b) on the previous page. The TE (TM) direction is defined as the direction that is parallel (perpendicular) to the surface of the sapphire substrate. From the light-light curves, there is a threshold at $\sim 800 \text{ kW/cm}^2$ and $\sim 1.6 \text{ MW/cm}^2$ for the TE and TM polarization, respectively. Below these thresholds, both polarizations have a single-broad emission spectra with a full-width half maximum of $\sim 15 \text{ nm}$. The single-broad emission peak in the spectra is the ASE that is sustained by the slab waveguide, as indicated by the solid arrows of the inset in the lower-right-hand side corner of the Figure 4.4 (a). Above these thresholds, the emission output for both polarizations increases rapidly as the pump power intensifies. At the same time, sharp peaks with a linewidth of less than 0.4 nm appear in the spectra for both polarizations, as shown in the insets of the upper-left-hand side corner in Figure 4.4 (a) and (b). These peaks are the lasing modes of the laser emission output [246]. Besides, more peaks emerge with the further increase in the pump power intensity, typically noted in random laser [32,247]. These lasing peaks are not strong enough to suppress the spontaneous emission peak probably due to the small excitation area. The peaks are not Fabry-Perot lasing modes from the slab

waveguide, but they are caused by the formation of the closed-loop optical paths, shown by the dashed arrows of the inset in the lower-right-hand side corner of the Figure 4.4 (a). The ZnO nanorod arrays scatter light into different directions and when the scattered light returns to the starting point where it is originated from, then a closed-loop path is formed. The solid arrows indicate the light scattered inside the ZnO epilayers that are unable to form closed-loop path, causing the broad emission spectra.

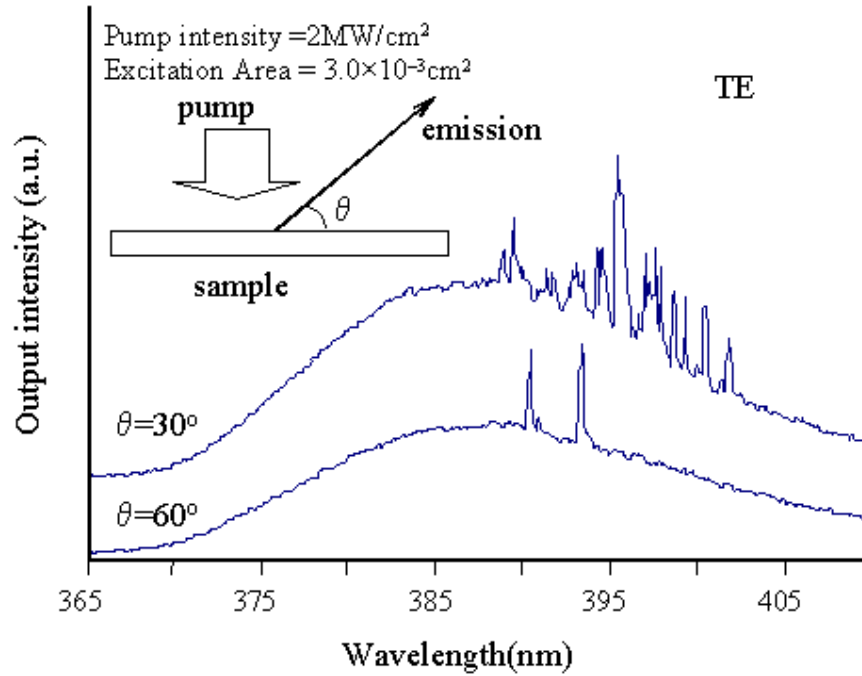


Figure 4.5 Spectra of the TE polarization radiate from 30° to 60° from the sample surface. The pump intensity is 2 MW/cm^2 and the excitation area is kept at $3 \times 10^{-3} \text{ cm}^2$.

Similar sharp emission peaks are observed in the spectra collected at different angles to the surface of the sample, as shown in the inset of Figure 4.5. The

excitation intensity and the excitation area are kept at 2 MW/cm^2 and $3 \times 10^{-3} \text{ cm}^2$, respectively. These lasing modes are recorded in different observation angles (θ) and this is one of the characteristics of random laser [248]. Moreover, it is noted that different emission spectrum are detected at different observation angles and the emission spectra shows more lasing peaks as the observation angle decreases. This is because the propagation of light waves is most efficient in the direction parallel to the sample surface and confined by the waveguide formed from the ZnO epilayers.

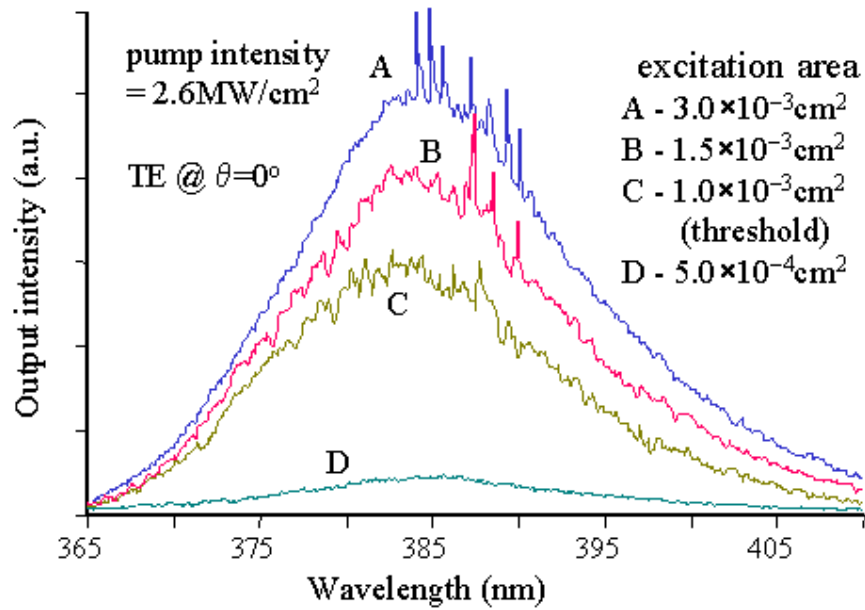


Figure 4.6 Spectra of the TE polarization of the sample when the excitation area is (from top to bottom) 3×10^{-3} , 1.5×10^{-3} , 1×10^{-3} and $5 \times 10^{-4} \text{ cm}^2$. The excitation intensity is 2.6 MW/cm^2 .

Figure 4.6 shows changes in the emission spectra of the ZnO nanorod arrays embedded in the ZnO epilayers with different excitation areas of 3×10^{-3} , 1.5×10^{-3} ,

1×10^{-3} and $5 \times 10^{-4} \text{ cm}^2$ while the pump intensity is kept at 2.6 MW/cm^2 . It is noted that below the critical area of $1 \times 10^{-3} \text{ cm}^2$, no lasing mode emerges from the spectrum. However, as the excitation area is larger than $1 \times 10^{-3} \text{ cm}^2$, sharp peaks with a linewidth of less than 0.4 nm appear in the spectrum. This is because there exists a critical excitation area below which optical amplification is not sufficient to sustain lasing [249]. Furthermore, it is observed that when the excitation area is increased, there are more lasing peaks observed in the spectrum. This correlation is established, based on the fact that the larger the excitation area, the greater number of closed-loop paths of scattering light can be formed.

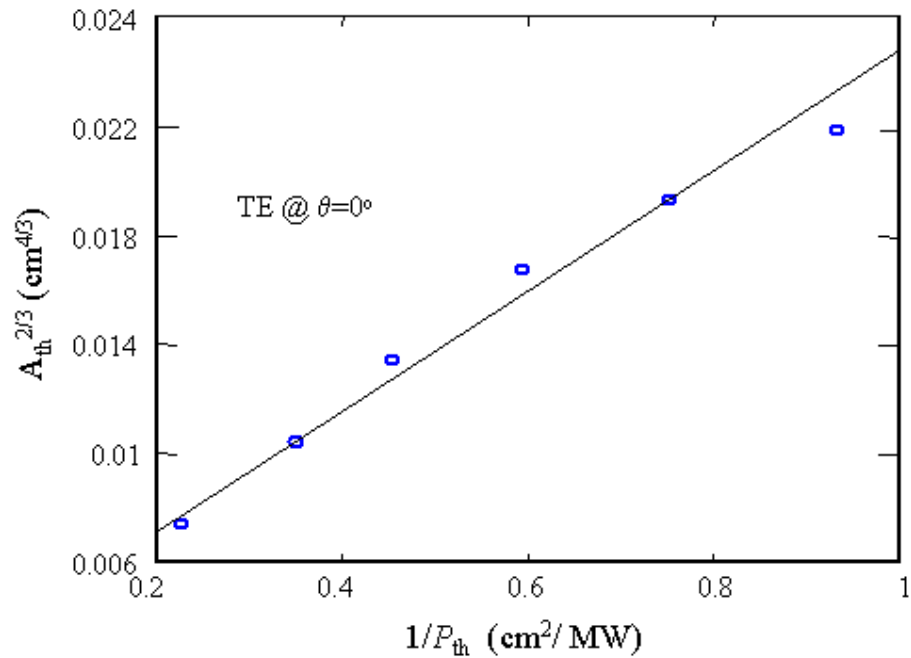


Figure 4.7 Dependence of the threshold pump area (A_{th}) on the threshold pump power (P_{th}) of the ZnO nanorod arrays embedded in the ZnO epilayers for the TE polarization.

Other than the measurement mentioned, the relationship between the threshold pump area (A_{th}) and the threshold pump power (P_{th}) is also another important characteristic of random laser action. On the previous page, Figure 4.7 shows the dependence of A_{th} on P_{th} of the sample for the TE polarization. In the figure, different values of $A_{th}^{2/3}$ are plotted against the corresponding P_{th}^{-1} and the relationship is a straight line. As the value of P_{th}^{-1} is increased, the value of $A_{th}^{2/3}$ increases proportionally. Their relationship can be explained by the random laser theory. It is known that the critical volume $V_{th} = A_{th}$ (threshold excitation area) $\times d$ (thickness of ZnO) is related to the threshold gain length (l_g) and the scattering mean-free path (l_s) of the highly disordered gain media by $V_{th} \sim (l_s l_g)^{3/2}$ [32], as given in equation (4.3). Besides, optical gain (g) is proportional to l_g^{-1} and threshold pump intensity (P_{th}) is proportional to l_g^{-1} [235]. Hence, l_g^{-1} can be expressed as $l_g^{-1} \sim (\delta g / \delta P) P_{th}$, where $\delta g / \delta P$ is a constant. Therefore, $A_{th}^{2/3}$ is linearly related to P_{th}^{-1} by the equation (4.4),

$$A_{th}^{2/3} \sim l_s d^{-2/3} (\delta g / \delta P)^{-1} P_{th}^{-1} \quad (4.4)$$

and the relationship implies that the lasing threshold characteristics of the ZnO nanorods embedded in the ZnO epilayers agreed with the random laser theory.

4.3 Conclusion

In conclusion, coherent random lasing takes place after the deposition of ZnO layer is because of 1) the ZnO and MgO thin-film layers act as a waveguide to confine the scattering of light inside the ZnO layer (i.e., MgO has a smaller refractive index than ZnO), and 2) the ZnO thin-film layer provides sufficient gain to the

light scattered between nanorods. In this case, the distributions and sizes of the scatterers can be controlled before they are embedded into the ZnO epilayers. Random lasing action is the mechanism behind the lasing phenomenon that takes place inside the sample because: 1) after the pump lasing threshold intensities (TE at $\sim 800 \text{ MW/cm}^2$ and TM at $\sim 1.6 \text{ MW/cm}^2$), the number of lasing peaks observed in the emission spectra increases as the pump intensity increases, 2) the lasing peaks in the spectrum do not have a constant mode spacing, 3) different emission spectrum with lasing peaks can be detected with different observation angles, 4) the pump lasing threshold is reduced when the excitation area is increased, and 5) the relationship between the lasing threshold and the excitation area agrees well with that of the random laser theory, as given in equation (4.3).

CHAPTER 5 ZnO Thin-film Random Lasers

5.1 Introduction

Lasing is demonstrated from the ZnO nanorod arrays embedded in epilayers. However, it is difficult to integrate with other silicon-based electrical and optical components. Moreover, it requires the use of expensive sapphire substrates and the involvement of the filtered cathodic vacuum arc (FCVA) and metalorganic vapor-phase epitaxy (MOVPE) technique to realize random lasing, meaning higher costs and more parameters to be optimized. Therefore, we proposed to post-growth anneal the ZnO films on Si in this chapter, as deposited by the FCVA technique, to realize random lasing.

5.2 ZnO Thin-film Random Lasers

5.2.1 Design of the ZnO Thin-film Random Lasers

In CHAPTER 3, the SiO₂-buffered ZnO ridge waveguide fabricated by the filtered cathodic vacuum arc (FCVA) method offers good optical gain and emission intensity. It also provides optical confinement in the lateral and transverse directions. Hence, the proposed ZnO thin-film random lasers fabricated by the FCVA technique is based on the ridge structure, as shown in Figure 5.1. Moreover, a post-growth annealing method is proposed to generate ZnO grains and voids [250,251] and it is efficient in low-temperature deposition FCVA technique. The

development of grains and voids increases the randomness and the refractive index contrast of the ZnO films, leading to the strong scattering of light [252]. The developed disordered grains act as the multiple scatterers and change the propagation directions of light. They lead to the formation of the closed-loop paths of light in the ZnO thin films, as indicated by the yellow arrows in Figure 5.1. More importantly, the annealing temperature and time [251] are capable of controlling the development of grains and voids, and indirectly manipulating the random lasing cavities.

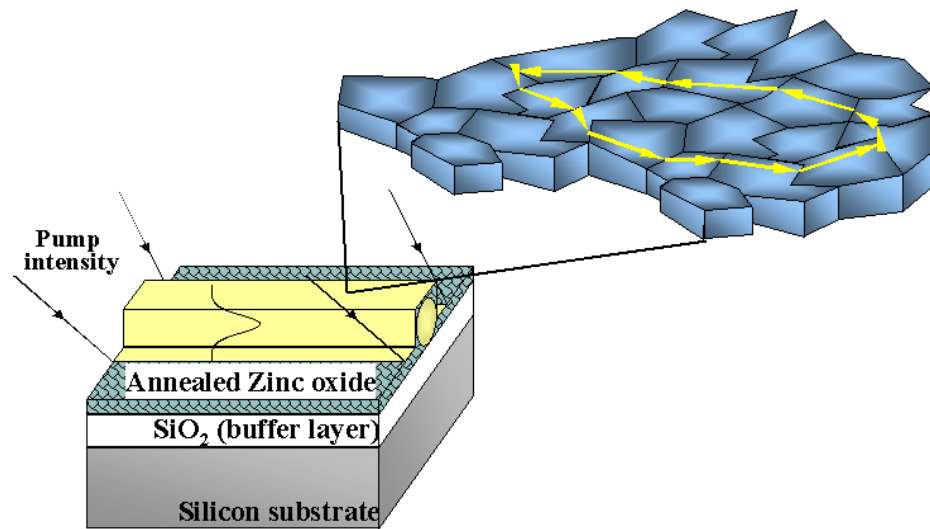


Figure 5.1 Schematic diagram of the ZnO thin-film random laser.

5.2.2 Fabrication of the ZnO Thin-film Random Lasers

The ZnO thin-film random laser was fabricated according to the procedures shown in Figure 5.2. First, in Figure 5.2 (a), a Si substrate was thermally oxidized to form a SiO₂ layer (420 nm) on itself, a ZnO thin-film layer (200 nm) was fabricated on top by following the steps and procedures stated in section 3.2.2. Next, the sample

underwent post-growth annealing in a quartz tube that was opened at both ends and inside a standard Lindberg-type furnace for the development of grains and voids shown in Figure 5.2 (b). After the sample was placed inside the quartz tube that was located at the center of furnace, temperature of the furnace was set to heat up from room temperature to 900 °C within ~20 min. Then the furnace temperature dwelled for a period of time, T_a , at a constant temperature of 900 °C. Following that, the sample was cooled down to room temperature before it was taken out of the furnace. The annealing temperature profile was selected to reduce the thermal strain and stress developed at the Si/SiO₂ and the SiO₂/ZnO interfaces. Besides, T_a was chosen to be 900 °C so that it was higher than the ZnO growth temperature for the effective developments of ZnO grains and voids that were critical to the formation of the random scatterers in random lasing. Finally, photoresist lines were coated on the annealed ZnO planar waveguide, followed by plasma etching with the procedures and parameters stated in section 3.3.2. After the removal of photoresist, the ZnO ridge waveguide random laser was formed, as shown in Figure 5.2 (c).

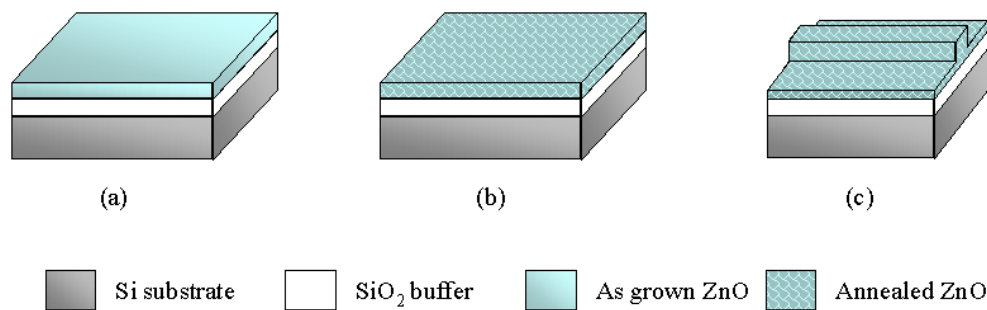


Figure 5.2 Fabrication procedures of the proposed ZnO ridge waveguide random laser. (a) The SiO₂ buffer layer is formed on the silicon substrate by thermal oxidation, followed by the deposition of ZnO thin film on a SiO₂ buffer layer by

the FCVA technique. (b) The sample is post-growth annealed. (c) Deposition of line masks on the ZnO thin film for the preparation of plasma etching. (d) ZnO ridge waveguide random laser is formed from plasma etching the photoresist unmask region and the subsequent removal of photoresist line mask that protects the ridge.

5.2.3 Characterization of ZnO Thin-film Random Lasers

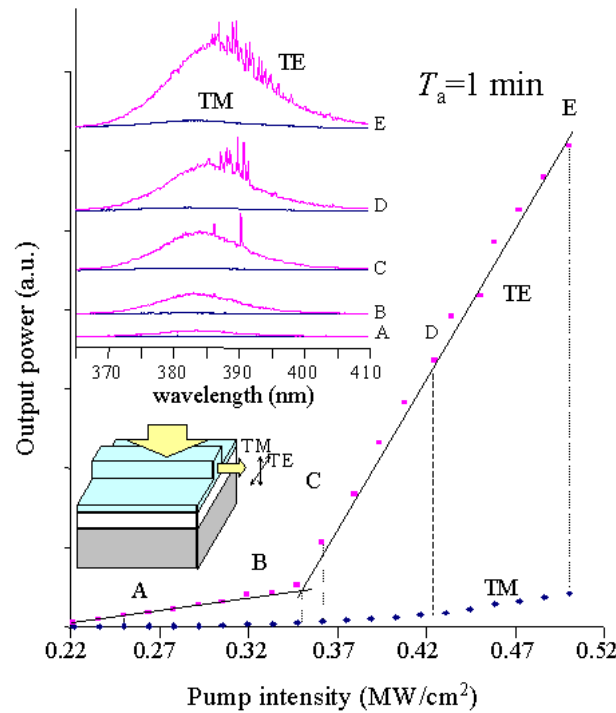


Figure 5.3 Light-light curve and the emission spectra of the sample after post-growth annealing for $T_a = 1$ min.

The light-light curves and the emission spectra of the sample with $T_a = 1$ min are shown in Figure 5.3. The TE and the TM polarizations are defined as the directions

that are parallel and perpendicular to the surface of the substrate, respectively, as illustrated in the inset. At pump intensities below $\sim 0.35 \text{ MW/cm}^2$, both light-light curves increase slowly and linearly with the increase in pump powers. Besides, a broad spontaneous emission peak is noted for both polarizations from the spectra, stretching from ~ 370 to $\sim 410 \text{ nm}$. It shows that the electron hole plasma (EHP) process is the dominant mechanism behind the recombination process [27]. However, when the excitation power exceeds this threshold ($\sim 0.35 \text{ MW/cm}^2$) for the transverse-electric (TE) polarization, the slope of the light-light curve increases suddenly. This variation in gradient is caused by the lasing peaks (linewidth less than 0.4 nm) that emerge from the spectra. They appear at $\sim 390 \text{ nm}$ of the board spectra that have a FWHM of $\sim 15 \text{ nm}$. The number of lasing TE modes increases as pump power increases because more lasing cavities can be formed with higher optical gain to overcome the scattering losses. Although more lasing modes are formed, they cannot suppress the amplified spontaneous emission (ASE) peak observed in the as-growth sample, due to the optical confinement of the ridge waveguide structure. Another reason is that the grains and the voids of the ZnO thin-film waveguide laser are not well developed within a short period of annealing time ($T_a = 1 \text{ minute}$). Hence, the contrast in the reflectivity is not large and the laser cavities inside the ZnO thin films are weakly formed. As for the transverse-magnetic (TM) polarization, the change in the light-light curve gradient and the presence of lasing modes in the spectra are not noted.

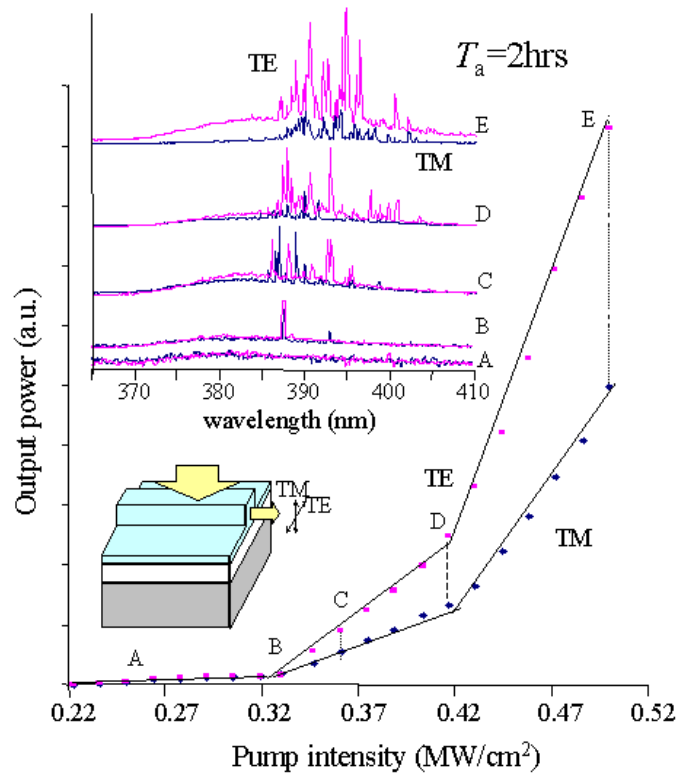


Figure 5.4 Light-light curve and the emission spectra of the sample after post-growth annealing for $T_a = 2$ h.

Figure 5.4 shows the light-light curves and the emission spectra of the sample with $T_a = 2$ h. A broad emission peak is noted below the pump intensity of ~ 0.33 MW/cm². Above it, lasing peaks are observed in both polarizations from the spectra at ~ 390 nm, each having a linewidth of less than 0.4 nm. This is accompanied with the increase of slope in the light-light curves for both polarizations. The number of lasing modes increases with the increase of pump intensities. As the pump power is ~ 0.42 MW/cm², a second group of lasing modes at around 400 nm are noted and it causes the slope of the light-light curve to increase further. This is triggered by the formation of a second group of laser cavities with higher losses by the higher optical excitation. Besides, the intensities

ratio of the lasing peaks to that of the ASE peak is larger for the sample with $T_a = 2$ h than that of the sample with $T_a = 1$ min. The lasing modes are stronger in the sample with $T_a = 2$ h because the ZnO voids and the grains of the waveguide laser are well developed and the reflectivity contrast between the grains and the voids is large.

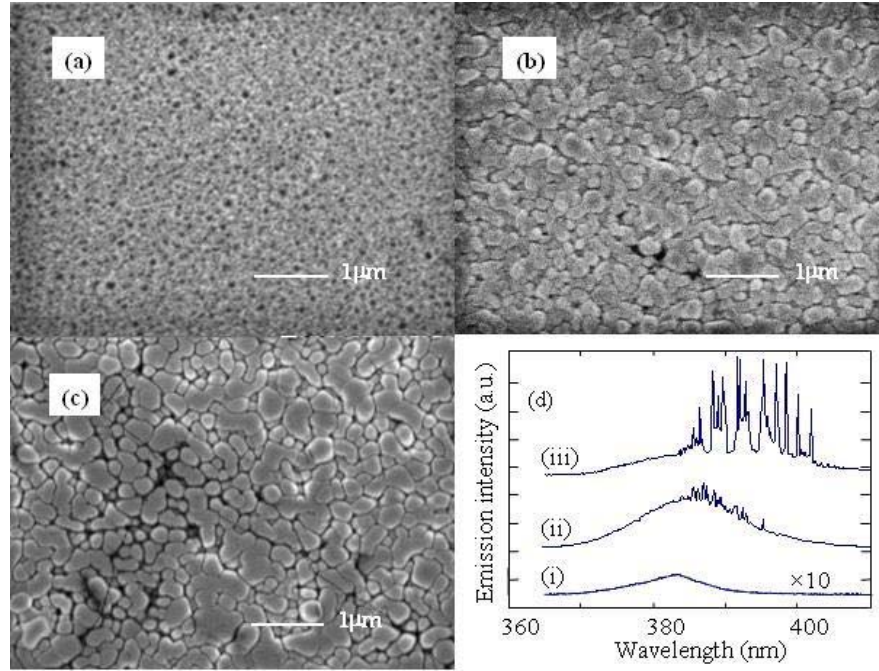


Figure 5.5 Scanning electron microscope (SEM) images of ZnO thin films: (a) as-grown, (b) $T_a = 1$ min, and (c) $T_a = 2$ h. (d) Emission spectra of the ZnO thin films: (i) as-grown, (ii) $T_a = 1$ min, and (iii) $T_a = 2$ h.

Figure 5.5 (a) shows the SEM images of the as-growth sample. The ZnO grains of the as-growth sample are small and packed together closely. In Figure 5.5 (b) and (c) gives the ZnO thin films that are annealed at 900 °C for $T_a = 1$ min and $T_a = 2$ h, respectively. For the case of $T_a = 1$ min, the corresponding grains and voids start to develop with average grain size of about ~100 nm. The underdeveloped grains and voids lead to the small intensities ratio between the lasing peaks and the ASE

peak in the emission spectrum. For the case of $T_a = 2$ h, the average grain size is about ~ 170 nm. The fully developed grains and voids in the ZnO thin film leads to the strong lasing modes when compare with the sample for $T_a = 1$ min. Figure 5.5 (d) shows the emission spectra of ZnO films: (i) as-grown, (ii) $T_a = 1$ min, and (iii) $T_a = 2$ h. It is observed that the ultraviolet (UV) ASE peak intensity in Figure 5.5 (d) (ii) is ~ 20 times of that in Figure (d) (i). This increment is due to the enhancement of UV ASE by annealing. On the contrary, prolong annealing will degrade the UV ASE as shown in Figure 5.5 (d) (iii), which shows that the corresponding UV ASE peak intensity is ~ 0.4 time of that in Figure 5.5 (d) (ii). Besides, it is noted that the emission intensity of the lasing peak in Figure 5.5 (d) (iii) is ~ 2 times to that obtained in Figure 5.5 (d) (ii).

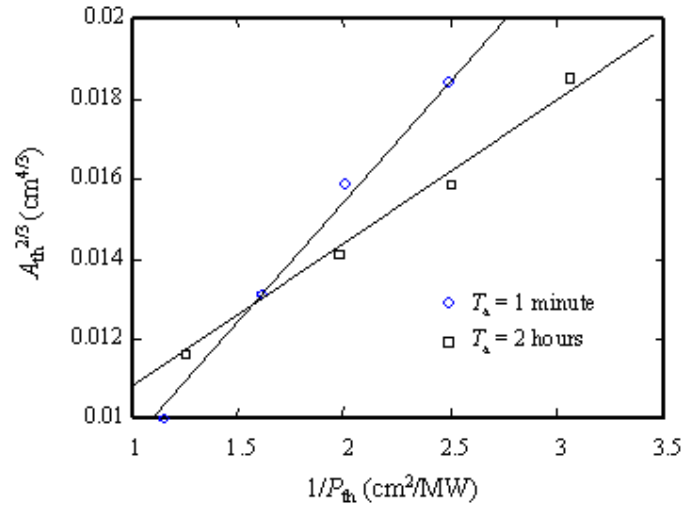


Figure 5.6 Plot of $A_{th}^{2/3}$ against P_{th}^{-1} for the post-growth samples with $T_a = 1$ min, and $T_a = 2$ h.

Plot of the dependence of threshold pump area (A_{th}) on pump threshold (P_{th}) of the post-growth samples with $T_a = 1$ min, and $T_a = 2$ h for the TE polarization is shown in Figure 5.6. For both samples, the graphs are straight lines that conform

to the equation (4.4) in consistency to the random laser theory. The gradients of the lines for samples with $T_a = 1$ min and $T_a = 2$ h are $\sim 6.3 \times 10^{-3}$ and $\sim 3.6 \times 10^{-3}$ $\text{MWcm}^{-2/3}$, respectively. The sample annealed for a longer time has a smaller gradient, meaning that the scattering length is shorter in equation (4.4), assuming that $\delta g / \delta P$ is a constant. These values of gradient are smaller compared to that of the ZnO nanorods embedded in the ZnO epilayers ($\sim 2 \times 10^{-2} \text{MWcm}^{-2/3}$). Hence, the results reflect that the scattering length is in the ascending order of the annealed samples with $T_a = 2$ h, $T_a = 1$ min and the nanorods embedded in the epilayers.

5.3 Coherent and Incoherent ZnO Thin-film Random lasers

Closed-loop paths are formed and coherent random lasing action is observed [253,254] in both the ZnO nanorods embedded in the ZnO epilayers and the annealed ZnO thin-film lasers. In fact, there is another kind of random lasing action known as the incoherent random lasing [255]. As discussed in CHAPTER 4, when photons are excited in an active random medium, each photon may cause one or more photons to be produced by stimulated emission before leaving the medium. As the photon number increases drastically, incoherent random lasing action is resulted [238]. These two types of random lasing action are demonstrated and their formation conditions determined in ZnO powder [238]. However, there is no report on similar investigation being performed on ZnO thin films, although thin-film random laser has a greater commercial value. Therefore, it is proposed to study the conditions that cause the two types of random lasing action in the ZnO epilayers on silicon substrates.

5.3.1 Design of the Coherent and Incoherent ZnO Thin-film Random Lasers

In the design of the coherent and incoherent ZnO thin-film random lasers, MgO is selected as the buffer layer. It is used as the buffer material, since the ZnO epilayer comprised with a thin-film MgO layer has demonstrated to provide gain and induce random lasing actions in the ZnO nanorod arrays embedded in it, in CHAPTER 4. The results imply that the MgO-buffered ZnO thin-film silicon-based device is comparable to that made from the SiO₂ buffer layer.

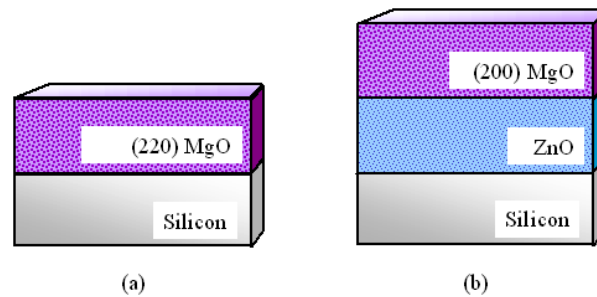


Figure 5.7 Proposed schematic of the two different configurations that give rise to MgO film that is dominated in the (a) (220)-orientation and (b) (200)-orientation.

For the fabrication of incoherent random laser, a ZnO thin film is to be deposited onto the sample as shown in Figure 5.7 (a), followed by annealing. The deposition of the MgO film on (100)-oriented Si is to be done at low deposition temperature in order to obtain MgO film to be in the (220)-orientation [256]. The MgO film is required to be in the (220)-orientation so that the MgO grains will not undergo drastic development due to its low grain boundary mobility [257]. After the MgO deposition, annealing is carried out before the deposition of the ZnO layer. This is to ensure that the MgO grains are well developed and do not have much change in

size during the second annealing. Hence, the ZnO grains and voids will not experience significant development due to the well-developed underlying layer. This leads to incoherent random lasing due to weak scattering strength. Next, MgO films that are strongly dominated in the (200)-orientation have been demonstrated [258] by annealing of MgO film grown on sapphire, but sapphire is expensive and not compatible to other silicon-base devices. Hence, a MgO thin film is grown on a thin layer of ZnO on a Si substrate, as shown in Figure 5.7 (b). Since ZnO has a structure resembling that of sapphire, it is anticipated that MgO films grown on ZnO thin films behave similarly. As a result, when annealing is carried out for the sample with a thin-film ZnO layer deposited on top, the sample gives rise to the formation of a coherent random laser. In contrast to the incoherent random laser, the MgO film of this sample is required to be (200)-oriented. Under this condition, the ZnO grains and voids, responsible for light scattering, are well developed as the sample undergoes annealing. In these random lasers, buffer layers with different orientations are used and different processing procedures are carried out. This is to induce differences in: 1) the adhesion force between the MgO and ZnO interface, and 2) the mobility of grain boundary [257, 259], leading to the difference in size of the ZnO grains and voids.

5.3.2 Fabrication of the Coherent and Incoherent ZnO Thin-film Random Lasers

In the fabrication of the proposed incoherent random waveguide laser, a layer of MgO (800 nm) was deposited on a Si substrate, using the method in section 4.2.2.

Following that the sample was annealed at 900 °C inside a standard Lindberg-type furnace for 1 h. Subsequently, a layer of ZnO of thickness 200 nm was grown on top of the MgO layer by the FCVA technique. The fabrication parameters and procedures were identical to that of the MgO fabrication, but a Zn (99.9%) target was used instead of the Mg target. Next, the entire sample was annealed at 900 °C for 3 h inside the Lindberg-type furnace in open air.

For fabricating the proposed ZnO coherent waveguide laser, a ~80 nm-thick ZnO layer was deposited on a silicon substrate. Then a layer of MgO (800 nm), followed by a layer of ZnO (200 nm), was coated on top of the ZnO layer, using the procedures and the parameters discussed in section 4.2.2. The entire sample was annealed at 900 °C for 3 h.

5.3.3 Characterization of the Coherent and Incoherent ZnO Thin-film Random Lasers and Discussion

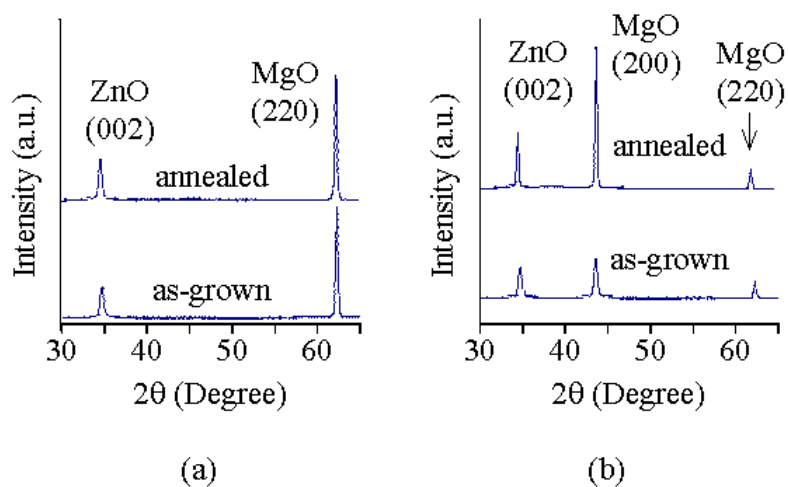


Figure 5.8 X-ray diffraction spectra (XRD) of the as-deposited and the annealed (a) ZnO-MgO-Si and (b) ZnO-MgO-ZnO-Si samples.

Figure 5.8 on the previous page shows the XRD patterns for the as-deposited and annealed (a) ZnO-MgO-Si and (b) ZnO-MgO-ZnO-Si samples. In Figure 5.8 (a), there are two sharp peaks noted in both the as-deposited and annealed samples, at $2\theta = \sim 62.3^\circ$ and $\sim 34.4^\circ$. They correspond to the (220)-oriented MgO and the *c*-axis (002)-oriented ZnO thin films, respectively. Besides, it is noted that after annealing, the ZnO and MgO average grain size experiences an insignificant change of about ~ 4 and ~ 5 nm, respectively, when compared to the as-deposited sample. Using the Scherrer formula, the average grain size (d) of the ZnO epilayers is estimated, as shown by the equation (5.1) [260] below:

$$d = \frac{0.9\lambda}{B \cos(\theta_B)}, \quad (5.1)$$

where λ (~ 0.154 nm) is the x-ray wavelength, θ_B is the Bragg diffraction angle and B is the full-width at half-maximum (FWHM) of a diffraction peak in the XRD spectrum. One of the reasons for the slow grain enlargement in the second annealing stage is that the MgO grain size is stabilized after the pre-annealed step. Therefore, the ZnO grain growth is hampered by the small variation in the grain size inside the MgO thin-film layer. Hence, the ZnO grains in the upper epilayer are held back from growing by this force. In contrast to the samples without the ZnO thin film in between the Si and MgO layer, three prominent peaks are noted in the XRD patterns in Figure 5.8 (b). Apart from the peaks at $2\theta = \sim 62.0^\circ$ and $\sim 34.5^\circ$ that are observed in the ZnO-MgO-Si samples Figure 5.8(a), there is an additional peak at $2\theta = \sim 43.0^\circ$ that corresponds to the (200)-oriented MgO thin films in the ZnO-MgO-ZnO-Si samples. Besides that, the peak at $2\theta = \sim 62.0^\circ$ is at a lower intensity and surpassed by the intensities of the other two peaks ($2\theta = \sim 34.5^\circ$ and $\sim 43^\circ$) in the as grown samples. Moreover, the intensities of those two

peaks become stronger for the annealed samples, accompanied by the reduction of the FWHM of their peaks. On the contrary, the peak at $2\theta = \sim 62.0^\circ$ is being suppressed. From the equation (5.1), the difference in the average grain size before and after annealing are ~ 34 and ~ 39 nm for the (002)-oriented ZnO and the (200)-oriented MgO films, respectively. The enlargement of MgO grains in the (200)-oriented MgO film is attributed to its high mobility of grain boundary [257,259]. Furthermore, there is no pre-annealing process as an intermediate step so that the MgO grains can be well developed. As for the growth of ZnO grains, it is unrestricted by the low adhesion force at the ZnO/MgO interface, due to the (200) orientation of the MgO films.

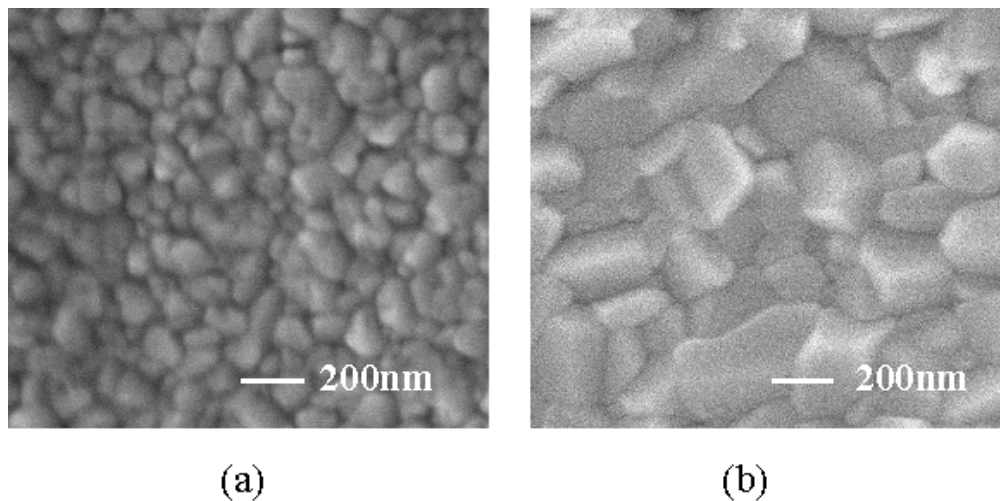


Figure 5.9 SEM images of the ZnO surface of the (a) annealed ZnO-MgO-Si sample and (b) annealed ZnO-MgO-ZnO-Si sample.

The SEM images of the ZnO surface of the (a) annealed ZnO-MgO-Si sample and (b) annealed ZnO-MgO-ZnO-Si sample are shown in Figure 5.9. They show that the ZnO grains in the annealed ZnO-MgO-ZnO-Si sample are larger and better developed than the annealed ZnO-MgO-Si sample.

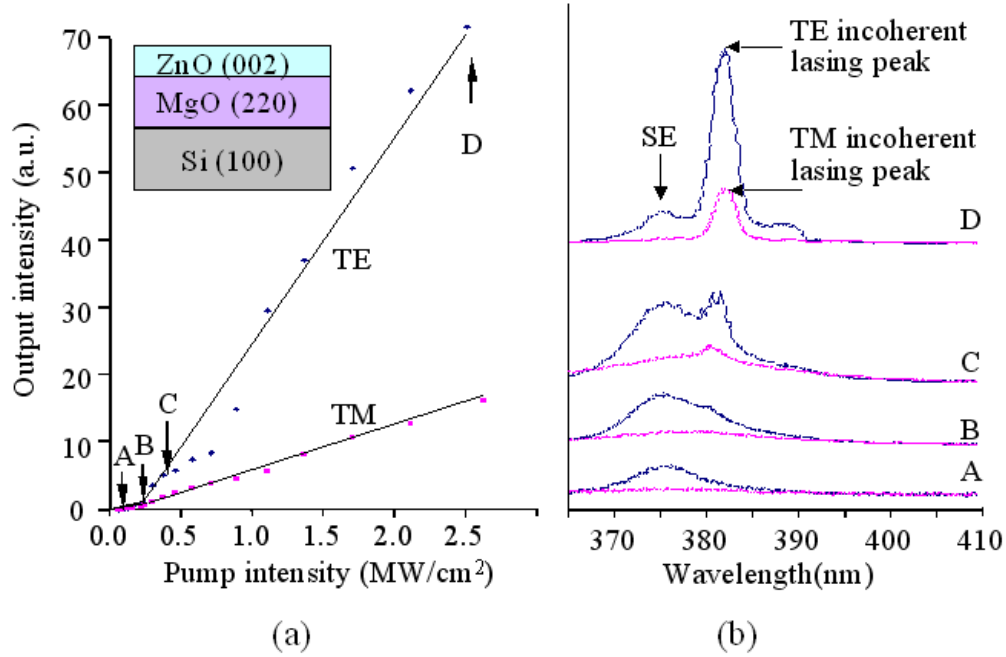


Figure 5.10 (a) Light-light curves for the two polarizations of the annealed ZnO-MgO-Si sample and (b) the corresponding emission spectra of the two polarizations, with the MgO layer pre-annealed prior to the deposition of the ZnO layer, followed by annealing of the entire sample. SE: spontaneous emission.

The light-light curves for the two polarizations of the annealed ZnO-MgO-Si sample and the corresponding emission spectra of the two polarizations are shown in Figure 5.10. For both polarizations, there is a threshold observed at ~ 0.3 MW/cm^2 . Below their thresholds, the light-light curves for both polarizations increase gradually with the increase in pump power. Above their thresholds, their intensities rise rapidly with the narrowing of linewidth noted in the corresponding spectra. It is noted that the spectral linewidth reduces from ~ 11 to ~ 4 nm. The sudden variation in the gradient of the light-light curves with linewidth narrowing in the spectra suggests that incoherent random lasing is demonstrated inside the ZnO-MgO-Si sample.

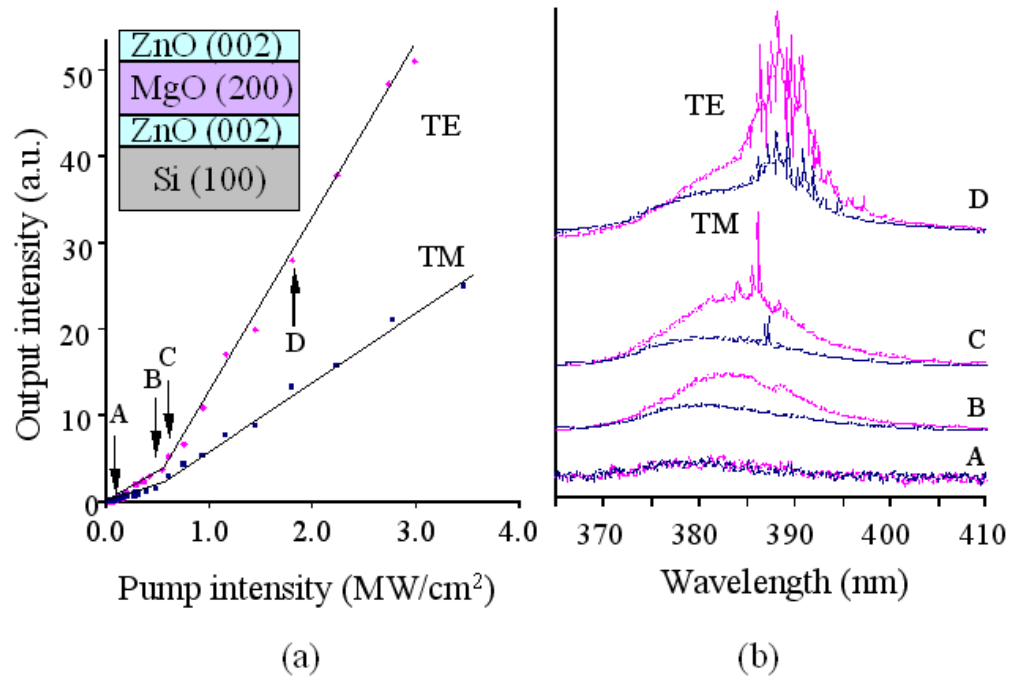


Figure 5.11 (a) Light-light curves for the two polarizations of the annealed ZnO-MgO-ZnO-Si sample and (b) the corresponding emission spectra of the two polarizations, with the entire sample annealed at 900 °C for 3 h.

The light-light curves and the corresponding emission spectra for the two polarizations of the ZnO-MgO-ZnO-Si sample annealed at 900 °C for 3 h are shown in Figure 5.11. It is noted that there is a threshold at ~ 0.48 MW/cm² for both polarizations, after which the gradient of two light-light curves is increased. This is attributed to the appearance of lasing modes with linewidth less than ~ 0.4 nm in the spectra for both polarizations. With further increase in the pump intensity, the number of sharp peaks from the spectra increases.

5.4 Conclusion

To conclude, the post-growth annealed ZnO films (for $T_a = 1$ min and 2 h) exhibit random laser characteristics that: 1) there exist a lasing threshold intensity (for (i) $T_a = 2$ h: TE and TM at ~ 0.33 MW/cm², and for (ii) $T_a = 1$ min: TE at ~ 0.35 MW/cm²), after which the number of lasing peaks in the emission spectrum increases as the pump intensity increases, 2) no constant mode spacing is observed in the lasing emission spectrum, 3) at different observation angles, different lasing emission spectrum is observed, 4) the lasing threshold increases as the pump area reduces and below a critical size, lasing stops, and 5) for different excitation areas, each lasing threshold is related to the corresponding excitation area by the equation (4.3). Therefore, it is shown that the post-growth annealing method effectively generates a highly disordered medium that leads to random lasing with the development of grains and voids. Besides, it is shown that different UV and visible lasing cavities can be formed by controlling the annealing temperature and time (APPENDIX E). Hence, it has been demonstrated that the FCVA technique is one of the most efficient methods in the production of highly disordered ZnO thin films. The reason behind is that the development of grains and voids is most effective by post-growth annealing ZnO film that is deposited at low temperature [261].

Furthermore, the sample with the MgO buffer layer preferred in the (220)-orientation and with the pre-annealed treatment, it shows incoherent feedback from the underdeveloped ZnO grains and voids. On the contrary, for the sample with (200)-orientated MgO dominated in the buffer layer and without the pre-annealing

step, coherent random lasing is achieved in the sample. This is realized by the well-developed grains and voids formed during the annealing of the entire sample. Coherent random lasing action is resulted in the sample. Therefore, it is shown that different material and process engineering of the ZnO epilayers brings about coherent and incoherent random lasing actions inside the ZnO epilayers. It is also equally important that the FCVA method is capable of growing the ZnO epilayer on MgO buffer that forms the random lasers. This implies that the technique can be generalized as a method for the fabrication of random lasers with coherent and incoherent feedbacks on different types of substrates. In addition, the use of MgO buffer layer other than SiO₂ opens up the possibility of inducing different levels of stress or strain at the ZnO and buffer interface. It is believed that the different stress or strain conditions in the ZnO/buffer interface determine either the EHP or free exciton radiative recombination process to dominate [262]. This unleashes the feasibility of fabricating random lasers with different lasing wavelengths with different materials as buffer layers.

CHAPTER 6 Low-loss and Directional Output ZnO Thin-film Ridge Waveguide Random Lasers

6.1 Introduction

In CHAPTERS 4 and 5, it is shown that ZnO structures can achieve lasing through scattering even in the absence of mirrors that provide feedback for the cavity. Besides that, the simple material and process engineering of the samples is discussed to generate the different random lasing cavities. Although these random lasers pose a different perspective and open up new possibilities in the ZnO ultraviolet (UV) laser research, the undesired emission characteristics of random laser remains. The major disadvantages of random lasers are that they have high scattering losses [34], non-axial and non-directional emission output [33] caused by the scattered optical paths within the lasing cavities that can be formed in any orientations. These shortcomings have to be overcome by new designs to make the thin-film ZnO random lasers, or all random lasers in general, to be compatible to the conventional facet-emitted lasers.

Therefore, dye solution [263] has been used to show directional emission in the backward direction of the pump beam. Furthermore, there are reports in using the two-photon pumping model [264] and reflective mirrors [265,266,267] to reduce the lasing threshold and improve on the control of the random laser emission output direction. In this chapter, we proposed the use of a capped layer to improve on the lasing threshold and the direction control in ZnO random lasers. This is possible because the capped layer can prevent non-axial emission and reduces

scattering loss, in the highly disordered ZnO thin-film ridge waveguide. The improved efficiency of the lasing characteristics from the optical feedback of the random lasers is also investigated.

6.2 Low-loss and Directional Output ZnO Thin-film Ridge Waveguide Random Lasers

6.2.1 Design of the Low-loss and Directional Output ZnO Thin-film Ridge Waveguide Random Lasers

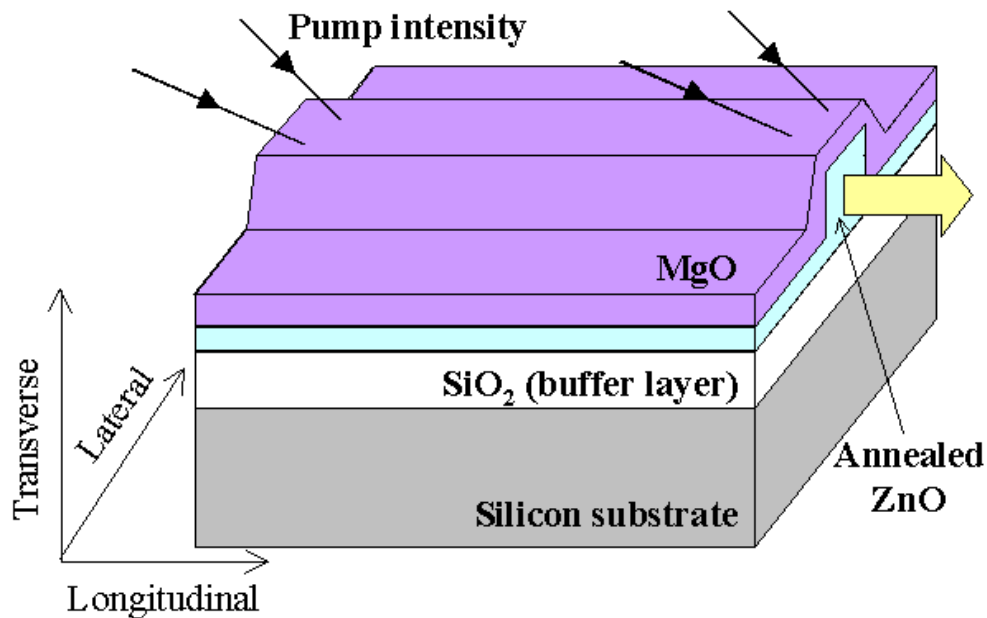


Figure 6.1 Proposed schematic diagram of the ZnO thin-film ridge waveguide random laser with a MgO capped layer.

Figure 6.1 shows the proposed schematic diagram of the ZnO thin-film ridge waveguide random laser with a MgO capped layer. First, the annealed ridge waveguide random laser design is used to confine the closed-loop paths of light to

be formed inside the ridge. Moreover, most closed-loops are made up of scattered optical paths that are along the longitudinal direction under excitation. This is based on the assumption that the gain length is longer than the width of the ridge, resulting coherent feedback unlikely to be established in that direction. On the other hand, the gain length is shorter than the length of the ridge, causing a higher probability of having the oscillation cavities observed in the longitudinal direction. Hence, all or majority of the random lasing outputs are guided in the intended direction. Secondly, a cap layer is deposited on top of the ridge waveguide to reduce the scattering loss of the random laser, as shown by the schematic in Figure 6.1. In addition, MgO is selected as the material for this cap layer. This is because the refractive index of MgO (1.75) is smaller than that of the ZnO thin-film layer (2.1) so that total internal reflection can be achieved inside the ZnO active layer.

6.2.2 Fabrication of the Low-loss and Directional Output ZnO Thin-film Ridge Waveguide Random Lasers

First, an annealed ZnO ridge waveguide random laser was made. Its fabrication procedures and parameters were identical to that described in Figure 5.2 (a) and (b). A SiO₂ buffer layer (~420 nm) was formed on a Si substrate by thermal dry oxidation. Subsequently, a ZnO film (~200 nm) was deposited on top of the SiO₂ surface by the filtered cathodic vacuum arc (FCVA) technique and the entire sample underwent post-growth annealing. Next, photoresist lines (AZ5214) were coated on the annealed ZnO layer, as stated in Figure 5.2 (c). After that, the unprotected ZnO thin film was being etched away by the ion-beam sputtering

method. The chamber was pumped down to the typical base pressure of $\sim 2 \times 10^{-6}$ Torr. Then argon gas supply was subsequently switched on and its flow rate was set to ~ 14 standard cubic centimeters per minute. During the etching process, the chamber pressure, the ion-beam current and voltage were at $\sim 1 \times 10^{-4}$ Torr, ~ 100 mA and 800 V, respectively. The sample was etched for ~ 500 s at the etching rate of ~ 12 nm/min. With the removal of the photoresist, ZnO ridges with height, width and separation of 100 nm, 2 μ m and 500 μ m, respectively, were formed. A different method was used to etch the ZnO thin film to form the ridge structure. This was to show that other than the plasma-enhanced chemical vapor deposition technique, ion-beam sputtering was also capable of etching ZnO thin films effectively. After the ridge structure was formed, the sample was optically characterized. Following that, a MgO layer of thickness ~ 200 nm was deposited on the surface of the ZnO ridge by the FCVA technique, using the parameters and procedures described in section 4.2.2. With the MgO capped layer, the optical properties were investigated. On the other hand, Al is to be deposited on one of the facets of the sample, to act as a mirror and reflect the scattered light waves that would have escaped from the facet of the sample without the Al coating. Before the deposition of Al, the surface of the sample was coated with photoresist using the procedures stated in Figure 5.2 (c). This was to prevent Al to be coated onto the surface unintentionally, obstructing the optical excitation beam to shine on the sample. Then a layer of Al was deposited onto the sample by the electron-beam deposition technique. In prior to the deposition, a crucible with Al pellets was put into the deposition chamber that was subsequently pumped down to a base pressure of 3×10^{-6} Torr. During the deposition process, the pressure and the

substrate temperature were at $\sim 4 \times 10^{-6}$ Torr and 90 °C, respectively, with beam current and voltage of 60 mA and 6 kV, respectively.

6.2.3 Characterization of the Low-loss and Directional Output ZnO Thin-film Ridge Waveguide Random Lasers and Discussion

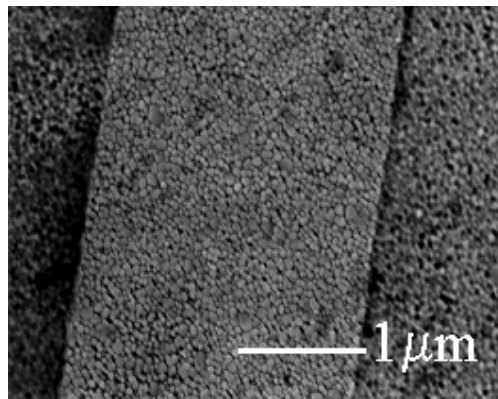


Figure 6.2 Scanning electron microscope image of the annealed ZnO thin film after etching a ridge structure by ion-beam sputtering.

Figure 6.2 shows the scanning electron microscope image of the annealed ZnO thin film after etching a ridge structure by the ion-beam sputtering technique. The image shows that the two sidewalls of the ridge are well defined and clear cut. This demonstrated that other than the plasma-enhanced chemical vapor deposition technique, ion-beam sputtering is also capable of etching ZnO thin film effectively and easily controlled by varying the ion-beam current and voltage.

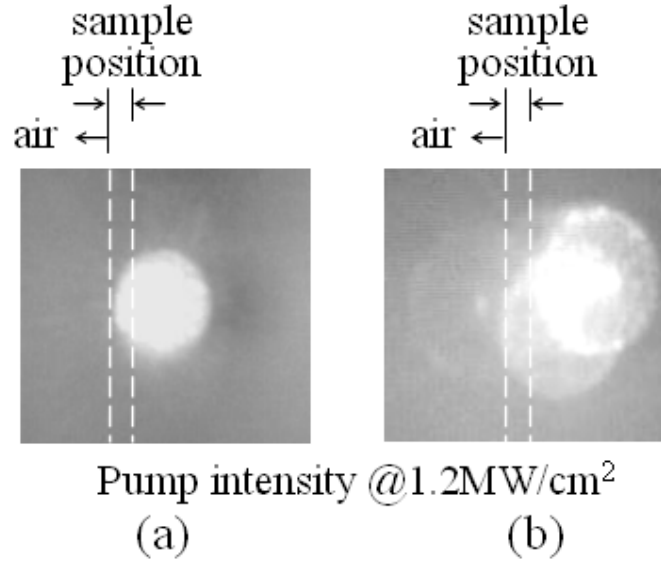


Figure 6.3 Transverse-electric (TE) emission far-fields of the samples (a) with and (b) without MgO capped layer at pump intensity of 1.2 MW/cm^2 . The dashed lines indicate the location of the sample.

Figure 6.3 shows the TE far-field emission profiles of the ridge waveguide random lasers, (a) with and (b) without MgO-capped layer under excitation of a pump strip at pump intensity of 1.2 MW/cm^2 . A single circular bright emission spot is observed in the profile for the sample with the MgO capped layers. This shows that the MgO-capped layer is successful in redirecting and guiding light into the intended direction. In contrast, multiple circular emission spots are noted from the field profile for the sample without the MgO capped layer. Comparing these two results, the ridge waveguide random laser with the MgO capped layer shows superior performance in terms of yielding directional emission, instead of non-axial emission in the sample without the MgO capped layer.

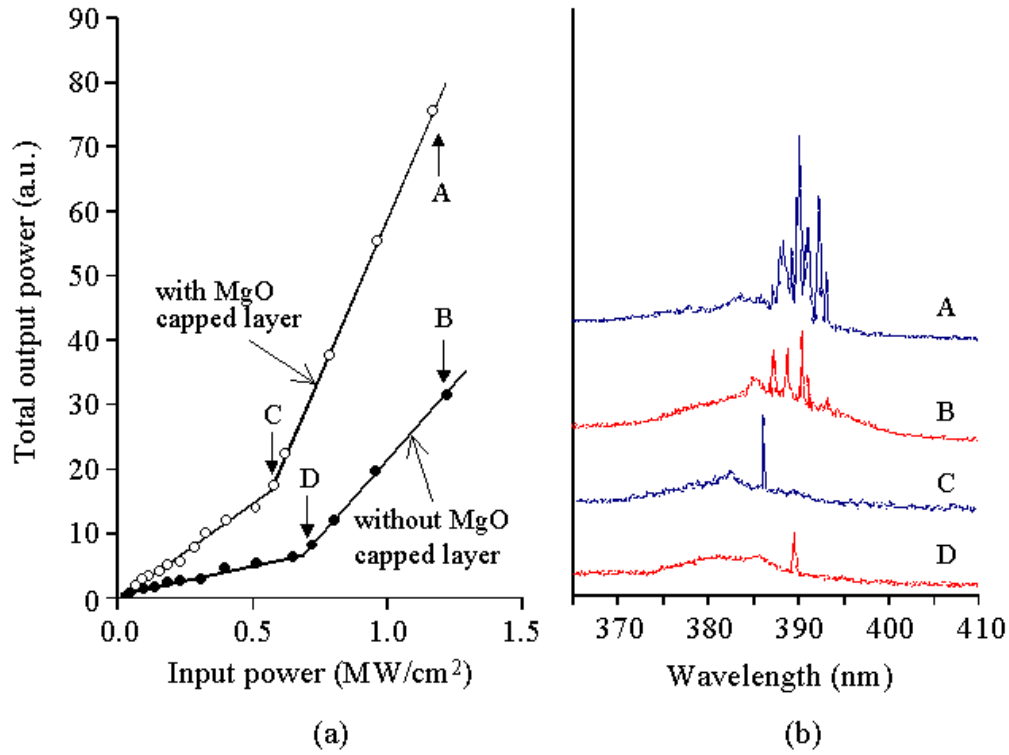


Figure 6.4 Unpolarized (a) light-light curves and (b) emission spectra of the samples with (○) and without (●) MgO capped layer measured at room temperature.

The unpolarized light-light curves and corresponding emission spectra of the samples with (○) and without (●) MgO capped layer are shown in Figure 6.4. In Figure 6.4 (a), the unpolarized light-light curves for both the sample with and without MgO capped layer show a threshold at ~ 0.61 and ~ 0.69 MW/cm², respectively. Above these thresholds, sharp peaks with linewidth of less than 0.4 nm emerges in each of the corresponding spectrum in Figure 6.4 (b). The number of these peaks increases with the increase in the pump intensities. Results show that both samples exhibit coherent random lasing. Besides, it is noted that the threshold pump power is reduced by ~ 0.08 MW/cm² and the output emission

intensity is increased by more than 2 times, with the introduction of the MgO capped layer onto the sample. This implies that the MgO capped layer is capable of redirecting the scattered light in the unwanted direction, into the ZnO thin-film layer.

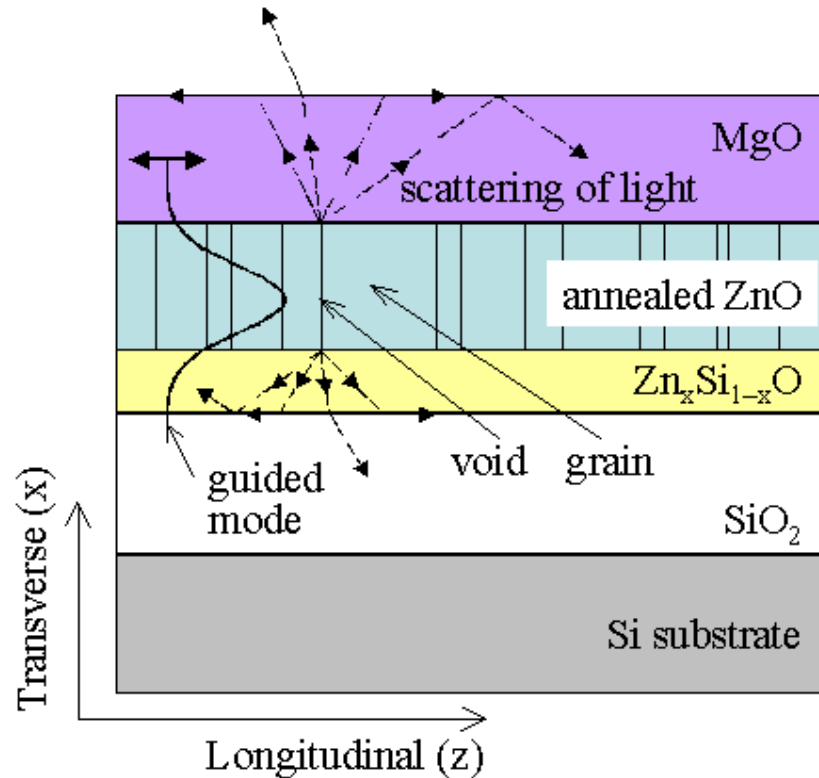


Figure 6.5 Schematic cross section of the annealed ZnO ridge waveguide with MgO capped layer. The dashed arrows indicate light rays that are being total internally reflected by the MgO capped and $\text{Zn}_x\text{Si}_{1-x}\text{O}$ layers.

Figure 6.5 shows the cross sectional view of the annealed ZnO ridge waveguide with the MgO capped layer. With the MgO capped layer, it demonstrates that most of the scattered light rays, as indicated by the dashed arrows in Figure 6.5, are either total internally reflected back into the active medium or guided in the longitudinal direction. On the contrary, without the MgO capped layer, these light

rays are scattered and escaped from the ridge sidewalls and ceiling, and the voids. They are to be considered as the scattering loss. This brings about the relatively higher pumping threshold, lower emission intensity and non-axial emission output, when compared to the sample with the MgO capped layer. Furthermore, there is a $\text{Zn}_x\text{Si}_{1-x}\text{O}$ layer in between the ZnO and SiO_2 interface that performs same function of redirecting the scattering light into the desired direction.

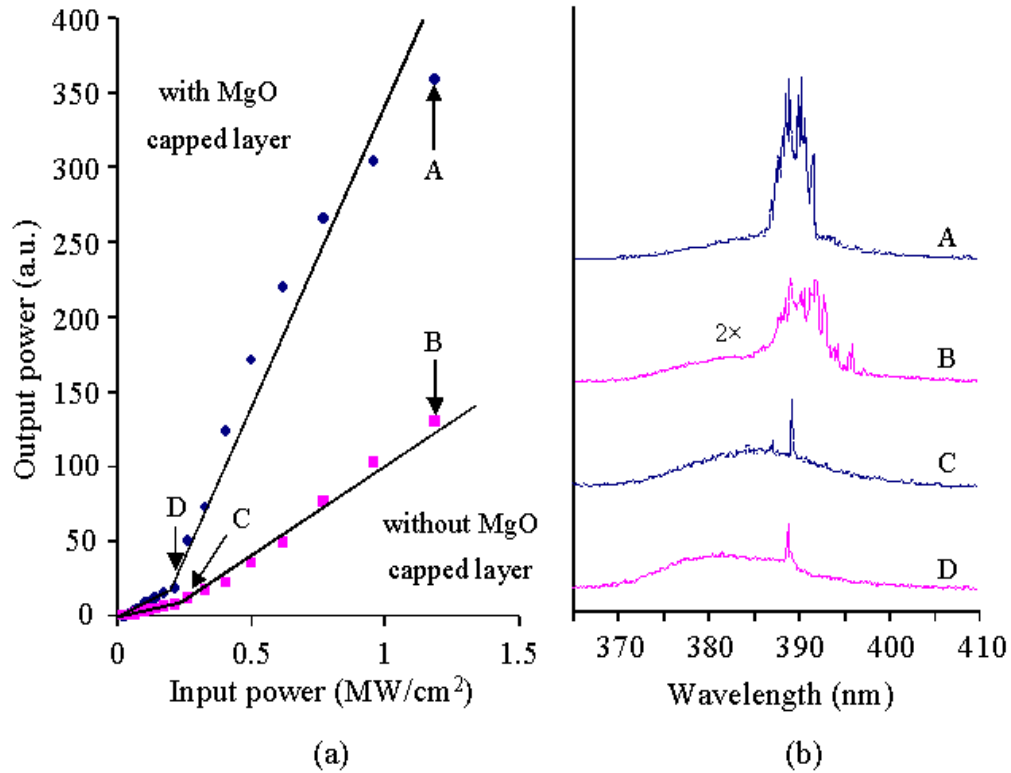


Figure 6.6 Unpolarized (a) light-light curves and (b) emission spectra of the samples coated with Al on one of the facets with (●) and without (■) MgO capped layer measured at room temperature.

Figure 6.6 shows the unpolarized (a) light-light curves and (b) emission spectra of the samples coated with Al on one of the facets with (●) and without (■) MgO capped layer measured at room temperature. In Figure 6.6 (a), there exist a pump

threshold for both of the samples. They are at ~ 0.21 and ~ 0.26 MW/cm² for the sample with (●) and without (■) MgO capped layer, respectively. Other than showing that the MgO capped layer has an effect on lowering the threshold, it is noted that the Al coating also produce the same outcome in lowering the threshold. When they are compared to the sample without the Al coating in Figure 6.4 (a), the pump thresholds are lowered by ~ 0.4 and ~ 0.43 MW/cm², respectively, for the samples with and without the MgO capped layer. Furthermore, with the Al coating, the output emission intensities are increased by ~ 4 times for both samples regardless of the presence of the MgO capped layers. In Figure 6.6 (b), the lasing modes stretch from ~ 387 to ~ 397 nm in B and they are reduced to ~ 387 to ~ 392 nm in A. Besides, the number of lasing modes is reduced with improved feedback. These results appear to disagree with that noted in Figure 6.4, where there is an increase in the number of lasing modes and a wider spectral lasing range (Increase from range ~ 387 to ~ 391 nm to ~ 387 to ~ 393 nm). The observation is probably due to the excitation of another group of lasing cavities. They are closed-loop paths that originally have a much higher losses without the feedback from the MgO coating. The postulation is valid, judging by the difference in the wavelength positions of the lasing peaks at pump intensity slightly above pump threshold in Figure 6.6 (b) and Figure 6.4 (b).

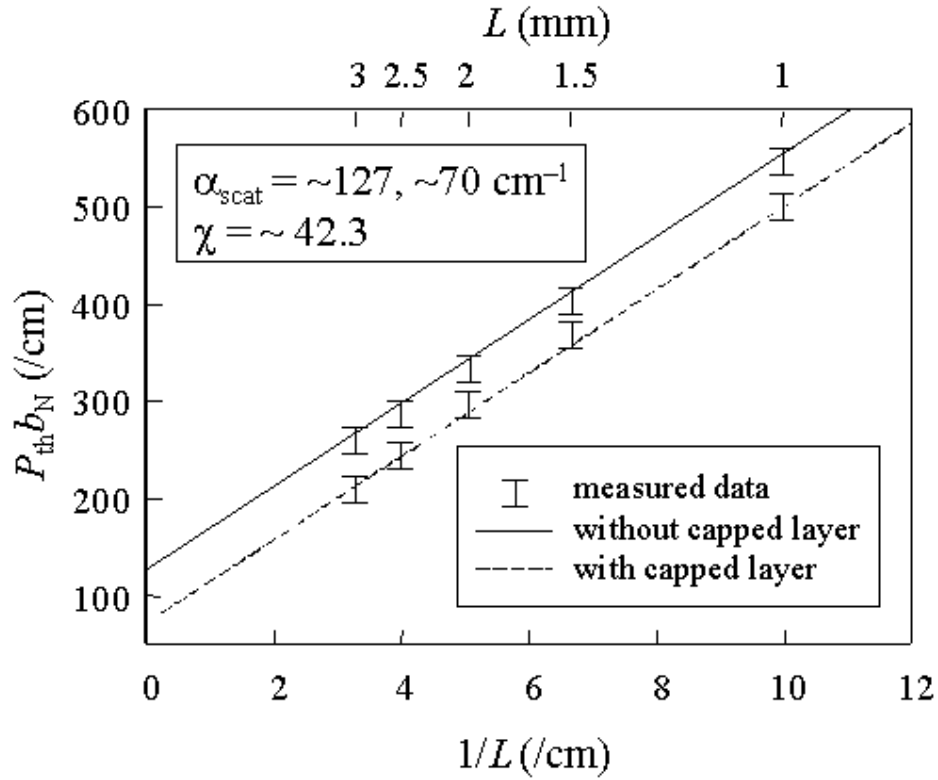


Figure 6.7 Plots of $P_{th}b_N$ versus L^{-1} for the samples with (dashed line) and without (solid line) MgO capped layer where P_{th} was measured from the samples by varying L from 1 to 3 mm. $b_N = 0.77 \times 10^{-3} \text{ cmW}^{-1}$ is used in the plot.

Figure 6.7 shows the plots of $P_{th}b_N$ versus L^{-1} for the samples with and without MgO capped layer where the pump threshold (P_{th}) was measured from the samples by varying their lengths (L) from 1 to 3 mm, with $b_N = 0.77 \times 10^{-3} \text{ cmW}^{-1}$. The measured data points are plotted with 5 % tolerance error bars in the values of $P_{th}b_N$. Besides, the two sets of data that correspond to the samples with and without the MgO capped layer are each fitted by a straight line, within the allowed tolerance and the difference in the gradients of the two lines is limited to a maximum of 1 %. These two fitted lines are given by equation (6.1)

$$b_N P_{th} = \alpha_{scat} + \chi L^{-1}, \quad (6.1)$$

where α_{scat} and χ are the scattering loss and normalized cavity loss of the random cavities, respectively. The details of arriving at this equation are given in APPENDIX F. For the graph, it is noted that when $L^{-1} = 0$, $P_{th}b_N = \alpha_{scat}$, and this value can be obtained from the y-intercept of each fitted lines. Hence, α_{scat} for the samples with and without MgO capped layer are found to be ~ 70 and $\sim 127 \text{ cm}^{-1}$, respectively. This reduction in α_{scat} caused by the MgO capped layer are considered to be significant as the measured waveguide loss of the ZnO ridge waveguide is $\sim 45 \text{ cm}^{-1}$. Moreover, the gradients of the two fitted lines are similar. This implies that resonant conditions in the longitudinal direction remains unchanged since they are not in resonance with the radiation fields, regardless the presence of the MgO capped layer.

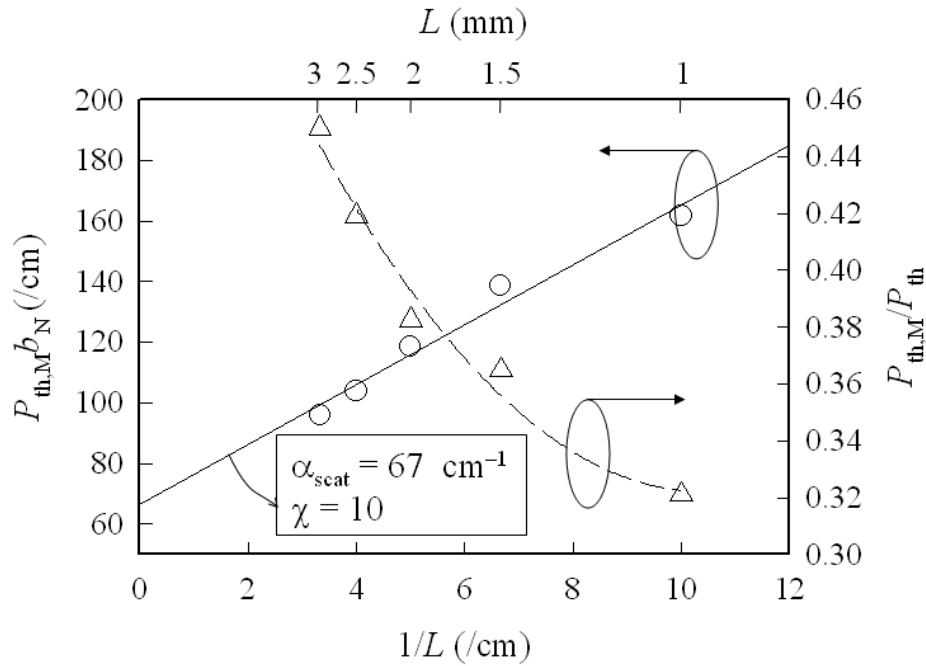


Figure 6.8 Plots of $P_{th,M}b_N$ (solid line) and $P_{th,M}/P_{th}$ (dashed line) versus L^{-1} . The solid line is obtained from linear regression fitting within 5% tolerance (i.e., $b_N P_{th} \pm 5 \text{ cm}^{-1}$). $b_N = 0.77 \times 10^{-3} \text{ cmW}^{-1}$ is used in the plot.

In Figure 6.8 on the previous page, the solid straight line is fitted to the set of data points that plot out $P_{th,M}b_N$ versus L^{-1} , where $P_{th,M}$ is the pump threshold of the sample with the MgO- capped layer and coated with Al on one of the facets with different length (L) and b_N is a constant ($= 0.77 \times 10^{-3}$ cm/W). It is obtained from a linear regression fitting with 5 % tolerance of the $P_{th,M}$ values and still denoted by the equation (6.1). This is because that the cavity loss of the Al coated samples is comprised of the cavity loss of the Fabry-Perot cavity formed by the Al coating and the random cavities. They are both proportional to L^{-1} so that the cavity loss for the sample with Al coating will be roughly proportional to L^{-1} . Moreover, the value of α_{scat} is not significantly affected by the change in the cavity loss or the excitation strip length, but it is more dependent on the random cavities. From the y-intercept of the graph, it is observed that the value of α_{scat} is ~ 67 cm $^{-1}$. This value is slightly less than that ($\alpha_{scat} = \sim 70$ cm $^{-1}$) obtained from Figure 6.7 and the amount of decrease is less than expected, possibly caused by the non-uniformity in the direction and intensity of reflection distribution within the Al coated facet. The reflectivity variation is probably affected by: 1) the roughness of the facet, and 2) the non-uniform thickness of the Al layer that is resulted from the deposition of thin films on a rough surface. Another observation noted between the samples with and without the Al coating is that χ reduces from ~ 43 to ~ 10 for the sample coated with Al. With the optical feedback from the Al coating, the pump threshold of the random cavities can be drastically reduced. On the other hand, in the same figure, data plots of $P_{th,M}/P_{th}$ versus L^{-1} are fitted by the dashed line within 5 % tolerance of the $P_{th,M}/P_{th}$ values, where P_{th} is the pump threshold of the sample with the MgO-capped layer without the coating of Al. It is noted that $P_{th,M}/P_{th}$ increases with the increase of L , appears to be in contradiction with the theoretical prediction

obtained by Feng and coworkers [267]. In their model, they suggested that $P_{th,M}/P_{th}$ decreases with the increase of L , with $P_{th,M}/P_{th}$ and L related by the equation (6.2), with the derivation given in the APPENDIX G,

$$\frac{P_{th,M}}{P_{th}} \sim \frac{L}{\xi} e^{-L/\xi}, \quad (6.2)$$

where ξ is the localization length or the length of the closed-loop path formed, of the lasing modes. Their results are different from our observations because the localization lengths of the pump and the lasing light are identical in their model and their pumping scheme [267] is different from ours.

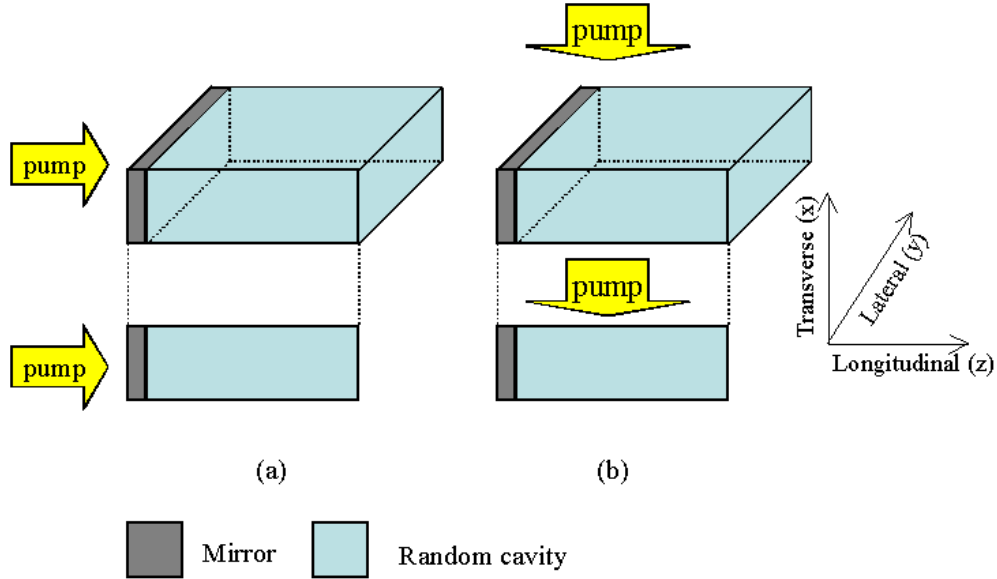


Figure 6.9 Schematic illustrations of the pumping scheme of random cavity with a mirror proposed by (a) Feng and coworkers [267] and (b) our group.

Figure 6.9 shows the schematic illustrations of the different pumping scheme of random cavity with a mirror proposed by (a) Feng's group [267] and (b) our group. In their proposal, the excitation source is injected in the direction parallel to the

longitudinal direction as shown in Figure 6.9 (a). For our group, the pump source is parallel to the transverse axis as given in Figure 6.9 (b). As a result, the coupling between the re-injected light and the lasing modes is most effective near to the coated facet.

6.3 Conclusion

In conclusion, the problems of high scattering loss and in-directional optical output in ZnO thin-film random cavities are solved. This is realized by the deposition of a MgO capped layer on the annealed ZnO thin-film ridge waveguide laser. Further to give out a bright directional emission beam, the sample with the MgO capped layer has a lower pump threshold and higher emission intensity. In addition, the scattering loss is reduced from ~ 127 to $\sim 70 \text{ cm}^{-1}$, suggesting that the MgO capped layer is effective in re-injecting the scattered light into the ZnO thin-film layer. Furthermore, it is demonstrated that the pump threshold of the sample is reduced with Al coating on one facet as optical feedback. The optical feedback shows to be more effective for sample with a shorter length.

The proposed ZnO random lasers can achieve high-performance ultraviolet lasing that is compatible with that of the conventional facet-emitted lasers. Besides, when this design is integrated with strategy and design [268,269] that gives single-mode high-power lasing characteristic, major disadvantages of random lasers are solved.

CHAPTER 7 ZnO Heterojunctions Light-emitting Diodes

7.1 Introduction

We have demonstrated that the filter cathodic vacuum arc (FCVA) technique is capable of fabricating ZnO ultraviolet (UV) waveguides and random lasers. However, all of these light-emitting devices fabricated by the FCVA technique are optically driven and there is no evidence that this technique is capable of making electrically powered ZnO UV light-emitting devices. On the contrary, in this chapter, we have shown that the FCVA technique is also capable of fabricating heterojunction light-emitting diodes (LEDs) that is made up of two different types of semiconductors. Al-doped ZnO and SiC are used as the *n*- and *p*-type materials. This implies that it is one of the potential cost-effective techniques to fabricate laser diodes in the future.

7.2 ZnO Heterojunction Light-emitting Diodes

7.2.1 Design of the ZnO Heterojunction Light-emitting Diodes

Recently, we have demonstrated UV photoluminescence (PL) at room temperature from n-ZnO:Al fabricated on lattice-mismatched substrates at low substrate temperature (<150° C) [211]. In addition, the n-ZnO:Al films exhibit resistivity ($< 8 \times 10^{-4} \Omega\text{cm}$) and carrier concentration ($> 10^{21} \text{ cm}^{-3}$) comparable to that of the n-

ZnO:Ga films [211,214]. Hence, we propose the fabrication of the n -ZnO:Al/ p -SiC(4H) heterojunction light-emitting diodes (LEDs) by the FCVA technique at low deposition temperature ($\sim 150^\circ\text{C}$).

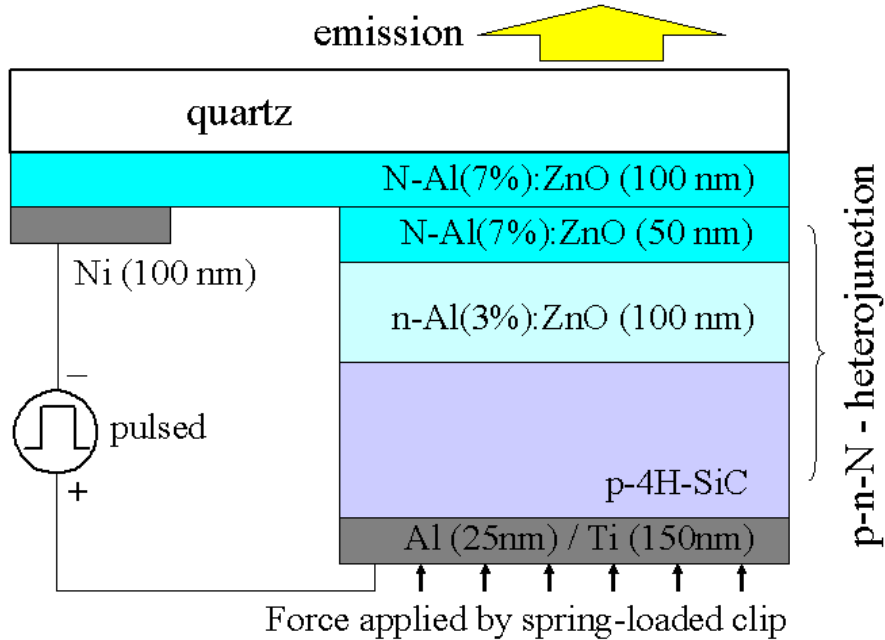


Figure 7.1 Proposed schematic diagram of the n -ZnO:Al/ p -SiC (4H) heterojunction LED structure and the suggested setup for light detection.

The fabrication of p -type ZnO remains a challenge to the ZnO research communities [270] because the dopants may be compensated by defect [271] or the low solubility of the dopant in the host material [272]. Hence, a heterojunction approach is used to fabricate a p - n heterojunction LED. Figure 7.1 shows the proposed schematic diagram of the n -ZnO:Al/ p -SiC (4H) heterojunction LED structure and the suggested setup for light detection. A p -doped single-side polished 4H-SiC wafer, purchased from CREE Inc., is chosen to be the substrate and the hole injection layer of the p - n heterojunction LED. This is because it has high values of hole concentration ($\sim 1 \times 10^{19} \text{cm}^{-3}$) and carrier mobility (~ 120

cm²/Vs). As for the electron injection layer, ZnO:Al (3%) is selected because of its optimal level of carrier concentration ($> 1 \times 10^{20} \text{ cm}^{-3}$) and mobility ($\sim 7.2 \text{ cm}^2/\text{Vs}$) [211]. Then on top of the ZnO:Al (3%) layer, there is a ZnO:Al (7%) layer as the transparent injector of electron. It is in contact with a coated quartz substrate by a spring-loaded clip that pushed the device tight onto the quartz substrate, as shown in Figure 7.1, for the setup in light detection. As a result, the metallization on the ZnO:Al(7%) of the LED is not needed so that the fabrication procedures can be simplified and the device can be reused in other characterization experiments. For the contact on the SiC substrate, an Al layer is used because it has a large work function ($\sim 4.28 \text{ eV}$) [273] and is inexpensive when compared to gold, while having reasonably low resistivity of $2.65 \times 10^{-6} \Omega\text{cm}$ [273]. Besides, Al/Ti contact [274,275] has demonstrated to form good ohmic contact on SiC with low resistivity. It is believed that the two elements in the Al/Ti contact individually forms alloy with the SiC substrate [276] that leads to the ohmic resistance characteristics. For the metalization on the coated quartz substrate, Ni is selected as the material since it has been shown that it forms good ohmic contact with ZnO:Al films [277].

7.2.2 Fabrication of the ZnO Heterojunction Light-emitting Diodes

In the fabrication of the ZnO heterojunction LED, first, a piece of *p*-SiC (4H) was cleaned in the sequence as follows: acetone ultrasonic clean for 15 min; followed by alcohol ultrasonic clean for 15 min; followed by deionized (DI) water rinse; followed by a 5:1:1 mixture of H₂O:NH₄OH:H₂O₂ heated to 80 °C for 15 min;

followed by DI water rinse for 5 min; followed by a 1:50 mixture of HF:H₂O for 15s; followed by DI water rinse for 25s; followed by a 5:1:1 mixture of H₂O:HCl:H₂O₂ heated to 80 °C for 15 min. After these steps, the substrate was dried in a Lindberg box furnace at 110 °C for 30 min.

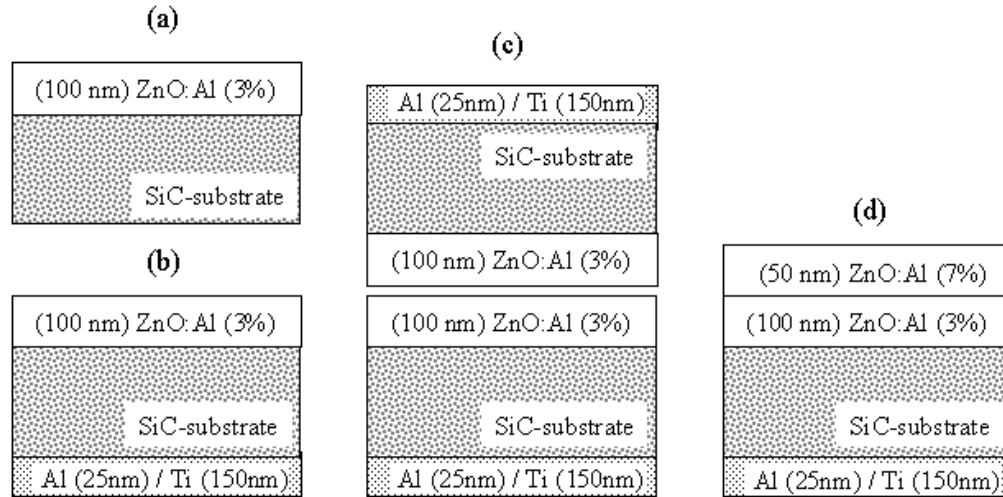


Figure 7.2 Fabrication procedures of the proposed ZnO heterojunction LED. (a) Deposition of a ZnO:Al (3%) layer on the polished surface of the *p*-SiC substrate by the FCVA technique. (b) Deposition of an Al layer, then a Ti layer, by electron-beam evaporation. (c) Undergoing rapid thermal annealing with another identical sample stacked on top at 800 °C for 5 min in a N₂ environment. (d) Deposition of ZnO:Al (7%) layer on top of the ZnO:Al (3%) layer by the FCVA technique.

Next, on the polished side of the *p*-SiC substrate, a 100 nm-thick *n*-ZnO:Al (3%) layer was fabricated by the FCVA technique, as shown in Figure 7.2 (a). A 3 at. % of Al containing Zn target with was used. During the deposition process, the substrate temperature and oxygen partial pressure were set to 150 °C and 5×10^{-4} Torr, respectively [211]. These conditions were used to produce the optimal level of carrier concentration and mobility. Subsequently, the sample was placed into an

electron-beam deposition chamber and it was then pumped down to a base pressure of 3×10^{-6} Torr. The evaporation of Al pellets in a crucible was carried out at a beam current of 60 mA and a beam voltage of 6 kV. During the deposition process, the pressure and the substrate temperature were at $\sim 4 \times 10^{-6}$ Torr and 90 °C, respectively. After a 25 nm-thick Al layer was coated on the unpolished side of the *p*-SiC, the crucible holder was rotated to another crucible that contains Ti pellets. Then the Ti evaporation process began when the base pressure returned to 3×10^{-6} Torr and the substrate temperature dropped to room temperature. The beam current was 70 mA and the beam voltage was 7 kV. During the deposition process, the pressure and the substrate temperature remained unchanged (i.e., $\sim 4 \times 10^{-6}$ Torr and 90 °C). The process was stopped when a Ti layer of thickness 150 nm was coated on top of the Al layer, as shown in Figure 7.2 (b). The sample was taken out from the chamber after the substrate temperature had dropped to room temperature. Following that, as shown in Figure 7.2 (c), another identical sample was made and it was stacked on top of the other sample (i.e., face-to face). With the two ZnO:Al (3%) surfaces of the samples touching each other, both underwent rapid thermal annealing (RTA). The annealing process was performed at ~ 800 °C for ~ 5 min in a N₂ environment. The RTA process was to change contact behavior of the Al/Ti contacts on the SiC to ohmiclike from Schottky behavior [275]. Moreover, the change in the surface roughness of the thin films before and after annealing was less significant in the face-to-face RTA process when compared to that of the films without using the face-to-face approach [278]. Another advantage of adopting the face-to-face RTA method was to suppress the defect-related deep-level emission while improving the near-band-edge emission in the ZnO:Al films [278,279]. Finally, as shown in Figure 7.2 (d), a 50 nm-thick layer of ZnO:Al (7%) was

deposited on top of the ZnO:Al (3%) layer by the FCVA technique. The fabrication procedures and parameters of the ZnO:Al (7%) thin-film layer were the same as those of the ZnO:Al (3%) thin-film layer, but a Zn target with 7 at. % of Al was used.

As for the coated quartz substrate that was required for the setup in light detection, a layer of ZnO:Al (7%) thin-film layer of thickness ~ 100 nm was deposited on a quartz substrate, with the FCVA deposition parameters remained unchanged. Following that, a photoresist layer was coated on top and exposed to UV radiation through a mask with two rectangular patterns, of width, length and separation of 1 mm, 2 mm and 1.5 mm, respectively. The detailed experimental procedures and conditions were given in section 3.3.2. Then, Ni was coated onto the unmask regions by the electron-beam evaporation method discussed previously. During the process, a beam current of 60 mA and a beam voltage of 7 kV were used to evaporate the Ni pellets in a crucible.

7.2.3 Characterization of the ZnO Heterojunction Light-emitting Diodes and Discussion

The solid lines in Figure 7.3 on the next page, give the current-voltage characteristics of the Al/Ti metallization on *p*-SiC before and after rapid thermal annealing at 800 °C for 5 min while the dash line shows the current-voltage characteristics of the Ni metallization on n-ZnO:Al (7%). It is noted that they are the current-voltage characteristics of two contacts of dimension 1×2 mm² and

separation of 1.5 mm apart. For the solid lines, the Schottky behavior of the two as-deposited Al/Ti contacts on the p -SiC is changed to ohmiclike behavior by RTA for 5 min at 800 °C in a N_2 environment. It is observed that linear current-voltage dependence of the Al/Ti metal-contact on the p -SiC has been achieved. The contact resistivity of the Al/Ti metal-contact is relatively higher than expected because of the fact that Al can be easily oxidized [273,275]. Besides, the linear current-voltage dependence of the Ni contacts on the ZnO:Al (7%) layer is attained even for the as-deposited film without the RTA process.

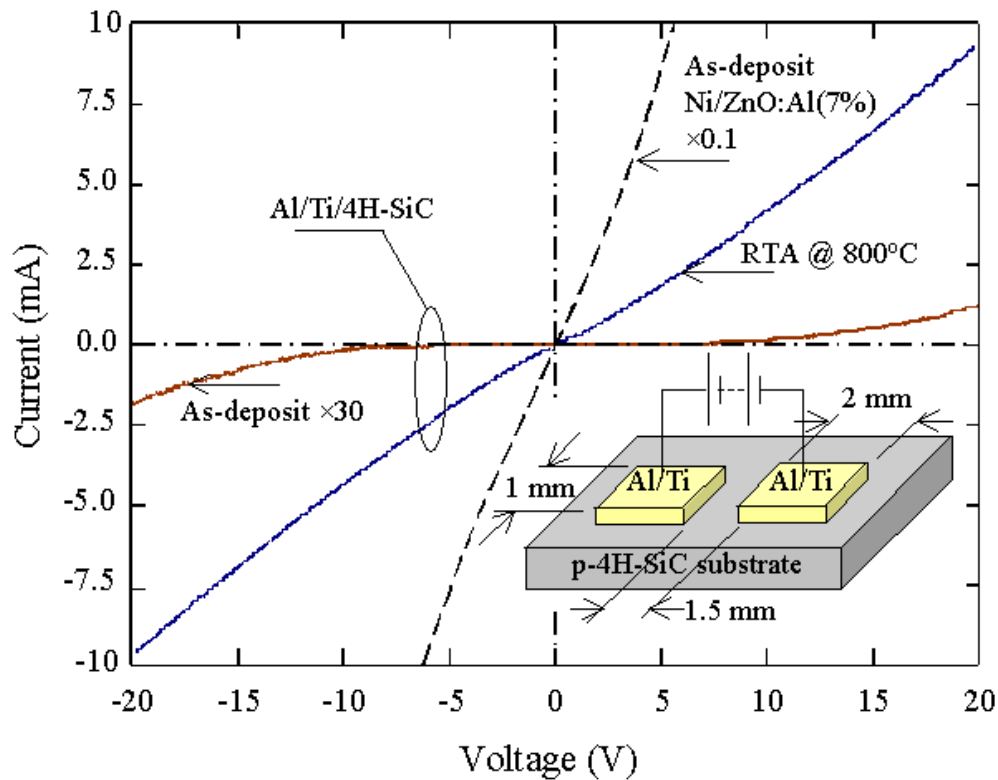


Figure 7.3 Solid lines: current-voltage characteristics of the Al/Ti metallization on p -SiC before and after rapid thermal annealing at 800 °C for 5 min. Dash line: current-voltage characteristics of the Ni metallization on n -ZnO:Al(7%).

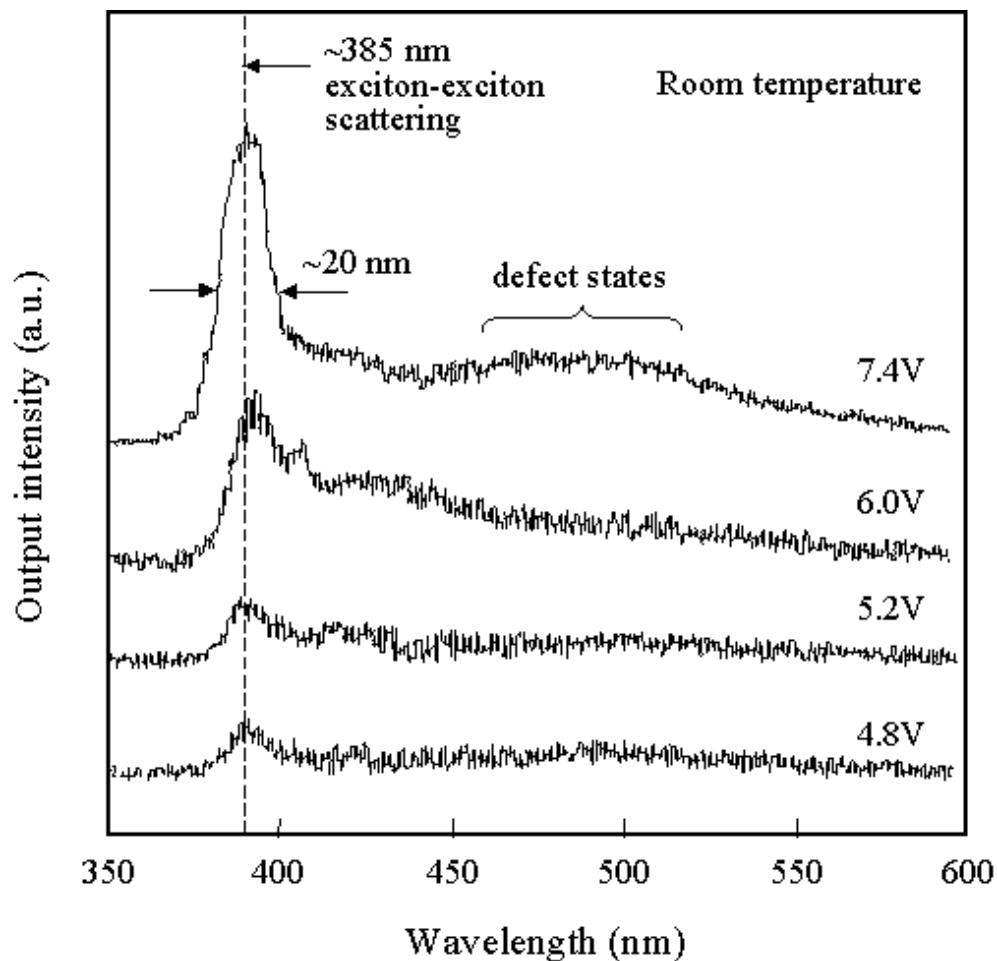


Figure 7.4 Room-temperature electroluminescence (EL) spectra of the n -ZnO:Al(3%)/ p -SiC(4H) heterojunction LED at various forward biased voltage.

Figure 7.4 shows the room-temperature EL spectra of the n -ZnO:Al(3%)/ p -SiC(4H) heterojunction LED under different forward biasing voltage. The details in obtaining the EL spectra are stated in the APPENDIX H. When the device is under forward biased condition, at biasing voltage of 4.8 V, an UV emission peak is noted at ~385nm. The emission intensity of the UV peak increases with the increase of biasing voltage. At a forward biased voltage of 7.4 V, the full width at

half maximum (FWHM) of the UV peak is ~ 20 nm. The UV EL peak implies that the negligible influence of the heterointerface defect is surpassed by the effective near-band-edge radiative recombination demonstrated by the device. Moreover, for forward biased voltages greater than 6V, a weak defect peak that stretches between ~ 430 to ~ 530 nm and has a maxima at ~ 490 nm, is observed from the EL spectra. This defect peak is probably due to the defect-related deep-level emission of the *n*-ZnO:Al film.

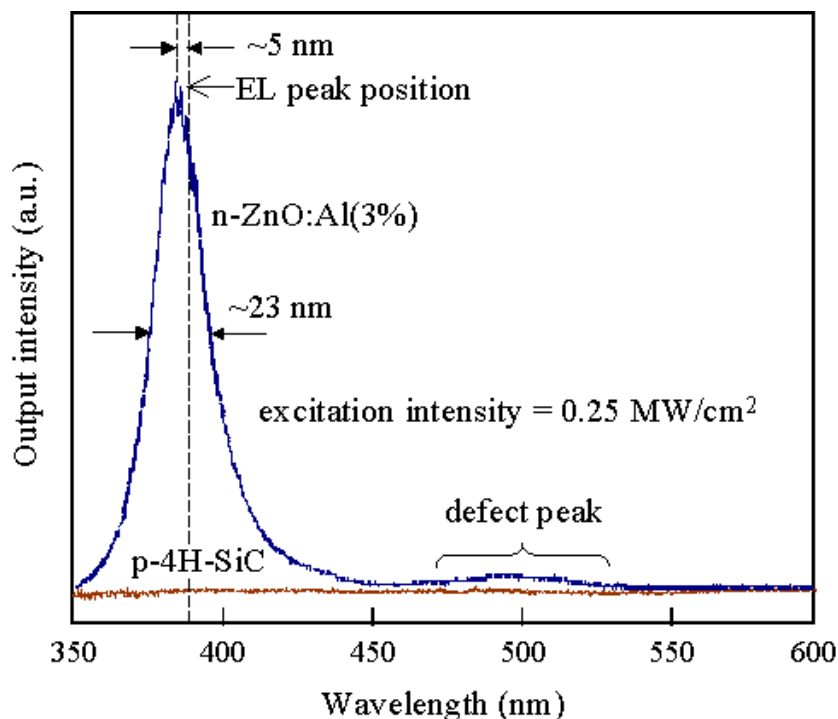


Figure 7.5 Room-temperature PL spectra of an annealed ZnO:Al(3%)/*p*-SiC and a bare *p*-SiC(4H) substrate under the optical excitation by a frequency tripled Nd:YAG laser (355 nm) at pulsed operation (6 ns, 10 Hz).

The room-temperature PL spectra of an annealed ZnO:Al(3%)/*p*-SiC and a bare *p*-SiC(4H) substrate are given in Figure 7.5. The spectra show that there is no measurable light emission noted from the *p*-SiC (4H) substrate as expected, since it is an indirect-bandgap semiconductor. On the contrary, the annealed

ZnO:Al(3%)/*p*-SiC sample displays a strong UV peak at ~380 nm and a weak defect peak at ~490 nm in the PL spectrum. The strong emission peak at ~380 nm indicates that the free exciton recombination (APPENDIX A) is the main mechanism behind the radiative recombination process in the *n*-ZnO:Al(3%) film. However, this predominant process is switched to exciton-exciton scattering when it is under electrical excitation, as marked by the ~5 nm difference between EL (~385 nm) and PL (~380 nm) emission peak position. The discrepancy is probably caused by the more efficient excitation resulted from the optical pumping than that of the electrical excitation. With optical pumping, the energy of photons can be optimized according to the band gap of ZnO. Furthermore, the *n*-ZnO:Al(3%) film shows *c*-axis orientation, that is vertical growth to the substrate, as indicated by the X-ray diffraction (XRD) patterns in the Figure 7.6. This orientation (002) has the lowest surface energy; hence the ZnO film resulted in this orientation to minimize the surface energy within the deposited film and between the deposited film and the substrate surface [25].

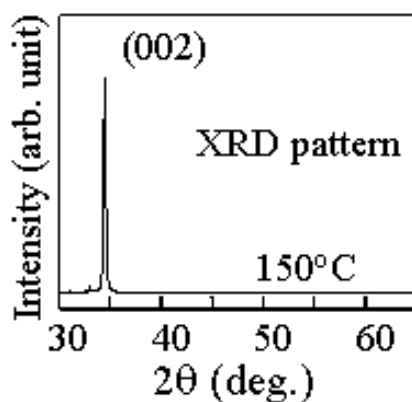


Figure 7.6 XRD pattern of the AlZnO thin film deposited on the SiC substrate at 150°C.

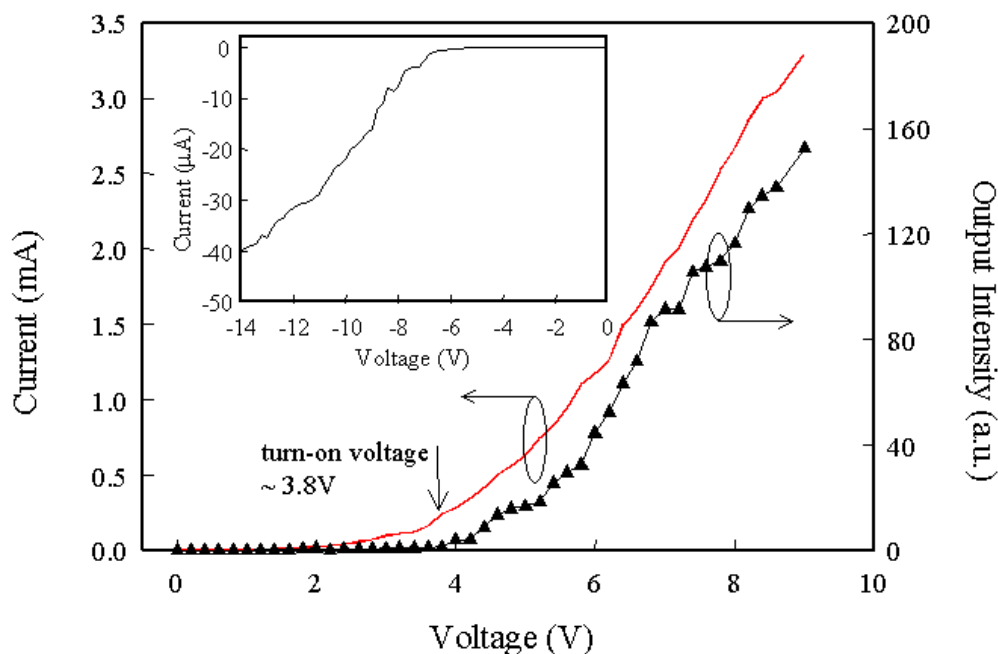


Figure 7.7 Room-temperature current-voltage and light-voltage characteristics of the $n\text{-ZnO:Al(3\%)/p-SiC(4H)}$ heterojunction LED. The insert shows the enlarged current–voltage curve at reverse biased.

The room-temperature current-voltage (—) and light-voltage (▲) characteristics of the $n\text{-ZnO:Al(3\%)/p-SiC(4H)}$ heterojunction LED is shown in Figure 7.7. The details of the experiment are illustrated in APPENDIX I. The current-voltage characteristic of the heterojunction shows a rectifying behavior with a turn-on voltage of ~ 3.8 V. The current increases exponentially as the biasing voltage increases. As the biasing voltage increases to ~ 9 V, the measured current is ~ 3.3 mA. Moreover, it is noted that the current density (J) and the applied voltage (V) show a $\sim J\text{-}V^1$ relationship due to the effect of the large ohmic contact resistance, below forward biasing voltage of 1.2 V. When the forward biased voltage is above this value, a $\sim J\text{-}V^2$ relationship is observed. This could be due to the space-charge limited current, that is possibly related to the wide band-gap materials [280]. Next,

when the heterojunction is in reverse biased condition, a small leakage current of less than $10^{-2} \mu\text{A}$ is noted, for reverse biased voltages below 6V. For the light-voltage characteristics, the optical intensity is not measurable below forward biased of 3.8 V. After 3.8 V, the output intensity rises almost linearly with the increase in the biasing voltage, signifying the recombination of electrons and holes.

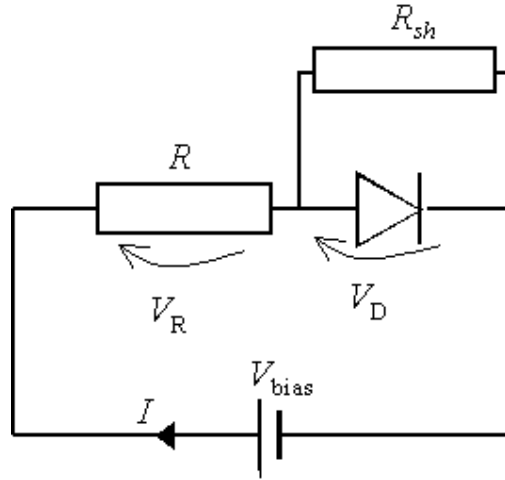


Figure 7.8 Proposed electrical circuit model for the heterojunction LED for the calculation of the ideal factor.

If I_o is the saturation current, V_D is the diode voltage, then the ideality factor (η) of the heterojunction LED can be found from the ideal diode equation:

$$I = I_o [\exp(qV_D / \eta kT) - 1], \quad (7.1)$$

where T ($= 300\text{K}$) is the temperature, q is the electron charge and k is the Boltzman constant. Using the circuit model as shown in Figure 7.8, Eq (7.1) is modified into:

$$I = I_o [\exp(qV_D / \eta kT) - 1] + \frac{V_D}{R_{sh}}, \quad (7.2)$$

where the shunt resistance (R_{sh}) is included into the equation. The ideality factor is calculated to be ~ 6 , with the consideration of a series resistance (R) of $\sim 1\text{ k}\Omega$ and a shunt resistance (R_{sh}) of greater than $50\text{ k}\Omega$. The calculation details are given in APPENDIX J. The series resistance (R) is attributed to: 1) the large ohmic contact resistance of the Al/Ti metal-contact on the p-SiC, 2) the resistance of SiC and 3) the ZnO:Al layer. This large value of R also gives rise to the higher than expected turn-on voltage of $\sim 3.8\text{ V}$ (Figure 7.7), demonstrated by the heterojunction device. Hence, an additional voltage across R is added to V_D that is expected to be $\sim 3.3\text{ V}$, since the band-gap of ZnO and p-SiC are ~ 3.3 and $\sim 3.28\text{ eV}$ approximately. Besides, R_{sh} is to show that there is current flowing directly from the n-ZnO:Al layer to the Al/Ti metal-contact. This is probably due to insufficient masking on the edge of the p-SiC, during the deposition processes of the n-ZnO:Al layer and the Al/Ti metal-contact, to prevent them from in touching each other.

7.3 Conclusion

The fabrication of the n-ZnO:Al/p-SiC(4H) heterojunction LEDs by the FCVA technique at low deposition temperature ($\sim 150^\circ\text{C}$) has been demonstrated. The device shows diodelike rectifying current-voltage characteristics, with a turn-on voltage of $\sim 3.8\text{ V}$. At $\sim 7.4\text{ V}$, the device exhibits a UV EL peak at wavelength of $\sim 385\text{ nm}$ at room temperature, with FWHM of $\sim 20\text{ nm}$. This implies that the concentration of nonradiative defects of the n-ZnO:Al films is negligible. The n-ZnO:Al films have: 1) low resistivity since the generation of the ionized Zn-Al plasma takes place before the the oxidation of the deposited species, reducing the chance of Al being oxidized, and 2) high crystalline quality because the removal of

the micro-particle in the Zn-Al plasma by the double-bend design of the FCVA technique is effective.

A ZnO UV LED with ZnO:Al-based active layer is demonstrated by the FCVA technique at low deposition temperature. This proves that the FCVA technology is capable of fabricating electrically pumped light-emitting devices at low deposition temperature. Furthermore, the lattice-matching requirement is not necessary for this method between the *n*- and *p*-type materials that make up the diode. Therefore, the *n*-ZnO:Al film seems to be one of the potential candidates to be applied in the fabrication of the ZnO UV LEDs and the future diode lasers, as the electron injection layer and active layer.

CHAPTER 8 Conclusion and Recommendations for Future Research

8.1 Conclusion

The filtered cathodic vacuum arc (FCVA) technique allows the deposition of ZnO films on lattice-mismatched substrates at low temperature with optical and electrical properties that are comparable to other deposition techniques. The following summarized the capabilities of FCVA deposition technique for the fabrication of ZnO light emitting devices:

ZnO thin-film planar waveguides were fabricated on lattice-mismatched SiO₂-buffered Si substrates at ~230°C by the FCVA technique. The waveguides exhibited amplified spontaneous emission with a peak wavelength at ~385 nm and had a maximum net optical gain of ~70 cm⁻¹ in the TE polarization at pump intensity of ~1.9 MW/cm². The net optical gain was improved to 120cm⁻¹ by introducing a ridge structure into the planar waveguide.

Apart from observing amplified spontaneous emission and waveguiding effect in ZnO epilayers, we have also realized random lasing action in them, by embedding ZnO nanorods inside. The ZnO epilayers were fabricated by the FCVA technique. They were comprised of ZnO and MgO layers that did not exhibit random lasing. On the other hand, the ZnO nanorods on sapphire substrate with the designed distribution and sizes were also not capable of random lasing. However, when the ZnO nanorods were embedded in the ZnO epilayers, random lasing was resulted

from the strongly scattered optical waves inside the sample that experienced a higher optical gain. The pump threshold intensities were $\sim 800 \text{ kW/cm}^2$ and $\sim 1.6 \text{ MW/cm}^2$ for the transverse-electric (TE) and transverse-magnetic (TM) polarizations, respectively.

In order to allow the integration of our random laser with other silicon based components, we proposed a post-growth annealing method to realize ultraviolet (UV) ZnO thin-film random lasers on Si substrates fabricated by the FCVA technique. The annealing temperature and duration controlled the development of ZnO grains and voids that were responsible for the random lasing action. The method is especially efficient for ZnO films deposited at low temperature in the FCVA technique. For samples annealed at 900°C for 1 min and 2 hrs, they showed pump threshold intensities of ~ 0.35 and $\sim 0.33 \text{ MW/cm}^2$ for the TE polarizations, respectively. Moreover, coherent and incoherent random lasing actions in ZnO thin films can be realized by the modification of material compositions and the variation of fabrication processing steps, based on the post-growth annealing method. Restrictions of growth in ZnO grains and voids were noted in the annealing of ZnO films grown on a (220)-oriented MgO layer with pre-annealed treatment. The underdeveloped ZnO grains and voids led to the formation of the incoherent random lasing cavities. Conversely, it was proven that the ZnO grains and voids experienced unrestricted growth in annealing on a (200)-orientated MgO layer without pre-annealed treatment. Coherent random lasing cavities were established from the well-developed grains and voids.

Furthermore, the undesired characteristics of high scattering loss and non-directional emission output in the ZnO thin-film random cavities have been eradicated. It was achieved by a MgO capping layer on the annealed ZnO ridge waveguide random laser. With this design, the sample emitted a bright directional emission beam by the re-injection of the scattered light into the ZnO thin films from the MgO capping layer. With the MgO capped layer, the scattering loss was reduced from ~ 127 to $\sim 70 \text{ cm}^{-1}$. Furthermore, Al is coated on one of the facets of the MgO-capped samples as optical feedback. It is shown that the pump threshold is reduced and the optical feedback is more effective for shorter samples.

Other than realizing optically pumped UV ZnO devices, we designed and realized an electrical $n\text{-ZnO:Al}/p\text{-SiC(4H)}$ heterojunction light-emitting diode (LED) by the FCVA technique at low deposition temperature ($\sim 150^\circ\text{C}$). At room temperature, the device showed an UV electroluminescence peak at wavelength of $\sim 385 \text{ nm}$ with full width at half maximum of $\sim 20 \text{ nm}$, at $\sim 7.4 \text{ V}$. The $n\text{-ZnO:Al}$ films fabricated by the FCVA method proves to be an efficient electron injection layer that is difficult to be achieved by most of the deposition methods. In the making of the $n\text{-ZnO:Al}$ films, the oxidation is well suppressed as the ionized Zn-Al plasma is generated before it is mixed with oxygen.

To conclude, it has been demonstrated that the FCVA technique is one of the most cost-effective methods in mass-producing ZnO UV waveguides, lasers and LEDs. The growth of ZnO UV waveguides and lasers on the lattice-mismatched Si substrates facilitate their integration with other Si-based electrical or optical devices. Hence, the FCVA technique is justified to be one of the best candidates in

achieving them since it allows the deposition of films on a lattice-mismatched underlying layer with low substrate temperature.

8.2 Recommendations for Future Research

In CHAPTER 4, coherent feedback has been demonstrated in the ZnO nanorods embedded in the ZnO epilayers. However, incoherent feedback action from the ZnO nanorods has not been reported. Besides that, it is necessary to investigate the conditions and the transition regime that leads to the two different types of optical feedback.

A post-growth annealing method is illustrated in CHAPTER 5, to generate random lasing cavities inside the ZnO films. In fact, more investigations are required to study the formation characteristics of random lasing under the influence of: 1) annealing temperature, 2) annealing duration, 3) the thickness of the ZnO layer and 4) the thickness of the buffer layer.

Random lasers with low-loss and directional emission output are realized and reported in CHAPTER 6. Besides, it has been demonstrated that the ratio ($P_{th, M}/P_{th}$) of the pumping threshold of a one-Al-mirror random laser ($P_{th, M}$) to that of a random laser without mirror (P_{th}) is increased with the increase of the laser cavity length (L). This finding disagrees with that reported by Feng and coworkers [267]. Hence, it is necessary to find out a theoretical explanation and to carry out experiments that will assist to justify our finding. In addition, it is also crucial to further reduce the lasing threshold of these random lasers. This will lead to the

optimization and analysis of the MgO cap layer fabricated at different deposition conditions and the exploration in the possibility of using another alternative material as the cap layer. Finally, further investigation is required to realize a single-mode, low-loss and directional random laser.

In CHAPTER 7, the fabrication of UV ZnO heterojunction LEDs by the FCVA technique is reported. Hence, this leads to the initiative to investigate the FCVA method in the fabrication of *p*-type ZnO films, in order to realize UV ZnO homojunction LEDs, using ZnO as the *p*-type and *n*-type materials. The values of carrier concentration and electron mobility of the *p*-type ZnO films fabricated at different deposition conditions and parameters should also be studied. Besides, with the knowledge and experience of making the ZnO UV random lasers and LEDs made by the FCVA technique, it helps to build a foundation in realizing an electrically pumped ZnO UV random laser. Furthermore, the electrically pumped random lasers can be in the form of thin films, powders and nanorods. The conditions and transition regime of the coherent and incoherent random lasing actions of these lasers should be explored as well. Finally, the electrically pumped random laser can be modified into a low-loss, directional random laser with high-power and single-mode emission.

In this thesis, random lasers have been discussed to eliminate the need for cleaved mirrors, the study of surface-emitting lasers (SEL) is also important to be carried out. This will trigger investigations for the transparent electrodes and dielectric mirrors for the optically or electrically pumped surface-emitting ZnO UV lasers.

AUTHOR'S PUBLICATIONS (Related to this thesis)

Journal Papers

1. S. F. Yu, **Clement Yuen**, S. P. Lau, Y. G. Wang, H. W. Lee, and B. K. Tay, "Ultraviolet amplified spontaneous emission from zinc oxide ridge waveguides on silicon substrate", Appl. Phys. Lett. **83**, 4288-4290 (2003). Times cited: 12
2. S. F. Yu, **Clement Yuen**, S. P. Lau, and W. J. Fan, "Design and fabrication of zinc oxide thin-film ridge waveguides on silicon substrate with ultraviolet amplified spontaneous emission", IEEE J. Quantum Electron. **40**, 406-412 (2004). Times cited: 2
3. S.F. Yu, **Clement Yuen**, S.P. Lau, and H.W. Lee, "ZnO thin-film random lasers on silicon substrate", Appl. Phys. Lett. **84**, 3244-3246 (2004). Times cited: 11
4. S. F. Yu, **Clement Yuen**, S. P. Lau, W. I. Park, and Gyu-Chul Yi, "Random laser action in ZnO nanorod arrays embedded in ZnO epilayers", Appl. Phys. Lett. **84**, 3241-3243 (2004). Times cited: 30
5. **Clement Yuen**, S. F. Yu, Eunice S. P. Leong, H. Y. Yang, S. P. Lau, N. S. Chen, and H. H. Hng, "Low-loss and directional output ZnO thin-film ridge waveguide random lasers with MgO capped layer", Appl. Phys. Lett. **86**, 031112-031114 (2005). Times cited: 1

5. **Clement Yuen**, S. F. Yu, Eunice S. P. Leong, H. Y. Yang, S. P. Lau and H. H. Hng, "Formation conditions of random laser cavities in annealed ZnO epilayers", IEEE J. Quantum Electron. **41**, 970- 973 (2005). Times cited: 1

6. **Clement Yuen**, S. F. Yu, S. P. Lau, Rusli, and T. P. Chen, "Fabrication of n-ZnO:Al/p-SiC(4H) heterojunction light-emitting diodes by filtered cathodic vacuum arc technique", Appl. Phys. Lett. **86**, 241111-241113 (2005). Times cited: 4

7. **Clement Yuen**, S. F. Yu, S. P. Lau, and George C. K. Chen, "Design and fabrication of ZnO light-emitting devices using filtered cathodic vacuum arc technique", J. Cryst. Growth **287**, 204-212 (2006). Times cited: 0

Conference Papers

1. S. F. Yu, Eunice S. P. Leong, S. P. Lau and **Clement Yuen**, "Formation of Random Laser Action in ZnO Thin Films", 5th International Conference on Thin Film Physics and Application (TFPA2004), May 31 – Jun. 2, 2004, Shanghai, China. Times cited: 0

2. **Clement Yuen**, S. F. Yu, Eunice S. P. Leong, S. P. Lau, and H.Y. Yang, "Zinc oxide coherent and incoherent random laser from heterolayers on silicon", The 3rd International Workshop on ZnO and Related Materials, Oct. 5 – 8, 2004, Sendai, Japan. Times cited: 0

3. **Clement Yuen**, S. F. Yu, S. P. Lau, Rusli, T. P. Chen, H. D. Li, A. P. Abiyasa, N. S. Chen, T. S. Heng, X. H. Ji, S. P. Leong, and H. Y. Yang, “Fabrication of n-ZnO:Al/p-SiC (4H) heterojunction light-emitting diodes by filtered cathodic vacuum arc (FCVA) technique”, 3rd International Conference on Materials for Advanced Technologies & IUMRS and 9th International Conference on Advanced Materials, Jun. 3 – 8, 2005, Singapore. Times cited: 0

Patent

S.F. Yu, **Clement Yuen**, S.P. Lau, “Zinc Oxide Thin-Film Random Lasers on Silicon Substrate”, US Provisional Patent, ETPL ref: SRC/P//1670/US.

AUTHOR'S PUBLICATIONS (Not related to this thesis)

Journal Papers

1. Y. G. Wang, **Clement Yuen**, S. P. Lau, S. F. Yu, and B. K. Tay, "Ultraviolet lasing of ZnO whiskers prepared by catalyst-free thermal evaporation", Chem. Phys. Lett. **377**, 329-332 (2003). Times cited: 6
2. X. W. Sun, S. F. Yu, C. X. Xu, **C. Yuen**, B. J. Chen, and S. Li, "Room-temperature ultraviolet lasing from zinc oxide microtubes", Jpn. J. Appl. Phys. **42**, L1229-L1231 (2003). Times cited: 18
3. **Clement Yuen**, S. F. Yu, X. W. Sun, C. X. Xu, Eunice S. P. Leong, S. P. Lau, and C. K. Chen, "Ultraviolet lasing phenomenon of zinc oxide hexagonal microtubes", Jpn. J. Appl. Phys. **43**, 5273-5278 (2004). Times cited: 1
4. C. X. Xu, X. W. Sun, **Clement Yuen**, B. J. Chen, S. F. Yu, and Z.L. Dong, "Ultraviolet amplified spontaneous emission from self-organized network of zinc oxide nanofibers", Appl. Phys. Lett. **86**, 011118-011120 (2005). Times cited: 1
5. H. D. Li, S. F. Yu, A. P. Abiyasa, **Clement Yuen**, S. P. Lau, H. Y. Yang, and Eunice S. P. Leong, "Strain dependence of lasing mechanisms in ZnO epilayers", Appl. Phys. Lett. **86**, 261111-261113 (2005). Times cited: 0

6. S. P. Lau, H. Y. Yang, S. F. Yu, **Clement Yuen**, Eunice S. P. Leong, H. D. Li, and H. H. Hng, "Flexible ultraviolet random lasers based on nanoparticles", *Small* **1**, 956-959 (2005). Times cited: 0

Conference Papers

1. S. F. Yu, **Clement Yuen**, Daniel Lau Shu Ping and Tay Beng Kang "Optical pumped ZnO thin film UV resonators on silicon substrate", 2nd International Conference on Materials for Advanced Technologies & IUMRS - International Conference in Asia 2003, Jun. 29 – Jul. 4, 2003, Singapore. Times cited: 0

2. S. F. Yu, X. W. Sun, **C. Yuen** and S. P. Lau, "Investigation of the ultraviolet lasing characteristics of zinc oxide hexagonal microtubes", IEEE/LEOS International Conference on "Numerical Simulation of Semiconductor Optoelectronic Devices (NUSOD)", Oct. 13 – 16, 2003, Tokyo, Japan. Times cited: 0

3. X. W. Sun, S. F. Yu, C. X. Xu, **C. Yuen**, and B. J. Chen, "UV light-source from zinc oxide microtube", 8th Asian Symposium on Information Display, Feb. 14 – 17, 2004, Nanjing, China. Times cited: 0

4. S. P. Lau, H. Y. Yang, S. F. Yu, **C. Yuen**, and E. S. P. Leong, "Optically pumped flexible ultraviolet random laser", The 3rd International Workshop on ZnO and Related Materials, Oct. 5 – 8, 2004, Sendai, Japan. Times cited: 0

APPENDIX A ZnO Properties and ZnO Nanorods

A.1 Crystal Structure

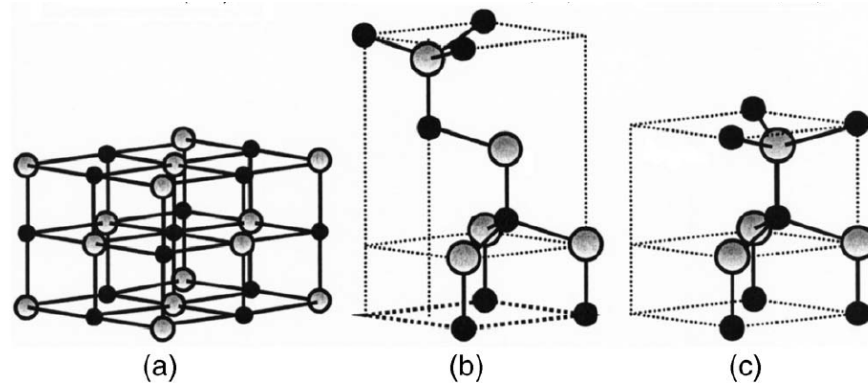


Figure A.1 Stick and ball representation of ZnO crystal structures: (a) cubic rocksalt (B1), (b) cubic zinc blende (B3), and (c) hexagonal wurtzite (B4). The shaded gray and black spheres denote Zn and O atoms, respectively [233].

Figure A.1 gives the 3 different types of ZnO crystal structures and they are (a) rocksalt, (b) zinc blende and (c) hexagonal. For the rocksalt structure, it can be produced under high pressure, while the zinc-blende crystal structure can be achieved by forming on cubic substrates. On the other hand, ZnO normally forms in the hexagonal crystal structure with the two lattice parameters, $a = 3.25 \text{ \AA}$ and $c = 5.12 \text{ \AA}$.

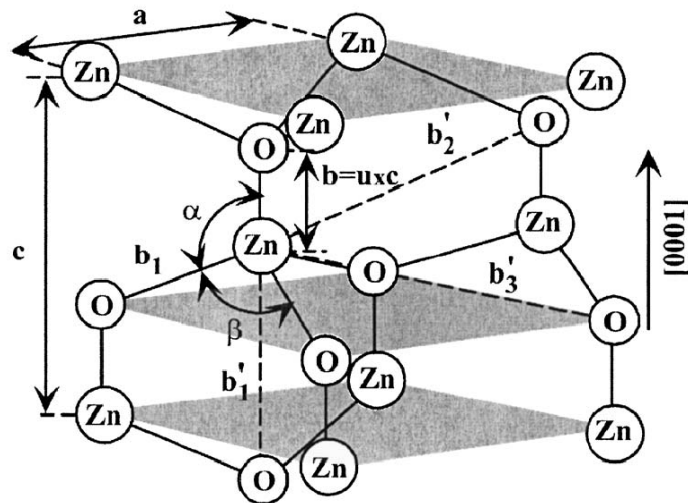


Figure A.2 Schematic representation of a wurtzitic ZnO structure having lattice constants a in the basal plane and c in the basal direction; u parameter is expressed as the bond length or the nearest-neighbor distance b divided by c . α and β are the bond angles.

The structure is composed of layers occupied by zinc atoms alternate with layers occupied by oxygen atoms and this is illustrated by the schematic representation of the wurtzitic ZnO structure in Figure A.2. The structure consists of two interpenetrating hexagonal-close-packed sublattices, with the Zn (O) layer at a distance of $u \times c$ in the direction of c -axis to the nearest Zn (O) layer. The u value increases as the c/a ratio reduces to maintain the four tetrahedral distances of the bonds of a Zn (O) atom that is tetrahedrally coordinated to four O (Zn) atoms.

A.2 Band Structure and Other ZnO Properties

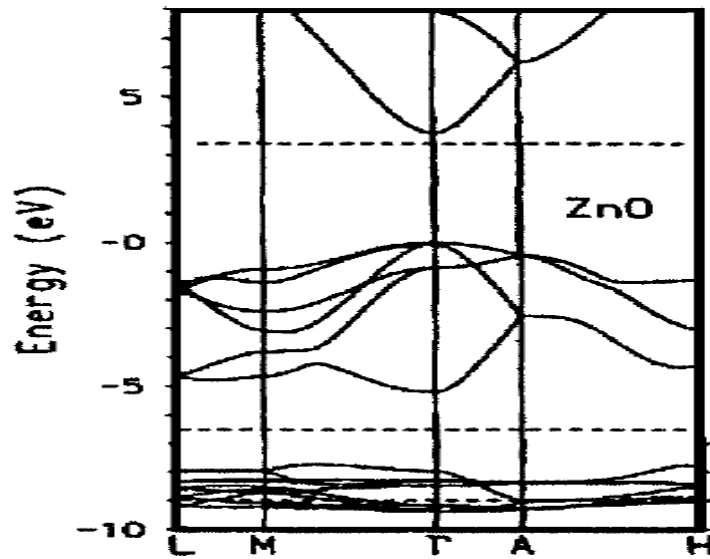


Figure A.3 Low-density approximation bulk-band structure of ZnO as calculated using a self-interaction corrected pseudopotential. The horizontal dashed lines indicate the measured gap energy and d-band width [281].

Figure A.3 gives the band structure of ZnO and it shows that ZnO is a direct semiconductor material. ZnO has a band-gap energy of 3.2 eV and it can be lowered [154] or increased [282] by substituting other elements into the epitaxial films while maintaining the wurtzite structure. Table A.1 on the next page gives some of the other properties of wurtzite ZnO.

Appendix A

a_0 (Lattice parameters at 300 K)	0.324 95 nm
c_0 (Lattice parameters at 300 K)	0.520 69 nm
c_0/a_0 (Lattice parameters at 300 K)	1.602 (ideal hexagonal structure shows 1.633)
u	0.345
Density	5.606 g/cm ³
Stable phase at 300 K	Wurtzite
Melting point	1975 °C
Thermal conductivity	0.6, 1–1.2
Linear expansion coefficient (/°C)	a_0 : 6.5×10^{-6} c_0 : 3.0×10^{-6}
Static dielectric constant	8.656
Refractive index	2.008, 2.029
Energy gap	3.4 eV, direct
Intrinsic carrier concentration	$<10^6$ cm ⁻³
Exciton binding energy	60 meV
Electron effective mass	0.24
Electron Hall mobility at 300 K for low n-type conductivity	200 cm ² /V s
Hole effective mass	0.59
Hole Hall mobility at 300 K for low p-type conductivity	5–50 cm ² /V s

Table A.1 Properties of wurtzite ZnO [283].

Additionally, optical transitions of ZnO have been studied by different experimental techniques and strong room temperature near-band-edge ultraviolet (UV) peak at ~3.2 eV is observed [284]. Besides, defect-related transitions can be observed in the emission spectra. Defects like: 1) doubly ionized zinc vacancies and ionized interstitial Zn⁺ [285], 2) oxygen vacancies [286], and 3) interstitial O [287], in ZnO films causes the films to exhibit a blue-green emission, centered at around 500 nm.

Under optical pumping, when a photon excites an electron of the valance band into the conduction band, a hole is formed in the valance band. Hence, an exciton is formed due to the binding of the electron and hole. As they recombine, a photon

with energy of about 3.26 eV is emitted in ZnO. This is known as free exciton recombination [288]. Moreover, when optically pumped stimulated emission is observed in ZnO films, the two main recombination processes behind responsible for the emission mechanisms are exciton-exciton scattering and electron-hole plasma (EHP) recombination. Exciton-exciton scattering occurs when inelastic collision take place between excitons, an exciton is being excited and a photon with energy,

$$E_n = E_{ex} - E_b^{ex} \left(1 - \frac{1}{n^2} \right) - \frac{3}{2} k_B T \quad (n = 2, 3, 4, \dots, \infty), \quad (\text{A.1})$$

where E_{ex} is the free-exciton energy, E_b^{ex} is the binding energy of the exciton (60 meV), n is the quantum number of the envelope function, and $k_B T$ is the thermal energy [233]. Hence, a value of 15 meV ($E_2 - E_\infty$) is expected for the maximum difference in the energies of photons. It is the main process behind the emission mechanism when the electron-hole pair density is smaller than that of Mott density ($3.7 \times 10^{19} \text{ cm}^{-3}$), near the threshold of the optical gain spectra [27]. On the other hand, electron-hole plasma recombination is the recombination of an electron and a hole, resulting in the formation of a photon. It is formed when coulomb interactions cause the ionization of excitons [233]. This phenomenon becomes the more dominating process behind the emission mechanism when the electron-hole pair density is greater than that of Mott density. Moreover, this process takes over as the excitation densities increases after the threshold in the optical gain spectra, accompanied by shifting of emission peak in the emission spectra [233].

A.3 ZnO Nanorods

ZnO nanorods and nanowires can be obtained by different growth methods. The major fabrication techniques for ZnO nanorods are: 1) vapor phase synthesis via thermal evaporation method [289,290] or vapour-liquid-solid (VLS) process [291], 2) metal-organic chemical vapor deposition [241], 3) chemical synthesis via hydrothermal synthesis [292], reverse micelle [293], sol-gel, aqueous solution [294] and biomineralization methods [295]. Besides, nanorod arrays that are vertically aligned with uniform thickness and length distributions have been fabricated by VLS process with metal catalysts [15], template-assisted growth [296], electrical field alignment [297] or catalyst-free metalorganic chemical vapor deposition (MOCVD) method [298]. The fabrication of ZnO nanorods has attracted much emphasis by the ZnO research community because they have shown potential for ZnO nanodevice applications in nanorod heterostructures [299], quantum structures [300], alloying and doping of ZnO nanorods [301], nanolasers [15], field emission [302], gas sensor [303] and electron transport properties [304].

APPENDIX B Photoluminescence

B.1 Optical Setup

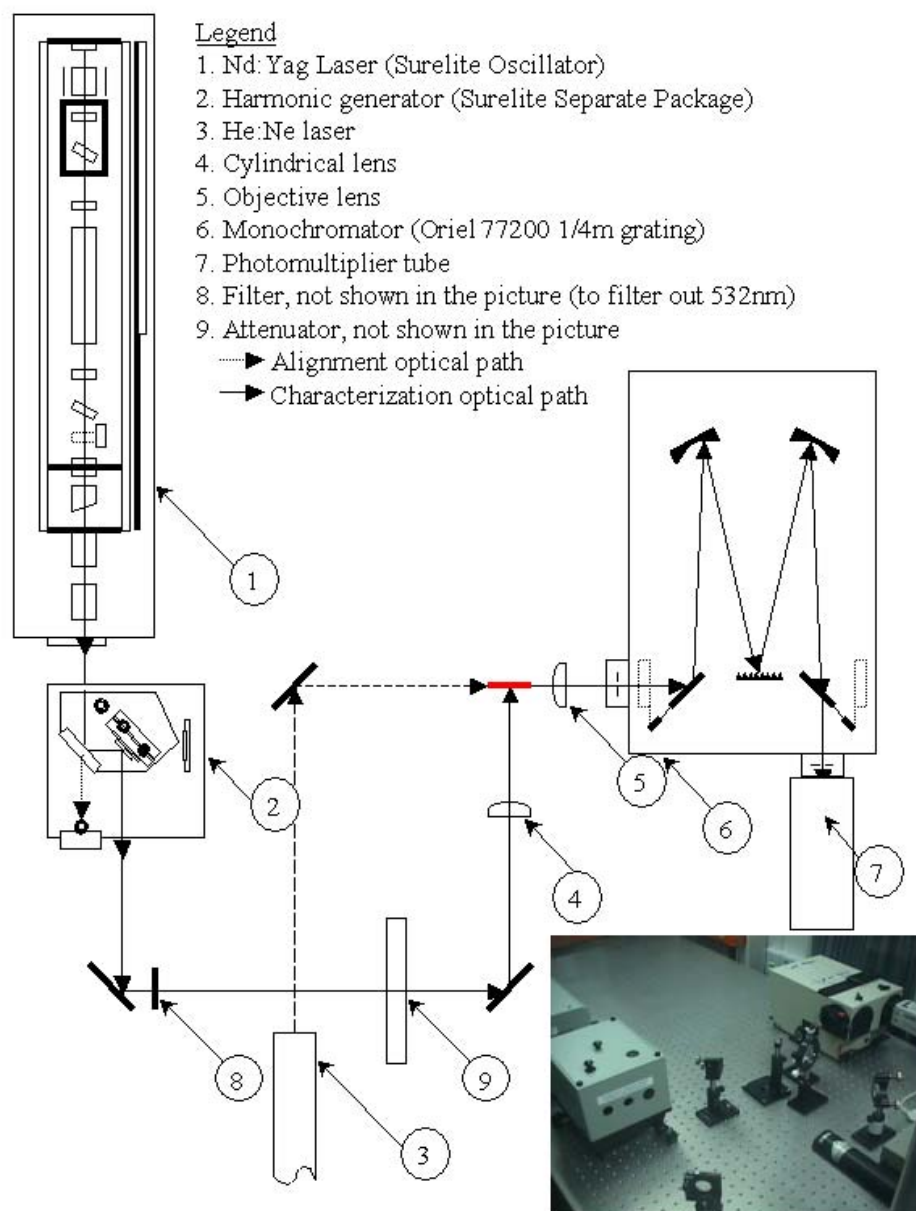


Figure B.1 Optical setup for the photoluminescence measurement.

Figure B.1 shows the setup of the photoluminescence (PL) measurement. The Nd:YAG laser (Surelite III-10Hz), the Surelite Separation Package (SSP), the monochromator (Oriel 77200 1/4m grating), the He:Ne laser, lens and mirrors were adjusted to the same height with respect to the optical table and secured. A SSP-3 was installed inside the SSP to isolate the YAG second, third and fourth harmonic from the fundamental. The shutter of the SSP-3 was closed to dispose the unused 1064nm and 532nm residual beam. The Surelite doubling component, 532nm, was adjusted to a minimum and filtered out by a filter (10SWF-450) to reduce the unwanted components from pumping and heating the sample under investigation. The same was done for the 266nm component and the 355nm component was tune to a maximum.

In the alignment of optics, the Nd:YAG laser was off, while the He:Ne laser was switched on and aimed into the objective lens in front of the input slit assembly, without the sample. Position of the objective lens was adjusted until the detector output signal registered a maximum. This step was repeated and the input and output slit widths were reduced until both slit widths were at 10 μm . It was noted that a built-in transimpedance amplifier silicon detector (Oriel 70336) was used in placed of the photomultiplier tube (PMT) (Oriel 77345) as shown in the position in Figure B.1. This was to prevent the PMT from being damaged by the He:Ne laser that was used to assist the alignment. The silicon detector was connected to a lock-in amplifier (Oriel Merlin 70100) for collecting the data.

Next, a sample was placed at the position, as indicated by the red line in Figure B.1. With the He:Ne laser off and the Nd:YAG laser (10 Hz, tripling 355nm

output) on, it was optically pumped onto the sample at 90° , focused by a cylindrical lens. The emission at the facet of the sample was collimated into the input slit assembly of the monochromator, via the objective lens. At 355 nm, the delay between the signal outputted from the silicon detector and the reference signal from a pulse controlling circuit (B.4) were noted and input into the lock-in amplifier (SR 510). Subsequently, the position of the sample was readjusted until reasonable level of signal was observed around the emission wavelengths, with the PMT fixed onto the output slit assembly in place of the silicon detector.

B.2 Equipment Communication

The communication flow of the entire system was designed as shown Figure B.2 on the next page. Two lock-in amplifiers (SR510 and Oriel Merlin 70100) were connected to a switch box and the output from the switch box was connected to the serial port of a computer. Communication between the computer and the lock-in amplifiers were in American Standard Code for Information Interchange (ASCII) and data transfer was in full-duplex asynchronous communication mode. Besides that, a stepper motor was connected to the printer port of the computer. Communication between the computer and the stepper motor was also in ASCII code and the communication mode was simplex and asynchronous. There was no handshake status in transmission and reception data control. The bit rate was chosen to be 9,600 bits/s, the number of data bits per character was 8 bit, parity type used was none and the number of stop bits was 1 bit. This setting also applied to the two lock-in amplifiers. Furthermore, the stepper motor was connected to a monochromator and wavelength of the monochromator was synchronized by

Appendix B

means of calibration at the beginning of the computer program. The program matched with the wavelength by the relative displacement to the calibrated wavelength. Hence, emission intensities at different wavelengths can be stored into the computer in a text file.

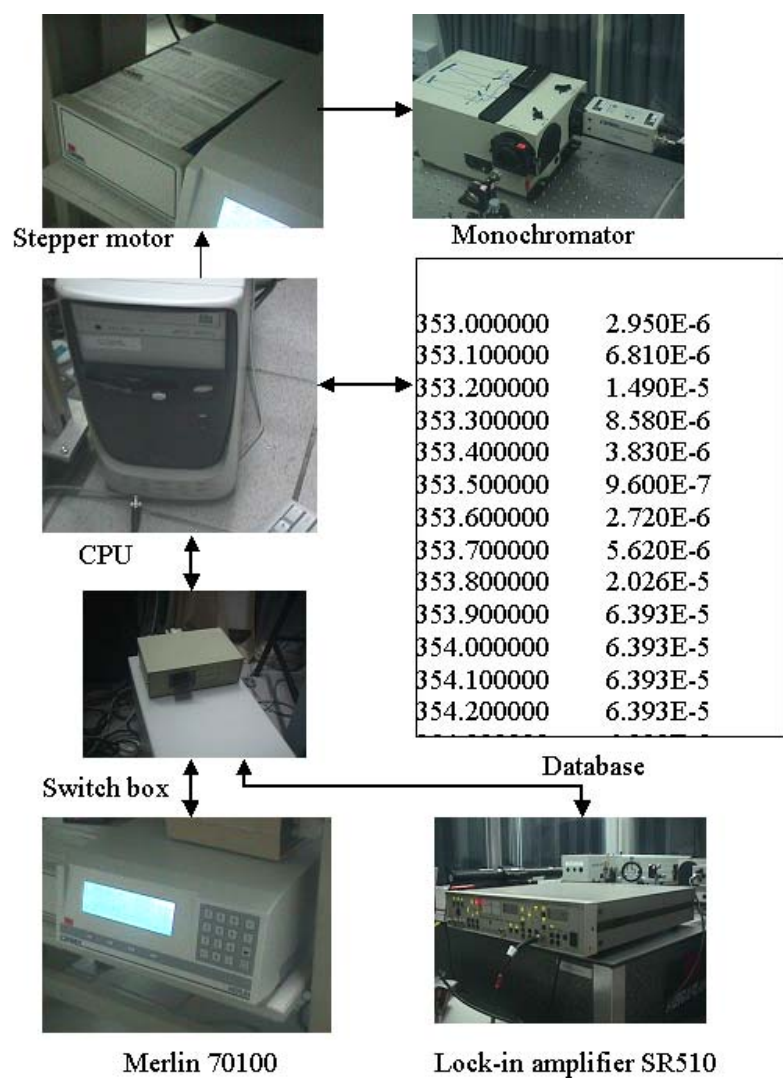


Figure B.2 Communication flow of the entire system.

B.3 Entire Layout

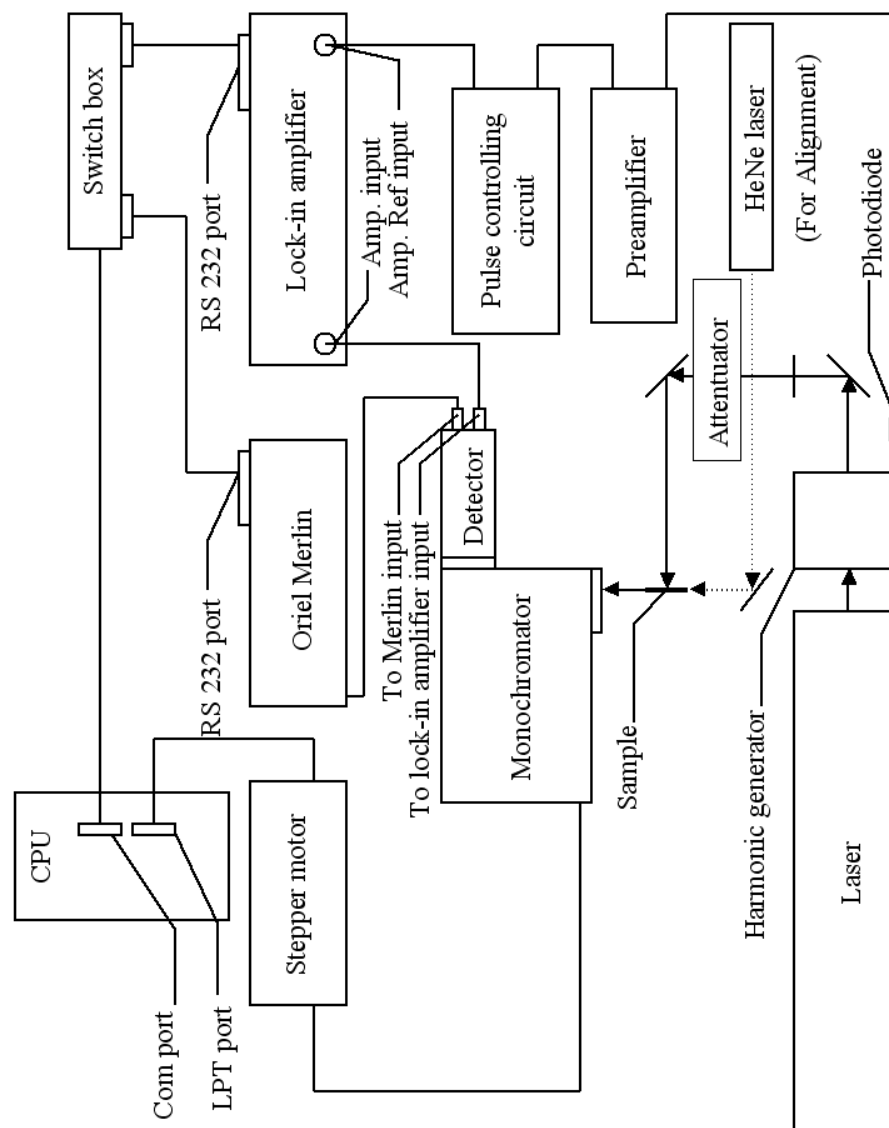


Figure B.3 Entire layout of the system.

The entire layout of the system was setup as shown in Figure B.3. The printer and serial port of the computer were connected to the stepper motor and the switch box, respectively. One of the connections of the switch box was connected to the serial port of the Merlin, while the other was connected to the SR510. Both the

Appendix B

input of the Merlin and SR510 were connected either to the Si detector or the PMT located at the output assembly of the monochromator. For the reference input of the SR510, it was linked to a pulse controlling circuit, a preamplifier and a photodiode that will be discussed in section B.4. The photodiode was placed in front of the harmonic generator that was part of the optical layout mentioned in section B.1.

B.4 Pulse Controlling Circuit

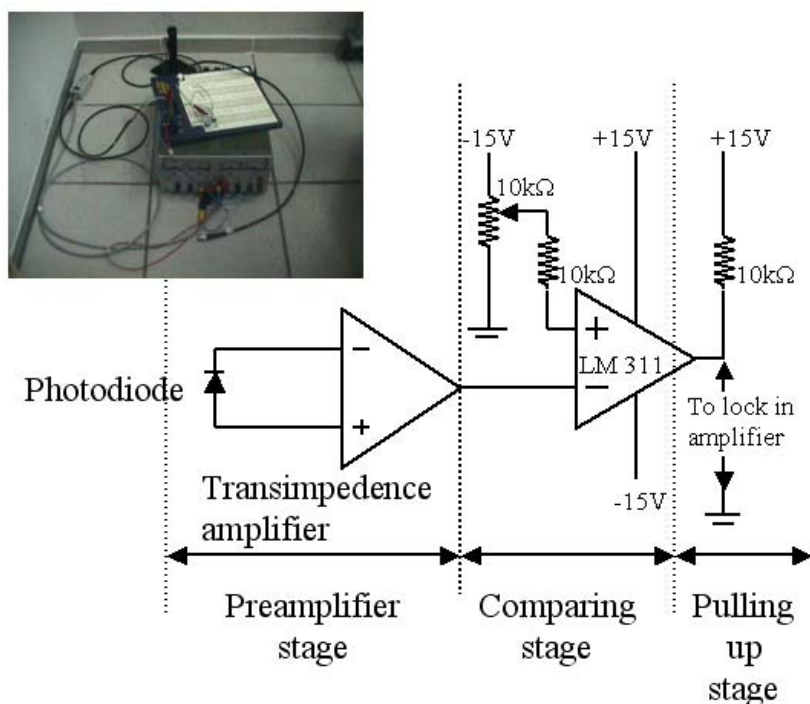


Figure B.4 Circuit diagram for changing the pulse width.

The pulse controlling circuit, as shown in Figure B.4, modified the pulse width and the waveform of the reference signal from the detector to fulfill the negative triggering mode requirements of the lock-in amplifier. The circuit was separated

into three stages. They were namely the preamplifier stage, the comparing stage and the pulling up stage. First, the preamplifier stage was to preamplify the reference pulse signal at the output of the photodiode. It provided transimpedance gain to the signal and to broaden the pulse width of the pulse. The pulse at the exit port of the Surelite Separation Package was detected by a photodiode (RS651-995) and amplified by a current preamplifier (Oriol 70710). The gain of the preamplifier and the time constant were set at 10^6 V/A and MAX-position, respectively. Secondly, function of the comparing stage was to compare the input pulse with a reference voltage. When the input voltage was lower than the reference voltage, the output transistor was off and no current flowed. The reverse was true when the input voltage was higher than the reference voltage. Changing the reference voltage changed the output pulse width. This stage was comprised of a resistor network, and a voltage comparator (National Semiconductor LM311). Finally, at the pulling up stage, the output gave a high voltage of 15V when the reference voltage was lower than the voltage of the pulse. It was at a low voltage, less than 1V otherwise, which satisfied the requirement for edge triggering of the lock-in amplifier. A 10k Ω resistor and a +15V dc power supply (Toward Electric Instruments, TPS4000) built up this stage.

The entire pulse controlling circuit was connected as shown in Figure B.5. A coaxial cable with a Bayonet Neill-Concelman (BNC) connected at one end while a photodiode was connected to the other. The coaxial cable was connected to the input of the current preamplifier. The output of the current preamplifier was connected to a BNC connector of a coaxial cable with the cathode connected to the ground and the anode connected to the input of the comparing stage. The output of

Appendix B

the pull up stage was connected to the reference input of the lock-in amplifier. The current preamplifier and the comparing and pull up stage shared the same ± 15 V and ground of the direct current power supply, as illustrated in the Figure B.5. Therefore, varying the reference voltage at the non-inverting input of the comparator modified the pulse width of the comparator output signal.

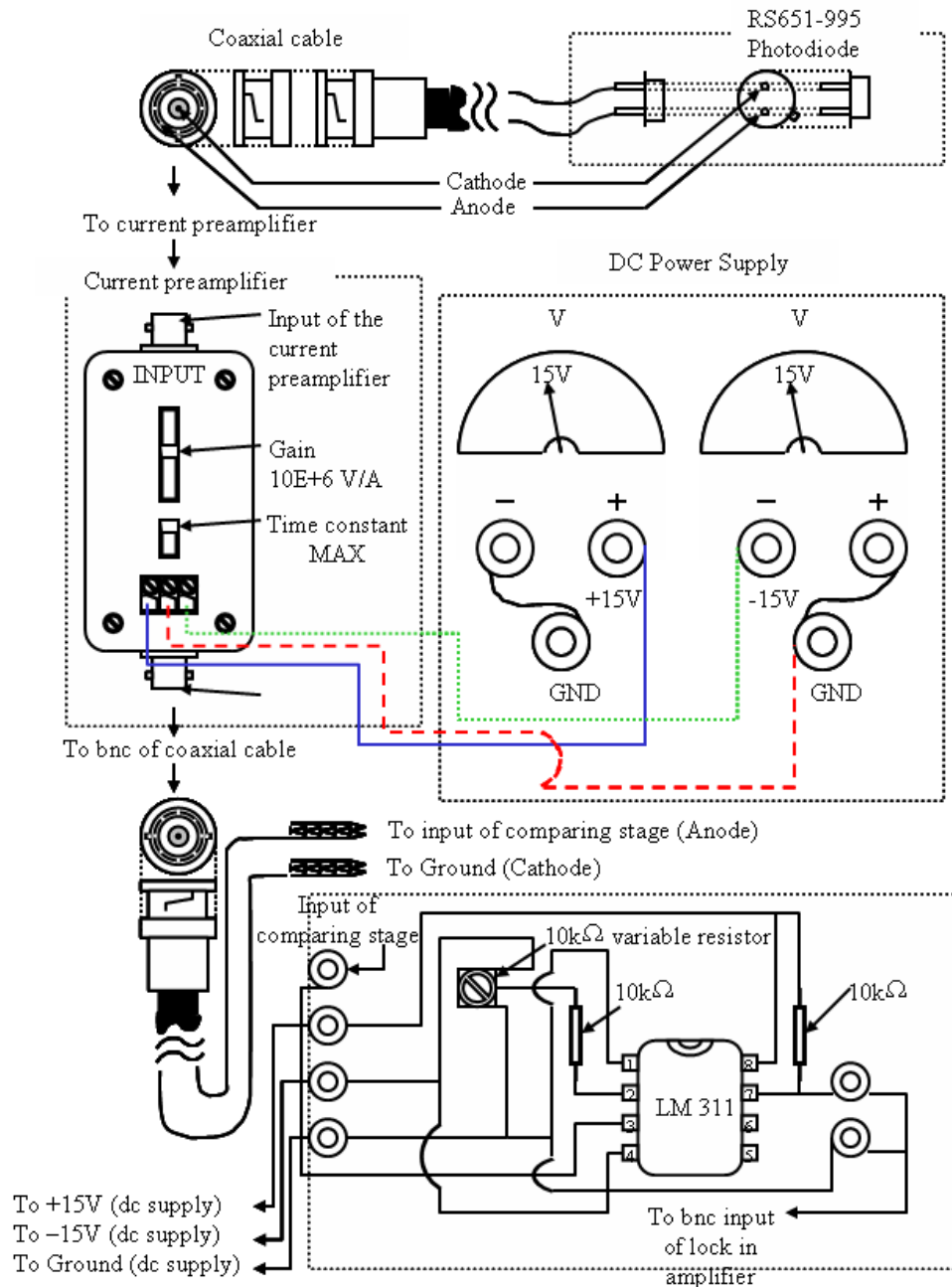
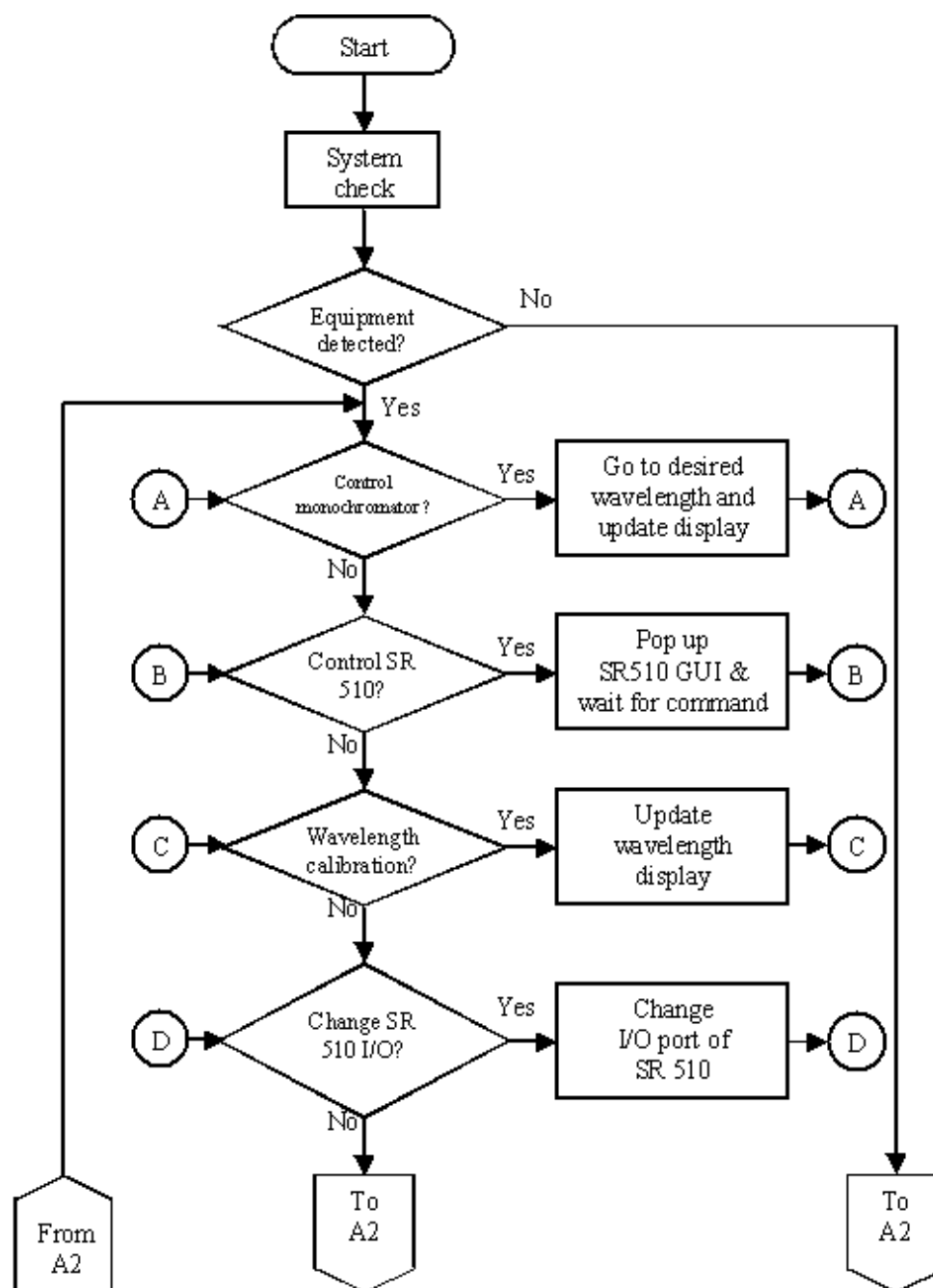


Figure B.5 Entire connection of the pulse controlling circuit.

B.5 Software Program



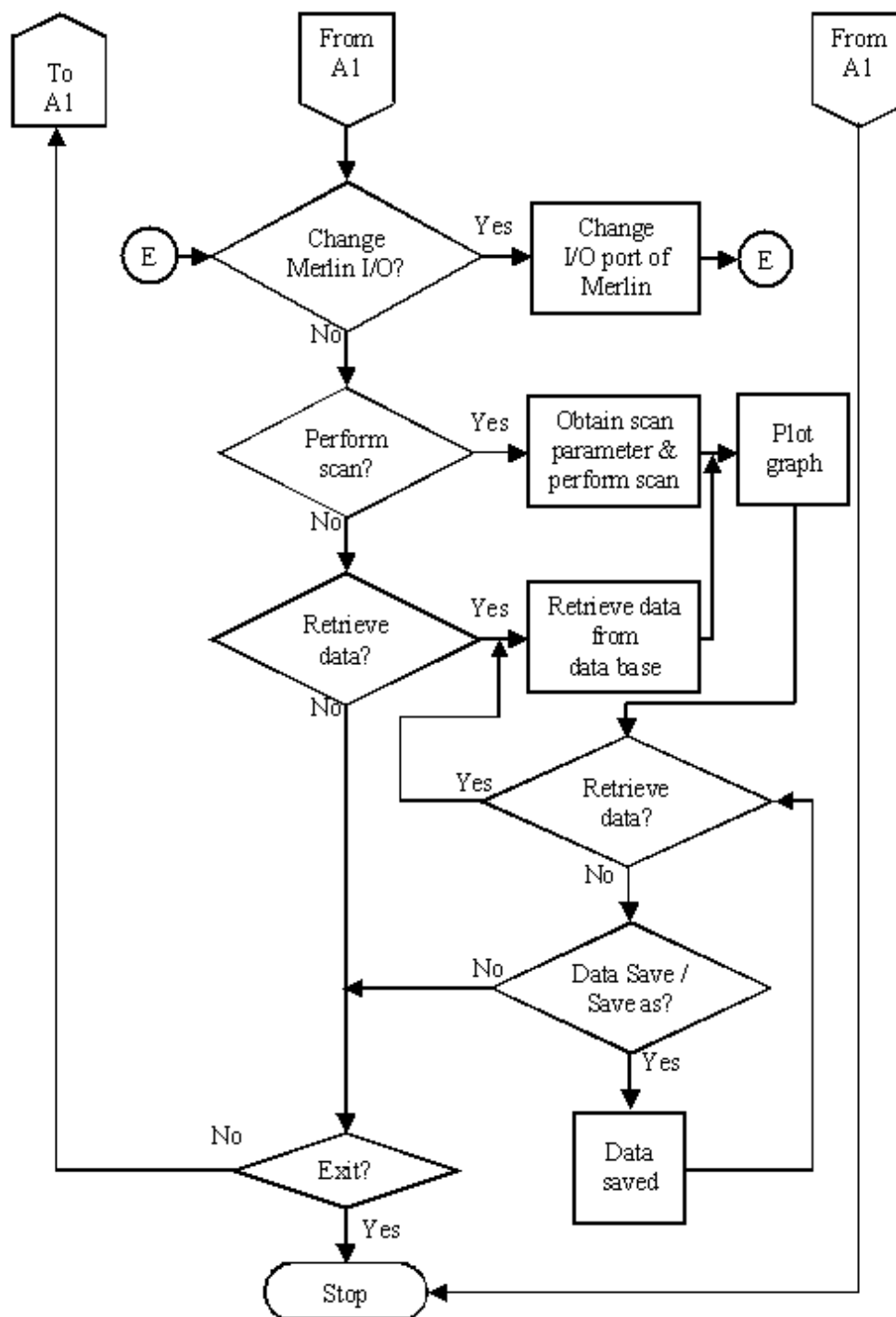


Figure B.6 Flow chart of the software program for the PL measurement.

A software program was used to record the data in the PL measurement, with its flow chart shown in Figure B.6. At the beginning of the software program, the

Appendix B

system performed an equipment check. This was to confirm that all necessary equipment was present; otherwise the program would halt the entire operation. Then selection was made on using either the Merlin or the SR510 for data collection. After that, the software was ready for the experiment and there were several options. First, data from the database could be retrieved and displayed in a graphical format. Second, the setting of the lock-in amplifier could be changed or the wavelength position of the monochromator altered. Finally, a scan could also be carried out.



Figure B.7 Graphical user interface (GUI) for the input of the scanning parameters.

A GUI for the input of the scanning parameters appeared when the parameter option was clicked on the scan menu, as shown in Figure B.7. The start and the end wavelengths were specified to be 365 and 410 nm. They were defined to set the two limits between which the wavelength ranges were to be scanned. The interval

Appendix B

was set to 0.1 nm and it meant that the wavelength would increase in step of 0.1 nm. Once the interval was entered, the points of the experiment were automatically recalculated. The number of readings per point and pause in between each reading were 1 and 1 s, respectively, as indicated in the Figure B.7. After filling up all the fields, the GO-button was clicked and a scan was started. After the scan was completed, the data was saved by clicking the save spec option in the file menu of the spectrum interface. Next, the power of the laser was adjusted and the procedures described were repeated to obtain another spectrum at different pumping powers. The light-light curve was resulted by plotting the different areas under the spectra against the various respective pumping powers.

APPENDIX C Variable Stripe Length Method

Measurement

C.1 Optical Setup

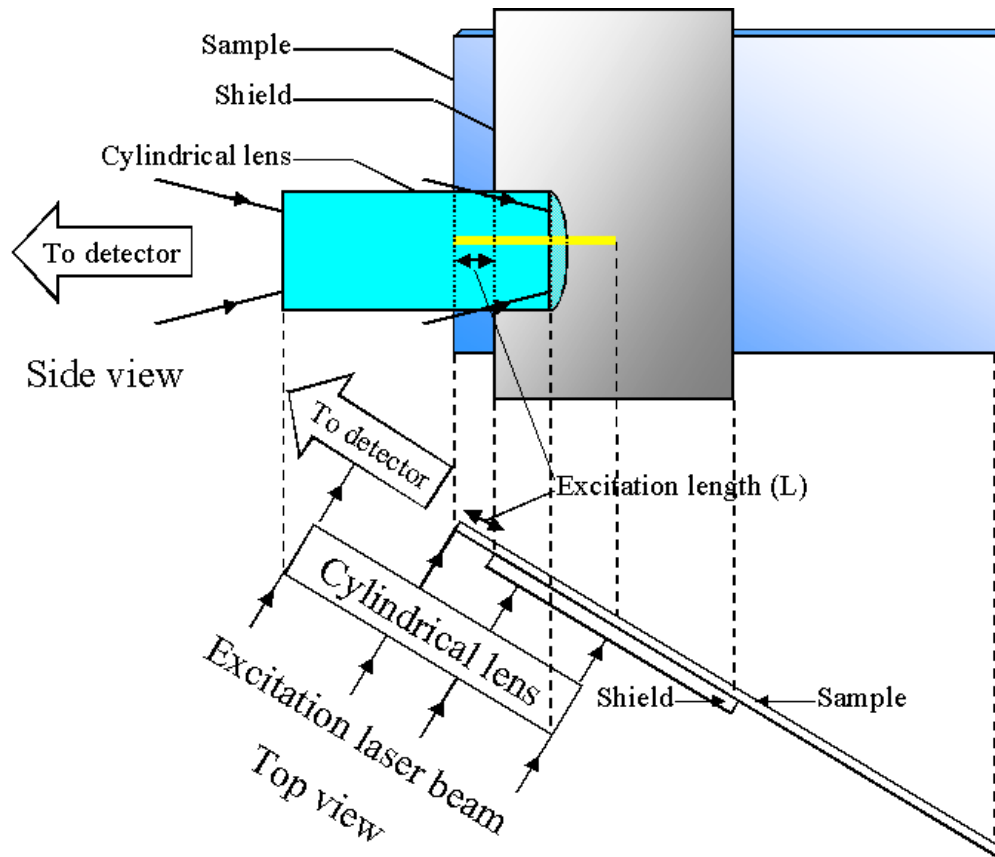


Figure C.1 Optical setup of the variable stripe length method measurement.

Light amplification inside the waveguide was measured by a variable stripe length method (VSL). The alignment of optics and sample, and obtaining the phase relation between the reference and detected signal were carried out as mentioned in APPENDIX B. In the VSL method, as indicated by the Figure C.1, the Nd:YAG laser beam (Surelite III-10 Hz, tripling 355nm output) was focused by a cylindrical lens into a stripe onto the sample. The stripe started at the facet of the thin film.

C.2 Measurement for VSL Method

The light emitted from the facet was collected by an objective lens into the monochromator. Different lengths of pumping stripe (L) were obtained by shifting a moving shield. At the corresponding length, the total intensity detected from the facet of the thin film (I_{tot}) was recorded. Then the net optical gain (G) at that particular pump power was obtained by fitting the set of L and I_{tot} values into the equation [228] as shown below:

$$I_{\text{tot}}(L, \lambda) = \frac{I_{\text{sp}}(\lambda)}{G(\lambda)} [\exp(G(\lambda) \cdot L) - 1], \quad (\text{C. 1})$$

where I_{sp} was the spontaneous emission and λ was the wavelength of the net optical gain to be measured. Repeating the same procedures, different net optical gains were obtained at different pump powers.

APPENDIX D Far- and Near-Field Profile

D.1 Far-Field Profile

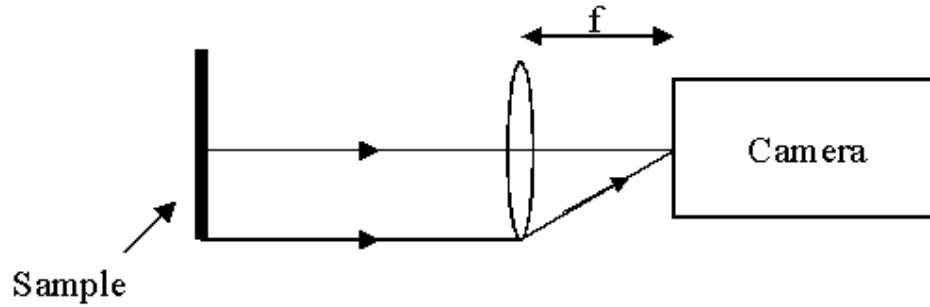


Figure D.1 Experimental setup for the far-field profile.

Figure D.1 gives the experimental setup for obtaining the far-field profile. The camera was positioned at the focal point of a focusing lens. Hence, parallel light rays passed through the lens and were focused into the camera.

D.2 Near-Field Profile

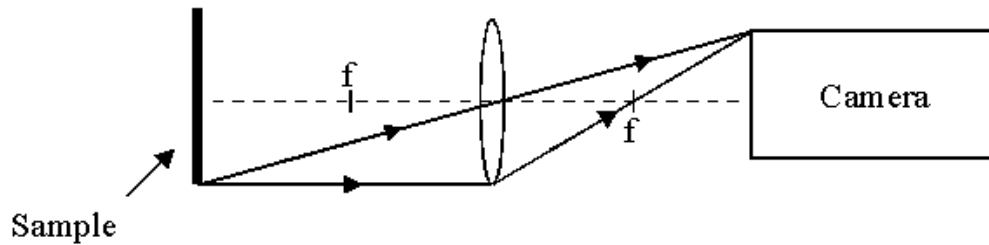


Figure D.2 Experimental setup for the near-field profile.

Figure D.2 shows the setup for obtaining the near-field profile from the sample. Image of the sample was focused onto the camera by using the relation,

$$\frac{1}{d_o} + \frac{1}{d_i} = \frac{1}{f}, \quad (\text{D.1})$$

Appendix D

where d_o is the distance between the sample and the lens, d_i is the distance between the camera and the lens and f is the focal length of the lens.

APPENDIX E Formation of UV and Visible Random Lasing Cavities at Different Annealing Temperature and Duration

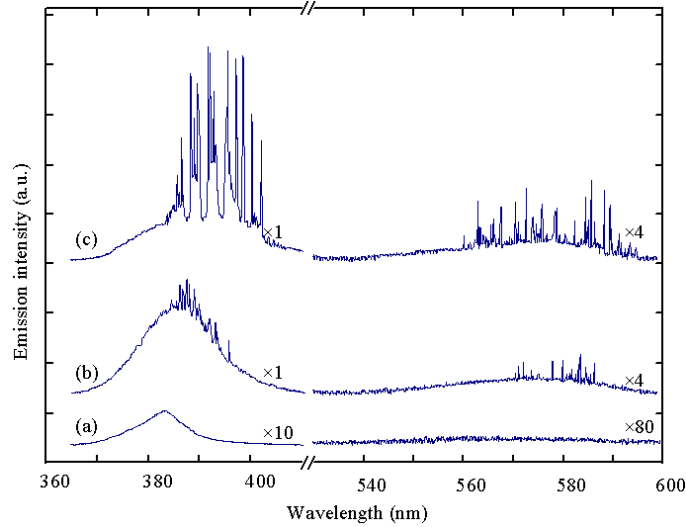


Figure E.1 Unpolarized emission spectra of ZnO films: (a) as-grown, (b) $T_a=1$ min, and (c) $T_a=2$ h.

Figure E.1 shows the unpolarized emission spectra of the ZnO films: (a) as-grown, (b) $T_a=1$ min, and (c) $T_a=2$ h, under pump intensity of ~ 1.5 MW/cm². In Figure E.1 (a), the spectra of as-grown ZnO film exhibit a ultraviolet (UV) and a visible peak at ~ 383 nm and ~ 565 nm, respectively. It is also noted that the ratio between the peak intensities of UV and visible spectra is ~ 60 . This means that the level of defect-related deep level emission (DLE) is as low as that of ZnO films fabricated by other methods [212,213]. For the case of ZnO film with $T_a=1$ min in Figure E.1 (b), the intensities of the amplified spontaneous emission (ASE) of the UV and DLE peaks are ~ 20 and ~ 100 times to that of the as-grown film. Both UV and visible emission are enhanced because of the removal of non-radiative

Appendix E

recombination centers by thermal annealing. Besides, random lasing is observed in both UV and visible wavelength with lasing threshold at $\sim 0.35 \text{ MW/cm}^2$ and $\sim 0.8 \text{ MW/cm}^2$, respectively (not shown). In Figure E.1 (c), the ratio between the peak intensities of UV and visible spectra is reduced from ~ 12 ($T_a=1 \text{ min}$) to ~ 8 ($T_a=2 \text{ h}$). This reduction implies that the DLE is enhanced through annealing for a longer time. Moreover, the sample exhibits random lasing at a lower lasing threshold (not shown) for the UV ($\sim 0.33 \text{ MW/cm}^2$) and visible spectra ($\sim 0.7 \text{ MW/cm}^2$).

Annealing temp. (°C)	T_a	I_{UV}/I_{VIS}	Lasing threshold (MW/cm^2)	
			UV	Visible
400 °C	1min	-	0.66	-
	2h	-	0.48	-
600 °C	1min	-	0.53	-
	2h	-	0.42	-
900 °C	1min	12	0.35	0.82
	2h	8	0.33	0.73
1000 °C	2h	6	0.32	0.61
1100 °C	2h	4	0.33	0.59

Table E.1 Lasing characteristics of the ZnO films annealed at 400 °C, 600 °C, and 900 °C (with $T_a=1 \text{ min}$ and 2h), and annealed at 1000 °C and 1100 °C. I_{UV}/I_{VIS} : the ratio between the peak intensities of UV and visible spectra at laser pumping power of $\sim 1.5 \text{ MW/cm}^2$.

Table E.1 above gives the different characteristics of the ZnO films annealed at 400 °C, 600 °C, and 900 °C (with $T_a=1 \text{ min}$ and 2h), and annealed at 1000 °C and 1100 °C. For samples annealed at same temperature with different T_a , the UV lasing threshold decreases with the increase in the annealing time. Similarly, the lasing threshold appears to be decreasing for the samples with same T_a but at different annealing temperature. This is because at higher temperature, ZnO grains

and voids are better developed with the increase in annealing temperature. However, for sample annealed at 1100 °C, the lasing threshold has not been changed with T_a as the UV emission is degraded at 1100 °C with annealing time.

Besides, random lasing is observed in the visible spectra for samples annealed at above 900 °C. Below 900 °C, samples exhibit weak DLE, since the defect states inside the ZnO films are not effectively introduced at a relatively low temperature. Moreover, it is noted that the lasing threshold for the visible spectra and the I_{UV}/I_{VIS} value decrease with the increase in annealing temperature. The decrease in lasing threshold and the value of I_{UV}/I_{VIS} is attributed to the enhancement in DLE through annealing [305]. Figure E.2 shows the lasing spectra of ZnO thin films annealed at (a) 900 °C, (b) 1000 °C, and (c) 1100 °C ($T_a=2$ h) with pumping intensity of ~ 1.5 MW/cm², showing the different I_{UV}/I_{VIS} values.

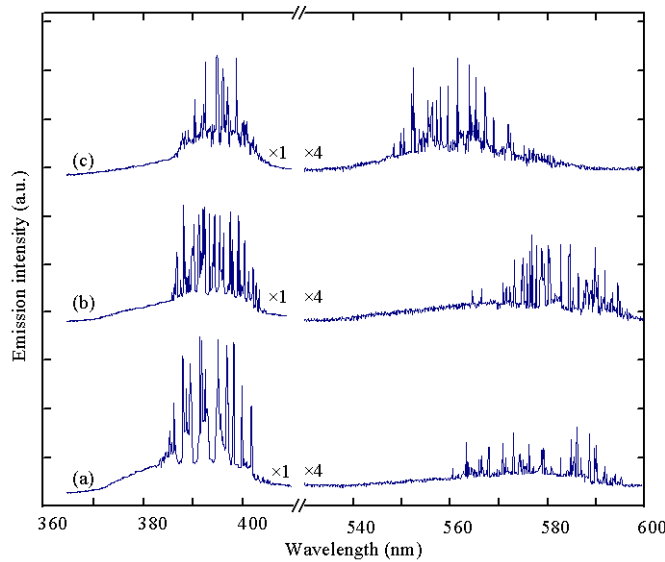


Figure E.2 Lasing spectra of ZnO thin films annealed at different temperature (a) 900 °C, (b) 1000 °C, and (c) 1100 °C with pumping intensity of ~ 1.5 MW/cm².

APPENDIX F Loss in Gain Threshold Equation

The scattering loss (α_{scat}) of the random cavities is related by the equation (F.1),

$$g_{th} = \alpha_{scat} + f(L), \quad (F.1)$$

where g_{th} is the threshold gain and $f(L)$ is the cavity loss of the random cavities.

This equation (F.1) can be approximated by equation (F.2),

$$g_{th} = \alpha_{scat} + \chi L^{-1}, \quad (F.2)$$

where χ is defined as the normalized cavity loss and L is the cavity length, based on the first order approximation of 1D random cavities [238]. This means that either by increasing the length of the cavity or reducing the cavity loss will reduce the pump threshold of the random lasers. Besides, the threshold gain can be expressed and approximated by the equation (F.3),

$$g_{th} \approx a_N(N_{th}), \quad (F.3)$$

where $a_N (=2 \times 10^{-16} \text{ cm}^2)$ is the differential gain and N_{th} is the threshold carrier concentration. This equation is obtained based on the assumption that the carrier concentration at threshold is very much greater than that at transparency and the annealed ZnO films has a linear excitonic gain [306]. On the other hand, N_{th} is related to the carrier rate equation (F.4) at threshold,

$$\eta P_{th} \lambda / d h c = N_{th} / \tau, \quad (F.4)$$

where the thickness of ZnO film (d) is 200 nm, the carrier lifetime (τ) is 0.4 ns, pump wavelength (λ) is at 355 nm, h is the Plank's constant, c is the velocity of light, and the coupling efficiency (η) is 0.108. The value of η is deduced by assuming only 87% of light is transmitted into the ZnO film, with 25% of the total excitation light illuminate the ridge structure and at most 50% of the pumped light

Appendix F

is converted to optical gain. Therefore, using equation (F.2), (F.3) and (F.4), it can be shown that P_{th} and α_{scat} are related to each other by the equation (F.5),

$$b_N P_{th} = \alpha_{scat} + \chi L^{-1} \quad (F.5)$$

where $b_N = \eta a_N \tau \lambda / d h c$.

APPENDIX G Derivation of Equation for One-mirror Random laser

For a one-mirror random laser [267], the gain distribution is

$$g(x) = G_0 A(x) e^{-x/\xi_p} \quad (\text{G.1})$$

It is assumed that the localized state is centered at the middle of the sample $x \approx L/2$ [307]. In graphical presentation, it is as shown below in Figure G.1. ξ_p is the localization length of the pump source and it gives the length of the closed-loop path formed by the pump source.

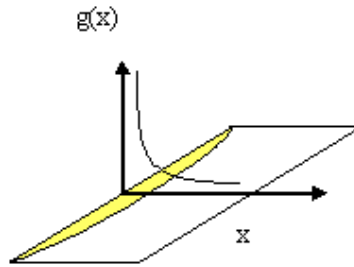


Figure G.1 Gain distribution inside a one-mirror random laser.

Their Intensity pattern is

$$I(x, x_0) = B(x, x_0) e^{-|x-x_0|/\xi_l} \quad (\text{G.2})$$

This is because they assumed that the medium to be strongly a localized medium.

Graphically, it is shown in Figure G.2 below.

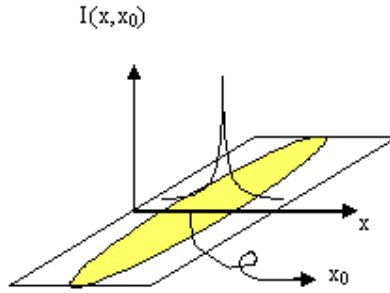


Figure G.2 Intensity pattern of the localized mode inside a one-mirror random laser.

They interpret the losses of modes for sample (without the coating of Al), δ_n , to be the summation of losses at the two facets (by substituting $x=0$ and $x=L$ in equation II above) and the mode loss δ_{0n} , due to absorption. As a result,

$$\delta_n \sim e^{-x_0 / \xi_l} + e^{-(L-x_0) / \xi_l} + \delta_{0n} \quad (\text{G.3})$$

Similarly, for the sample coated with aluminum at $x=0$, the mode losses, δ_m , would be comprised of the loss at the facet (by substituting $x=L$ in equation II above) and the mode loss δ_{0m} , due to absorption. In this case, they made an assumption that the mode at $x_0=0$, would lase first, as there are no other lasing source in the 1D cavity.

$$\delta_m \sim e^{-L / \xi_l} + \delta_{0m} \quad (\text{G.4})$$

At threshold, gain equals loss, therefore,

Appendix G

$$\int_0^L g(x)I(x, x_0)dx = \int_0^L G_0 A(x) e^{-x/\xi_p} B(x, x_0) e^{-|x-x_0|/\xi_l} dx = G_0 C \int_0^L e^{-x/\xi_p} e^{-|x-x_0|/\xi_l} dx = \delta \quad (G.5)$$

They put the localization length of the lasing light and the pump light to be equaled to localization length, $\xi_l = \xi_p = \xi$. Besides, since $L \gg \xi$ then the integral above becomes,

$$G_0 C \int_0^\infty e^{-x/\xi} e^{-|x-x_0|/\xi} dx = \delta \quad (G.6)$$

For the case without mirror, equation (G.6) becomes

$$\begin{aligned} G_0 C \int_0^L e^{-x/\xi} e^{-|x-x_0|/\xi} dx &= e^{-x_0/\xi} + e^{-(L-x_0)/\xi} + \delta_{0n} \\ \Rightarrow G_0 C \left[\int_0^{x_0} e^{-x/\xi} e^{(x-x_0)/\xi} dx + \int_{x_0}^L e^{-x/\xi} e^{-(x-x_0)/\xi} dx \right] &= e^{-x_0/\xi} + e^{-(L-x_0)/\xi} + \delta_{0n} \\ \Rightarrow G_0 C \left[\int_0^{x_0} e^{-x_0/\xi} dx + \int_{x_0}^L e^{-(2x-x_0)/\xi} dx \right] &= e^{-x_0/\xi} + e^{-(L-x_0)/\xi} + \delta_{0n} \\ \Rightarrow G_0 C \left[x_0 e^{-x_0/\xi} + \frac{\xi}{2} e^{-x_0/\xi} \right] &= e^{-x_0/\xi} + e^{-(L-x_0)/\xi} + \delta_{0n} \\ \Rightarrow G_0 C &= \frac{2}{\xi + 2x_0} e^{x_0/\xi} (e^{-x_0/\xi} + e^{-(L-x_0)/\xi} + \delta_{0n}) \\ G_{0nt}' &\sim \frac{2}{C_n (\xi + 2x_0)} (1 + e^{-(L-2x_0)/\xi} + \delta_{0n} e^{x_0/\xi}) \quad (G.7) \end{aligned}$$

For the case with mirror, equation (G.7) becomes

$$G_0 C \int_0^L e^{-x/\xi} e^{-|x-x_0|/\xi} dx = e^{-L/\xi} + \delta_{0m} .$$

Similarly, it could be simplified to be

$$G_{0mt} \sim \frac{2}{C_m \xi} (e^{-L/\xi} + \delta_{0m}) \quad (G.8)$$

When $x_0=0$, it reduces to

$$G_0 C [x_0 e^{-x_0/\xi} + \frac{\xi}{2} e^{-x_0/\xi}] = e^{-L/\xi} + \delta_{0m}$$

When δ_{0m} and δ_{0n} equal zero, x_0 to be $L/2$ and $L \gg \xi$, therefore referring to equation (G.7) and (G.8), as (G.7) is divided by (G.8),

$$\frac{G_{0mt}}{G_{0nt}} \sim \frac{\frac{2}{C_m \xi} (e^{-L/\xi} + \delta_{0m})}{\frac{2}{C_n (\xi + 2x_0)} (1 + e^{-(L-2x_0)/\xi} + \delta_{0n} e^{x_0/\xi})}$$

Finally,

$$\frac{G_{0mt}}{G_{0nt}} \sim \frac{L}{\xi} e^{-L/\xi} \quad (G.9)$$

where all constant are then omitted.

APPENDIX H Electroluminescence Measurement

H.1 Optical Setup

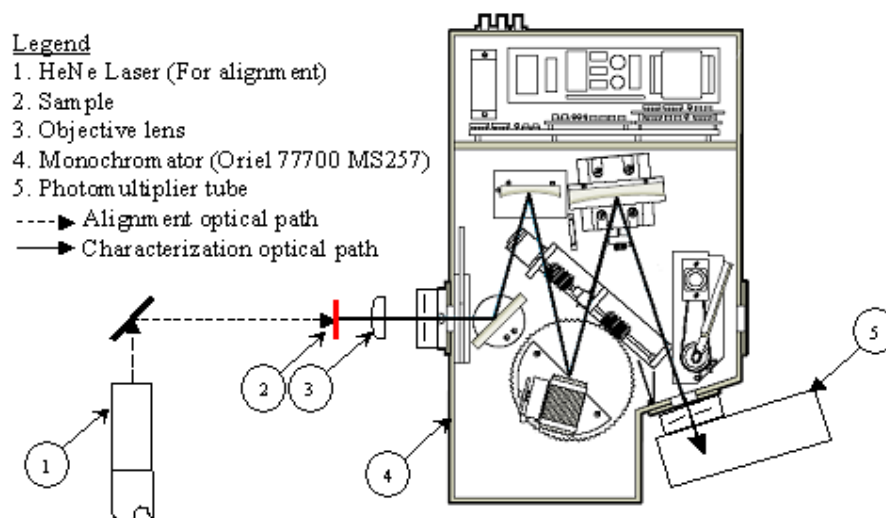


Figure H.1 Optical setup for the electroluminescence measurement.

The optical equipment for the electroluminescence measurement was set up, as shown in Figure H.1. The monochromator (Oriel 77700 MS257), the He:Ne laser and the mirror were adjusted to the same height with respect to the optical table and secured. In the alignment of optics, a built-in transimpedance amplifier silicon detector (Oriel 70336) was fixed at the output slit assembly of the monochromator, instead of the photomultiplier tube (PMT) (Oriel 77348). The same alignment procedures were carried out as described in APPENDIX B.

In the electroluminescence measurement, a sample was placed at the position indicated by the thick red line in Figure H.1. The sample was biased using a setup described in section H.4. In this measurement process, the silicon detector used for

alignment was removed and the PMT was mounted at the output assembly of the monochromator.

H.2 Equipment Communication

Three lock-in amplifiers (SR510, EG&G 7260 and Merlin 70100) and the monochromator (Oriel 77700 MS257) were connected to a general-purpose instrument bus (GPIB) card (PCI-GPIB) installed in a computer. They were controlled and configured through the IEEE-488 port. The interrupt request (IRQ) setting used was 9 and the memory ranges were from D6800000-D68007FF and D6000000-D6003FFF. The GPIB address of the SR510, the EG&G lock-in amplifier, the Merlin and the monochromator were 23, 12, 2 and 6, respectively. For the monochromator, it also occupied 1 bus address below the primary that was 5.

H.3 Entire layout

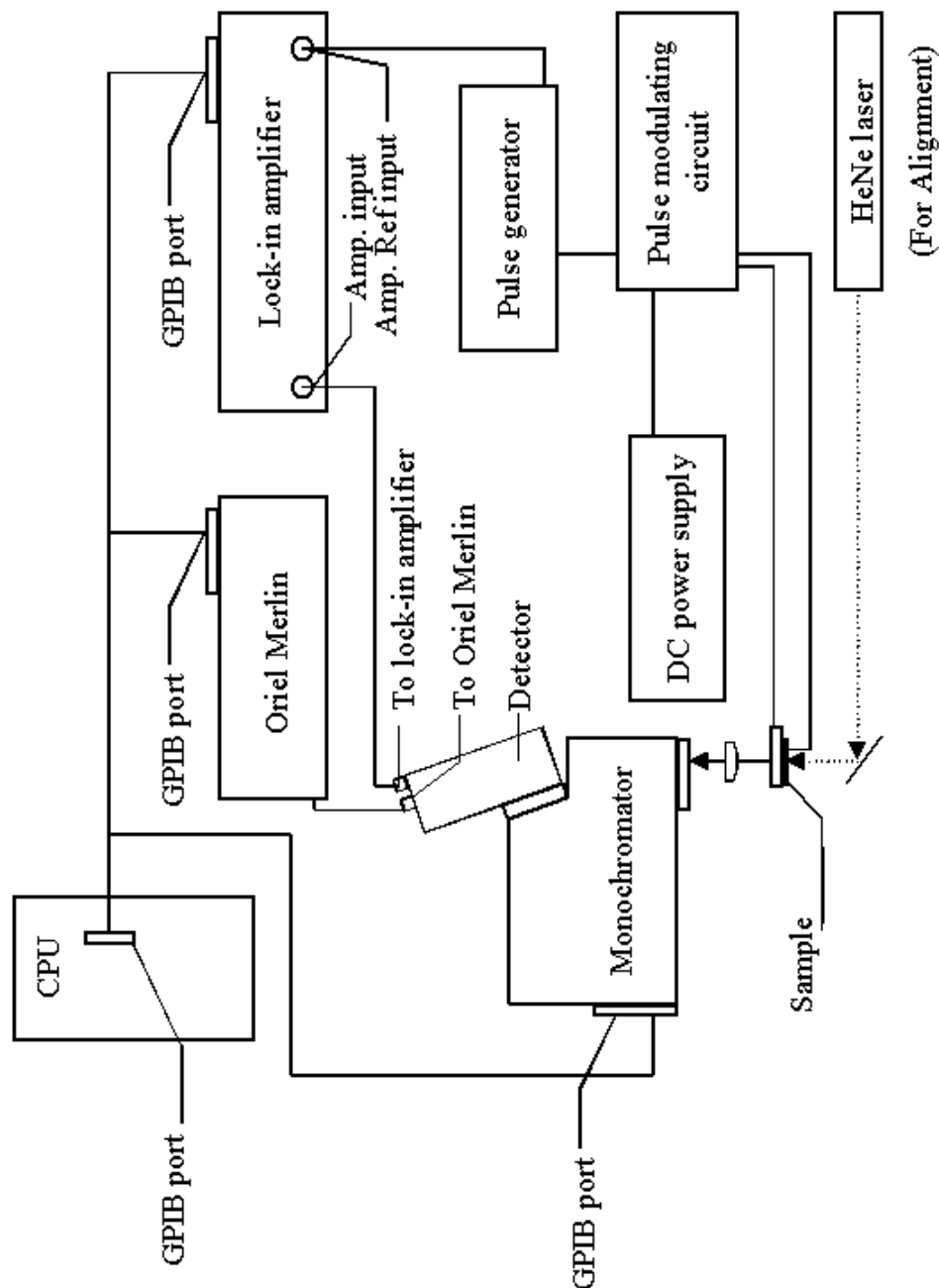


Figure H.2 Entire layout of the electroluminescence system.

The entire electroluminescence system was setup as shown in Figure H.2. The GPiB port of a central processing unit (CPU) was connected to: 1) a

monochromator (Oriel MS257), 2) an Oriel Merlin, and 3) a lock-in amplifier (SR510 or EG&G 7260). First, at the output assemble of the monochromator, it was connected to either a silicon detector or a PMT. The silicon detector or the PMT was connected to the Oriel Merlin or the amplifying input of the lock-in amplifier. Next, the reference input of the lock-in amplifier was connected to 50 Ω output of a pulse generator (Newtronics Model 200M STPC). The pulse generator was linked to a pulse modulating circuit, discussed in the next section, was powered by a DC power supply (Lodestar 6109).

H.4 Pulse Modulating Circuit

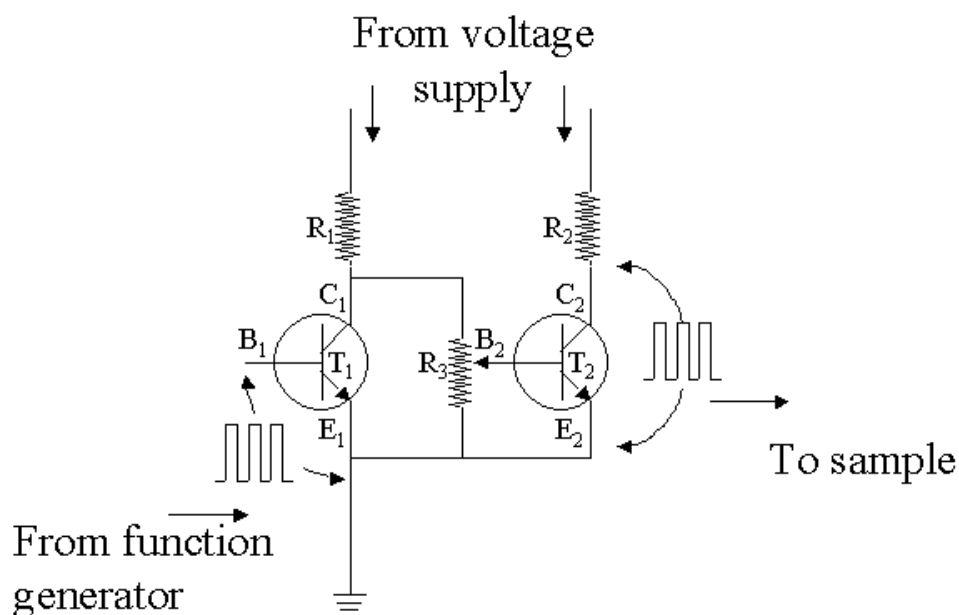


Figure H.3 Circuit diagram for the pulse modulating circuit.

A pulse source was used to bias the sample. It was needed to prolong the lifetime of the sample and to reduce the noise level of the signal with the lock-in technique. Hence, a pulse modulating circuit as illustrated in Figure H.3, was connected to

bias the sample. A pulse from a function generator biased the base and the emitter of the transistor (T_1). When there was a voltage difference (greater than the turn-on voltage of T_1) between B_1 and E_1 , T_1 was on. The collector (C_1) was shorted to E_1 and had a zero potential. On the contrary, C_1 was not shorted or grounded to E_1 when voltage difference across B_1 and E_1 was at zero. C_1 was at a voltage above zero potential since it was linked to the DC power supply through a resistor (R_1). Moreover, there was another transistor (T_2) in this circuit. The B_2 and E_2 of T_2 were connected to a 10 k Ω variable resistor that was connected across C_1 and E_1 . The emitter and base of T_2 was not directly connected to C_1 and E_1 of T_1 , so that the high voltage from the DC power supply did not exceed the rating of the emitter-base voltage of T_2 . Considering the entire modulating circuit, when voltage potential between B_1 and E_1 was high, the voltage potential between C_1 and E_1 was zero. This then caused the voltage potential between C_2 and E_2 to be high. Thus, the amplitude of the voltage waveform between C_2 and E_2 was modulated by the DC power supply, while the frequency and width of its pulse was approximated to be in synchronization with the pulse generated from the function generator.

Figure H.4 on the next page gives the entire setup of the pulse controlling circuit. For the pulse modulating circuit, it had two outputs. They were the ground and pulse output. The pulse output was connected to the ohmic contact on p -doped layer of the sample. On the other hand, the ohmic contact on n -doped layer was in contact with the Al:ZnO (7%) layer deposited on a piece of quartz. Besides, on the same piece of quartz, there was a nickel contact and it was connected to the ground of the pulse modulating circuit. With the positive and the negative output of a DC supply connected to the power supply and ground input of the pulse modulating

Appendix H

circuit, respectively, the pulse modulating circuit was powered up by the DC supply (Lodestar 6109). It was also noted that the negative and ground output of the DC supply were shorted together. Next, the anode and the cathode, of a coaxial cable with a Bayonet Neill-Concelman (BNC) connector, were linked to the pulse generator pulse output (Newtronics Model 200M STPC), were connected to the pulse input and ground of the pulse modulating circuit, respectively. Concurrently, the $50\ \Omega$ output of the pulse generator was connected to the lock-in amplifier through a coaxial cable.

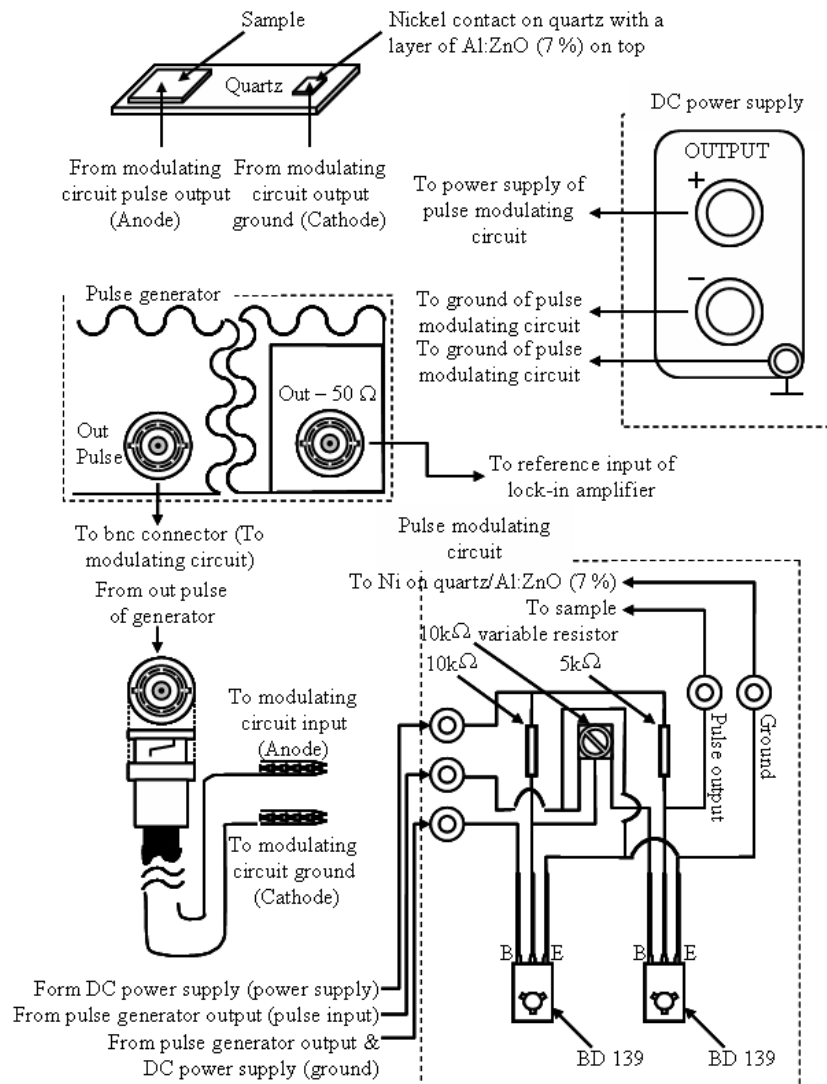
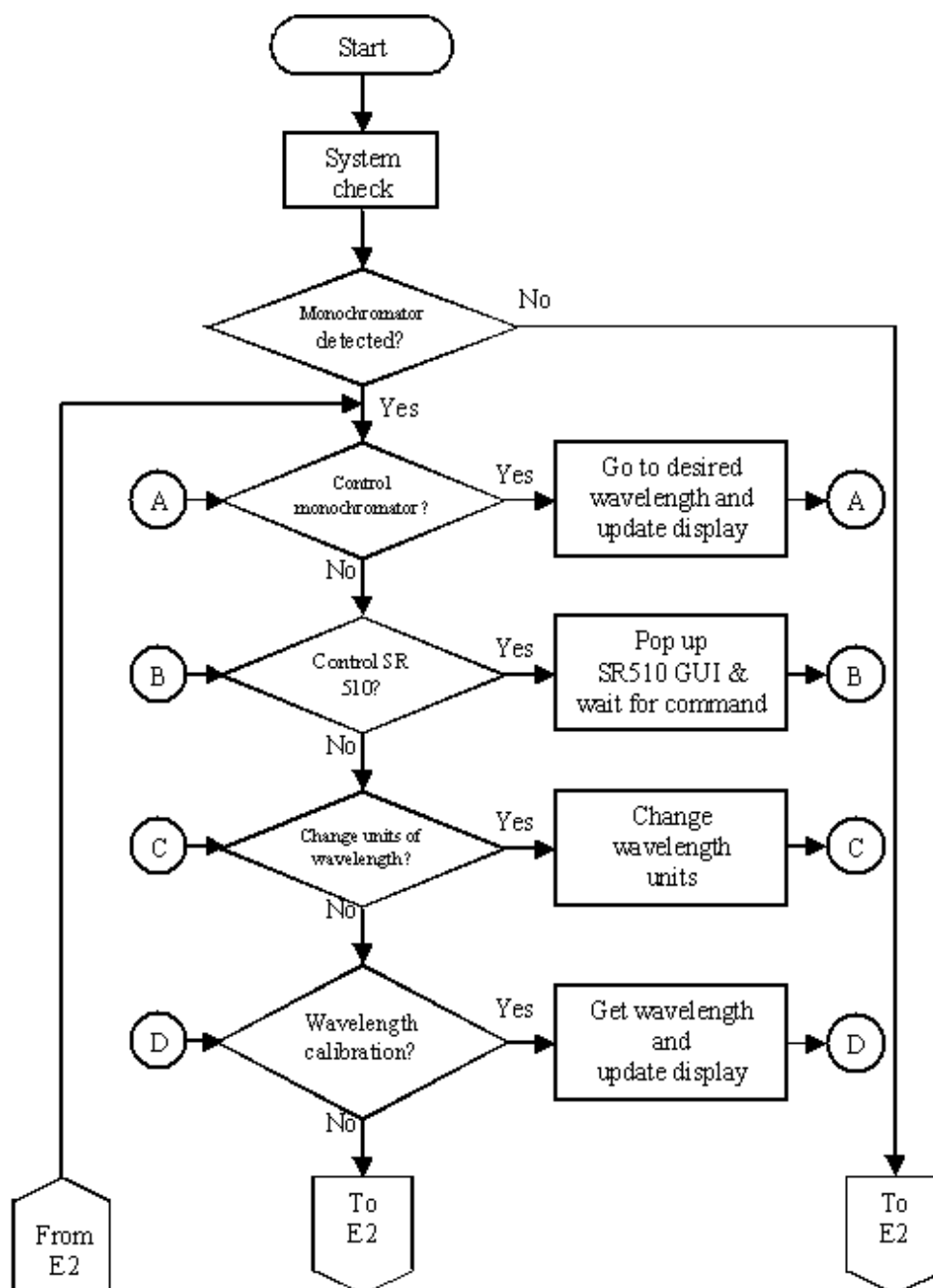
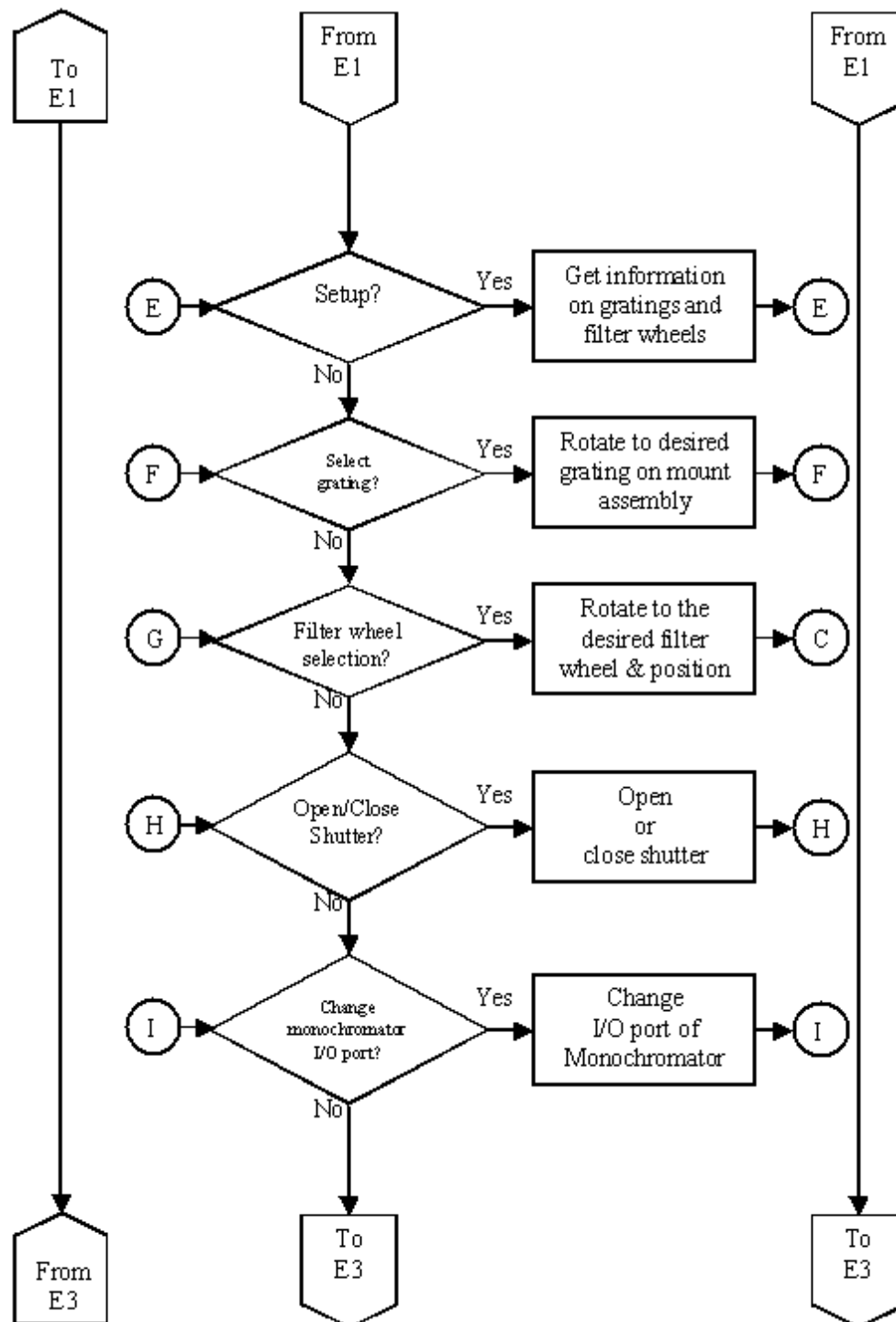


Figure H.4 Entire connection of the pulse controlling circuit.

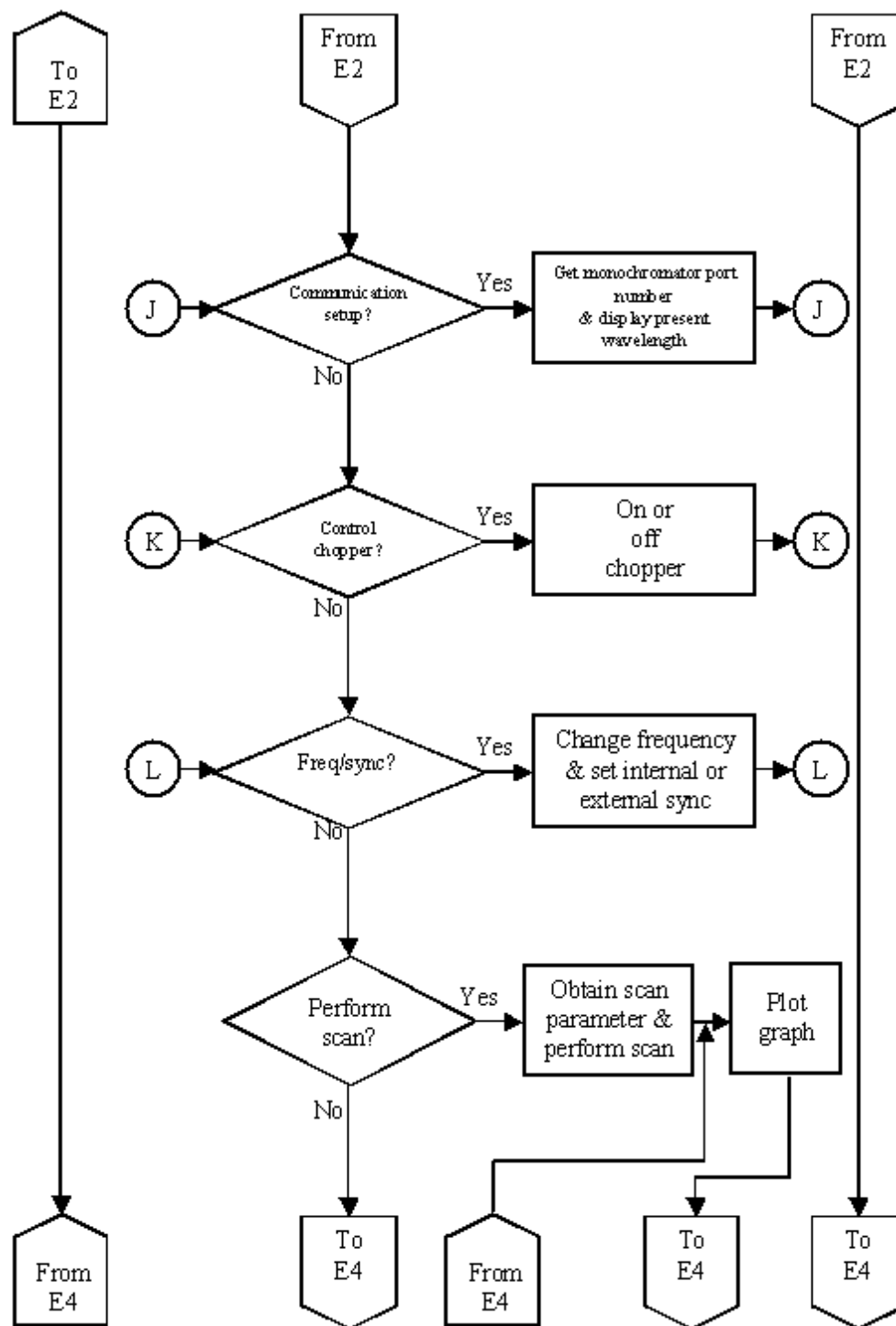
H.5 Software Program



Appendix H



Appendix H



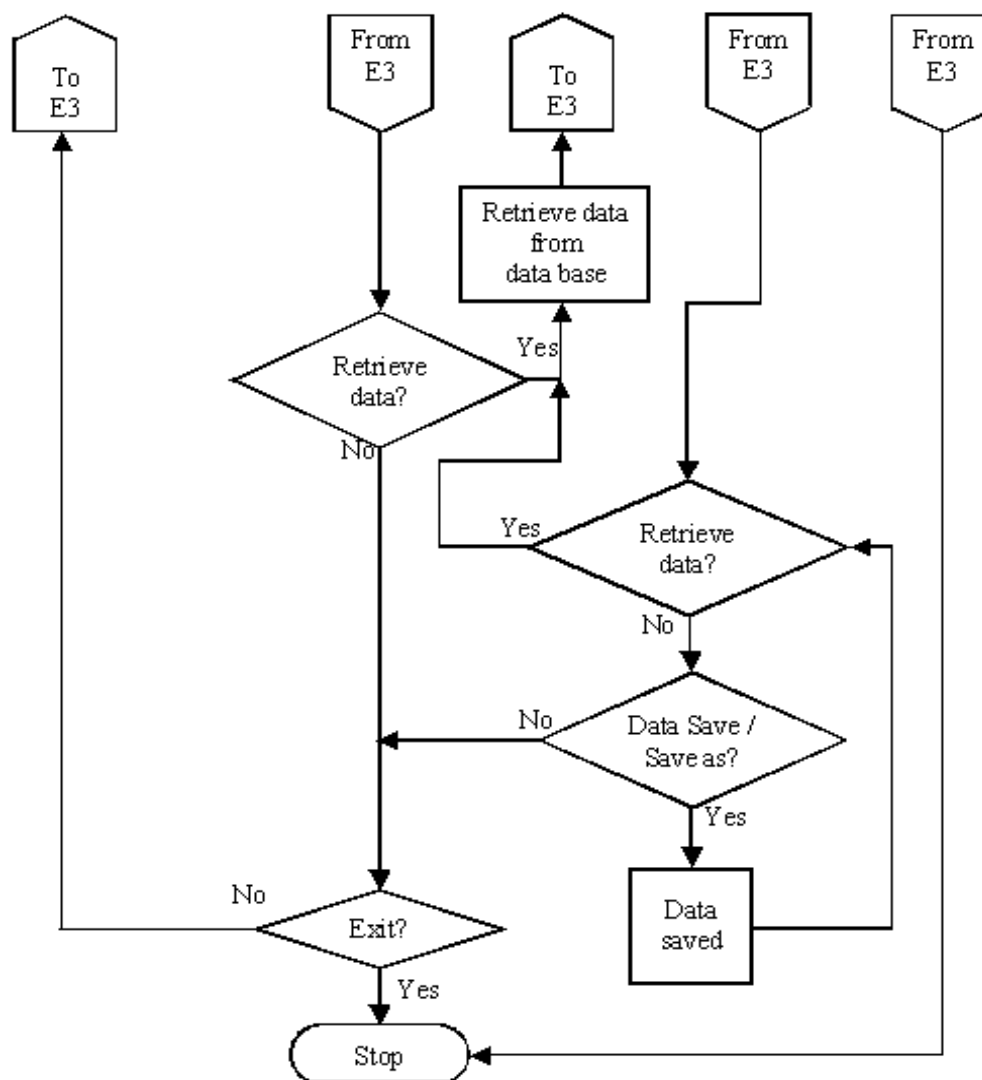
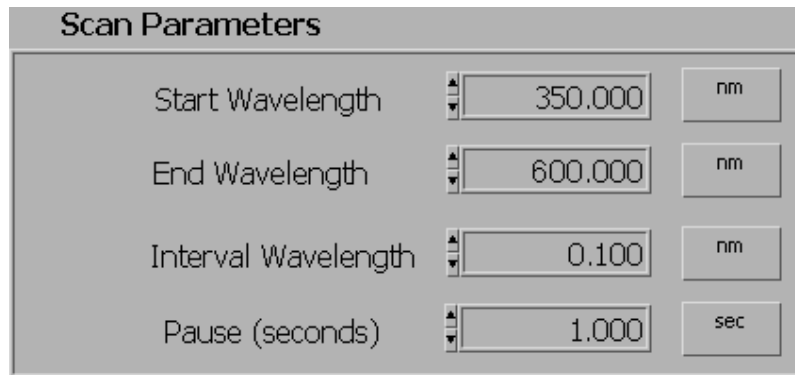


Figure H.5 Flow chart of the electroluminescence software program.

A software program, with flow chart shown in Figure H.5, was used to determine the electroluminescence of our devices. A connection test for the monochromator was carried out at the beginning of the software program in the electroluminescence measurement. The entire program would stop, if the monochromator were not detected. After that the Merlin, the SR510 or the EG&G 7260 was selected for data collection. Then the software was ready, with the options to: 1) control the monochromator, 2) control the lock-in amplifier, 3)

change the units for wavelength, 4) calibrate the monochromator, 5) perform a setup checking, 6) change the grating on rotating grating mount, 7) select the filter to be used, 8) open or close the shutter, 9) change the monochromator I/O port, 10) perform a communication check with the monochromator, 11) turn on or off the chopper for the Merlin, 12) select the frequency and type of synchronization of the Merlin, 13) retrieve and plot data in a graphical format, and 14) carry out a scan.



The image shows a software window titled "Scan Parameters". It contains four rows of input fields, each with a label, a numeric input box, and a unit button. The first row is "Start Wavelength" with the value "350.000" and a "nm" button. The second row is "End Wavelength" with the value "600.000" and a "nm" button. The third row is "Interval Wavelength" with the value "0.100" and a "nm" button. The fourth row is "Pause (seconds)" with the value "1.000" and a "sec" button. Each input box has small up and down arrow buttons on its left side.

Scan Parameters		
Start Wavelength	350.000	nm
End Wavelength	600.000	nm
Interval Wavelength	0.100	nm
Pause (seconds)	1.000	sec

Figure H.6 Entries for scan parameters.

On the GUI for the scan parameters entries in Figure H.6, the start and the end wavelengths of the scan parameters were specified to be 350 and 600 nm. It meant that the scan started at 350 nm and stopped at 600 nm. The interval wavelength was set to 0.1 nm such that the readings recorded were at a 0.1 nm wavelength interval. Besides that, there was an 1 s pause after the increment of 0.1 nm in wavelength between each successive reading, as shown by the pause field in the GUI. Subsequently, the red “Go Scan”-button was clicked and a scan started. After the scan completed, the save spec option in the file menu of the spectrum interface was clicked to save the data. Follow that, the DC voltage supply of pulse source was adjusted to a new value and the procedures described were repeated to obtain another spectrum under a different biasing condition.

Figure I.1 (a) and (b), on the previous page, shows the electrical and schematic diagram of the setup in the current-voltage and light-voltage measurement. The optical setup and the alignment of optics in the electroluminescence (EL) measurement also applied to this experiment. However, a multimeter (Keithley 2000) was connected in series with the heterojunction light-emitting diode (LED), as shown in Figure I.1 (a). Besides, an oscilloscope (Kikusui COS 6100) was connected to the points C_2 and E_2 , in parallel with the branch that comprised of the LED and the multimeter. In Figure I.1 (b), the LO input and the ground output of the multimeter were connected to the nickel contact on the Al:ZnO (7%)/Quartz and the ground of the pulse modulating circuit, respectively. It was also noted that the multimeter was connected to a computer through the general-purpose interface bus (GPIB) and the GPIB address was 1.

I.2 Software Program

Figure I.2 shows the flow chart of a software program used in the current-voltage and light-voltage measurement. This program was loaded after the equipment was setup and connected as stated in Figure I.1. Emission intensity and current reading were obtained from the lock-in amplifier and the multimeter, respectively, and plotted onto a graph. With biasing voltage noted from the oscilloscope, the DC power supply was then increased with a 0.2 V-step interval, as the indicating light on the graphical user interface (GUI) lighted up. These procedures were repeated from 0 to 9 V before the stop button on the GUI was clicked to stop the program. Finally, all the data were recorded into a text file.

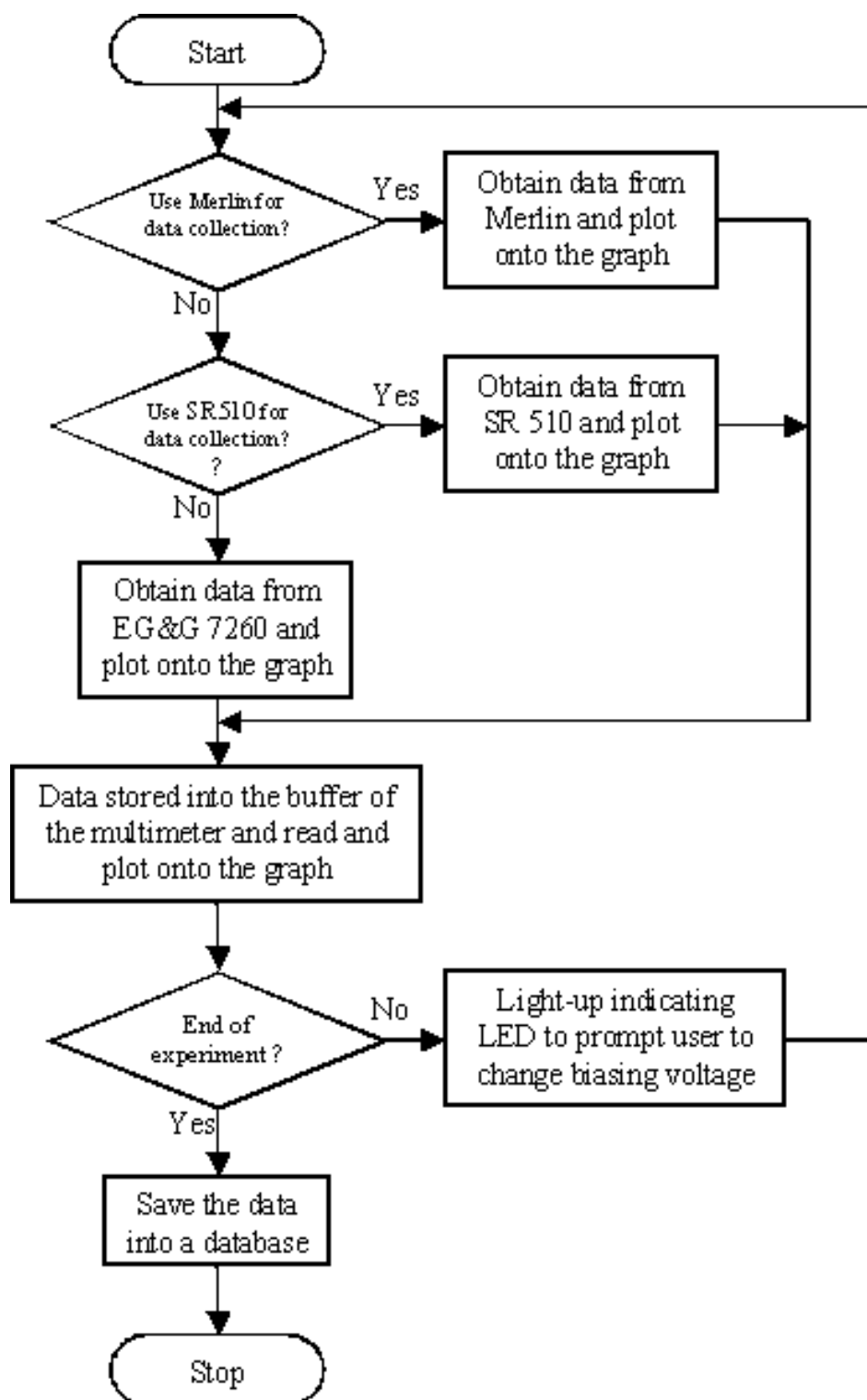


Figure I.2 Flow chart of the software program used in the current-voltage and light-voltage measurement.

APPENDIX J Ideality Factor in the Diode Equation

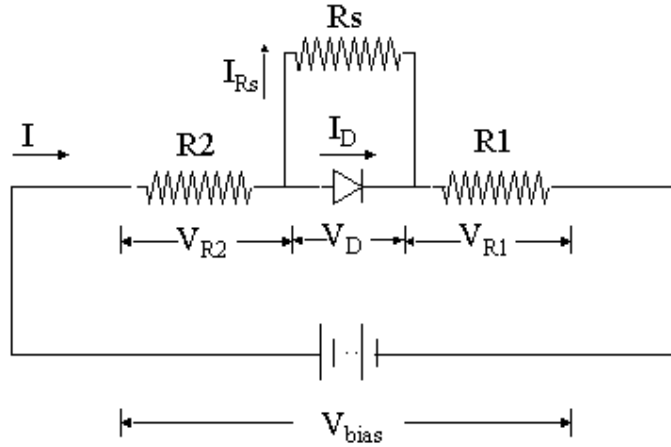


Figure J.1 Equivalent circuit of the heterojunction light-emitting diode (LED).

The heterojunction LED can be modeled by the equivalent circuit as shown in Figure J.1. If V_{bias} and I are the biasing voltage and current delivered by the power supply, respectively, then it can be shown from Kirchhoff's voltage law that,

$$V_{bias} = IR + V_D, \quad (J.1)$$

where V_D is the voltage drop across the diode and R is the summation of series resistances ($R1$, $R2$) that are mainly contributed by the contact of the n - and p -type material of the heterojunction. When R is taken to be 1550Ω , a data set of V_D could be obtained. Besides, I is related to the current that flows through the diode (I_D) and the shunt resistance (I_{Rs}) by the Kirchhoff's current law,

$$I = I_D + I_{Rs}. \quad (J.2)$$

In equation (J.2), I_D is given by the diode equation,

$$I_D = I_0 \left[e^{(qV_D/\eta kT)} - 1 \right], \quad (J.3)$$

where I_o and η are the saturation current and the ideality factor of the diode, respectively, q is the electron charge, k is the Boltzman constant and T is the temperature in Kelvin. On the other hand, I_{Rs} in equation (J.2) is given by,

$$I_{Rs} = V_D / R_s, \quad (J.4)$$

where R_s is the shunt resistance and arises due to the inadequate edge isolation during the deposition process. Based on (J.3) and (J.4), equation (J.2) becomes,

$$I = I_o \left[e^{(qV_D / \eta kT)} - 1 \right] + \frac{V_D}{R_s}. \quad (J.5)$$

As a result, by plotting I_D vs V_D (•), using the theoretical values based on equation (J.5), with $I_o \approx 1 \times 10^{-14}$ A, $R_s \approx 5 \times 10^4 \Omega$ and $\eta \approx 6$, it is found that the theoretical values (•) conform to the measured experimental data (■) as shown in Figure J.2, within 5% tolerance.

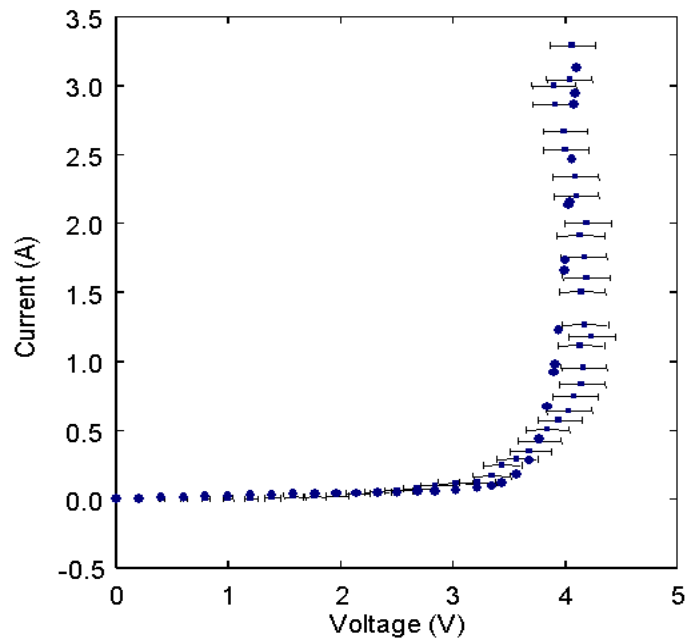


Figure J.2 I_D vs V_D curve plotted using measured experimental data (■) and theoretical values (•) based on equation (J.5).

REFERENCES

- [1] R. F. Service, "Will UV lasers beat the blues", *Science* **276**, 895-895 (1997).
- [2] J. V. Goodpaster, and V. L. McGuffin, "Fluorescence quenching as an indirect detection method for nitrated explosives", *Anal. Chem.* **73**, 2004-2011 (2001).
- [3] Y. Nishimura, A. Y. Hirakawa, M. Tsuboi, and S. Nishimura, "Raman spectra of transfer RNAs with ultraviolet lasers", *Nature* **260**, 173-174 (1976).
- [4] W. L. Barnes, and P. Andrew, "Quantum optics: Energy transfer under control", *Nature* **400**, 505-506 (1999).
- [5] J. Chappell, and K. Hahlbrock, "Transcription of plant defence genes in response to UV light or fungal elicitor", *Nature* **311**, 76-78 (1984).
- [6] V. S. Letokhov, "Laser biology and medicine", *Nature* **316**, 325-330 (1985).
- [7] I. M. Stender, R. Na, H. Fogh, C. Gluud, and H. C. Wulf, "Photodynamic therapy with 5-aminolaevulinic acid or placebo for recalcitrant foot and hand warts: randomised double-blind trial", *The Lancet* **355**, 963-966 (2000).
- [8] P. P. Lee, C. Yee, P. A. Savage, L. Fong, D. Brockstedt, J. S. Weber, D. Johnson, S. Swetter, J. Thompson, P. D. Greenberg, M. Roederer, and M. M. Davis, "Characterization of circulating T cells specific for tumor-associated antigens in melanoma patients", *Nature Medicine* **5**, 677-685 (1999).
- [9] A. Rosén, and G. Klein, "UV light-induced immunoglobulin heavy-chain class switch in a human lymphoblastoid cell line", *Nature* **306**, 189-190 (1983).
- [10] F. Bourre, and A. Sarasin, "Targeted mutagenesis of SV40 DNA induced by UV light", *Nature* **305**, 68-70 (1983).
- [11] S. Koizumi, K. Watanabe, M. Hasegawa, and H. Kanda, "Ultraviolet emission from a diamond pn junction", *Science* **292**, 1899-1901 (2001).
- [12] J. V. D. Lagemaat, M. Plakman, D. Vanmaekelbergh, and J. J. Kelly, "Enhancement of the light-to-current conversion efficiency in an *n*-SiC/solution diode by porous etching", *Appl. Phys. Lett.* **69**, 2246-2248 (1996).
- [13] V. L. Solozhenko, A. G. Lazarenko, J. P. Petitet, and A. V. Kanaev, "Bandgap energy of graphite-like hexagonal boron nitride", *J. Phys. Chem. Solid* **62**, 1331-1334 (2001).
- [14] J. Johnson, H. J. Choi, K. P. Knutsen, R. D. Schaller, P. Yang, and R. J. Saykally, "Single gallium nitride nanowire lasers", *Nature Materials* **1**, 106-110 (2002).
- [15] M. H. Huang, S. Mao, H. Feick, H. Yan, Y. Wu, H. Kind, E. Weber, R. Russo, and P. Yang, "Room-temperature ultraviolet nanowire nanolasers", *Science* **292**, 1897-1899 (2001).
- [16] Y. Z. Yoo, T. Chikyow, P. Ahmet, M. Kawasaki, T. Makino, Y. Segawa, and H. Koinuma, "High-temperature epitaxy of metastable sulfide on oxide substrates using stoichiometric transportation", *Adv. Mater.* **13**, 1624-1627 (2001).
- [17] M. A. Hines, P. G. Sionnest, "Bright UV-blue luminescent colloidal ZnSe nanocrystals", *J. Phys. Chem. B* **102**, 3655-3657 (1998).
- [18] C. E. Nebel, "Semiconductor materials: From gemstone to semiconductor", *Nature Materials* **2**, 431-432 (2003).
- [19] Z. K. Tang, G. K. L. Wong, P. Yu, M. Kawasaki, A. Ohtomo, H. Koinuma, and Y. Segawa, "Room-temperature ultraviolet laser emission from self-assembled ZnO microcrystallite thin films", *Appl. Phys. Lett.* **72**, 3270-3272 (1998).
- [20] D. M. Bagnall, Y. F. Chen, Z. Zhu, T. Yao, S. Koyama, M. Y. Shen, and T. Goto, "Optically pumped lasing of ZnO at room temperature", *Appl. Phys. Lett.* **70**, 2230-2232 (1997).
- [21] Y. Kashiwaba, K. Haga, H. Watanabe, B. P. Zhang, Y. Segawa, and K. Wakatsuki, "Structures and photoluminescence properties of ZnO films epitaxially grown by atmospheric pressure MOCVD", *Phys. Status Solidi B* **229**, 921-924 (2002).
- [22] Y. Chen, D. M. Bagnall, H. J. Koh, K. T. Park, K. Hiraga, Z. Q. Zhu, and T. Yao, "Plasma assisted molecular beam epitaxy of ZnO on c-plane sapphire: Growth and characterization", *J. Appl. Phys.* **84**, 3912-3918 (1998).
- [23] Y. G. Wang, S. P. Lau, H. W. Lee, S. F. Yu, B. K. Tay, X. H. Zhang, K. Y. Tse and H. H. Hng, "Comprehensive study of ZnO films prepared by filtered cathodic vacuum arc at room temperature", *J. Appl. Phys.* **94**, 1597-1604, (2003).
- [24] H. W. Lee, S. P. Lau, Y. G. Wang, B. K. Tay, and H. H. Hng, "Internal stress and surface morphology of zinc oxide thin films deposited by filtered cathodic vacuum arc technique", *Thin Solid Films* **458**, 15-19 (2004).

References

-
- [25] K. Y. Tse, H. H. Hng, S. P. Lau, Y. G. Wang, and S. F. Yu, "ZnO thin films produced by filtered cathodic vacuum arc technique", *Ceram. Int.* **30**, 1669-1674 (2004).
- [26] X. L. Xu, S. P. Lau, and B. K. Tay, "Structural and optical properties of ZnO thin films produced by filtered cathodic vacuum arc", *Thin Solid Films* **398**, 244-249 (2001).
- [27] Y. Chen, N. T. Tuan, Y. Segawa, H. J. Ko, S. K. Hong, and T. Yao, "Stimulated emission and optical gain in ZnO epilayers grown by plasma-assisted molecular-beam epitaxy with buffers", *Appl. Phys. Lett.* **78**, 1469-1471 (2001).
- [28] A. Yamamoto, T. Kido, T. Goto, Y. F. Chen, T. Yao, and A. Kasuya "Dynamics of photoexcited carriers in ZnO epitaxial thin films", *Appl. Phys. Lett.* **75**, 469-471 (1999).
- [29] T. Shiosaki, S. Ohnishi, Y. Hirokawa, and A. Kawabata, "As-grown CVD ZnO optical waveguides on sapphire", *Appl. Phys. Lett.* **33**, 406-407 (1978).
- [30] J. M. Hammer, D. J. Channin, M. T. Duffy, and J. P. Wittke, "Low-loss epitaxial ZnO optical waveguides", *Appl. Phys. Lett.* **21**, 358-360 (1972).
- [31] H. Cao, Y. G. Zhao, H. C. Ong, S. T. Ho, J. Y. Dai, J. Y. Wu, and R. P. H. Chang, "Ultraviolet lasing in resonators formed by scattering in semiconductor polycrystalline films", *Appl. Phys. Lett.* **73**, 3656-3658 (1998).
- [32] H. Cao, Y. Zhao, S. T. Ho, E. W. Seelig, Q. H. Wang, and R. P. H. Chang, "Random laser action in semiconductor powder", *Phys. Rev. Lett.* **82**, 2278-2281 (1999).
- [33] H. Cao, Y. G. Zhao, H. C. Ong, and R. P. H. Chang, "Far-field characteristics of random lasers", *Phys. Rev. B* **59**, 015107 (1999).
- [34] H. Cao, "Random lasers with coherent feedback", in optical properties of nanostructured random media, eds. V. M. Shalaev, Springer-Verlag, 2002.
- [35] J. M. Bian, X. M. Li, C. Y. Zhang, L. D. Chen, and Q. Yao, "Synthesis and characterization of two-layer-structured ZnO p-n homojunctions by ultrasonic spray pyrolysis", *Appl. Phys. Lett.* **84**, 3783-3785 (2004).
- [36] B. Ismail, M. Abaab, and B. Rezig, "Structural and electrical properties of ZnO films prepared by screen printing technique", *Thin Solid Films* **383**, 92-94 (2001).
- [37] S. K. Kim, S. A. Kim, C. H. Lee, H. J. Lee, S. Y. Jeong, and C. R. Cho, "The structural and optical behaviors of K-doped ZnO/Al₂O₃ (0001) films", *Appl. Phys. Lett.* **85**, 419-421 (2004).
- [38] Y. Z. Yoo, Y. Osaka, T. Fukumura, Z. Jin, M. Kawasaki, H. Koinuma, T. Chikyow, P. Ahmet, A. Setoguchi, and S. F. Chichibu, "High temperature growth of ZnS films on bare Si and transformation of ZnS to ZnO by thermal oxidation", *Appl. Phys. Lett.* **78**, 616-618 (2001).
- [39] B. X. Lin, Z. X. Fu, and Y. B. Jia, "Green luminescent center in undoped zinc oxide films deposited on silicon substrates", *Appl. Phys. Lett.* **79**, 943-945 (2001).
- [40] A. Hachigo, H. Nakahata, K. Higaki, S. Fujii, and S. Shikata, "Heteroepitaxial growth of ZnO films on diamond (111) plane by magnetron sputtering", *Appl. Phys. Lett.* **65**, 2556-2558 (1994).
- [41] B. N. Mukashev, S. Z. Tokmoldin, N. B. Beisenkhanov, S. M. Kikkarin, I. V. Valitova, V. B. Glazman, A. B. Aimagambetov, E. A. Dmitrieva, and B. M. Veremenithev, "Influence of structure changes of oxide films on their physical properties", *Mater. Sci. Eng. B* **118**, 164-169 (2005).
- [42] K. Iwata, T. Sakemi, A. Yamada, P. Fons, K. Awai, T. Yamamoto, M. Matsubara, H. Tampo, and S. Niki, "Growth and electrical properties of ZnO thin films deposited by novel ion plating method", *Thin Solid Films* **445**, 274-277 (2003).
- [43] S. Whangbo, H. Jang, S. Kim, M. Cho, K. Jeong, and C. Whang, "Properties of ZnO thin films grown at room temperature by using ionized cluster beam deposition", *J. Korean Phys. Soc.* **37**, 456-460 (2000).
- [44] B. S. Li, Y. C. Liu, Z. S. Chu, D. Z. Shen, Y. M. Lu, J. Y. Zhang, and X. W. Fan, "High quality ZnO thin films grown by plasma enhanced chemical vapor deposition", *J. Appl. Phys.* **91**, 501-505 (2002).
- [45] S. K. Ghandhi, R. J. Field, and J. R. Shealy, "Highly oriented zinc oxide films grown by the oxidation of diethylzinc", *Appl. Phys. Lett.* **37**, 449-451 (1980).
- [46] J. H. Hu, and R. G. Gordon, "Textured aluminum-doped Zinc-oxide thin-films from atmospheric-pressure chemical-vapor deposition", *J. Appl. Phys.* **71**, 880-890 (1992).
- [47] G. L. Mar, P. Y. Timbrell, and R. N. Lamb, "Factors influencing the chemical-vapor-deposition of oriented ZnO films using Zinc Acetate", *Chem. Mater.* **7**, 1890-1896 (1995).
- [48] J. B. Shim, N. Yoshimoto, and D. H. Yoon, "Surface and structure characteristics of ZnO co-doped LiNbO₃:Er thin films grown by liquid phase epitaxy method", *J. Cryst. Growth* **235**, 640-642 (2002).
-

References

-
- [49] E. M. Wong, and P. C. Searson, "ZnO quantum particle thin films fabricated by electrophoretic deposition", *Appl. Phys. Lett.* **74**, 2939-2941 (1999).
- [50] A. Borak, "Toward bridging the terahertz gap with silicon-based lasers", *Science* **308**, 638-639 (2005).
- [51] W. L. Ng, M. A. Lourenço, R. M. Gwilliam, S. Ledain, G. Shao, and K. P. Homewood, "An efficient room-temperature silicon-based light-emitting diode", *Nature* **410**, 192-194 (2001).
- [52] T. Shiozaki, T. Yamamoto, M. Yagi, and A. Kawabata, "Plasma-enhanced metalorganic chemical vapor deposition of c-axis oriented and epitaxial films of ZnO at low substrate temperatures", *Appl. Phys. Lett.* **39**, 399-401 (1981).
- [53] O. F. Z. Khan, and P. O'Brien, "On the use of zinc acetate as a novel precursor for the deposition of ZnO by low-pressure metal-organic chemical vapour deposition", *Thin Solid Films* **173**, 95-97 (1989).
- [54] B. Sang, A. Yamada, and M. Konagai, "Highly stable ZnO thin films by atomic layer deposition", *Jpn. J. Appl. Phys.* **37**, L1125-L1128 (1998).
- [55] R. Solanki, and G.J. Collins, "Laser induced deposition of zinc oxide", *Appl. Phys. Lett.* **42**, 662-663 (1983).
- [56] S. Oda, H. Tokunaga, N. Kitajima, J. I. Hanna, I. Shimuzu, and H. Kokado, "Highly oriented zinc oxide films prepared by MOCVD from diethylzinc and alcohols", *Jpn. J. Appl. Phys.* **24**, 1607-1610 (1985).
- [57] M. Yoshino, W.W. Wenas, A. Yamada, M. Konagai, and K. Takahashi, "Large-area ZnO thin films for solar cells prepared by photo-induced metalorganic chemical vapor deposition", *Jpn. J. Appl. Phys.* **32**, 726-730 (1993).
- [58] T. Maruyama, and A. Nakai, "Photo-assisted metalorganic chemical vapor deposition of zinc oxide films", *Jpn. J. Appl. Phys.* **28**, L346-L348 (1989).
- [59] F. T. J. Smith, "Metalorganic chemical vapor deposition of oriented ZnO films over large areas", *Appl. Phys. Lett.* **43**, 1108-1110 (1983).
- [60] W. I. Park, S. J. An, G. C. Yi, and H. M. Jang, "Metalorganic vapor phase epitaxial growth of high-quality ZnO films on Al₂O₃ (001)", *J. Mater. Res.* **16** 1358-1362 (2001).
- [61] T. Gruber, C. Kirchner, and A. Waag, "MOCVD growth of ZnO on different substrate materials", *Phys. Stat. Sol. B* **229**, 841-844 (2002).
- [62] J. F. Rommeluère, L. Svob, F. Jomard, J. M. Arroyo, A. Lusson, V. Sallet, and Y. Marfaing, "Electrical activity of nitrogen acceptors in ZnO films grown by metalorganic vapor phase epitaxy", *Appl. Phys. Lett.* **83**, 287-289 (2003).
- [63] X. Li, Y. Yan, T. A. Gessert, C. L. Perkins, D. Young, C. D. Hart, M. Young, and T. J. Coutts, "Chemical vapor deposition-formed p-type ZnO thin films", *J. Vac. Sci. Technol. A* **21**, 1342-1346 (2003).
- [64] X. Li, B. Keyes, S. Asher, S. B. Zhang, S. H. Wei, T. J. Coutts, S. Limpijumnong, and N. Ratchasima, and C. G. V. D. Walle, "Hydrogen passivation effect in nitrogen-doped ZnO thin films", *Appl. Phys. Lett.* **86**, 122107 (2005).
- [65] X. Li, Y. Yan, T. A. Gessert, C. D. Hart, C. L. Perkins, D. Young, and T. J. Coutts, "p-Type ZnO thin films formed by CVD reaction of diethylzinc and NO gas", *Electrochem. Solid St.* **6**, C56-C58 (2003).
- [66] J. Z. Wang, G. T. Du, B. J. Zhao, X. T. Yang, Y. T. Zhang, Y. Ma, D. L. Liu, Y. C. Chang, H. S. Wang, H. J. Yang, and S. R. Yang, "Epitaxial growth of NH₃-doped ZnO thin films on <0 2 2̄ 4> oriented sapphire substrates", *J. Cryst. Growth* **255**, 293-297 (2003).
- [67] F. G. Chen, Z. Z. Ye, W. Z. Xu, B. H. Zhao, L. P. Zhu, and J. G. Lv, "Fabrication of p-type ZnO thin films via MOCVD method by using phosphorus as dopant source", *J. Cryst. Growth* **281**, 458-462 (2005).
- [68] S. Y. Myong, S. J. Baik, C. H. Lee, W. Y. Cho, and K. S. Lim, "Extremely transparent and conductive ZnO:Al thin films prepared by photo-assisted metalorganic chemical vapor deposition (photo-MOCVD) using AlCl₃(6H₂O) as new doping material", *Jpn. J. Appl. Phys.* **36**, L1078-L1081 (1997).
- [69] J. D. Ye, S. L. Gu, S. M. Zhu, S. M. Liu, Y. D. Zheng, R. Zhang, and Y. Shi, "Fermi-level band filling and band-gap renormalization in Ga-doped ZnO", *Appl. Phys. Lett.* **86**, 192111 (2005).
- [70] Y. Li, G. S. Tompa, S. Liang, C. Gorla, Y. Lu, and J. Doyle, "Transparent and conductive Ga-doped ZnO films grown by low pressure metal organic chemical vapor deposition", *J. Vac. Sci. Technol. A* **15**, 1063-1068 (1997).

References

-
- [71] E. W. Forsythe, Y. L. Gao, L. G. Provost and G. S. Tompa, "Photoemission spectroscopy analysis of ZnO:Ga films for display applications", *J. Vac. Sci. Technol. A* **17**, 1761-1764 (1999).
- [72] W. W. Wenas, A. Yamada, M. Konagai, and K. Takahashi, "Textured ZnO thin films for solar cells grown by metalorganic chemical vapor deposition", *Jpn. J. Appl. Phys.* **30**, L441-L443 (1991).
- [73] Y. Zhang, G. Du, X. Wang, W. Li, X. Yang, Y. Ma, B. Zhao, H. Yang, D. Liu, and S. Yang, "X-ray photoelectron spectroscopy study of ZnO films grown by metal-organic chemical vapor deposition", *J. Cryst. Growth* **252**, 180-183 (2003).
- [74] B. P. Zhang, L. H. Manh, K. Wakatsuki, K. Tamura, T. Ohnishi, M. Lippmaa, N. Usami, M. Kawasaki, H. Koinuma, and Y. Segawa, "In-plane orientation and polarity of ZnO epitaxial films on as-polished sapphire (α -Al₂O₃) (0001) substrates grown by metal organic chemical vapor deposition", *Jpn. J. Appl. Phys.* **42**, L264-L266 (2003).
- [75] T. Gruber, C. Kirchner, K. Thonke, R. Sauer, and A. Waag, "MOCVD growth of ZnO for optoelectronic applications", *Phys. Stat. Sol. A* **192**, 166-170 (2002).
- [76] S. Liang, H. Sheng, Y. Liu, Z. Huo, Y. Lu, and H. Shen, "ZnO Schottky ultraviolet photodetectors", *J. Cryst. Growth* **225**, 110-113 (2001).
- [77] C. R. Gorla, N. W. Emanetoglu, S. Liang, W. E. Mayo, Y. Lu, M. Wraback, and H. Shen, "Structural, optical, and surface acoustic wave properties of epitaxial ZnO films grown on (01 $\bar{1}$ 2) sapphire by metalorganic chemical vapor deposition", *J. Appl. Phys.* **85**, 2595-2602 (1999).
- [78] M. Wraback, H. Shen, S. Liang, C. R. Gorla, and Y. Lu, "High contrast, ultrafast optically addressed ultraviolet light modulator based upon optical anisotropy in ZnO films grown on R-plane sapphire", *Appl. Phys. Lett.* **74**, 507-509 (1999).
- [79] H.W. Kim, K.S. Kim, and C. Lee, "Low temperature growth of ZnO thin film on Si(100) substrates by metal organic chemical vapor deposition", *J. Mater. Sci. Lett.* **22**, 1117-1118 (2003).
- [80] N. D. Kumar, M. N. Kamalasanan, and S. Chandra, "Metalorganic chemical vapor deposition technique for growing c-axis oriented ZnO thin films in atmospheric pressure air", *Appl. Phys. Lett.* **65**, 1373-1375 (1994).
- [81] J. Ye, S. Gu, S. Zhu, T. Chen, W. Liu, F. Qin, L. Hu, R. Zhang, Y. Shi, and Y. Zheng, "Raman and photoluminescence of ZnO films deposited on Si (111) using low-pressure metalorganic chemical vapor deposition", *J. Vac. Sci. Technol. A* **21**, 979-982 (2003).
- [82] I. Estermann, "Molecular beam technique", *Rev. Mod. Phys.* **18**, 300-323 (1946).
- [83] P. Fons, K. Iwata, S. Niki, A. Yamada, K. Matsubara, and M. Watanabe, "Uniaxial locked growth of high-quality epitaxial ZnO films on (11 $\bar{2}$ 0) α -Al₂O₃", *J. Cryst. Growth* **209**, 532-536 (2000).
- [84] H. B. Kang, K. Nakamura, S. H. Lim, and D. Shindo, "Epitaxial growth of ZnO films on (0001) sapphire at low temperatures by electron cyclotron resonance-assisted molecular beam epitaxy and their microstructural characterizations", *Jpn. J. Appl. Phys.* **37**, 781-785 (1998).
- [85] H. B. Kang, K. Nakamura, K. Yoshida, and K. Ishikawa, "Single crystalline ZnO films grown on (0001) Al₂O₃ substrate by electron cyclotron resonance-assisted molecular beam epitaxy technique", *Jpn. J. Appl. Phys.* **36**, L933-L935 (1997).
- [86] K. Sakurai, D. Iwata, S. Fujita, and S. Fujita, "Growth of ZnO by molecular beam epitaxy using NO₂ as oxygen source", *Jpn. J. Appl. Phys.* **38**, 2606-2608 (1999).
- [87] N. Izyumskaya, V. Avrutin, W. Schoch, W. A. E. Shaer, F. Reuss, T. Gruber, and A. Waag, "Molecular beam epitaxy of high-quality ZnO using hydrogen peroxide as an oxidant", *J. Cryst. Growth* **269**, 356-361 (2004).
- [88] K. Nakahara, T. Tanabe, H. Takasu, P. Fons, K. Iwata, A. Yamada, K. Matsubara, R. Hunger and S. Niki, "Growth of undoped ZnO films with improved electrical properties by radical source molecular beam epitaxy", *Jpn. J. Appl. Phys.* **40**, 250-254 (2001).
- [89] T. Ohgaki, N. Ohashi, H. Kakemoto, S. Wada, Y. Adachi, H. Haneda, and T. Tsurumi, "Growth condition dependence of morphology and electric properties of ZnO films on sapphire substrates prepared by molecular beam epitaxy", *J. Appl. Phys.* **93**, 1961-1965 (2003).
- [90] C. Morhain, M. Teisseire, S. Ve'zian, F. Vigue', F. Raymond, P. Lorenzini, J. Guion, G. Neu, and J. P. Faurie, "Spectroscopy of excitons, bound excitons and impurities in h-ZnO epilayers", *Phys. Stat. Sol. B* **229**, 881-885 (2002).
- [91] K. Nakahara, H. Takasu, P. Fons, A. Yamada, K. Iwata, K. Matsubara, R. Hunger, and S. Niki, "Interaction between gallium and nitrogen dopants in ZnO films grown by radical-source molecular-beam epitaxy", *Appl. Phys. Lett.* **79**, 4139-4141 (2001).
-

References

-
- [92] K. Nakahara, H. Takasu, P. Fons, A. Yamada, K. Iwata, K. Matsubara, R. Hunger, and S. Niki, "Growth of N-doped and Ga+N-codoped ZnO films by radical source molecular beam epitaxy", *J. Cryst. Growth* **237**, 503-508 (2002).
- [93] D. C. Look, D. C. Reynolds, C. W. Litton, R. L. Jones, D. B. Eason and G. Cantwell, "Characterization of homoepitaxial p-type ZnO grown by molecular beam epitaxy", *Appl. Phys. Lett.* **81**, 1830-1832 (2002).
- [94] A. B. M. A. Ashrafi, I. Suemune, H. Kumano, and S. Tanaka, "Nitrogen-doped p-type ZnO layers prepared with H₂O vapor-assisted metalorganic molecular-beam epitaxy", *Jpn. J. Appl. Phys.* **41**, L1281-L1284 (2002).
- [95] K. Iwata, P. Fons, A. Yamada, K. Matsubara, and S. Niki, "Nitrogen-induced defects in ZnO : N grown on sapphire substrate by gas source MBE", *J. Cryst. Growth* **209**, 526-531 (2000).
- [96] H. Kato, M. Sano, K. Miyamoto, and T. Yao, "Growth and characterization of Ga-doped ZnO layers on a-plane sapphire substrates grown by molecular beam epitaxy", *J. Cryst. Growth* **237**, 538-543 (2002).
- [97] H. J. Ko, Y. F. Chen, S. K. Hong, H. Wensch, T. Yao, and D. C. Look, "Ga-doped ZnO films grown on GaN templates by plasma-assisted molecular-beam epitaxy", *Appl. Phys. Lett.* **77**, 3761-3763 (2000).
- [98] T. Makino, K. Tamura, C. H. Chia, Y. Segawa, M. Kawasaki, A. Ohtomo, and H. Koinuma, "Optical properties of ZnO:Al epilayers: Observation of room-temperature many-body absorption-edge singularity", *Phys. Rev. B* **65**, 121201 (2002).
- [99] T. Makino, K. Tamura, C. H. Chia, Y. Segawa, M. Kawasaki, A. Ohtomo, and H. Koinuma, "Optical properties of ZnO:Al epilayers and of undoped epilayers capped by wider-gap MgZnO grown by laser MBE", *Phys. Stat. Sol. B* **229**, 853-857 (2002).
- [100] A. Ohtomo, K. Tamura, K. Saikusa, K. Takahashi, T. Makino, Y. Segawa, H. Koinuma, and M. Kawasaki, "Single crystalline ZnO films grown on lattice-matched ScAlMgO₄(0001) substrates", *Appl. Phys. Lett.* **75**, 2635-2637 (1999).
- [101] P. Fons, K. Iwata, A. Yamada, K. Matsubara, S. Niki, K. Nakahara, T. Tanabe, and H. Takasu, "Uniaxial locked epitaxy of ZnO on the a face of sapphire", *Appl. Phys. Lett.* **77**, 1801-1803 (2000).
- [102] Y. F. Chen, D. M. Bagnall, Z. Q. Zhu, T. Sekiuchi, K. T. Park, K. Hiraga, T. Yao, S. Koyama, M. Y. Shen, and T. Goto, "Growth of ZnO single crystal thin films on c-plane (0 0 0 1) sapphire by plasma enhanced molecular beam epitaxy", *J. Cryst. Growth* **181**, 165-169 (1997).
- [103] Y. Chen, H. J. Ko, S. K. Hong, and T. Yao, "Layer-by-layer growth of ZnO epilayer on Al₂O₃(0001) by using a MgO buffer layer" *Appl. Phys. Lett.* **76**, 559-561 (2000).
- [104] K. Miyamoto, M. Sano, H. Kato, and T. Yao, "Effects of ZnO/MgO double buffer layers on structural quality and electron mobility of ZnO epitaxial films grown on c-plane sapphire", *Jpn. J. Appl. Phys.* **41**, L1203-L1205 (2002).
- [105] H. J. Ko, Y. Chen, S. Hong, and T. Yao, "MBE growth of high-quality ZnO films on epi-GaN", *J. Cryst. Growth* **209**, 816-821 (2000).
- [106] M. Fujita, N. Kawamota, T. Tatsumi, K. Yamagishi, and Y. Horikoshi, "Molecular beam epitaxial growth of ZnO on Si substrate using ozone as an oxygen source", *Jpn. J. Appl. Phys.* **42**, 67-70 (2003).
- [107] N. Kawamoto, M. Fujita, T. Tatsumi, and Y. Horikoshi, "Growth of ZnO on Si substrate by plasma-assisted molecular beam epitaxy", *Jpn. J. Appl. Phys.* **42**, 7209-7212 (2003).
- [108] Y. Manabe, and T. Mitsuyu, "ZnO thin films prepared by the electron-cyclotron-resonance plasma sputtering method", *Jpn. J. Appl. Phys.* **29**, 334-339 (1990).
- [109] M. Kadota, T. Kasanami, and M. Minakata, "Piezoelectric characteristics of ZnO films deposited using an electron-cyclotron resonance sputtering system", *Jpn. J. Appl. Phys.* **31**, 3013-3016 (1992).
- [110] T. Tsurumi, S. Nishizawa, N. Ohashi, and T. Ohgaki, "Electric properties of zinc oxide epitaxial films grown by ion-beam sputtering with oxygen-radical irradiation", *Jpn. J. Appl. Phys.* **38**, 3682-3688 (1999).
- [111] F. Quaranta, A. Valentini, F. R. Rizzi, and G. Casamassina, "Dual-ion-beam sputter deposition of ZnO films", *J. Appl. Phys.* **74**, 244-248 (1993).
- [112] K. Yamaya, Y. Yamaki, H. Nakanishi, and S. Chichibu, "Use of a helicon-wave excited plasma for aluminum-doped ZnO thin-film sputtering", *Appl. Phys. Lett.* **72**, 235-237 (1998).
- [113] P. Sharma, A. Mansingh, and K. Sreenivas, "Ultraviolet photoresponse of porous ZnO thin films prepared by unbalanced magnetron sputtering", *Appl. Phys. Lett.* **80**, 553-555 (2002).
-

References

-
- [114] S. Jeong, B. Kim, and B. Lee, "Photoluminescence dependence of ZnO films grown on Si(100) by radio-frequency magnetron sputtering on the growth ambient", *Appl. Phys. Lett.* **82**, 2625-2627 (2003).
- [115] S. I. Park, T. S. Cho, S. J. Doh, J. L. Lee, and J. H. Je, "Structural evolution of ZnO/sapphire(001) heteroepitaxy studied by real time synchrotron x-ray scattering", *Appl. Phys. Lett.* **77**, 349-351 (2000).
- [116] M. K. Ryu, S. H. Lee, M. S. Jang, G. N. Panin, and T. W. Kang, "Postgrowth annealing effect on structural and optical properties of ZnO films grown on GaAs substrates by the radio frequency magnetron sputtering technique", *J. Appl. Phys.* **92**, 154-158 (2002).
- [117] L. Y. Chen, W. H. Chen, J. J. Wang, and F. C. N. Hong, and Y. K. Su, "Hydrogen-doped high conductivity ZnO films deposited by radio-frequency magnetron sputtering", *Appl. Phys. Lett.* **85**, 5628-5630 (2004).
- [118] K. K. Kim, J. H. Song, H. J. Jung, W. K. Choi, S. J. Park, and J. H. Song, "The grain size effects on the photoluminescence of ZnO/ α -Al₂O₃ grown by radio-frequency magnetron sputtering", *J. Appl. Phys.* **87**, 3573-3575 (2000).
- [119] K. Tominaga, S. Iwamura, Y. Shintani, and O. Tada, "Influence of bombardment by energetic atoms on c-axis orientation of ZnO films", *Jpn. J. Appl. Phys.* **21**, 999-1002 (1982).
- [120] S. J. Doh, S. I. Park, T. S. Cho, and J. H. Je, "Effects of grid bias on ZnO/ α -Al₂O₃ (0001) heteroepitaxy", *J. Vac. Sci. Technol. A* **17**, 3003-3007 (1999).
- [121] S. J. Chang, Y. K. Su, and Y. P. Shei, "High quality ZnO thin films on InP substrates prepared by radio frequency magnetron sputtering. I. Material study", *J. Vac. Sci. Technol. A* **13**, 381-384 (1995).
- [122] Y. T. Zhang, G. T. Du, D. L. Liu, X. Q. Wang, Y. Ma, J. Z. Wang, J. Z. Yin, X. T. Yang, X. K. Hou, and S. R. Yang, "Crystal growth of undoped ZnO films on Si substrates under different sputtering conditions", *J. Crys. Growth* **243**, 439-443 (2002).
- [123] A. V. Singh, R. M. Mehra, A. Wakahara and A. Yoshida, "p-type conduction in codoped ZnO thin films", *J. Appl. Phys.* **93**, 396-399 (2003).
- [124] K. K. Kim, H. S. Kim, D. K. Hwang, J. H. Lim, and S. J. Park, "Realization of p-type ZnO thin films via phosphorus doping and thermal activation of the dopant", *Appl. Phys. Lett.* **83**, 63-65 (2003).
- [125] D. K. Hwang, K. H. Bang, M. C. Jeong, J. M. Myoung, "Effects of RF power variation on properties of ZnO thin films and electrical properties of p-n homojunction", *J. Cryst. Growth* **254**, 449-455 (2003).
- [126] M. Sanmyo, Y. Tomita, and K. Kobayashi, "Preparation of zinc oxide films containing Be and N atoms by radio frequency magnetron sputtering", *Thin Solid Films* **472**, 189-194 (2005).
- [127] K. K. Kim, S. Niki, J. Y. Oh, J. O. Song, T. Y. Seong, S. J. Park, S. Fujita, and S. W. Kim, "High electron concentration and mobility in Al-doped n-ZnO epilayer achieved via dopant activation using rapid-thermal annealing", *J. Appl. Phys.* **97**, 066103 (2005).
- [128] R. P. Wang, L. L. H. King, and A. W. Sleight, "Highly conducting transparent thin films based on zinc oxide", *J. Mater. Res.* **11**, 1659-1664 (1996).
- [129] R. Cebulla, R. Wendt, and K. Ellmer, "Al-doped zinc oxide films deposited by simultaneous rf and dc excitation of a magnetron plasma: Relationships between plasma parameters and structural and electrical film properties", *J. Appl. Phys.* **83**, 1087-1095 (1998).
- [130] V. Assuncao, E. Fortunato, A. Marques, A. Goncalves, I. Ferreira, H. Aguas, and R. Martins "New challenges on gallium-doped zinc oxide films prepared by r.f. magnetron sputtering", *Thin Solid Films* **442**, 102-106 (2003).
- [131] T. Minami, H. Sato, H. Nanto, and S. Takata, "Group III impurity doped zinc oxide thin films prepared by rf magnetron sputtering", *Jpn. J. Appl. Phys.* **24**, L781-L784 (1985).
- [132] V. Assuncao, E. Fortunato, A. Marques, H. Aguas, I. Ferreira, M. E. V. Costa, and R. Martins, "Influence of the deposition pressure on the properties of transparent and conductive ZnO:Ga thin-film produced by r.f. sputtering at room temperature", *Thin Solid Films* **427**, 401-405 (2003).
- [133] E. Kay, "Magnetic field effects on an abnormal truncated glow discharge and their relation to sputtered thin-film growth", *J. Appl. Phys.* **34**, 760-768 (1963).
- [134] R. F. Bunshah, "Handbook of deposition technologies for films and coatings - Science, technology and applications", (2nd Edition) William Andrew Publishing/Noyes 1994.
- [135] P. R. Willmott, and J. R. Huber, "Pulsed laser vaporization and deposition", *Rev. Mod. Phys.* **72**, 315-328 (2000).
-

References

-
- [136] Rainer Waser (Editor), "Nanoelectronics and Information Technology – Advanced Electronic Materials and Novel Devices", Wiley-VCH Verlag GmbH & Co. 2003.
- [137] W. Prellier, A. Fouchet, B. Mercey, C. Simon, and B. Raveau, "Laser ablation of Co:ZnO films deposited from Zn and Co metal targets on (0001) Al_2O_3 substrates", *Appl. Phys. Lett.* **82**, 3490-3492 (2003).
- [138] R. D. Vispute, V. Talyansky, Z. Trajanovic, S. Choopun, M. Downes, R. P. Sharma, T. Venkatesan, M. C. Woods, R. T. Lareau, K. A. Jones, and A. A. Iliadis, "High quality crystalline ZnO buffer layers on sapphire (001) by pulsed laser deposition for III-V nitrides", *Appl. Phys. Lett.* **70**, 2735-2737 (1997).
- [139] H. Cao, J. Y. Wu, H. C. Ong, J. Y. Dai, and R. P. H. Chang, "Second harmonic generation in laser ablated zinc oxide thin films", *Appl. Phys. Lett.* **73**, 572-574 (1998).
- [140] V. Craciun, J. Elders, J. G. E. Gardeniers, and I. W. Boyd, "Characteristics of high quality ZnO thin films deposited by pulsed laser deposition", *Appl. Phys. Lett.* **65**, 2963-2965 (1994).
- [141] A. Mitra, and R. K. Thareja, "Photoluminescence and ultraviolet laser emission from nanocrystalline ZnO thin films", *J. Appl. Phys.* **89**, 2025-2028 (2001).
- [142] J. N. Zeng, J. K. Low, Z. M. Ren, T. Liew, and Y. F. Lu, "Effect of deposition conditions on optical and electrical properties of ZnO films prepared by pulsed laser deposition", *Appl. Surf. Sci.* **197**, 362-367 (2002).
- [143] F. K. Shan, B. C. Shin, S. W. Jang, Y. S. Yu, "Substrate effects of ZnO thin films prepared by PLD technique", *J. Eur. Ceram. Soc.* **197**, 362-367 (2002).
- [144] M. Okoshi, K. Higashikawa, and M. Hanabusa, "Pulsed laser deposition of ZnO thin films using a femtosecond laser", *Appl. Surf. Sci.* **154**, 424-427 (2000).
- [145] O. Lopatiuk, W. Burdett, and L. Chernyak, K. P. Ip, Y. W. Heo, D. P. Norton, S. J. Pearton, B. Hertog, P. P. Chow, and A. Osinsky, "Minority carrier transport in p-type $\text{Zn}_{0.9}\text{Mg}_{0.1}\text{O}$ doped with phosphorus", *Appl. Phys. Lett.* **86**, 012105 (2005).
- [146] Y. W. Heo, S. J. Park, K. Ip, S. J. Pearton, and D. P. Norton, "Transport properties of phosphorus-doped ZnO thin films", *Appl. Phys. Lett.* **83**, 1128-1130 (2003).
- [147] Y. W. Heo, Y. W. Kwon, Y. Li, S. J. Pearton, and D. P. Norton, "p-type behavior in phosphorus-doped (Zn,Mg)O device structures", *Appl. Phys. Lett.* **84**, 3474-3476 (2004).
- [148] A. Tsukazaki, H. Saito, K. Tamura, M. Ohtani, and H. Koinuma, M. Sumiya, S. Fuke, T. Fukumura, and M. Kawasaki, "Systematic examination of carrier polarity in composition spread ZnO thin films codoped with Ga and N", *Appl. Phys. Lett.* **81**, 235-237 (2002).
- [149] M. Joseph, H. Tabata, H. Saeki, K. Ueda, and T. Kawai, "Fabrication of the low-resistive p-type ZnO by codoping method", *Physica B* **302**, 140-148 (2001).
- [150] T. Ohshima, T. Ikegami, K. Ebihara, J. Asmussen, and R. K. Thareja, "Synthesis of p-type ZnO thin films using co-doping techniques based on KrF excimer laser deposition", *Thin Solid Films* **435**, 49-55 (2003).
- [151] M. Kumar, R. M. Mehra, A. Wakahara, M. Ishida, and A. Yoshida, "Epitaxial growth of high quality ZnO:Al film on silicon with a thin $\gamma\text{-Al}_2\text{O}_3$ buffer layer", *J. Appl. Phys.* **93**, 3837-3843 (2003).
- [152] S. J. Henley, M. N. R. Ashfold, and D. Cherns, "The growth of transparent conducting ZnO films by pulsed laser ablation", *Surf. Coat. Technol.* **177**, 271-276 (2004).
- [153] A. V. Singh, R. M. Mehra, N. Buthrath, A. Wakahara, and A. Yoshida, "Highly conductive and transparent aluminum-doped zinc oxide thin films prepared by pulsed laser deposition in oxygen ambient", *J. Appl. Phys.* **90**, 5661-5665 (2001).
- [154] M. Lorenz, E. M. Kaidashev, H. V. Wenckstern, V. Riede, C. Bundesmann, D. Spemann, G. Benndorf, H. Hochmuth, A. Rahm, H. C. Semmelhack, and M. Grundmann, "Optical and electrical properties of epitaxial $(\text{Mg,Cd})_x\text{Zn}_{1-x}\text{O}$, ZnO, and ZnO:(Ga,Al) thin films on c-plane sapphire grown by pulsed laser deposition", *Solid State Electron.* **47**, 2205-2209 (2003).
- [155] M. Hiramatsu, K. Imaeda, N. Horio, and M. Nawata, "Transparent conducting ZnO thin films prepared by XeCl excimer laser ablation", *J. Vac. Sci. Technol. A* **16**, 669-673 (1998).
- [156] A. Suzuki, T. Matsushita, T. Aoki, Y. Yoneyama, and M. Okuda, "Micro-textured milky ZnO:Ga thin films fabricated by pulsed laser deposition using second-harmonic-generation of Nd:YAG laser", *Jpn. J. Appl. Phys.* **38**, L71-L73 (1999).
- [157] S. Yata, Y. Nakashima, T. Kobayashi, "Improved crystallinity of ZnO thin films grown by the 'Aurora PLD method'", *Thin Solid Films* **445**, 259-262 (2003).
- [158] H. C. Ong, A. X. E. Zhu, and G. T. Du, "Dependence of the excitonic transition energies and mosaicity on residual strain in ZnO thin films", *Appl. Phys. Lett.* **80**, 941-943 (2002).
-

References

-
- [159] I. Satoh, T. Kobayashi, K. Katayama, T. Okada and T. Itoh, "Magneto-photoluminescence of novel magnetic semiconductor $\text{Zn}_{1-x}\text{Cr}_x\text{O}$ grown by PLD method", *Appl. Phys. A* **79**, 1445-1447 (2004).
- [160] E. Millon, O. Albert, J. C. Loulergue, J. Etchepare, D. Hulin, W. Seiler, and J. Perrière, "Growth of heteroepitaxial ZnO thin films by femtosecond pulsed-laser deposition", *J. Appl. Phys.* **88**, 6937-6939 (2000).
- [161] J. Perrière, E. Millon, W. Seiler, C. B. Leborgne, V. Craciun, O. Albert, J. C. Loulergue, and J. Etchepare, "Comparison between ZnO films grown by femtosecond and nanosecond laser ablation", *J. Appl. Phys.* **91**, 690-696 (2002).
- [162] N. J. Ianno, L. McConville, N. Shaikh, S. Pittal, and P.G. Snyder "Characterization of pulsed laser deposited zinc oxide", *Thin Solid Films* **220**, 92-99 (1992).
- [163] S. Choopun, R. D. Vispute, W. Noch, A. Balsamo, R. P. Sharma, T. Venkatesan, A. Iliadis, and D. C. Look, "Oxygen pressure-tuned epitaxy and optoelectronic properties of laser-deposited ZnO films on sapphire", *Appl. Phys. Lett.* **75**, 3947-3949 (1999).
- [164] E. M. Kaidashev, M. Lorenz, H. V. Wenckstern, A. Rahm, H. C. Semmelhack, K. H. Han, G. Benndorf, C. Bundesmann, H. Hochmuth, and M. Grundmann "High electron mobility of epitaxial ZnO thin films on c-plane sapphire grown by multistep pulsed-laser deposition", *Appl. Phys. Lett.* **82**, 3901-3903 (2003).
- [165] S. G. Lee, D. S. Hwang, Y. K. Park, and J. C. Park, "Deposition angle-dependent morphology of laser deposited $\text{YBa}_2\text{Cu}_3\text{O}_7$ thin films", *Appl. Phys. Lett.* **65**, 764-766 (1994).
- [166] H. Takikawa, K. Kimura, R. Miyano, and T. Sakakibara, "Cathodic arc deposition with activated anode (CADAA) for preparation of in situ doped thin solid films", *Vacuum* **65**, 433-438 (2002).
- [167] R. Miyano, K. Kimura, K. Izumi, H. Takikawa, and T. Sakakibara, "Preparation of metal nitride and oxide thin films using shielded reactive vacuum arc deposition", *Vacuum* **59**, 159-167 (2000).
- [168] W. Li, D. S. Mao, F. M. Zhang, X. Wang, X. H. Liu, S. C. Zou, Y. K. Zhu, Q. Li, and J. F. Xu, "ZnO:Zn phosphor thin films prepared by filtered arc deposition", *J. Vac. Sci. Technol. B* **19**, 1004-1007 (2001).
- [169] T. David, S. Goldsmith, R. L. Boxman, "Electro-optical and structural properties of thin ZnO films, prepared by filtered vacuum arc deposition", *Thin Solid Films* **447**, 61-67 (2004).
- [170] T. A. Edison, "Process of Duplicating Phonograms", US Patent 484 582, October 18, 1892.
- [171] H. Wroe, "The magnetic stabilization of low pressure d.c. arcs", *Br. J. Appl. Phys.* **9**, 488-491, 1958.
- [172] A. S. Gilmour Jr., and D. L. Lockwood, "Pulsed metallic-plasma generators", *Proc. IEEE* **60**, 977-991 (1972).
- [173] M. Kikuchi, S. Nagakura, H. Ohmura, and S. Oketani, "Structures of the metal films produced by vacuum-arc evaporation method", *Jpn. J. Appl. Phys.* **4**, 940-940 (1965).
- [174] I. Grimberg, V. N. Zhitomirsky, R. L. Boxman, S. Goldsmith, and B. Z. Weiss, "Multicomponent Ti-Zr-N and Ti-Nb-N coatings deposited by vacuum arc", *Surf. Coat. Technol.* **108**, 154-159 (1998).
- [175] E. Ertürk, and H. J. Heuvel, "Adhesion and structure of TiN arc coatings", *Thin Solid Films* **153**, 135-147 (1987).
- [176] H. Takikawa, K. Kimura, R. Miyano, and T. Sakakibara, "ZnO film formation using a steered and shielded reactive vacuum arc deposition", *Thin Solid Films* **377**, 74-80 (2000).
- [177] R. L. Boxman, V. Zhitomirsky, B. Alterkop, E. Gidalevich, I. Beilis, M. Keidar and S. Goldsmith, "Recent progress in filtered vacuum arc deposition", *Surf. Coat. Technol.* **86**, 243-253 (1996).
- [178] P. J. Martin, A. Bendavid and H. Takikawa, "Ionized plasma vapor deposition and filtered arc deposition; processes, properties and applications", *J. Vac. Sci. Technol. A* **17**, 2351-2359 (1999).
- [179] S. Anders, A. Anders, and I. Brown, "Macroparticle-free thin-films produced by an efficient vacuum-arc deposition technique", *J. Appl. Phys.* **74**, 4239-4241 (1993).
- [180] I. I. Beilis, A. Shashuri, D. Arbilly, S. Goldsmith, and R. L. Boxman, "Copper film deposition by a hot refractory anode vacuum arc", *Surf. Coat. Technol.* **177**, 233-237 (2004).
- [181] I. I. Beilis, S. Goldsmith, and R. L. Boxman, "The hot refractory anode vacuum arc: a new plasma source for metallic film deposition", *Surf. Coat. Technol.* **133**, 91-95 (2000).
- [182] I. G. Brown, "Cathodic arc deposition of films", *Annu. Rev. Mater. Sci.* **28**, 243-269 (1998).
-

References

-
- [183] S. Meassick, C. Chan, and R. Allen, "Thin film deposition techniques utilizing the anodic vacuum arc", *Surf. Coat. Technol.* **54**, 343–348 (1992).
- [184] H. Ehrich, J. Schuhmann, G. Musa, A. Popescu, and I. Mustata, "Adhesive metal films obtained by thermionic vacuum arc (TVA) deposition", *Thin Solid Films* **333**, 95–102 (1998).
- [185] M. M. M. Bilek, and W. I. Milne, "Filtered cathodic vacuum arc (FCVA) deposition of thin film silicon", *Thin Solid Films* **291**, 299–304 (1996).
- [186] A. Dickinson, I. G. Brown, R. A. MacGill, and M. R. Dickinson, "'Triggerless' triggering of vacuum arcs", *J. Phys. D: Appl. Phys.* **31**, 584–587 (1998).
- [187] A. G. Nikolaev, G. Y. Yushkov, E. M. Oks, R. A. MacGill, M. R. Dickinson, and I. G. Brown, "Vacuum arc trigger systems based on ExB discharges", *Rev. Sci. Instrum.* **67**, 3095–3098 (1996).
- [188] A. Anders, "Approaches to rid cathodic arc plasmas of macro- and nanoparticles: a review", *Surf. Coat. Technol.* **120**, 319–330 (1999).
- [189] R. L. Boxman, and S. Goldsmith, "A model for a uniform steady-state vacuum arc with a hot anode", *IEEE Trans. Plasma Sci.* **7**, 661–665 (1989).
- [190] R. L. Boxman, "Twenty-five years of progress in vacuum arc research and utilization", *IEEE Trans. Plasma Sci.* **25**, 1174–1186 (1997).
- [191] R. L. Boxman, "High-current vacuum arc column motion on rail electrodes", *J. Appl. Phys.* **48**, 1885–1890 (1977).
- [192] C. N. Tai, E. S. Koh, and K. Akari, "Macroparticles on TiN films prepared by the arc ion plating process", *Surf. Coat. Technol.* **43**, 324–335 (1990).
- [193] B. Juttner, "On the variety of cathode craters of vacuum arcs, and the influence of the cathode temperature", *Physica C* **114**, 255–261 (1982).
- [194] H. Randhawa, and P. C. Johnson, "Technical note: A review of cathodic arc plasma deposition processes and their applications", *Surf. Coat. Technol.* **31**, 303–318 (1987).
- [195] D. B. Boercker, S. Falabella, D. M. Sanders, "Plasma transport in a new cathodic arc ion-source -Theory and experiment", *Surf. Coat. Technol.* **53**, 239–242 (1992).
- [196] I. I. Aksenov, V. A. Belous, V. G. Padalka, and V. M. Khoroshikh. "Transport of plasma streams in a curvilinear plasma-optics system", *Sov. J. Plasma Phys.* **4**, 425–428 (1978).
- [197] H. Han, F. Ryan, and M. M. Clure, "Ultra-thin tetrahedral amorphous carbon film as slider overcoat for high areal density magnetic recording", *Surf. Coat. Technol.* **120**, 579–584 (1999).
- [198] S. Anders, A. Anders, M. R. Dickinson, R. MacGill, and I. G. Brown, "S-shaped magnetic macroparticle filter for cathodic arc deposition", *IEEE Trans. Plasma Sci.* **25**, 670–675 (1997).
- [199] I. I. Aksenov, V. A. Belous, V. V. Vasil'ev, Y. Y. Volkov, and V. E. Strel'nitskij, "A rectilinear plasma filtering system for vacuum-arc deposition of diamond-like carbon coatings", *Diam. Relat. Mater.* **8**, 468–471 (1999).
- [200] J. Storer, J. E. Galvin, and I. G. Brown, "Transport of vacuum arc plasma through straight and curved magnetic ducts", *J. Appl. Phys.* **66**, 5245–5250 (1989).
- [201] T. Schulke, and A. Anders, "Velocity distribution of carbon macroparticles generated by pulsed vacuum arcs", *Plasma Sources Sci. Technol.* **8**, 567–571 (1999).
- [202] A.I. Ryabchikov, and I.B. Stepanov, "Investigations of forming metal-plasma flows filtered from microparticle fraction in vacuum arc evaporators", *Rev. Sci. Instrum.* **69**, 810–812 (1998).
- [203] T. Utsumi, and J. H. English, "Study of electrode products emitted by vacuum arcs in form of molten metal particles", *J. Appl. Phys.* **46**, 126–131 (1975).
- [204] D. M. Sanders, and A. Anders, "Review of cathodic arc deposition technology at the start of the new millennium", *Surf. Coat. Technol.* **133**, 78–90 (2000).
- [205] X. Shi, B. K. Tay, and S. P. Lau, "The double bend filtered cathodic arc technology and its applications", *Int. J. Mod. Phys. B* **14**, 136–153 (2000).
- [206] X. Shi, D. I. Flynn, B. K. Tay, and H. S. Tan, "Filtered cathodic arc source", US6031239.
- [207] X. Shi, M. Fulton, D. Flynn, B. K. Tay, and H. S. Tan, "Filtered cathodic arc source deposition apparatus", US2003085123.
- [208] W. D. Davis, and H. C. Miller, "Analysis of the electrode products emitted by dc arcs in a vacuum ambient", *J. Appl. Phys.* **40**, 2212–2221 (1969).
- [209] I. G. Brown, "Vacuum arc ion sources", *Rev. Sci. Instrum.* **65**, 3061–3081 (1994).
- [210] R. L. Boxman, and S. Goldsmith, "Principles and applications of vacuum arc coatings", *IEEE Trans. Plasma Sci.* **17**, 705–712 (1989).
-

References

-
- [211] H. W. Lee, S. P. Lau, Y. G. Wang, K. Y. Tse, H. H. Hng, and B. K. Tay, "Structural, electrical and optical properties of Al-doped ZnO thin films prepared by filtered cathodic vacuum arc technique", *J. Cryst. Growth* **268**, 596-601 (2004).
- [212] S. Bethke, H. Pan, and B. W. Wessels, "Luminescence of heteroepitaxial zinc oxide", *Appl. Phys. Lett.* **52**, 138-140 (1988).
- [213] A. B. M. A. Ashrafi, A. Ueta, A. Avramescu, H. Kumano, I. Suemune, Y. W. Ok and T. Y. Seong, "Growth and characterization of hypothetical zinc-blende ZnO films on GaAs(001) substrates with ZnS buffer layers", *Appl. Phys. Lett.* **76**, 550-552 (2000).
- [214] T. Makino, Y. Segawa, S. Yoshida, A. Tsukazaki, A. Ohtomo, and M. Kawasaki, "Gallium concentration dependence of room-temperature near-band-edge luminescence in n-type ZnO:Ga", *Appl. Phys. Lett.* **85**, 759-761 (2004).
- [215] J. Ye, S. Gu, S. Zhu, T. Chen, L. Hu, F. Qin, R. Zhang, Y. Shi, and Y. Zheng, "The growth and annealing of single crystalline ZnO films by low-pressure MOCVD", *J. Cryst. Growth* **243**, 151-156 (2002).
- [216] H. Z. Wu, K. M. He, D. J. Qiu, and D. M. Huang, "Low-temperature epitaxy of ZnO films on Si (001) and silica by reactive e-beam evaporation", *J. Crystal Growth* **217**, 131-137 (2000).
- [217] S. A. Studenikin, N. Golego, and M. Cocivera, "Fabrication of green and orange photoluminescent, undoped ZnO films using spray pyrolysis", *J. Appl. Phys.* **84**, 2287-2294 (1998).
- [218] D. P. Shepherd, C. L. Bonner, C. T. A. Brown, W. A. Clarkson, A. C. Tropper, D. C. Hanna, and H. E. Meissner, "High-numerical-aperture, contact-bonded, planar waveguides for diode-bar-pumped lasers", *Opt. Commun.* **160**, 47-50 (1999).
- [219] C. L. Bonner, T. Bhutta, D. P. Shepherd, and A. C. Tropper, "Double-clad structures and proximity coupling for diode-bar-pumped planar waveguide lasers", *IEEE J. Quantum Electron.* **36**, 236-242 (2000).
- [220] J. M. Eggleston, T. J. Kane, K. Kuhn, J. Unternahrer, and R. L. Byer, "The slab geometry laser-part 1: theory", *IEEE J. Quantum Electron.* **20**, 289-301 (1984).
- [221] X. J. Lu, C. H. Jang, D. C. An, Q. J. Zhou, L. Sun, X. P. Zhang, R. T. Chen, and D. Dawson, "Polymeric multimode waveguide based electro-optic modulator with a vertically configured dumping planar waveguide," *Appl. Phys. Lett.* **81**, 795-797 (2002).
- [222] F. C. Blom, D. R. V. Dijk, H. J. W. M. Hoekstra, A. Driessen, and T. J. A. Popma, "Experimental study of integrated-optics microcavity resonators: Toward an all-optical switching device," *Appl. Phys. Lett.* **71**, 747-749 (1997).
- [223] S. Kim, "Expanded-core planar waveguide in variable optical attenuator", *Jpn. J. Appl. Phys.* **44**, 6042-6046 (2005).
- [224] S. M. Sze, "Physics of semiconductor devices," 2nd edition. New York: Wiley, 1981.
- [225] X. L. Xu, S. P. Lau, J. S. Chen, G. Y. Chen, and B. K. Tay, "Polycrystalline ZnO thin films on Si (100) deposited by filtered cathodic vacuum arc", *J. Crystal Growth* **223**, 201-205 (2001).
- [226] H. W. Lee, S. P. Lau, Y. G. Wang, B. K. Tay, and H. H. Hng, "Internal stress and surface morphology of zinc oxide thin films deposited by filtered cathodic vacuum arc technique", *J. Cryst. Growth* **458**, 15-19 (2004).
- [227] R. J. Deri, E. Kapon, and L. M. Schiavone, "Scattering in low-loss GaAs/AlGaAs rib waveguides", *Appl. Phys. Lett.* **51**, 789-791 (1987).
- [228] J. Velenta, I. Pelent, and J. Linnros, "Waveguiding effects in the measurement of optical gain in a layer of Si nanocrystal", *Appl. Phys. Lett.* **81**, 1396-1398 (2002).
- [229] J. M. Lee, K. M. Chang, K. K. Kim, W. K. Choi, and S. J. Park, "Dry etching of ZnO using an inductively coupled plasma," *J. Electrochem. Soc.* **148**, G1-G3 (2001).
- [230] K. Ip, K. H. Baik, M. E. Overberg, E. S. Lambers, Y. W. Heo, D. P. Norton, S. J. Pearton, F. Ren, and J. M. Zavada, "Effect of high-density plasma etching on the optical properties and surface stoichiometry of ZnO," *Appl. Phys. Lett.* **81**, 3546-3548 (2002).
- [231] M. A. Khan, C. J. Sun, J. W. Yang, Q. Chen, B. W. Lim, M. Z. Anwar, A. Osinsky, and H. Temkin, "Cleaved cavity optically pumped InGaN-GaN laser grown on spinel substrates", *Appl. Phys. Lett.* **69**, 2418-2420 (1996).
- [232] R. F. Pierret, "Semiconductor fundamentals", 2nd edition. New York: Addison-Wesley, 1988.
- [233] U. Ozgur, Y. I. Alivov, C. Liu, A. Teke, M. A. Reshchikov, S. Dogan, V. Avrutin, S. J. Cho, and H. Morkoc, "A comprehensive review of ZnO materials and devices", *Appl. Phys. Lett.* **98**, 041301 (2005).
- [234] D. S. Wiersma, "The smallest random laser", *Nature* **406**, 132-133 (2000).
-

References

-
- [235] G. V. Soest, "Experiments on random lasers", Ph.D. thesis, University of Twente Netherlands (2001).
- [236] H. Cao, "Lasing in Disordered Media", in "Progress in Optics", ed. E. Wolf, North-Holland, 2003, vol. 45.
- [237] V. S. Letokhov, "Generation of light by a scattering medium with negative resonance absorption", *Sov. Phys.—JETP* **26**, 835-840 (1968).
- [238] H. Cao, J. Y. Xu, Y. Ling, A. L. Burin, E. W. Seeling, X. Liu, and R. P. Chang, "Random laser with coherent feedback", *IEEE J. Sel. Top. Quantum Electron.* **9**, 111-119 (2003).
- [239] H. Cao, J. Y. Xu, E. W. Seelig, and R. P. H. Chang, "Microlaser made of disordered media", *Appl. Phys. Lett.* **76**, 2997-2999 (2000).
- [240] C. W. Teng, J. F. Muth, Ü. Özgür, M. J. Bergmann, H. O. Everitt, A. K. Sharma, C. Jin, and J. Narayan, "Refractive indices and absorption coefficients of $\text{Mg}_x\text{Zn}_{1-x}\text{O}$ alloys", *Appl. Phys. Lett.* **76**, 979-981 (2000).
- [241] W. I. Park, G. C. Yi, and H. M. Jang, "Metalorganic vapor-phase epitaxial growth and photoluminescent properties of $\text{Zn}_{1-x}\text{Mg}_x\text{O}$ ($0 \leq x \leq 0.49$) thin films", *Appl. Phys. Lett.* **79**, 2022-2023 (2001).
- [242] W. I. Park, D. H. Kim, S. W. Jung and G. C. Yi, "Metalorganic vapor-phase epitaxial growth of vertically well-aligned ZnO nanorods", *Appl. Phys. Lett.* **80**, 4232-4234 (2002).
- [243] M. Y. Han, J. H. Jou, "Determination of the mechanical properties of r.f.-magnetron-sputtered zinc oxide thin films on substrates", *Thin Solid Films* **260**, 58-64 (1995).
- [244] T. R. Taylor, P. J. Hansen, B. Acikel, N. Pervez, R. A. York, S. K. Streiffer, and J. S. Speck, "Impact of thermal strain on the dielectric constant of sputtered barium strontium titanate thin films", *Appl. Phys. Lett.* **80**, 1979-1980 (2002).
- [245] L. Fu, P. Lever, H. H. Tan, C. Jagadish, P. Reece, and M. Gal, "Suppression of interdiffusion in InGaAs/GaAs quantum dots using dielectric layer of titanium dioxide", *Appl. Phys. Lett.* **82**, 2613-2615 (2003).
- [246] H. Cao, J. Y. Xu, S. H. Chang, S. T. Ho, E. W. Seelig, and X. Liu, and R. P. H. Chang, "Spatial confinement of laser light in active random media", *Phys. Rev. Lett.* **84**, 5584-5587 (2000).
- [247] H. Cao, J. Y. Xu, S. H. Chang, and S. T. Ho, "Transition from amplified spontaneous emission to laser action in strongly scattering media", *Phys. Rev. E* **61**, 1985-1989 (2000).
- [248] B. G. Hoover, L. Deslauriers, S. M. Grannell, R. E. Ahmed, D. S. Dilworth, B. D. Athey, and E. N. Leith, "Correlations among angular wave component amplitudes in elastic multiple-scattering random media", *Phys. Rev. E* **65**, 026614 (2002).
- [249] Y. Ling, H. Cao, A. L. Burin, M. A. Ratner, X. Liu, and R. P. H. Chang, "Investigation of random lasers with resonant feedback", *Phys. Rev. A* **64**, 063808 (2001).
- [250] M. J. Rost, D. A. Quist, and J. W. M. Frenken, "Grains, growth and grooving", *Phys. Rev. Lett.* **91**, 026101 (2003).
- [251] C. E. Krill, L. Helfen, D. Michels, H. Natter, A. Fitch, O. Masson, and R. Birringer, "Size-dependent grain-growth kinetics observed in nanocrystalline Fe", *Phys. Rev. Lett.* **86**, 842-845 (2001).
- [252] F. J. P. Schuurmans, M. Megens, D. Vanmaekelbergh, and A. Lagendijk, "Light scattering near the localization transition in macroporous GaP networks", *Phys. Rev. Lett.* **83**, 2183-2186 (1999).
- [253] D. S. Wiersma, P. Bartolini, A. Lagendijk and R. Righini, "Localization of light in a disordered medium", *Nature* **390**, 671-673 (1997).
- [254] N. M. Lawandy, R. M. Balachandran, A. S. L. Gomes, and E. Sauvain, "Laser action in strongly scattering media", *Nature* **368**, 436-438 (1994).
- [255] R. V. Ambartsumyan, N. G. Basov, P. G. Kryukov, and V. S. Letokhov, "A laser with a nonresonant feedback", *IEEE J. Quantum Electron.* **2**, 442-446 (1966).
- [256] R. Huang, and A. H. Kitai, "Temperature-dependence of the growth orientation of atomic layer growth MgO", *Appl. Phys. Lett.* **61**, 1450-1452 (1992).
- [257] X.Y. Chen, K. H. Wong, C.L. Mak, X.B. Yin, M. Wang, J. M. Liu, and Z. G. Liu, "Selective growth of (100)-, (110)-, and (111)-oriented MgO films on Si(100) by pulsed laser deposition", *J. Appl. Phys.* **91**, 5728-5734 (2002).
- [258] W. J. DeSisto, and R. L. Henry, "Deposition of (100) orientated MgO thin films on sapphire by a spray pyrolysis method", *Appl. Phys. Lett.* **56**, 2522-2523 (1990).
-

References

-
- [259] C. V. Thompson, "Structure evolution during processing of polycrystalline films", *Annu. Rev. Mater. Sci.* **30**, 159-190 (2000).
- [260] B. D. Cullity, "Elements of X-ray diffractions", Addison-Wesley, Reading, MA, 1978.
- [261] C. H. Choi, and S. H. Kim, "Effects of post-annealing temperature on structural, optical, and electrical properties of ZnO and Zn_{1-x}Mg_xO films by reactive RF magnetron sputtering", *J. Crystal Growth* **283**, 170-179 (2005).
- [262] H. D. Li, S. F. Yu, A. P. Abiyasa, C. Yuen, S. P. Lau, H. Y. Yang, and E. S. P. Leong, "Strain Dependence of Lasing Mechanisms in ZnO Epilayers", *Appl. Phys. Lett.* **86**, 261111 (2005).
- [263] M. Shukri and R. L. Armstrong, "Coherent, directional, laserlike emission from random gain media", *Appl. Opt.* **39**, 4300-4305 (2000).
- [264] G. Zacharakis, N. A. Papadogiannis, and T. G. Papazoglou, "Random lasing following two-photon excitation of highly scattering gain media", *Appl. Phys. Lett.* **81**, 2511-2513 (2002).
- [265] H. Cao, Y. G. Zhao, X. Liu, E. W. Seelig, and R. P. H. Chang, "Effect of external feedback on lasing in random media", *Appl. Phys. Lett.* **75**, 1213-1215 (1999).
- [266] P. C. de Oliveira, J. A. McGreevy, and N. M. Lawandy, "External-feedback effects in high-gain scattering media", *Opt. Lett.* **22**, 895-897 (1997).
- [267] Y. Feng, and K. I. Ueda, "One-mirror random laser", *Phys. Rev. A* **68**, 025803 (2003).
- [268] S. F. Yu, and E. S. P. Leong, "High-power single-mode ZnO thin-film random lasers", *IEEE J. Quantum Electron.* **40**, 1186-1194 (2004).
- [269] C. Vanneste, and P. Sebbah, "Selective excitation of localized modes in active random media", *Phys. Rev. Lett.* **87**, 183903 (2001).
- [270] C. H. Park, S. B. Zhang, and S. H. Wei, "Origin of p-type doping difficulty in ZnO: The impurity perspective", *Phys. Rev. B* **66**, 073202 (2002).
- [271] W. Walukiewicz, "Defect formation and diffusion in heavily-doped semiconductors", *Phys. Rev. B* **50**, 5221-5225 (1994).
- [272] C. G. Van de Walle, D. B. Laks, G. F. Neumark, and S. T. Pantelides, "1st-principles calculations of solubilities and doping limits – Li, Na, and N in ZnSe", *Phys. Rev. B* **47**, 9425-9434 (1993).
- [273] S. N. Mohammad, "Contact mechanisms and design principles for alloyed ohmic contacts to *n*-GaN", *J. Appl. Phys.* **95**, 7940-7953 (2004).
- [274] V. A. Dmitriev, K. Irvine, M. Spencer, and G. Kelner, "Low resistivity ($\sim 10^{-5} \Omega\text{cm}^2$) ohmic contacts to 6H silicon carbide fabricated using cubic silicon carbide contact layer", *Appl. Phys. Lett.* **64**, 318-320 (1994).
- [275] N. A. Papanicolaou, A. Edwards, M. V. Rao, and W. T. Anderson, "Si/Pt Ohmic contacts to *p*-type 4H-SiC", *Appl. Phys. Lett.* **73**, 2009-2011 (1998).
- [276] B. J. Johnson, and M. A. Capano, "Mechanism of ohmic behavior of Al/Ti contacts to *p*-type 4H-SiC after annealing", *J. Appl. Phys.* **95**, 5616-5620 (2004).
- [277] J. O. Song, K. K. Kim, S. J. Park, and T. Y. Seong, "Highly low resistance and transparent Ni/ZnO ohmic contacts to *p*-type GaN", *Appl. Phys. Lett.* **83**, 479-481 (2003).
- [278] Y. G. Wang, S. P. Lau, X. H. Zhang, H. H. Hng, H. W. Lee, S. F. Yu, and B. K. Tay, "Enhancement of near-band-edge photoluminescence from ZnO films by face-to-face annealing", *J. Crystal Growth* **259**, 335-342, (2003).
- [279] J. Cho, J. Nah, M. S. Oh, J. H. Song, K. H. Yoon, H. J. Jung, and W. K. Choi, "Enhancement of photoluminescence and electrical properties of Ga-doped ZnO thin film grown on α -Al₂O₃(0001) single-crystal substrate by rf magnetron sputtering through rapid thermal annealing", *Jpn. J. Appl. Phys.* **40**, L1040-1043 (2001).
- [280] Y. I. Alivov, J. E. V. Nostrand, D. C. Look, M. V. Chukichev, and B. M. Ataev, "Observation of 430 nm electroluminescence from ZnO/GaN heterojunction light-emitting diodes", *Appl. Phys. Lett.* **83**, 2943-2945 (2003).
- [281] D. Vogel, P. Krüger, and J. Pollmann, "Ab initio electronic-structure calculations for II-VI semiconductors using self-interaction-corrected pseudopotentials", *Phys. Rev. B* **52**, R14316 (1995).
- [282] P. Bhattacharya, Rasmi R. Das, and R. S. Katiyara, "Fabrication of stable wide-band-gap ZnO/MgO multilayer thin films", *Appl. Phys. Lett.* **83**, 2010-2012 (2003).
- [283] S. J. Pearton, D. P. Norton, K. Ip, Y. W. Heo, and T. Steiner, "Recent advances in processing of ZnO", *J. Vac. Sci. Technol. B* **22**, 932-948 (2004).
- [284] D. M. Bagnall, Y. F. Chen, M. Y. Shen, Z. Zhu, T. Goto, and T. Yao, *J. Cryst. Growth* **184**, 605 (1998).
-

References

-
- [285] B. J. Jin, S. Im, and S. Y. Lee, "Violet and UV luminescence emitted from ZnO thin films grown on sapphire by pulsed laser deposition", *Thin Solid Films* **366**, 107-110 (2000).
- [286] E. G. Bylander, "Surface effects on the low-energy cathodoluminescence of zinc oxide", *J. Appl. Phys.* **49**, 1188-1195 (1978).
- [287] H. J. Egelhaaf and D. Oelkrug, "Luminescence and nonradiative deactivation of excited states involving oxygen defect centers in polycrystalline ZnO", *J. Cryst. Growth* **161**, 190-194 (1996).
- [288] D. M. Bagnall, Y. F. Chen, Z. Zhu, T. Yao, M. Y. Shen, and T. Goto, "High temperature excitonic stimulated emission from ZnO epitaxial layers", *Appl. Phys. Lett.* **73**, 1038-1040 (1998).
- [289] B. D. Yao, Y. F. Chan, and N. Wang, "Formation of ZnO nanostructures by a simple way of thermal evaporation", *Appl. Phys. Lett.* **81**, 757-759 (2002).
- [290] L. Y. Lao, J. G. Wen, and Z. F. Ren, "Hierarchical ZnO nanostructures", *Nano Lett.* **2**, 1287-1291 (2002).
- [291] R. S. Wagner, and W. C. Ellis, "Vapor-liquid-solid mechanism of single crystal growth", *Appl. Phys. Lett.* **4**, 89-90 (1964).
- [292] J. M. Wang, and L. Gao, "Wet chemical synthesis of ultralong and straight single-crystalline ZnO nanowires and their excellent UV emission properties", *J. Mater. Chem.* **13**, 2551-2554 (2003).
- [293] Z. Q. Li, Y. Xie, Y. J. Xiong, R. Zhang, and W. He, "Reverse micelle-assisted route to control diameters of ZnO nanorods by selecting different precursors", *Chem. Lett.* **32**, 760-761 (2003).
- [294] L. Vayssieres, "Growth of arrayed nanorods and nanowires of ZnO from aqueous solutions", *Adv. Mater.* **15**, 464-466 (2003).
- [295] Z. R. R. Tian, J. A. Voigt, J. Liu, B. McKenzie, and M. J. Mcdermott, "Biomimetic arrays of oriented helical ZnO nanorods and columns", *J. Am. Chem. Soc.* **124**, 12954-12955 (2003).
- [296] Y. Li, G. W. Meng, L. D. Zhang, and F. Phillipp, "Ordered semiconductor ZnO nanowire arrays and their photoluminescence properties", *Appl. Phys. Lett.* **76**, 2011-2013 (2000).
- [297] O. Harnack, C. Pacholski, H. Weller, A. Yasuda, and J. M. Wessels, "Rectifying behavior of electrically aligned ZnO nanorods", *Nano Lett.* **3**, 1097-1101 (2003).
- [298] W. I. Park, G. C. Yi, M. Y. Kim, and S. J. Pennycook, "ZnO nanoneedles grown vertically on Si substrates by non-catalytic vapor-phase epitaxy", *Adv. Mater.* **14**, 1841-1843 (2002).
- [299] S. J. An, W. I. Park, G. C. Yi, Y. J. Kim, H. B. Kang, and M. Kim, "Heteroepitaxial fabrication and structural characterizations of ultrafine GaN/ZnO coaxial nanorod heterostructures", *Appl. Phys. Lett.* **84**, 3612-3614 (2004).
- [300] W. I. Park, G. C. Yi, M. Kim, and S. J. Pennycook, "Quantum confinement observed in ZnO/ZnMgO nanorod heterostructures", *Adv. Mater.* **15**, 526-529 (2003).
- [301] Q. Wan, Q. H. Li, Y. J. Chen, T. H. Wang, X. L. He, X. G. Gao, and J. P. Li, "Positive temperature coefficient resistance and humidity sensing properties of Cd-doped ZnO nanowires", *Appl. Phys. Lett.* **84**, 3085-3087 (2004).
- [302] L. F. Dong, J. Jiao, D. W. Tuggle, J. M. Petty, S. A. Elliff, and M. Coulter, "ZnO nanowires formed on tungsten substrates and their electron field emission properties" *Appl. Phys. Lett.* **82**, 1096-1098 (2003).
- [303] Q. Wan, Q. H. Li, Y. J. Chen, T. H. Wang, X. L. He, and J. P. Li, "Fabrication and ethanol sensing characteristics of ZnO nanowire gas sensors", *Appl. Phys. Lett.* **84**, 3654-3656 (2004).
- [304] Q. H. Li, Q. Wan, Y. X. Liang, and T. H. Wang, "Electronic transport through individual ZnO nanowires", *Appl. Phys. Lett.* **84**, 4556-4558 (2004).
- [305] H. D. Li, S. F. Yu, S. P. Lau, and E. S. P. Leong, "Simultaneous formation of visible and ultraviolet random lasings in ZnO films", *Appl. Phys. Lett.* **89**, 021110 (2006).
- [306] J. Ding, H. Jeon, T. Ishihara, M. Hagerott, and T. Yao, "Excitonic gain and laser emission in ZnSe-based quantum wells", *Phys. Rev. Lett.* **69**, 1707-1710 (1992).
- [307] A.L.Burin, M.A.Ratner, H.Cao, and S.H.Chang, "Random laser in one dimension", *Phys. Rev. A*, **88**, 093904 (2002).
-